

UNVEILING THE LOCAL-TO-GLOBAL PROPERTY FUNCTIONS OF  
TRANSIENT AND ACTIVE SOFT MATTER: FROM DYNAMIC GELS TO FIRE  
ANTS

by

ROBERT JAMES WAGNER

B.S., Union College, 2013

A thesis submitted to the  
Faculty of the Graduate School of the  
University of Colorado in partial fulfillment  
of the requirement for the degree of  
Doctor of Philosophy  
Program of Material Science & Engineering  
2022

Committee Members:

Franck Vernerey

Francois Barthelat

Nikolaus Correll

Loren Hough

Rong Long

Wagner, Robert James (Ph.D., Material Science & Engineering)

Unveiling the Local-To-Global Property Functions of Transient and Active Soft

Matter: From Dynamic Gels to Fire Ants

Thesis directed by Associate Professor Franck J. Vernerey

“Dynamic networks” contain bonds that may disconnect and reattach reversibly, imbuing them with nonlinear, viscoelastic mechanical response. Their mechanical response is further complicated when they are comprised of active constituents that can independently do mechanical work as in the case of “active networks”. Even dynamic and active networks composed of seemingly simple constituents may display complex emergent mechanics. Indeed, active networks may even spontaneously morph, locomote, and perturb their surroundings in a way that seemingly violates the first and second laws of thermodynamics if viewed at the material scale (i.e., not accounting for local energy storage and the entropic increases associated with local energy conversion processes). Given the rich mechanical behaviors such systems may demonstrate, engineers aiming to create synthetic versions of dynamic and active networks – whether they be dynamic gels used as tissue engineering scaffolds or swarms of modular robots tasked with completing collective functions – seek to understand how the local, physical interactions in these systems beget their globally emergent responses. In an effort to predictively design these networks, or inversely understand their structure-property functions, engineers often employ multiscale models ranging from continuum approaches (e.g., statistical mechanics) to high fidelity discrete methods (e.g., molecular dynamics). However, hierarchical network structures and transient bonds can introduce steep property gradients and non-affine deformation that render continuum approaches ill-suited for modeling dynamic networks. Furthermore, effective thermodynamic violations imparted by activity render constitutive modeling particularly difficult for

active networks. While high resolution discrete approaches circumvent these issues, they often suffer from high computational cost that makes it difficult to properly map microscale tuning parameters to the emergent macroscale mechanical responses. Therefore, researchers have turned to a tertiary class of discrete, mesoscale network models that coarse-grain constituents to reduce computational expense, but sustain information about networks' microstructures.

In this dissertation, I introduce one such novel, discrete network model and exhibit its general applicability to both dynamic and active networks. In Chapter II of this dissertation, I introduce the discrete model and compare its mechanical stress predictions for star-shaped dynamic polymer networks (undergoing creep and stress relaxation) to those of a state-of-the-art continuum approach, Transient Network Theory (TNT). In Chapter III, I utilize the model to append TNT and introduce a coupled and physically motivated rule of mixture for dynamic networks containing multiple bond types in series that dissociate at different timescales. In Chapter IV, I exhibit the model's use for applied science by using it to accurately predict the topological and mechanical properties of tetra- and octa-poly(ethylene glycol) gels. Finally, in Chapters V and VI I utilize the model to elucidate a set of local interaction rules between fire ants (*S. Invicta*) that may reproduce the emergent treadmilling and protrusion growth dynamics observed experimentally in their collectively aggregated rafts. While proper application of the introduced model to any given system is always contingent on due consideration and capture of the underlying, first-order physics, this body of work demonstrates the robustness and generality of this illuminating and much needed mesoscale framework.

## DEDICATION

This work is dedicated to my cousin, William (“Billy”) Vegso, my Aunt Kathie Dilks Flannery, and our late dog, Blanca.



## ACKNOWLEDGEMENTS

This document reports the majority of successful work we completed during my graduate research. However, the journey was predominantly shaped by the greater volume of “struggles” that are not reflected here. The abandoned projects, manuscript rejections, and countless hours spent trouble-shooting experiments or debugging code may be invisible to audiences of this work, but they are well-known to those who supported me along the way. I am eternally grateful to these individuals.

First, I would like to thank my advisor, Professor Franck J. Vernerey. Besides heavily investing time and funding in me, he taught me to recognize “abandoned projects” as precursors to successful ones; “manuscript rejections” as opportunities to improve the clarity, scientific robustness, and impactfulness of our work; and time I spent “failing” as hours invested in my own efficacy as a researcher. Franck instilled in me ambition to always accomplish more, flexibility to adapt goals to circumstance, and tenacity deriving from the fact that there is always a path forward to those who look for it. While his high expectations were stressful at times, his console was reassuring when needed. As a member of Franck’s group I was also fortunate enough to befriend and learn from brilliant peers. Edu, Shankar, Tong, Sam, Kyle, Prakhar, Jothi, Kieran, Dhileep, Ethan, Kristen, Guillaume, Madison, Xinfu, and Jinyue taught me perseverance and provided camaraderie I will always carry with me.

I would also like to thank the members of my dissertation committee, Prof. F. Barthelat, Prof. L. Hough, Prof. R. Long, and Prof. N. Correll, as well as the other academic mentors and collaborators I have been fortunate to learn from over the years. Amongst these are R. Schwartz (Harriton), H. Kritzer (Harriton), Prof. A. Anderson (Union College), Prof. A. Rapoff (Union College) Prof. R. Bucinell (Union College), Prof. W. Keat (Union College), Dr. Y. Wu (GE), A. Yousef (GE), D. Havelka (GE), J. Pallini (GE), Prof. C. Bowman (CU Boulder), Prof. S. Bryant (CU Boulder), Prof. V. Ferguson (CU Boulder), Prof. B. McLeod (CU Boulder), L. Rose (CU Boulder), Dr. B. Cox (Arachne Consulting), Dr. L. Xu (Jiangsu University), Prof. T. Ware (Texas

A&M), and Prof. M. Silbserstein (Cornell). Each of these individuals played a crucial and positive role in guiding me on my path.

Finally, I would like to thank my family and friends. Mom, Dad, Grace, Amy, Carwen, Blanca, and Lily, there are no words to express how indebted I am to you. The same is true of my beloved friends, Antonio, Carissa, Dwight, Julia, Connor, Aubrey, Bella, Pat, Eric, Brendan, Stephen, Greta, Matt, Tony, Elisa, Zoe, Zac, Jenna, Wahab, Riley, Nolan, Hunter, Nick, Luke, Tyler, Elle, Kyle F., Whitney, Brock, Adam, Atjen, Ebenezer, Keith, Ryan, Dave, Kyle T., Andre, Mikey, Charlie, and everyone else who has caringly broken my focus to provide sustaining bouts of laughter and joy. You make it all worthwhile.

## CONTENTS

### CHAPTER

I.	Introduction.....	1
II.	A network model of transient polymers: exploring the micromechanics of nonlinear viscoelasticity.....	4
III.	Microscale, computational investigation of dynamic polymers with multiple timescales informs TNT .....	43
IV.	A mesoscale model for the micromechanical study of gels.....	59
V.	Treadmilling and protrusion growth in fire ant rafts .....	114
VI.	Computational exploration of treadmilling and protrusion growth observed in fire ant rafts .....	141
VII.	Summary and future work .....	174

BIBLIOGRAPHY.....	176
-------------------	-----

### APPENDIX

A.	Supporting Information for Chapter II.....	195
B.	Supporting Information for Chapter III.....	200
C.	Supporting Information for Chapter IV.....	216
D.	Supporting Information for Chapter V .....	222
E.	Supporting Information for Chapter VI.....	229

## TABLES

### Table

4.1	Primary model parameters .....	83
4.2	Macromer inputs for the networks of <b>Fig. 4.12</b> .....	100

## FIGURES

### Figure

2.1	Introduction to dynamic networks.....	7
2.2	Pairwise forces on crosslinks .....	12
2.3	Attached bond lifetime statistics .....	14
2.4	Detached bond lifetime statistics.....	18
2.5	Discrete network homogenization .....	21
2.6	Intrinsic viscosity of network model.....	25
2.7	Effects of loading rate .....	29
2.8	Micromechanical origins of mismatch with TNT.....	33
2.9	Effects of network coordination .....	35
2.10	Micromechanical study of non-affine deformation.....	37
2.11	Phantom chain theory and chain conformation.....	38
3.1	Hybrid network schematic.....	44
3.2	Fitting the general ROM.....	48
3.3	Network percolation with respect to SB fraction and crosslink functionality.....	49
3.4	Fitting the coupled ROM.....	51
3.5	Micromechanical chain relaxation.....	54
3.6	Experimental validation .....	56
4.1	Hierarchical length scales of gels .....	61
4.2	Deformation of a gel .....	67

4.3	Chronological steps of numerical model.....	69
4.4	Solute concentration scaling in a gel.....	73
4.5	Numerical implementation of effective mixing forces in 1D .....	75
4.6	Outcomes of numerical implementation in 2D .....	76
4.7	Applied boundary conditions .....	81
4.8	Phase separation of polymer suspensions.....	86
4.9	Validation of the model's predicted <i>ab initio</i> topologies .....	90
4.10	Validation of the model's predicted swelling mechanics .....	93
4.11	Validation of the model's predicted stress response .....	95
4.12	Mechanical predictions of gels with different functionalities and chain lengths .....	99
4.13	Chain distribution functions of gels with $L = 44 \text{ nm}$ and different functionalities.....	101
4.14	Fracture of gels with $L = 44 \text{ nm}$ and different functionalities....	102
4.15	RDFs of gel's crosslinks with $L = 44 \text{ nm}$ and different functionalities.....	105
4.16	Void characteristics of gels with $L = 44 \text{ nm}$ and different functionalities .....	106
4.17	Mechanical predictions for extended parameter sweep.....	109
5.1	Networked fire ant rafts form dynamic structures.....	115
5.2	Trajectory analysis of non-edge-encountering surface ants .....	124
5.3	Quantifying structural retraction.....	128
5.4	Treadmilling of fire ant rafts .....	129
5.5	Characterizing protrusion growth and directional motion.....	131

5.6	Numerical model results .....	135
6.1	Treadmilling review .....	142
6.2	Agent-based model schematic.....	153
6.3	Comparing treadmilling dynamics .....	155
6.4	Comparing protrusion dynamics .....	162
6.5	Dynamic effects of activity level .....	164
6.6	Ant activity phases.....	167

## CHAPTER I

### INTRODUCTION

“Transient networks” contain bonds that may disconnect and reattach reversibly, imbuing them with viscoelasticity, enhanced mechanical toughness, and the ability to self-heal [1]–[3]. The complexity of transient networks is compounded when their elemental units convert locally stored energy into mechanical work. Such is the case of “active networks”, which may spontaneously morph, locomote, or apply stresses to their environment [4], [5]. Even when composed of relatively simple agents correlated through elementary physics or heuristic rules, active materials often display complex emergent functions, as seen in the phase separation of self-propelled colloids [6], [7], collective migration of epithelial cells [8]–[10], or – as explored here – spontaneous land-bridge formation by fire ants (*S. Invicta*) [11], [12]. For both transient and active networks, predicting how the underlying physics or interactions modulate global response is paramount for engineers developing synthetic instances of these materials. For example, mapping the local input parameters of a transient gel to its emergent mechanical properties may aid the predictive design of gels with targeted moduli for applications in tissue engineering [13]–[16]. Likewise, the means to rapidly explore heuristic interactions between agents in a swarm may empower engineers to forecast the emergent formations of swarming robots before design and fabrication [17]–[20]. As such, efficient methods for mapping local-to-global property functions in these networks are widely sought after by researchers across a range of disciplines.

While experimental methods of investigation constitute irrefutable representation of these networks, they require tightly controlled conditions to probe the independent effects of single design parameters [21]–[23], and are limited in their



ability to illuminate certain local feature such as micro- and nanoscale topology, or magnitudes of effective forces between “socially” interacting agents [24], [25]. Furthermore, large sample sizes are required for systems displaying high variance (as is often the case in biology) or rarely occurring probabilistic features [11], [26], [27]. Consequently, researchers often supplement experimental results with multi-scale modeling approaches [28]–[30] including continuum techniques that treat networks as smooth, homogenous materials [31]–[37], and discrete methods that model networks as assemblies of distinct particles [38]–[42]. Continuum approaches are favored for their low computational cost but invoke limiting assumptions, restrict exploration of stochastic effects, and reveal little of the detailed microstructure in a network. In contrast, high fidelity approaches such as molecular dynamics [43]–[45] provide detailed microstructural information, but typically suffer from high computational cost that limits the length and time scales of investigation.

Towards addressing these issues, we here introduce a mesoscale modelling framework that maintains the network-scale fidelity of high resolution approaches yet reduces computational cost through statistical coarse graining of the elemental building blocks in transient or dynamic networks (e.g., polymeric chains or individual ants, respectively) [3]. In Chapter II, we introduce the model and utilize its permissiveness of micromechanical investigation to elucidate limitations of a state-of-the-art continuum approach, Transient Network Theory (TNT) [1], [3]. In Chapter III, we then leverage the discrete network model to append TNT for incorporation of features such as topologically dependent stable bond relaxation in hybrid transient networks containing multiple bond types in series [13], [46]–[48], thereby demonstrating the model’s ability to motivate physically meaningful amendments to continuum theory. Complimenting Chapter II’s and Chapter III’s focuses on informing continuum theory, Chapter IV then illustrates the discrete network model’s ability to predict the mechanical responses of a physical material when the

appropriate physics are incorporated: that of tetra- and octa-poly(ethylene glycol) based gels [49]. Finally, Chapters V and VI exhibit the discrete model’s ability to be retrofit for the study of active systems. In Chapter V, we experimentally introduce and explore the dynamics of aggregated rafts comprised entirely of red imported fire ants (*S. Invicta*). Specifically, we introduce the recyclic mechanism of “treadmilling” that allows these rafts to undergo unyielding morphogenesis, including the growth of tether-like land bridges comprised entirely of ants [11]. In Chapter VI, we subsequently retrofit the discrete framework with mechanisms such as active contraction and stochastic, agent-based decision-making algorithms, to mimic ant rafts, thus allowing us to elucidate a set of local interaction rules that can reproduce the observed emergent morphogenesis [12].

## CHAPTER II

### A NETWORK MODEL OF TRANSIENT POLYMERS: EXPLORING THE MICROMECHANICS OF NONLINEAR VISCOELASTICITY

The object of this chapter is to provide the reader a general view of the proposed discrete numerical network model, of which iterations will be used throughout the remainder of this work. We first reiterate the definition and significance of dynamic networks. We then briefly overview the transient network theory (TNT) [1] for Gaussian dynamic networks before describing the simplest iteration of the novel discrete approach. Finally, we utilize this model to explore the limitations of a reduced form of TNT.

#### 2.1 Introduction

Dynamic networks, defined by arrangements of filaments or chains inter-linked by reversible bonds, are omnipresent in both natural and synthetic materials. These materials range from thermally transient microemulsions [50] or molecular motor-driven microtubule networks [51], to interlinked clusters of insects such as fire ants [52], [53] or honeybees [54] at the macroscopic level. Reversible bonds in these networks tend to dissociate from stressed configurations and re-associate into relatively stress-free states, conferring dynamic networks with remarkable viscoelastic properties, including the ability to stress relax [33] crack propagation [2], and self-heal [55] at timescales governed by the underlying bond kinetics [1]. Relating the local chain properties and topologies of such networks to their global mechanical response is highly sought after by researchers aiming to elucidate the origins of biophysical phenomena [56], as well as those interested in the predictive design of meta-materials with suitably tough mechanical properties, the ability to self-repair [57], or the ability to facilitate active transport [58].

Towards this aim, many methods of modelling dynamic networks have been developed, including both microscale methods such as molecular dynamics (MD) or dissipative particle dynamics (DPD) simulations, and macroscale statistical mechanics approaches [29]. While the former methods simulate every elementary unit in a system (e.g., atom, molecule or Kuhn segment) to predict the microstructural evolution with high precision [59], they are computationally expensive. As such, modelling statistically representative volume elements (RVEs) - material unit cells that capture the full range of structural microphases - is often impractical when using these methods for amorphous materials. In contrast, continuum scale approaches such as the continuum model introduced by Hui, et al. (2012) [35] or transient network theory (TNT) [1] manage to make a connection between bond kinetics and the emerging material response while requiring few computational resources. However, they usually rely on smoothing assumptions that restrict researchers from exploring the role of local heterogeneities or microstructural features. While statistical and computational approaches have been developed to relate damage to the macroscopic material response [60], [61], these models often remain bound to coarse-graining assumptions such as, isotropy, affine deformation and - commonly - idealized chains or bond dynamics. Isotropy is reasonably assumed for some, but not all, dynamic networks [2], whereas the affine assumption is typically violated at the network scale and slightly over-predicts stress [62], [63]. Furthermore, assumptions of idealized chain force-extension models and constant bond dynamics are typically violated at intermediate to high chain stretches [64]–[66].

To address these shortcomings, researchers have developed a number of multiscale models residing between the elemental length scale of MD simulations and material length scale of continuum approaches, which we will here refer to as the “mesoscale”.<sup>1</sup>

---

<sup>1</sup> While researchers of condensed matter physics often define the \say{mesoscale} as residing distinctly between the nanometer (i.e., atomistic or molecular) and micrometer length scales [29], our interest in exploring a wide breadth of dynamic networks - including macroscopic systems - prompts us to use this term in reference to any length scale at which constituents are coarse-grained as single members.

Rather than simulate the elemental units of a network, mesoscale models generally coarse-grain entire chains and prescribe their mechanical properties through statistical representations such as the ideal Gaussian model [67]. In doing so, these models avert high computational cost while still permitting investigation of the detailed microstructural changes that occur during network evolution [29]. Mesoscale models have been extensively used to study the effects of non-affine deformation in permanent networks [68]–[70], revealing that the affine assumption limits continuum models' abilities to predict the mechanics of networks near the percolation threshold [71]. By extension, this also limits continuum models in cases where damage occurs during deformation [2], [61]. In contrast, mesoscale models easily permit probabilistic rupture of bonds through models such as Eyring's [65] or Bell's [72] theory, while inherently tracking the topological evolution of the network. Such mesoscale methods may be applied directly to entire networks [73], [74] or incorporated into "quasicontinuum" models [30], [75], [76] in which regions of high micro-structural interest (e.g., those undergoing plastic deformation or damage) are examined mesoscopically, while elements of lower interest (i.e., homogenous regions) are captured through statistical continuum models. Through both methods, researchers have employed mesoscale models in the examination of permanent damage, mechanical toughness, and loading rate-dependence, to determine how these features are affected by chain properties and concentrations [74]–[77]. A natural extension of such work is to then apply mesoscale modeling in the exploration of dynamic networks in which the dissociation of bonds is reversible. Indeed, researchers in the biophysics community have examined active dynamic systems such as actin-myosin or cytoskeletal networks using mesoscale modeling approaches [56], [66]. However, inclusion of activity in these systems obfuscates the isolated effects of traits such as topology, chain properties, and bond kinetics, which researchers of thermally driven dynamic networks (e.g., vitrimers [46], [78]) are most immediately concerned with. In the study of inactive polymers with reversible bonds, other researchers have employed the more traditional methods of MD-Monte Carlo simulations to directly study [79] or develop specific statistical approaches in the

study of features such as self-healing and adhesion of dynamic polymers [80]. However, these methods are inhibited by the same computational costs and inaccessibility to larger time and length scales discussed earlier. Ergo, there remains much to be learned through the development and application of a general mesoscale framework for networks with reversible bonds.

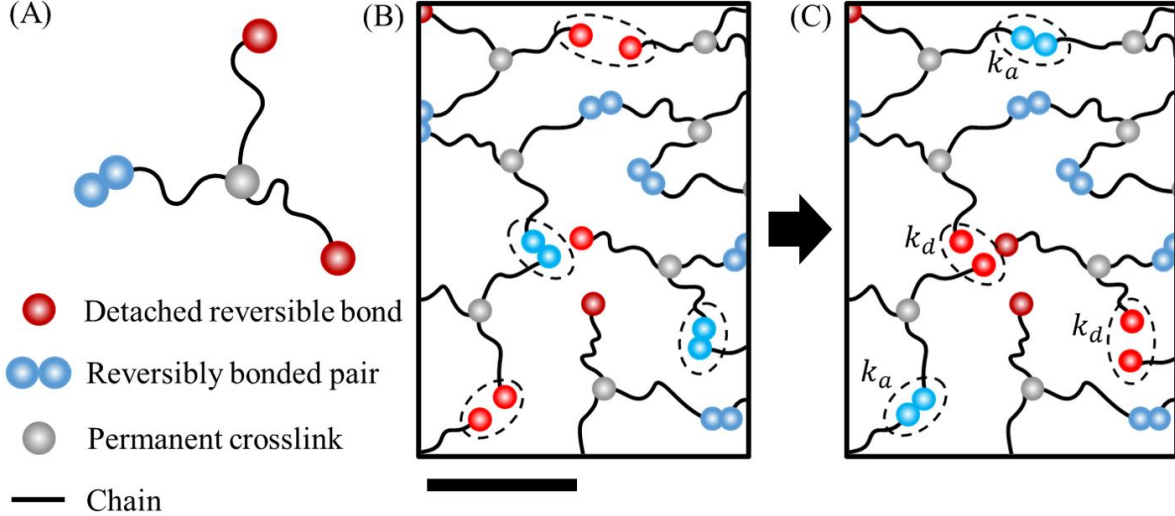


**Figure 2.1. Introduction to dynamic networks.** (A) A single sample constituent with three possible attachments is shown. Per the legend, grey nodes represent permanent crosslinks, blue nodes represent reversibly bonded pairs, red nodes represent detached reversible bonds and black curves represent chains. (B-C) A sample network (B) before and (C) after a series of attachment and detachment events (denoted by  $k_a$  and  $k_d$ , respectively) is depicted. The scale bar represents approximately  $1\zeta$  where  $\zeta$  is the characteristic spacing between permanent crosslinks in the network.

Moving in this direction, we here introduce a discrete, mesoscopic, network model with dynamically cross-linking connections that may represent a broad scope of systems ranging from vitrimers [81] to gel networks [48]. Our main contribution is at two levels. First, we introduce the mesoscale model, which captures the time-dependent mechanical responses of networks with dynamic connections, and allows us to relate them directly to networks' topological evolution. This model incorporates not only probabilistic bond detachment, but also reattachment events, thus broadening the scope of networks that may be explored from permanent networks (with or without damage), to those that may flow and self-heal. In the first iteration

of this model, we focus on networks of flexible chains permanently cross-linked to one another at one end in a star-like configuration and containing reversible binding sites at their free ends, which we will refer to as “stickers” (**Fig. 2.1**). As the first application of this model and second contribution of this work, we compare the predictions of this approach to those of the existing continuum TNT [1], thereby allowing us to explore the limitations of the statistical approach directly as they relate to the underlying network properties and loading conditions. In the remainder of this manuscript, we briefly describe the TNT for dynamic networks of Gaussian chains, introduce the discrete model, and then explore the mechanical responses predicted by each of these methods.

## 2.2 Transient Network Theory for Gaussian networks

The TNT begins with the statistical treatment of networks comprised of randomly oriented flexible chains connected by reversible bonds with intrinsic association and dissociation rates,  $k_a$  and  $k_d$ , respectively. The elastic energy of these networks derives from the entropic elasticity of their connected chains, which is expressed in terms of their end-to-end vectors  $\mathbf{r}$ . For a population of Gaussian chains, the most probable end-to-end distance or “reference state” is expressed by the product  $\sqrt{N}b$ , where  $N$  and  $b$  are the number and length of Kuhn segments in a chain, respectively [64]. For convenience, the physical state of a chain is taken as the stretch vector  $\boldsymbol{\lambda} = \mathbf{r}/(\sqrt{N}b)$ , such that  $\boldsymbol{\lambda}$  is a unit vector when chains are in their reference state. To provide a statistical description of the network, one then introduces the distribution function  $\phi(\boldsymbol{\lambda}, t)$  that characterizes the number density of chains found in configuration  $\boldsymbol{\lambda}$ . Since this distribution describes the physical state of the full population, it can be used to calculate important macroscopic quantities such as the elastic energy, stress, or viscous relaxation [1], [33], [53].

Let us now consider a small network volume, subjected to an overall deformation history, characterized by the time-dependent deformation gradient tensor  $\mathbf{F}(t)$ . At a

given time, this function can be used to evaluate the velocity gradient tensor through the relation  $\mathbf{L} = \dot{\mathbf{F}}\mathbf{F}^{-1}$  where the superimposed dot represents the material time derivative. From this knowledge, it is possible to construct an evolution equation for the distribution function over time if a relationship is postulated between global deformation  $\mathbf{L}$  and local chain deformation  $\dot{\boldsymbol{\lambda}}$ . The simplest and most common assumption is given by the instantaneously affine approximation [33] that reads  $\dot{\boldsymbol{\lambda}} = \mathbf{L}\boldsymbol{\lambda}$ . In this case, it can be shown that the material time derivative of the distribution takes the form of the Fokker-Planck equation [1]:

$$\dot{\phi} = -\mathbf{L} : \left( \frac{\partial \phi}{\partial \boldsymbol{\lambda}} \otimes \boldsymbol{\lambda} \right) - \phi \text{Tr}(\mathbf{L}) + k_a c_d p_0 - k_d \phi, \quad (2.1)$$

where  $c_d$  is the concentration of detached chains and  $p_0(\boldsymbol{\lambda})$  describes the probability density function at which chains reattach to the network. The function  $p_0(\boldsymbol{\lambda})$  is usually taken as an anisotropic, multivariate Gaussian with variance  $\sqrt{N}b$  to express the fact that chains reconnect into a relaxed conformation. In this work, we concentrate on incompressible networks, characterized by  $\det(\mathbf{F}) = 1$ , or alternatively,  $\text{Tr}(\mathbf{L}) = 0$ . This therefore implies that the second term on the right-hand side of Eqn. (2.1) vanishes in the remainder of this manuscript. Given the evolution of the chain distribution ( $\phi$ ) through Eqn. (2.1), and assuming the force-extension ( $f - \lambda$ ) response of a single chain is known, the stress in the network can be directly evaluated through the virial formula as [1]:

$$\boldsymbol{\sigma} = \|\phi \mathbf{f} \otimes \boldsymbol{\lambda}\| + \pi \mathbf{I}. \quad (2.2)$$

We here concentrate on a reduced form of the TNT [1], where the chain distribution is described by its covariance matrix  $\boldsymbol{\mu} = \frac{3}{c} \|\phi(\boldsymbol{\lambda}) \boldsymbol{\lambda} \otimes \boldsymbol{\lambda}\|$ , also known as the conformation tensor. Focusing on the case where the rates of chain dissociation  $k_d$  and association  $k_a$  are constants and independent of deformation, then the concentration of attached (and therefore detached) chains quickly reaches a steady state that is not affected by the loading history. This steady state concentration given by:

$$c = \frac{k_a}{k_a + k_d} c_t, \quad (2.3)$$



where  $c_t$  is the total chain density. Furthermore, the Fokker-Planck equation can be replaced by its reduced form, that describes the evolution of the conformation tensor as follows [1]:

$$\dot{\boldsymbol{\mu}} = \mathbf{L}\boldsymbol{\mu} + \boldsymbol{\mu}\mathbf{L}^T - k_d(\boldsymbol{\mu} - \mathbf{I}). \quad (2.4)$$

If the network is initially stress-free, this equation is complemented by the initial condition  $\boldsymbol{\mu} = \mathbf{I}$ , where  $\mathbf{I}$  is the identity tensor. It can be shown that a general solution of this equation is [1]:

$$\boldsymbol{\mu}(t) = \mathbf{F}\mathbf{F}^T e^{-k_d t} + k_d \mathbf{F} \left( \int_0^t (\mathbf{F}_\tau^{-1} \mathbf{F}_\tau^{-T}) e^{-k_d(t-\tau)} d\tau \right) \mathbf{F}^T \quad (2.5)$$

where the deformation gradient  $\mathbf{F}_\tau = \mathbf{F}(\tau)$ . Although many flexible chains exhibit a severe, non-linear strain-stiffening response when deformed near their contour lengths, for simplicity, we here assume that the force-extension relation is that of a linear Gaussian chain taking the form  $\mathbf{f} = 3kT\boldsymbol{\lambda}$  where  $kT$  is the thermal energy. In this case, the stress simplifies to [1]:

$$\boldsymbol{\sigma} = ckT\boldsymbol{\mu} + \pi\mathbf{I} \quad (2.6)$$

Combining this equation with the general solution for the conformation tensor (Eqn. (2.5)) leads to the prediction of the stress tensor for an arbitrary deformation history  $\mathbf{F}(t)$ . The TNT has been amply used to understand the molecular origin of the viscoelastic response by transient networks [1], [33], [53], [82]–[85]. It however hinges on a number of assumptions that could affect the validity and accuracy of its prediction in certain conditions. Among those assumptions are (a) the affinity of the chain deformation, (b) the assumption of constant association and dissociation kinetics, and (c) the linear force-extension response of the flexible chains. To explore these limitations, we here construct a discrete, transient network model that does not rely on these restrictions.

### 2.3 Discrete model of transient networks

The topology of transient networks can be very diverse. Without compromising generality, we here present a model that consist of a network of star-shaped units

whose branches may reversibly bind with one another, in line with the depiction of **Fig. 2.1**. As a discrete model that represents the end-to-end vector of every chain, this framework inherently captures the non-affine response of the network as it undergoes conformational changes during deformation. Similarly, given bond dynamics, the framework also captures non-affine changes due to network reconfiguration. Furthermore, the bond dissociation rate of attached chains is prescribed a statistical dependence on force through Eyring's theory [65], while the association rate of detached chains is governed by their proximity to neighboring open chains and their timescale of tethered Rouse diffusion [80], thus rendering the assumption of constant kinetic rates unnecessary. Finally, the chains are assigned a nonlinear force-extension relationship through the Padé approximation of Langevin chains [86], capturing the enthalpic stiffening of chains from the stretching of intra-constituent bonds as they near full extension (as opposed to just entropic stiffness from unfolding) [87]. In the remainder of this section, we detail the prescribed force-distance relationships (both the attraction of mutually bonded nodes due to chain forces and repulsion of neighboring nodes due to volume exclusion), bond kinetics (both detachment and attachment), and integration of single chains into a network.

### 2.3.1 Elastic and repulsive interactions in a transient network

Networks' constitutive properties are intrinsically tied to the constitutive properties of their elemental building blocks. Therefore, due consideration must be given to the assignment of a force-extension relationship,  $f(\lambda)$ , for jointly connected chains in the model. In many networks of flexible chains, a nonlinear stiffening occurs when members are stretched close to some finite contour length. To prescribe a finite contour length, we employ the Padé approximate for Langevin chains [86] for which the corresponding free energy is:

$$u_c(\lambda) = kT \left[ \frac{\lambda^2}{2} - N \log(N - \lambda^2) \right]. \quad (2.7)$$

Notably, the force in a Langevin chain diverges in the limit  $\lambda \rightarrow \sqrt{N}$  (i.e.,  $r \rightarrow L$ ), enforcing that  $f \rightarrow \infty$  when the chains are stretched to their full contour length (**Fig. 2.2.A**). This nonlinear divergence at high chain stretch is common to polymeric chains. In fully extended polymer chains, the conformational degrees of freedom are minimized and the stiffness of the chains is no longer entropically driven, rather it is governed by the much stiffer stretching of covalent bonds between monomers [88].

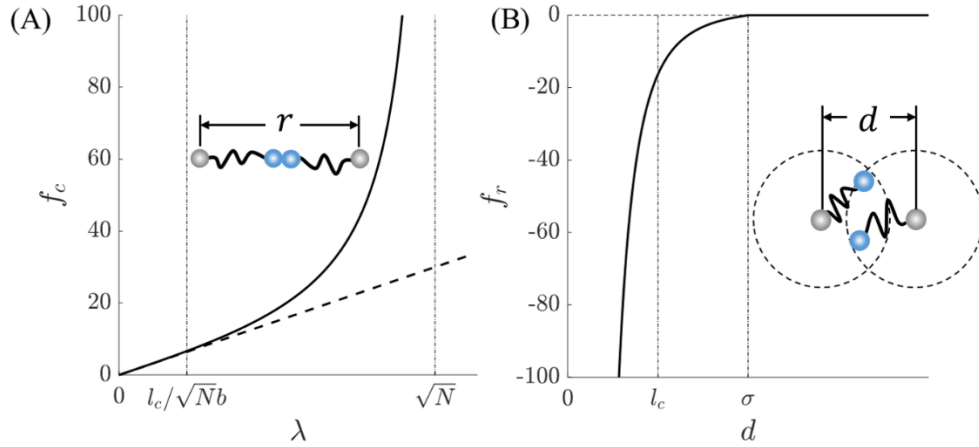


**Figure 2.2. Pairwise forces on crosslinks.** (A) The entropic tensile force of an attached chain is plotted with respect to extension,  $\lambda = r/(\sqrt{N}b)$ . Both the Gaussian (dashed black line) and Langevin (solid black curve) chain models are displayed. The nominal spacing between nearest neighboring permanent crosslinks,  $l_c$ , and the chain contour length,  $\lambda = \sqrt{N}$  are denoted for reference. (B) The repulsive force between neighboring units due to volume exclusion is plotted with respect to separation distance,  $d$ . Again,  $l_c$  is marked for reference. The length scale above which repulsion goes to zero,  $R$ , is also denoted.

This model relies on the freely-jointed assumption that there is no energetic penalty for changing the angle between adjacent chain segments (i.e., bending). Employing freely-jointed chains simplifies our network model by eliminating moments on our permanent crosslinks, instead ensuring that the force from a chain always occurs pairwise and in-line with the centers of mass of the nodes to which it is connected. It also permits us to assume a circumferentially symmetrical radial distribution for unattached chains such that the stickers are equally likely to occupy any azimuth about their tethered node. However, with no energetic penalty for bending the chains have no finite rest length and are always in tension, which - in the absence of any repulsive potential - will cause traction-free networks to converge to a single point.

To mitigate this non-physical effect, we introduce soft volume exclusion between permanent crosslinks through a generic inverse repulsion potential of the form [89]:

$$u_R(d) = \begin{cases} E \left[ \gamma \left( \frac{d}{R} \right) + \left( \frac{R}{d} \right)^\gamma \right], & \text{if } d < R \\ 0, & \text{if } d \geq R \end{cases}, \quad (2.8)$$

where  $E$  is a characteristic energy scale,  $R$  is the effective particle radius,  $\gamma$  is a scaling parameter that defines how soft the particle is (where setting  $\gamma$  lower decreases the particle stiffness), and  $d$  is the pairwise separation distance between neighboring nodes' centers of mass. From Eq. (2.8), we may derive the repulsive force according to  $\partial u_R / \partial d$ , which gives  $f_R = \gamma E (1/R - R^{\gamma/d} (\gamma + 1))$  when  $d < R$  while  $f_R(d) = 0$  otherwise. Thus, the total force acting between an adjacent set of bonded nodes becomes the sum of the tensile chain force and repulsive volume exclusion force. Ultimately,  $E$  and  $R$  are set such that the net force between a bonded pair becomes zero at a distance of  $R = 2l_c$ , which ensured that the networks always hosted some effective pressure from volume exclusion, and which led to negligible stress in equilibrated networks regardless of chain concentration (see Section 2.3.4). Additionally,  $\gamma$  is set to 2 in order to achieve a very soft pairwise repulsion. We set the contour length of an attached chain to  $Nb = 3.5$  units of length, and assume monodispersity, which enforces that chains remain close to the linear regime of the tensile force when connected to nearest neighbors. Note that while the Langevin contribution to the pairwise force between nodes exists only if said nodes are mutually bonded, volume exclusion force is maintained between all nodes within the radial separation distance  $d \leq R$ , hence the distinction between center of mass separation distance “ $d$ ” and chain end-to-end distance “ $r$ ”.

### 2.3.2 Force-dependent bond dissociation

At the constitutive level, the process of detachment is governed by the competition between the binding energy,  $\Delta G$ , of reversible bonds and the force-dependent free energy,  $\Psi(f)$ , stored in the bonds' chains. If the free energy in the chain exceeds this binding energy ( $\Psi(f) > \Delta G$ ), then the bond will detach while if the energy barrier is

not eclipsed the bond will remain attached. As such, bond detachment is an inherently force-dependent phenomenon. In many of the systems modeled, such as polymeric networks, the force produced in a chain contains a random diffusion-governed, entropic contribution. Therefore, the detachment process will appear probabilistic at the mesoscale and so we employ an average rate to describe random dissociation events.

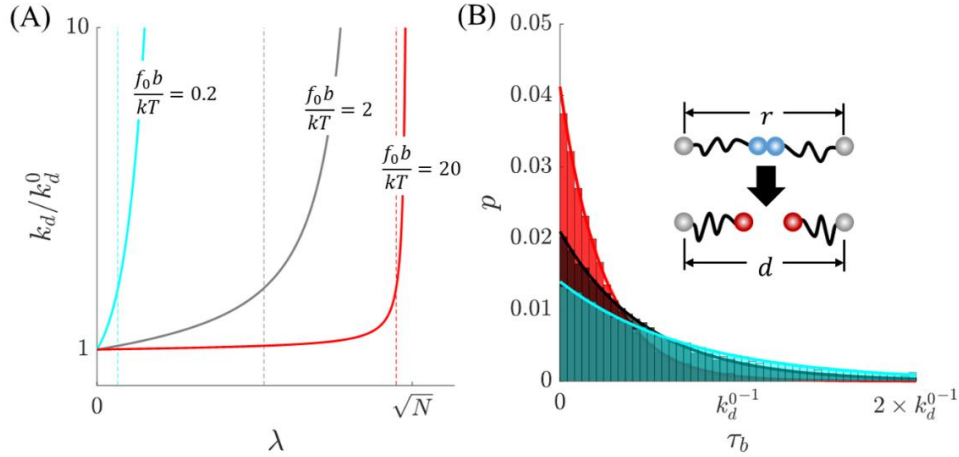


**Figure 2.3. Attached bond lifetime statistics.** (A) Rate of unbinding as a function of chain stretch is plotted for three different values of bond force sensitivity,  $f_0$ . The vertical dashed lines represent the stretches at which  $f = f_0$  (or  $k_d = e$ ) for each value of  $f_0$ . (B) Statistics of the bond lifetime of an attached chain when  $f_0 = 2kT/b$ , are plotted for three different values end-to-end distance,  $r$ :  $r = l_c$  (cyan),  $r = 2l_c$  (black), and  $r = 3l_c$  (red), where  $l_c$  is nominal spacing between nearest neighboring permanent cross links.

One commonly employed statistical model for force-dependent detachment in both mesoscale [56] and continuum approaches [2] is Eyring's theory, which describes the average bond detachment rate  $k_d$  (or average inverse bond lifetime,  $k_d = 1/\tau_b$ ) according to:

$$k_d = k_d^0 \exp\left(\frac{f x_d}{kT}\right), \quad (2.9)$$

where  $k_d^0$  is the force-free detachment rate and  $x_d$  is the detachment activation length scale that characterizes the force-sensitivity through  $f_0 = kT/x_d$  [65]. The effects of force sensitivity are displayed in **Fig. 2.3.A**. When  $f_0$  is on the order of  $20kT/b$ , there is very little extension-dependence of  $k_d$  until  $\lambda \rightarrow \sqrt{N}$ . In contrast, when  $f_0$  is on the order of  $0.2kT/b$ ,  $k_d$  is more than tenfold greater than  $k_d^0$  at the initial separation

distance between nearest neighbors,  $l_c$ . As  $f_0$  will greatly impact the connectivity and therefore stiffness of the networks in this model, further investigation into its effects may be considered in future work. However, here  $f_0$  is held at  $2kT/b$ , which produces an intermediate force-dependent effect on  $k_d$  wherein  $f$  reaches  $f_0$  at  $r \approx 2.5l_c$ . Regardless of  $f_0$ , under no applied load ( $f = 0$ ), the stress-free rate of detachment due to random fluctuation is given by  $k_d^0$ . From Eqn. (2.9) we see that as force increases, the detachment rate increases exponentially. Referencing the force-extension relationship of attached chains (Fig. 2.2.A) we see that the detachment rate diverges and the bond lifetime goes to zero in the extensile limit  $r \rightarrow L$  (or  $\lambda \rightarrow \sqrt{N}$ ). It should be noted that Eqn. (2.9) is also synonymous with the Bell model originally employed to predict slip bond detachment kinetics between cells [72], thus generalizing its application beyond the systems Eyring originally studied.

To gauge the effects of this coarse-grained detachment algorithm on a single chain, we conduct a simple benchmark problem. Two chains whose reversible binding sites are initially attached, have their permanently cross-linked ends held apart at some constant chain length,  $r$ . The nominal detachment rate,  $k_d$ , in this chain is then computed through Eqn. (2.9). From a numerical view point, the detachment kinetics of a detached chain can be seen as a stochastic process, where each event is considered independent. It can therefore be considered as a Poisson process with average rate  $k_d$ . The differential probability  $P_d$  for an attachment event to occur during a time interval  $t$  and  $t + dt$  therefore follows the relation:

$$dP_d = k_d e^{-k_d t} dt. \quad (2.10)$$

Discretizing  $t$  by some small numerical timestep,  $\Delta t$ , and accounting for the memorylessness of the exponential function, we may rewrite this relationship such that the probability of detachment at any given timestep in the model is taken as:

$$P_d = 1 - e^{-k_d \Delta t}. \quad (2.11)$$

Time is stepped in increments of  $\Delta t$ , and a random number,  $a$ , in the range  $a \in [0,1]$  is checked against  $P_d$ . If,  $a \leq P_d$ , the bond is detached, the bond lifetime is recorded, and the simulation stops. This process is repeated for 20,000 observations over three

separate values of  $r$  ( $r = l_c$ ,  $r = 2l_c$ , and  $r = 3l_c$ ). The resulting probability mass functions of bond lifetime are presented in **Fig. 2.3.B**, which agree with the continuous distributions predicted by Eqn. (2.10). As  $r$  increases, the tail of the histogram shortens and the peak of the distribution increases indicating a shorter average bond lifetime for highly stretched chains, as expected from Eqn. (2.9). In contrast, decreasing  $r$  elongates the tail of the distribution and reduces the peak value, indicating that shorter chains have longer average bond lifetimes.

### 2.3.3 Kinetics of bond association

Let us now concentrate on estimating the lifetime of a dangling bond, that is attached to a fixed node as shown in **Fig. 2.4.A**. While other researchers have successfully employed Bell's theorem for the reattachment of bonds that fasten together "hidden lengths" or phantom loops [90], this approach requires that the reversible bonds reside along the lengths of the polymers and that the chains remain intact, albeit elongated, after bond rupture. However, bond breakage in the networks examined here results in complete chain scission and the formation of two dangling chains, which are tethered only at one end to their permanent cross-links. Under such conditions, assuming negligible long-range potential between the free stickers and that the bond transition length scale is very small (such that bonds reform when two free stickers effectively come into contact), then bond association kinetics depend primarily on the diffusion of detached stickers. When detached, a dangling flexible chain explores the space surrounding the central node through a sub-diffusive Rouse process. Following Stukalin, et al. (2013) [80], and assuming sufficiently flexible, ergodic chains, we designate  $\tau_0$  as the time it takes for this bond to move through the molecular distance  $b$ . This time depends on both temperature and the friction coefficient between the dangling chain and its surrounding medium. Following the Rouse diffusion model, the mean square displacement  $\langle \Delta r^2(t) \rangle$  of the dangling bond around its anchoring node increases as a square-root of time following:

$$\langle r^2(t) \rangle = b^2 \sqrt{t/\tau_0}, \quad (2.12)$$

for  $\tau_0 < t < \tau_R$ , where  $\tau_R$  is the Rouse time of the dangling chain given by  $\tau_R = \tau_0 N^2$ . Let us now estimate the three-dimensional volume  $V$  explored by the bond over time (**Fig. 2.4.A**). This volume may be estimated by the mean square displacement as  $V(t) = \langle \Delta r^2(t) \rangle^{3/2}$ , which, combined with Eqn. (2.12) yields the relation:

$$V(t) = b^3(t/\tau_0)^{3/4}. \quad (2.13)$$

To obtain a scaling law for the average lifetime of a free dangling chain, we postulate that a binding event occurs when the exploration volume  $V(t)$  is equal to the volumes at which two dangling chains, attached to nodes separated by a distance  $d$ , intersect (i.e.,  $V \approx d^3$ ). Applying this to Eqn. (2.13) gives the average life time of a free dangling chain as  $\tau \approx \tau_0(d/b)^4$ . In other words, the average rate of association  $k_a = 1/\tau$  scales nonlinearly with the distance between two nodes according to the power law:

$$k_a \approx \frac{1}{\tau_0} \left( \frac{b}{d} \right)^4, \quad (2.14)$$

where  $k_a = 0$  if  $d > Nb$ . Note that this scaling law based on the work of Stukalin, et al. (2013) [80], yields a rough estimation of the lifetime of a dangling chain and may be improved in a number of ways. For instance, the recombination of two dangling chains that belong to the same node is not considered here, but is expected to decrease the lifetime of these free chains. While this work ignores such effects for clarity, they may be included in ulterior versions of the model.

As with the detachment kinetics, the recombination kinetics of two dangling chains may be viewed as a stochastic process, where each event is independent, thereby being treated as a Poisson process with average rate  $k_a$ . Thus, the differential probability  $P_a$  of an attachment event occurring during the time interval  $t$  and  $t + dt$  follows the relation:

$$dP_a = k_a e^{-k_a t} dt, \quad (2.15)$$

where  $k_a$  is a function of both time and chain separation through Eqn. (2.14). Therefore, to gauge the effects of this coarse-grained attachment process on a single chain, we conduct another simple benchmark problem. As with the detachment process, we discretize  $t$ , giving the attachment probability within a discrete timestep



as  $P_a = 1 - e^{-k_a \Delta t}$ . Two detached tethers separated by a fixed distances of  $d = l_c$ ,  $d = 2l_c$ , and  $d = 3l_c$  are allowed to bond and their unbound lifetime is recorded. The resulting probability mass functions from 20,000 detached lifetime observations each, are presented in **Fig. 2.4.A**, which agree with the continuous distributions predicted by Eqn. (2.15). As  $d$  decreases, the tail of the histogram shortens significantly and the peak of the distribution increases indicating a shorter average unbound lifetime between nodes in close proximity, as expected from Eqn. (2.14). In contrast, increasing  $d$  lengthens the tail of the distribution and decreases the peak value, indicating an increased average unbound lifetime, with very few attachment events occurring at any given lifetime when  $d = 3l_c$  in the observed time interval.

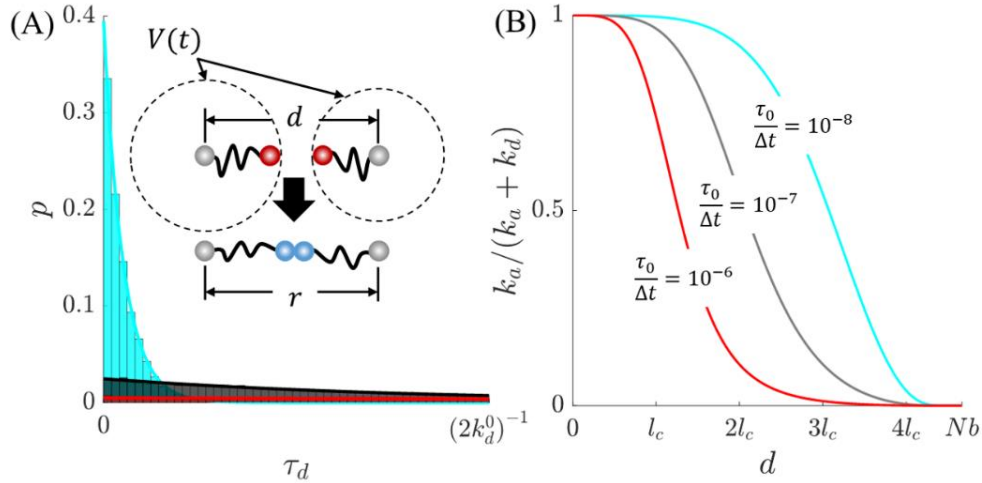


**Figure 2.4. Detached bond lifetime statistics.** (A) Statistics of the free sticker lifetime are plotted for three different values separation distance,  $d: d = l_c$  (cyan),  $d = 2l_c$  (black), and  $d = 3l_c$  (red), where  $l_c$  is nominal spacing between nearest neighboring permanent cross links. (B)  $k_a/(k_a + k_d)$  is plotted with respect to separation distance,  $d$ , for three different values of the diffusion sticker timescale,  $\tau_0$ , which predicts the fraction of chains that will be attached at a given value of  $d$  ( $f_0$  is held at  $2kT/b$ ).

The combined effects of  $k_a(d, t)$  and  $k_d(r)$  are illustrated in **Fig. 2.4.B** by plotting the ratio  $k_a/(k_a + k_d)$  with respect to node separation distance  $d$  (which is synonymous with  $r$  for bonded nodes). This ratio predicts the steady state fraction of chains that will be attached at a given end-to-end distance. It remains close to one for small separations at which  $k_d$  will diminish (**Fig. 2.3.B**) and  $k_a$  will increase (**Fig. 2.4.A**). Similarly, it approaches zero in the limit  $r \rightarrow Nb$ . To also highlight the effect

of the sticker diffusion timescale, **Fig. 2.4.B** displays  $k_a/(k_a + k_d)$  for three values of  $\tau_0$ :  $\tau_0 = 10^{-6}\Delta t$ ,  $\tau_0 = 10^{-7}\Delta t$ , and  $\tau_0 = 10^{-8}\Delta t$ . When  $\tau_0$  is increased (i.e., when it takes longer for the sticker to travel a distance  $b$ ), the fraction of attached chains at a given distance generally decreases, as expected given the corresponding reduction in  $k_a$  through Eqn. (2.14). Specifically, when  $\tau_0 = 10^{-8}\Delta t$ , the fraction of attached chains remains close to one until  $d > 2l_c$ , while when  $\tau_0 = 10^{-6}\Delta t$ , the fraction of attached chains only remains close to one when  $d < l_c$ . As with  $f_0$ ,  $\tau_0$  greatly impacts the connectivity and therefore mechanical properties of the networks. In the scope of this work,  $\tau_0$  is set to  $10^{-7}\Delta t$ , such that the predicted fraction of attached chains transitions from one to zero within the approximate node separation range of this model ( $l_c < d < 4l_c$ ) (see **Fig. 2.4.B**).

### 2.3.4 Network model and algorithm

To explore the mechanical response of transient networks, we here concentrate on two-dimensional, plane stress RVEs with periodic boundary conditions (**Fig 2.5**). The details of applied periodic boundary conditions are provided in the Supplementary Information. For simplicity, these RVEs are initially square domains  $\Omega_0$  that contain star-shaped units (with  $n$  dangling chains) whose centers (nodes) act as permanent cross-link sites (**Fig. 2.1**). The free ends of the dangling chains each possess a sticker that can reversibly connect to the dangling chains of neighboring units as discussed above. While many branched dynamic networks include reversible binding sites along the intermediate length of their structural chains [74], [91], [92], we here focus on star-shaped units because it allows us to begin by comparing TNT to the relatively simple case of a monodisperse network with a comparatively homogeneous cross-link distribution. We next describe the numerical approach used to explore the mechanical behavior of these transient networks.

**Network generation.** To generate the networks,  $\mathcal{N}$  nodes are initially positioned within the domain  $\Omega_0$  at Cartesian coordinates  $\mathbf{X}^\alpha$  ( $\alpha \in [1, \mathcal{N}]$ ). For computational

efficiency, the number of nodes included in the RVEs is set to  $\mathcal{N} = 225$ , such that minimum domain width at full deformation remains larger than the contour length of a single chain, thus ensuring that a chain cannot simultaneously span opposite boundaries of the RVE. Increasing the domain size further induces no change in global network stress (see Appendix A.I for details). To ensure a uniform node distribution, node placement follows a 2D Poisson's point process originating at the domain's center  $([0,0])$ . The initial network configuration is then achieved by randomly linking chains according to the kinetics of bond association and dissociation described in the previous sections. The chain concentration  $c_t$  is tuned in this process through the number  $n$  of dangling chains assigned to each node. For simplicity, we posit here that two chains branching from the same node cannot form a connection. To enforce periodicity of the network, nodes across opposite domain boundaries are also allowed to connect and disconnect, as if neighboring one another. Note that in this coarse-grained approach, the dangling chains and stickers themselves are not explicitly modeled when detached. Rather, when a connection forms between cross-link  $\alpha$  and its neighbor  $\beta$ , a chain of length  $Nb$  and end-to-end vector  $\mathbf{r}^{\alpha\beta} = \mathbf{x}^\beta - \mathbf{x}^\alpha$  is regarded with some resultant pairwise force,  $\mathbf{f}^{\alpha\beta}$ , acting on cross-link  $\alpha$  due to  $\beta$ . In the simulations, we therefore only visually represent the chains when they form connections between nodes.

Prior to applying any deformation, the initiated networks are dynamically equilibrated until they reach steady state. Here steady state is defined by equilibration of the network stress (**Fig. 2.5**), defined later in the subsection

**Network deformation and stress calculation.** It should be noted that other benchmarks for steady state, such as the average number of connections  $Z$  per node or mean orientation of the chain end-to-end distribution, consistently stabilized before network stress.

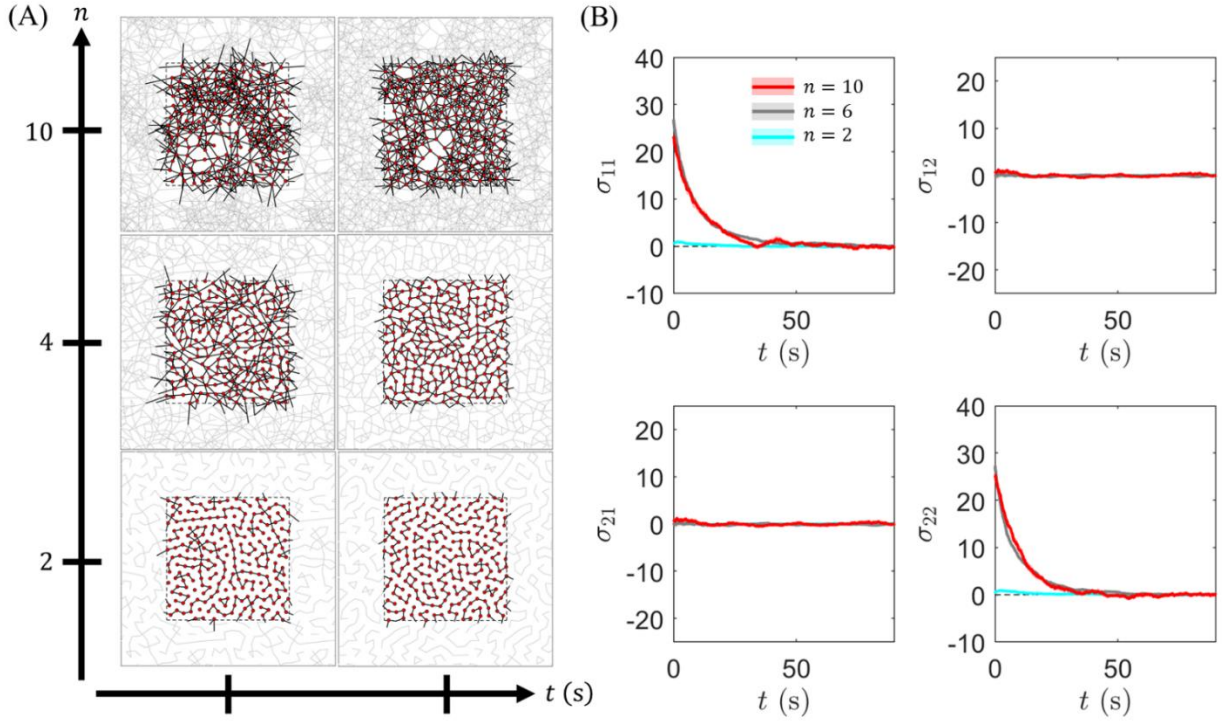


**Figure 2.5. Discrete network homogenization.** (A) Snapshots of networks with  $n = 10$  (top row),  $n = 4$  (middle row) and  $n = 2$  (bottom row) are shown at initiation (left column) and at the end of a 90 second dynamic equilibration process (right column). Red dots represent permanent crosslink sites and black lines represent connected chains. Grey lines represent the periodically replicated chains. Note that permanent crosslinks are reduced in size for visual clarity when plotted. (B) The four components of in-plane virial stress are plotted with respect to time.

**Applying deformation.** In this work, a global, but periodic network deformation is applied over time by imposing a macroscopic deformation gradient  $\mathbf{F}(t)$ . For this, the initially square window is deformed by updating the coordinates of its corners via the mapping

$$x_j(t) = F_{ij}(t)X_i, \quad (2.16)$$

Where  $x_j$  and  $X_i$  are the component of the corner points of the domain in their current and initial configuration, while  $F_{ij}$  are the components of the applied deformation gradient. For the purposes of this work, no shear components of  $\mathbf{F}$  are applied, such that the window always remain orthogonal. The distortion of the window affects the distance between periodic pairs of nodes on opposite boundaries, thus triggering traction forces at the domain bounds. The deformation gradient  $\mathbf{F}(t)$  is stepped in time increments of  $\Delta t$ , which is set such that  $k_d^{-1}$ ,  $k_a^{-1}$ , and the inverse of the applied

strain rate  $\dot{\epsilon}^{-1}$  are all at least two orders of magnitude higher than  $\Delta t$  and a maximum average of one stress free detachment event would occur for every one hundred tethers within a discrete time step (see Appendix A.1 for details). This ensures that the network configuration due to bond dynamics and conformation due to non-affine deformation modes are updated with ample frequency as deformation is applied.

**Network deformation and stress calculation.** After the deformation is stepped, the unbalanced traction forces at the boundaries trigger the motion of nodes in the network until they reach their next equilibrium state. Force equilibration is achieved using a forward Euler, steepest descent algorithm [93]. Thus, the position of node  $\alpha$  at iteration  $k$ ,  $\mathbf{x}_k^\alpha$ , is updated according to:

$$\mathbf{x}_{k+1}^\alpha = \mathbf{x}_k^\alpha + \eta^{-1} \mathbf{f}_k^\alpha, \quad (2.17)$$

where  $\mathbf{f}^\alpha = \sum_\beta \mathbf{f}^{\alpha\beta}$  is the unbalanced force acting on node  $\alpha$ , and  $\eta$  is simply a numerical overdamping coefficient set such that the residual force converges towards zero. Note that  $\mathbf{f}^\alpha$  is inclusive of the tensile chain forces, as well as the repulsive volume exclusion forces. No random force due to Brownian noise is included in the scope of this work as the size of the units considered are such that isotropic noise will have a negligible net effect on diffusion. In contrast, the size of the tethered stickers is not large enough to mitigate Brownian noise, and therefore thermal noise is lumped into the kinetic rates of bond dynamics.

Iteration of Eqn. (2.17) proceeds until the unbalanced forces nearly vanish for all nodes. To reduce the computational cost without a significant reduction in accuracy, the threshold for the maximum and mean residual unbalanced forces are set to less than 5% and 2.5% of  $kT/x_d$ , respectively. We note here that force equilibration is assumed to occur significantly faster than the timescale of bond kinetics or applied deformation, such that neither bond dynamics nor applied deformation are updated during this procedure. At the end of each equilibration step, the stretched state of chains along with pairwise volume exclusion interactions culminate in some average true stress,  $\sigma$ , which is computed using the virial formulation given by:

$$\sigma_{ij} = \frac{1}{2V} \sum_{\alpha}^{\mathcal{N}} \sum_{\beta} r_i^{\alpha\beta} \otimes f_j^{\alpha\beta}, \quad (2.18)$$

where  $V$  is the domain volume [94]. We here exclude the inertial term of the virial stress commonly seen in atomistic or molecular scale discrete models, (due to the overdamped assumption which invokes that the nodes' inertia are negligible) and instead use the virial formulation inherent to the continuum model (Eqn. (2.2)).

**Bond dynamics.** After force equilibration, bond dynamics are enabled following the algorithms for attachment and detachment described earlier. Note that the networks examined are non-associative, in that the number of attached chains need not be conserved (i.e., bond exchange reactions are not prerequisite for dynamics to occur). The algorithm repeats the three steps described above (applying deformation, equilibrating network force, and updating network configuration due to bond dynamics) until the network has undergone the full prescribed deformation history.

## 2.4 Results

Here we report the predicted statistical and mechanical responses of discretely modeled transient networks, and compare them to those predicted by the TNT. Two main mechanical signatures are explored: (a) the rate-dependence of the network response and (b) the dynamics of its stress-relaxation. To achieve this, RVEs containing  $\mathcal{N} = 225$  permanent cross-links are deformed per the load history described as follows and plotted in **Fig. 2.6.A**:

- In the first stage, a uniaxial stretch is applied at constant true strain rate  $\dot{\epsilon}$  up to a stretch of 100% (**Fig. 2.6.A-D.0-2**). Deformation is applied in the Cartesian basis  $\{\mathbf{e}_1, \mathbf{e}_2\}$  (**Fig. 2.6.D**) through the deformation gradient  $\mathbf{F} = \text{diag}(F_{11}, F_{22})$ . The constant strain rate is achieved through the relation  $F_{22} = \exp(\dot{\epsilon}t)$  and incompressible deformation is enforced through the condition  $F_{11} = 1/F_{22}$  (i.e.,  $\det \mathbf{F} = 1$ ).

- In the second stage, a relaxation regime ensues in which the stretch is held constant until equilibrium is achieved (**Fig. 2.6.A-D.2-4**).

In the loading regime, the solution of the TNT given by Eqn. (2.5) can be estimated numerically over time. In the relaxation regime, the deformation gradient remains constant and the solution Eqn. (2.5) takes the simple form:

$$\boldsymbol{\mu}(t - t_0) = \boldsymbol{\mu}_0 \mathbf{e}^{-k_d(t-t_0)}, \quad t \geq t_0, \quad (2.19)$$

where  $t_0$  is the final loading time (i.e., when relaxation begins) and  $\boldsymbol{\mu}_0 = \boldsymbol{\mu}(t_0)$  is the conformation tensor at  $t_0$ . Eqn. (2.19) predicts that the stress decays exponentially to zero with a decay rate of  $k_d$  (**Fig. 2.6.B.2-4**). The TNT also provides a general representation of the chain statistics during network deformation. Since only axial stretches are applied here, the conformation tensor remains diagonal with components  $\boldsymbol{\mu} = \text{diag}(\mu_1, \mu_2)$ . As discussed in Vernerey, et al. (2017) [1], this tensor can be represented by an ellipse with semi-axes  $\mu_1$  and  $\mu_2$  in the directions  $\mathbf{e}_1$  and  $\mathbf{e}_2$ , respectively. This ellipse represents the normalized mean-square stretch of the chains in different orientations (**Fig. 2.6.C**). To produce statistically representative results from the discrete model, each of these conditions is imposed onto an ensemble of fifty different networks from which the average stress responses and chain distributions are measured. These results are illustrated in **Fig. 2.6** for a reference network, with a chain concentration of  $c \approx 15\zeta^{-2}$  (or average connectivity  $Z \approx 8.4$ ), deforming at a strain rate  $\dot{\epsilon} = k_d^0$ . Good agreement with the continuum prediction is obtained when the dissociation rate used in the TNT matches the average bond dissociation rate,  $\bar{k}_d$ , measured from numerical results ( $\bar{k}_d \approx 6.5k_d^0$ ). Here,  $\bar{k}_d$  is taken as the total number of detachment events in the network per time step, normalized by the total number of attached chains at the beginning of said time step. Significantly, the observation that  $\bar{k}_d \neq k_d^0$  is a consequence of force-dependent detachment through Eqn. (2.9). In the remainder of this work, the applied strain rate is normalized by the rate  $\bar{k}_d$ , thus introducing the non-dimensional Weissenberg number  $W = \dot{\epsilon}/\bar{k}_d$ .

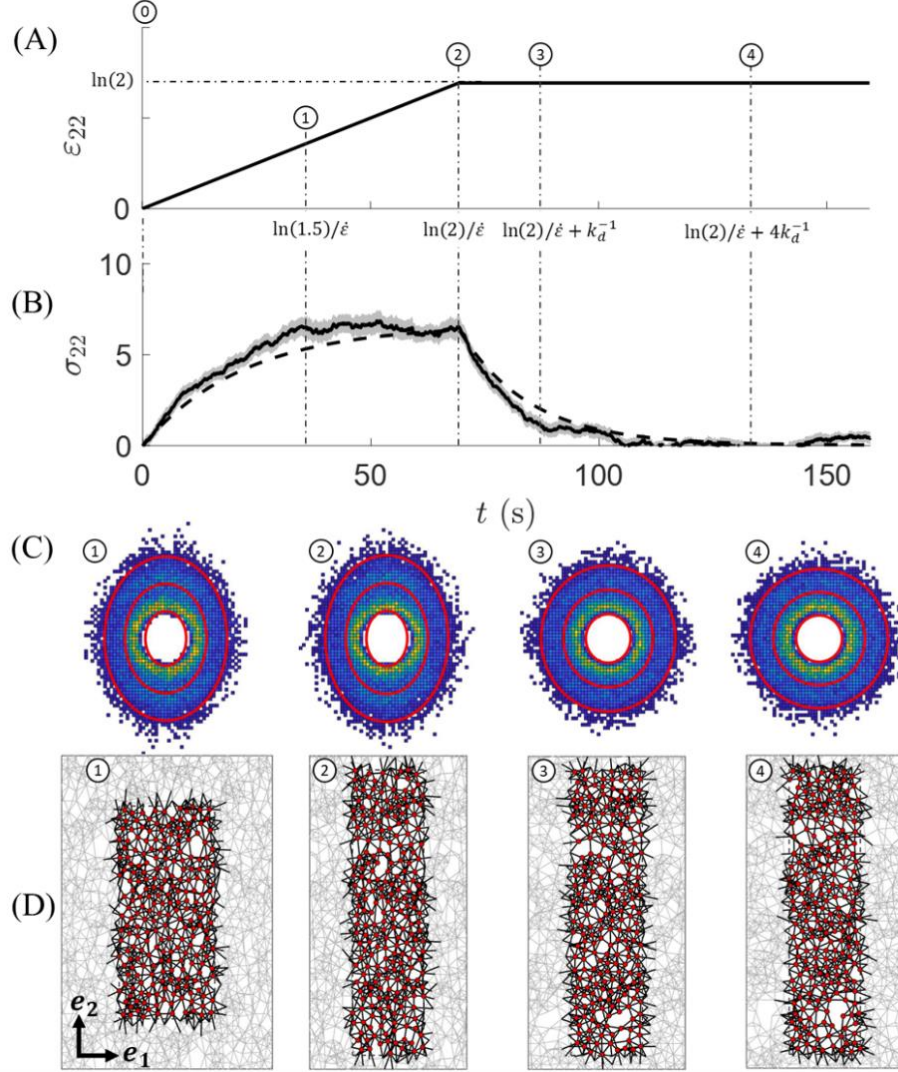


**Figure 2.6. Intrinsic viscosity of network model.** (A) True strain in the direction of extension,  $\varepsilon_{22} = \ln F_{22}$ , is plotted with respect to simulation time. Loading is applied at a constant true strain rate until the network is stretched by 100% (i.e., until time  $t = \ln(2)/\dot{\varepsilon}$ ), after which the network is held in its deformed state until the stress fully relaxed. (B) The normal component of virial stress in the vertical direction is plotted with respect to time when  $W \approx 1/6$  and  $c \approx 15\zeta^{-2}$ . The stress response shown is the ensemble average of 50 numerical experiments. Standard error, plotted as a shaded area around the curve, constitutes less than 5% of the mean. The stress response computed from (5) is plotted as a dotted curve. (C) The ensemble joint distributions of  $\mathbf{r}^{ab}$  from ten numerical experiments are displayed as 2D histograms.  $\mathbf{r}$ , as predicted by  $\mathbf{r} = \mu \mathbf{r}_0$ , is plotted as red ellipses for initial end-to-end lengths of  $|\mathbf{r}| = [0.5, 1, 1.5]$ . (D) Snapshots of one numerical network during deformation are displayed for reference. (C-D) The designations 1-4 represent the network (1) at a stretch of 1.5, (2) at a stretch of 2 when loading is initially halted, (3) at time  $t = k_d^{-1}$  into stress relaxation, and (4) time  $t = 4k_d^{-1}$  into stress relaxation.

Both the stress response in time,  $\sigma(t)$  (**Fig. 2.6.B**) and the distribution functions of connected chains' end-to-end vectors, (**Fig. 2.6.C**) are reasonably well-predicted by Eqn. (2.6) for the conditions given ( $W \approx 1/6$  and  $Z \approx 8.4$ ). Generally, during loading,



chains are stretched in the direction of applied tension as indicated by the elongation of the joint distribution functions in **Fig. 2.6.C.1-2**, resulting in the generation of tensile stress in the loading direction (**Fig. 2.6.B.1-2**). Once loading is ceased (**Fig. 2.6.A-D.2-4**), the joint distribution begins to revert to an isotropic state (**Fig. 2.6.C.3**) and the stress relaxes (**Fig. 2.6.B.3**). Eventually, the network reverts fully to the stress-free, isotropic state associated with  $\mu_0 = I$ .

It is however worthwhile to note that some deviation occurs during both the loading and stress relaxation phases. In the the stress predicted by the discrete model is initially slightly greater than that predicted by Eqn. (2.6), likely due to the divergence of force associated with Langevin chains, which is not captured by the idealized continuum model. Yet, despite this initially higher stiffness, we see that the peak stresses at the time when loading is ceased (**Fig. 2.6.B.2**) roughly coincide between the discrete and continuum models. This is because a region of roughly steady state stress (i.e., creep) is predicted by the discrete model in later loading stages. This stress plateau is not observed in the continuum model whose modulus always remains finite in the deformation range depicted. Notable discrepancies also exist during the stress relaxation regime, where the initial reduction in stress occurs faster for the discrete model than it does for the continuum model, indicating that the stress of the former does not decay exponentially. Both the creep response and non-exponential stress-relaxation of the discrete model may be attributed to three main mechanisms not captured by the continuum model: (a) non-affine microstructural deformation, (b) nonlinear chain response, and (c) force-dependence of the bond dissociation rate  $k_d$ . While the observed differences are mild given the low loading rate ( $W < 0.5$ ) and high connectivity ( $Z \gg 2$ ) presented in **Fig. 2.6**, we now explore the conditions under which the continuum model fails to capture the network mechanics predicted by the discrete model.

### 2.4.1 Effects of strain rate

To better understand the limitations of the TNT with regards to strain rate, we first sweep  $W \in [1/8, 1/4, 1/2, 1, 2]$ , while holding the total chain concentration  $c_t$  constant (therefore holding a fixed connectivity  $Z \approx 8.4$ ). The global mechanical stress responses of networks loaded at various strain rates are displayed during deformation and relaxation in **Fig. 2.7.A** and **2.7.B**, respectively. To elucidate the underlying micro-mechanical phenomenon that drives deviation in global stress between the continuum and discrete model predictions, the constant and stretch-dependent detachment rates ( $k_d$ ),s of a single chain in the continuum and discrete models, respectively, are plotted with respect to  $r$  in **Fig. 2.7.E**. The percent deviation between the values of  $k_d$  from each model are also plotted with respect to  $r$  in **Fig. 2.7.E**, to show that  $k_d$  of highly stretched chains deviates significantly between the models. The maximum values of  $k_d$  at four different times corresponding to (1) partway through loading, (2) at peak loading, (3) partway through stress relaxation, and (4) near complete stress relaxation are denoted for the lowest (blue) and highest (red) strain rates, respectively.

**Nonlinear Langevin chains stiffen the network response during initial loading.** It is well-known that the affine assumption leads to over-prediction of true stress; however the results depicted in **Fig. 2.7.A** show that during the initial loading, the stress predicted by the TNT is consistently underestimated across all strain rates. This is not observed for discrete networks of Gaussian springs (see Appendix A.2, **Fig. A.2.A**). It is therefore attributed to the use of Langevin chains in the discrete model, whose force, as modeled through the Padé approximation [86], not only exceeds that of ideal chains at any stretch (albeit, minutely below  $\lambda = l_c/(\sqrt{N}b)$ ), but also undergoes divergence as chains are stretched to their contour lengths (**Fig. 2.2.A**). As such for fixed values of  $N$ ,  $b$ ,  $c_t$ , the Langevin chain model always produces networks with higher predicted stiffness than those comprised of linear chains and the effect is exacerbated at high stretches. Therefore, the continuum model should

always under-predict the network stress, regardless of the loading history. Yet, the stress responses during the relaxation regime in **Fig. 2.7.B** indicate that this is not the case.

**Network connectivity is conserved despite force and separation-dependent bond dynamics.** Given force-dependent detachment through Eqn. (2.9), we find that there exists an increase in the mean detachment rate,  $\bar{k}_d$ , during deformation. This is exemplified in **Fig. 2.7.E** (for the case of  $W \approx 1/2$ ) by the slight increase of the mean during times of loading (designated by the blue tags labeled “1” and “2”), versus times of relaxation (denoted by the blue tags labeled “3” and “4”). The increase in mean detachment rate during deformation is negligible for low strain rates (e.g.,  $W \approx 1/8$ ), but as high as 15% for high strain rates (i.e.,  $W \approx 2$ ) immediately highlighting a limit of the constant  $k_d$  assumption when applied to networks undergoing fast loading. Even more pronounced is the impact of high loading rate on the maximum value of  $k_d$  for a single bond. In the case of  $W \approx 1/2$ , some bonds became stretched enough to undergo a forty-fold increase in  $k_d$  over the mean effective value used to fit the continuum model, which occurred during peak loading (designated by the red tag labeled “2”). Later we examine how local increase in  $k_d$  impacts the networks' stress response during loading and relaxation; but first we note that escalation of  $k_d$  drives a corresponding increase in the mean attachment rate,  $\bar{k}_a$ , which is taken as the total number of attachment events in the network per time step, normalized by the total number of detached chains at the beginning of said time step. The increase in  $\bar{k}_a$  is attributed to an increase in the number of attachment opportunities that occur at high strain rates due to both the higher detachment rate of chains and the mutual introduction of yet unattached tethers into each other's fields of reach. Despite this rise in bond reaction rates, the average connectivity  $\bar{Z}$  of the network remains constant. This suggests that  $\bar{k}_d$  and  $\bar{k}_a$  increase proportionally such that the steady state concentration predicted by Eqn. (2.3) remains valid for all deformation rates observed. Nevertheless, the increased bond kinetics act as a softening mechanism whose effects, as discussed below, are most pronounced at higher strain rates.

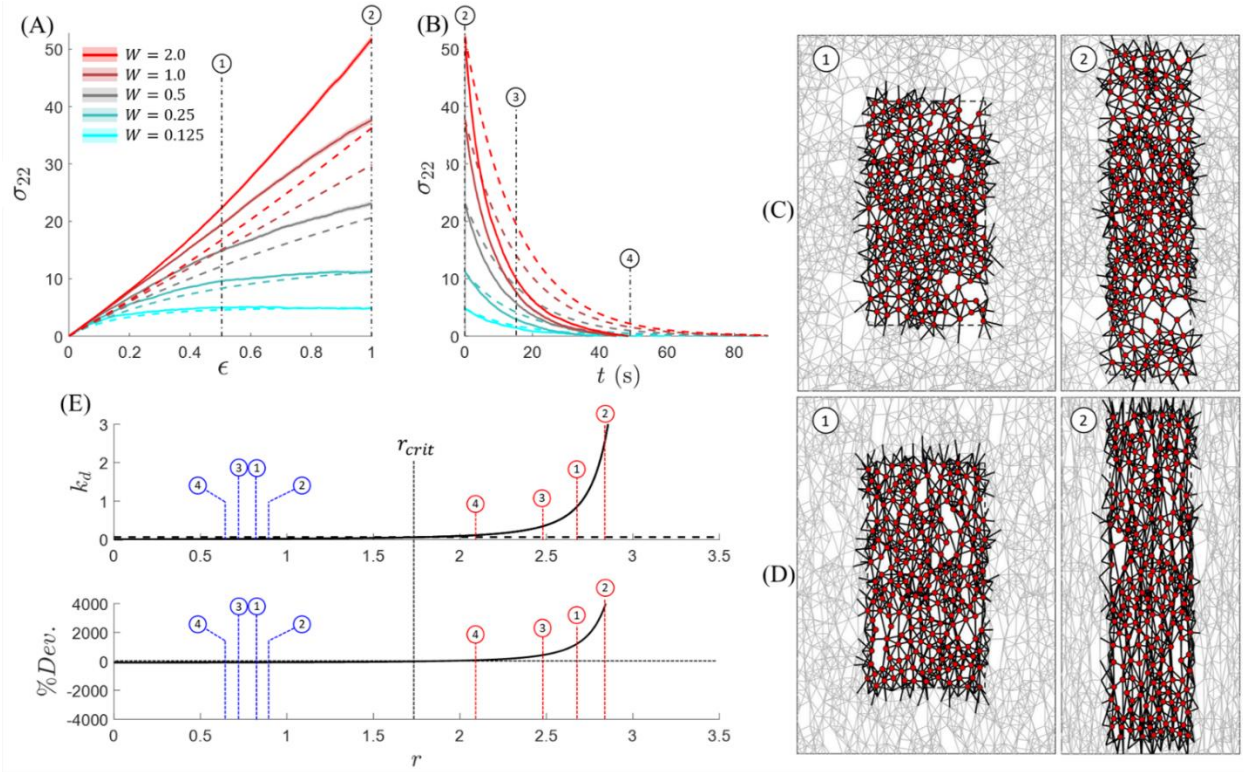


**Figure 2.7. Effects of loading rate.** (A) Normal stresses from creep experiments are plotted with respect to engineering strain,  $\epsilon = F_{22} - 1$ , for  $W \approx 1/8$  (cyan),  $W \approx 1/4$  (teal),  $W \approx 1/2$  (grey),  $W \approx 1$  (maroon), and  $W \approx 2$  (red). (B) Normal stresses from relaxation experiments are plotted with respect to time for three different initial values of stress. All results from the discrete model are plotted as continuous curves with standard error represented by the shaded region, and results from TNT are plotted as dotted curves. (C-D) The corresponding networks at times 1 (left) and 2 (right) are depicted when (C)  $W \approx 1/8$  and (D)  $W \approx 2$  to highlight the effect of strain rate on chains' stretches and orientations. (E) Top: Bond dissociation rate,  $k_d$  is plotted with respect to  $r$  for Eyring's theory employed in the discrete model (continuous black curve) and the constant  $k_d$  assumption used in the continuum model (dotted black line). Bottom: the percent deviation between the continuum and discrete model dissociation rates is plotted with respect to  $r$ . Where the percent deviation transitions from negative to positive is labeled  $r_{crit}$ , as chains with  $r > r_{crit}$  will undergo faster dissociation than predicted by the continuum model. The four values denoted in blue represent the average values of  $r$  for times (1-4) when  $W \approx 1/8$ . Similarly, the four values denoted in red represent the maximum values of  $r$  for times (1-4) when  $W \approx 2$ .

**Force-dependent bond detachment entails non-exponential stress relaxation.** The most obvious effect of force-dependent detachment is the non-exponential decay of stress which occurs during relaxation as observed in **Fig. 2.7.B**. More specifically, once loading is ceased, the discrete network stress initially decays faster than the continuum model predicts and the degree of disagreement is greater for larger stresses (as in the case of higher loading rates). To understand this

response, we examined the percentage of chains whose end-to-end distances  $r$ , exceeds the value at which the local detachment rate equals that of the value fitted to the TNT,  $r_{crit}$  (**Fig. 2.7.E**). As expected, **Fig. 2.8.A-B** demonstrate that this percentage is generally higher during loading (at times “1” and “2”) than during relaxation (at times “3” and “4”), and this effect is more pronounced for higher strain rates. This increased percentage of highly stretched chains explains the non-exponential decay of stress in the direction of applied loading for a few reasons. Firstly, the non-linearity of Eqn. (2.9) ensures that the bond dissociation rates of chains stretched beyond  $r_{crit}$  are orders of magnitude higher than those of bonds in the regime  $r < r_{crit}$ . Thus, the bonds detaching more frequently are those which are highly stretched, which - given any monotonically increasing force-extension relationship - are also those carrying the most tensile load and thus disproportionately contributing to the global stress response. Secondly, this effect is exacerbated by the use Langevin chains, which ensures that not only are the highly stretch chains contributing disproportionately to the stress, but they do so non-linearly due to the divergent chain force in the limit  $\lambda \rightarrow \sqrt{N}$ . Finally, as illustrated through the joint distribution functions of  $\mathbf{r}$  (**Fig. 2.8.C**), the majority of chains stretched past a distance of  $r_{crit}$  are oriented with their larger component in the direction of global stretch ( $\mathbf{e}_2$ ); therefore, as these chains detach, they will principally reduce the reported stress component  $\sigma_{22}$ . While these effects are most noticeable during stress-relaxation, closer examination also reveals that they impact the stress response observed during loading as well.

**Force-dependent bond dynamics begets steady-state creep regardless of strain rate.** Under the assumption of a constant dissociation rate  $k_d$ , the TNT predicts that a network subjected to a constant true strain rate (characterized by  $W$ ) will experience a steady-state true tensile stress of the form:

$$\sigma = ckT \frac{W}{(1+W)(1-2W)}, \quad (2.20)$$

which notably diverges when  $W \geq 0.5$ . This result can readily be obtained by setting the term on the left-hand side of Eqn. (2.4) to zero. In other words, when  $W \geq 0.5$ , the rate of energy dissipation due to chain detachment is overtaken by the rate of elastic storage due to deformation, such that the elastic energy increases infinitely with time. However, as displayed by **Fig. 2.8.D**, discrete networks isochorically stretched to 250% of their original length do not exhibit such a singularity. Instead, the discrete model predicts that steady state creep is reached for strain rates up to  $W = 1$ . This observation is attributed to the stretch-dependency of  $k_d$ . Indeed for networks that are stretched slowly ( $W \approx 0.1$ ) the percentage of chains exceeding  $r_{crit}$  remains close to 1% (**Fig. 2.8.A-B**, cyan curve) throughout deformation while for networks that are stretched quickly ( $W \approx 1$ ), the percentage of chains exceeding  $r_{crit}$  can reach close to 15% (**Fig. 2.8.A-B**, maroon curve). The faster dissociation rate of these highly stretched chains mitigates storage of elastic energy such that a finite steady state stress is always observed. We note that steady state could not be reached for networks stretched at high rates without introducing exceedingly large Lagrangian deformation of the unit cell and so  $W$  is limited to the regime  $W \leq 1$  with the given deformation approach. It is however expected that a steady creep will be obtained for any value of  $W$  based on the above analysis. Worth noting, is that at times the networks are observed to undergo a drop in stress rather than achieving steady state. Such cases occur when voids nucleate in regions of initially lower chain concentration, as exemplified by **Fig. 2.8.E**.

Here, we define a void as a gap in the network's cross-link distribution whose characteristic height and width are both too large to permit locally sustained percolation. This occurs when the rate of attachment across said gap is an order of magnitude less than the corresponding rate of detachment (i.e.,  $k_a/(k_a + k_d) \lesssim 10\%$ ), which - referencing **Fig. 2.4.B** - corresponds to a node separation of roughly  $3l_c$ . Therefore, although voids will not assume perfectly circular geometries, we loosely classify voids as vacant regions whose areas,  $A_v$ , satisfy the normalized condition  $A_v^* = A_v/[\pi(3l_c/2)^2] \geq 1$ . Given this definition, transient voids appear to occur at every

strain rate despite incompressible loading conditions. However, preliminary results suggests that voids constitute a greater average areal fraction,  $\bar{\varphi}$ , of the networks when high strain rates are applied (e.g.,  $\bar{\varphi} \approx 1.3 \pm 0.5\%$  when  $W \approx 0.125$ , whereas  $\bar{\varphi} \approx 2.5 \pm 0.5\%$  when  $W \approx 1$ ). This increase in  $\bar{\varphi}$  emerges from a concurrent increase in the maximum number of voids observed existing simultaneously ( $n_v$ ), average void area ( $\bar{A}_v^*$ ) and average void lifetime ( $\bar{T}_v$ ). Specifically,  $n_v = 3$  versus 1,  $A_v^* = 1.67 \pm 0.20$  versus  $1.36 \pm 0.1$ , and  $\bar{T}_v^* = \bar{T} \times k_d^0 = 0.105 \pm 0.050$  versus  $0.047 \pm 0.016$  for  $W \approx 1$  versus  $W \approx 0.125$ , respectively. Such defects are hypothesized as the cause of mechanical failure in associative networks such as vitrimers [95]. Indeed a decline in stress (as opposed to steady-state creep) is observed in cases where large voids develop. Thus, to ensure that force-dependent bond detachment alone, and not softening due to void nucleation, is responsible for the average observed induction of creep, cases in which voids formed are excluded in the computation of steady state stress reported in **Fig. 2.8.D**. Furthermore, additional factors such as the goodness of solvent may significantly impact the onset of damage and consequently the global stress response in real materials such as gels [96]. Therefore, these factors should be considered on a material-specific basis for in-depth studies of damage. Nevertheless, these preliminary results generally suggests that damage in rate dependent transient networks is exacerbated by increased loading rate. Additionally, the emergence of voids represents a consequence of mesoscopic heterogeneity that influences global mechanical response, yet which the continuum model cannot predict: weakening due to nucleation of defects that are too large to heal on the timescale of individual bond exchanges. As such, further investigations of damage in transient networks may be conducted via this model in forthcoming work.

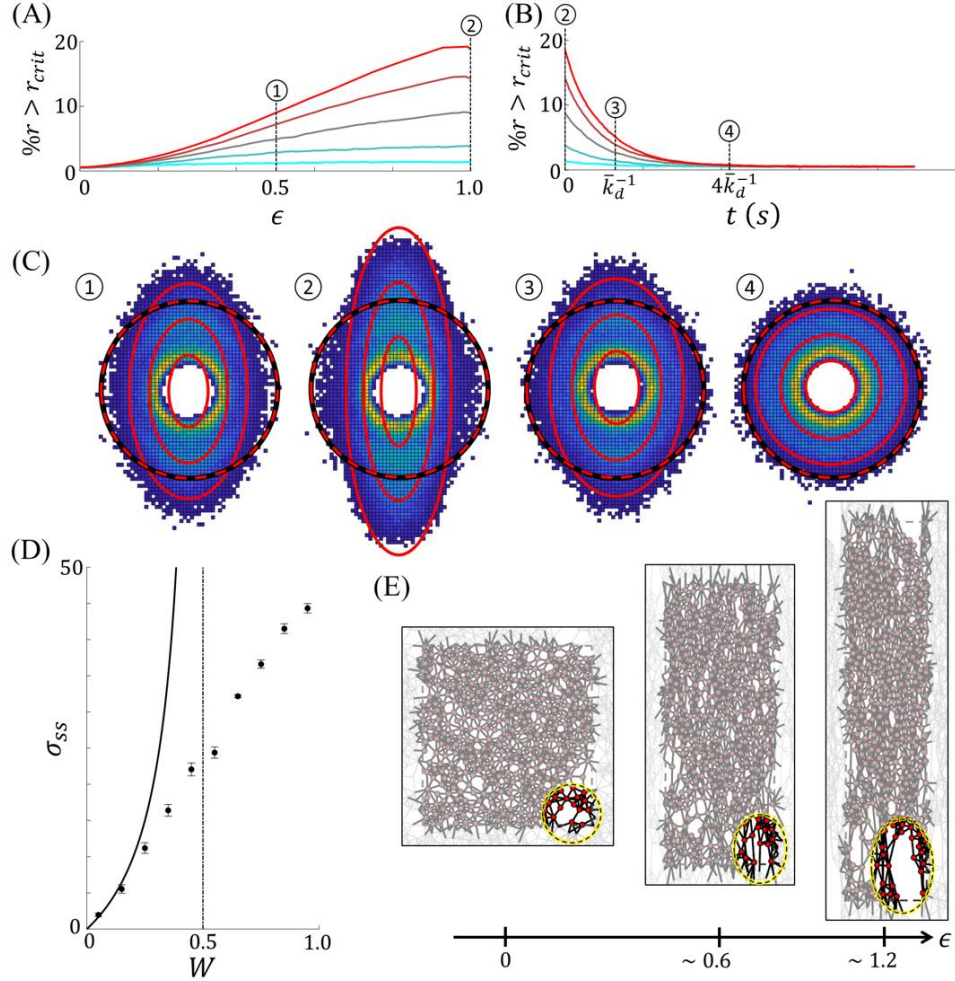


**Figure 2.8. Micromechanical origins of mismatch with TNT.** (A-B) The percentage of chains stretched above  $r_{crit}$  during (A) creep and (B) stress relaxation is plotted with respect to engineering strain and time, respectively. Results from three values of true  $W$ :  $W = 1/8$  (cyan),  $W = 1/4$  (teal),  $W = 1/2$  (grey),  $W = 1$  (maroon), and  $W = 2$  (red) - are shown. (C) The ensemble joint distributions of  $\mathbf{r}$  from ten numerical experiments are displayed as 2D histograms for  $W = 2$ .  $\mathbf{r}$ , as predicted by  $\mathbf{r} = \mu \mathbf{r}_0$ , is plotted as red ellipses for initial end-to-end lengths of  $|\mathbf{r}_0| = [0.5, 1, 1.5]$ .  $r_{crit}$  is plotted as a red dashed circle to visually illustrate the fraction of chains that are above or below the threshold, as well as their orientation. (D) Steady state stress is plotted with respect to  $W$  for the numerical model as discrete data, and the continuum theory as a continuous black curve. The vertical dotted line at  $W = 0.5$  denotes where the steady state stress predicted by the continuum model diverges. (E) A network deforming at a rate of  $W = 0.85$  is depicted at three different strains and highlights a region where the local void nucleation occurs.



### 2.4.2 Effects of chain concentration

Having observed the effects of strain rate on the network response, we now turn to explore the effects of chain concentration at low strain rates. For this, we sweep the number of tethers per node,  $n \in [2, 4, 10]$ , which produces measured chain concentrations of  $c \approx 15\zeta^{-2}$  ( $Z \approx 8.4$ ),  $c \approx 6.5\zeta^{-2}$  ( $Z \approx 3.6$ ), and  $c \approx 3.3\zeta^{-2}$  ( $Z \approx 1.8$ ), respectively, while deforming the domain at a relatively low strain rate of  $W \approx 1/6$ .

**Low chain concentration leads to over-predicted network stress by the continuum approach.** We confirm that at high concentrations the continuum model predicts the stress response of the discrete model fairly well throughout the deformation history, barring the discrepancies discussed in Section 2.4.1. However, at lower concentrations, when  $c \leq 6.5\zeta^{-2}$  ( $Z \approx 3.8$ ), the TNT overestimates the stress response (**Fig. 2.9.A**). Observing the probability joint distribution functions of  $\mathbf{r}$  (**Fig. 2.9.B-C**), it is clear that at low concentrations, chains tend to occupy the shorter (i.e., lower energy) configurations available to them more readily. Therefore, it is unsurprising that the networks stress is reduced for domains with fewer chains. That chains occupy these lower energy states to begin with is driven by the distance-dependent rates of  $k_a$  and  $k_d$  discussed in Section 2.3, which ensure that higher fractions of chains will occupy lower end-to-end distance configurations (**Fig. 2.4.B**). Yet, another possible softening effect is that units in networks with lower connectivity have higher conformational degrees of freedom and may deform non-affinely, as needed, to a lower energy state than that predicted by TNT (which assumes instantaneously affine chain evolution  $\dot{\mathbf{r}} = \mathbf{L}\mathbf{r}$ ).

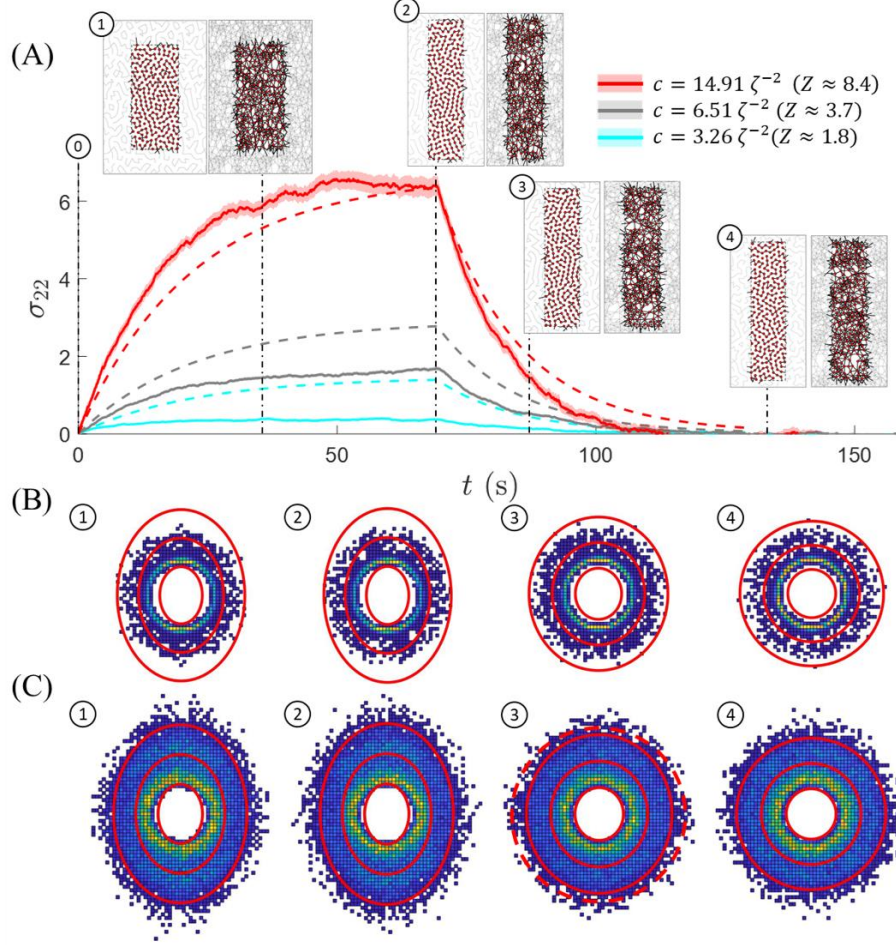


**Figure 2.9. Effects of network coordination.** (A) The stress response for the full loading history of **Fig. 2.6.A** is plotted with respect to time for  $Z \approx 1.8$  (cyan),  $Z \approx 3.6$  (grey), and  $Z \approx 8.4$  (red), respectively. Solid curves with shaded regions represent discrete data with standard error, while dotted curves represent the stress response predicted by TNT. The inset depictions of the networks at each time visually illustrate how  $n$  influences the network topology through chain concentration. Insets on the left always depict networks for which  $n = 2$ , while insets on the right depict networks with  $n = 10$ . (B-C) The ensemble joint distributions of  $\mathbf{r}$  from ten numerical experiments are displayed as 2D histograms for (B)  $n = 2$  and (C)  $n = 10$ .  $\mathbf{r}$ , as predicted by  $\mathbf{r} = \mu \mathbf{r}_0$ , is plotted as red ellipses for initial end-to-end lengths of  $|\mathbf{r}_0| = [0.5, 1.5]$ .

**Both bond kinetics and conformational changes contribute to non-affine deformation within a finite time interval.** As discussed above, the continuum model relies on the instantaneously affine assumption that the rate change of a chain's end-to-end vector evolves according to  $\dot{\mathbf{r}} = \mathbf{L}\mathbf{r}$  where  $\mathbf{L}$  is the globally applied velocity gradient. To approximately test this in the discrete model, we quantified the extent of non-affine network deformation according to:

$$\delta u^* = \left\langle \frac{\|\delta \mathbf{u}\|}{\|\mathbf{u}_{aff}\|} \right\rangle, \quad (2.21)$$

where  $\langle \rangle$  denotes taking the ensemble average over all  $N^{\alpha\beta}$  chains that remain attached during the time interval from  $t$  to  $t + \tau$ ,  $\delta \mathbf{u} = \mathbf{r}^{\alpha\beta}(t + \tau) - \mathbf{r}_{aff}^{\alpha\beta}(t + \tau)$ , and  $\mathbf{u}_{aff} = \mathbf{r}_{aff}^{\alpha\beta}(t + \tau) - \mathbf{r}^{\alpha\beta}(t)$  [97]. Here,  $\mathbf{r}^{\alpha\beta}$  and  $\mathbf{r}_{aff}^{\alpha\beta}$  represent the actual and affinely predicted chain end-to-end vectors, respectively, at time  $t + \tau$ . The latter,  $\mathbf{r}_{aff}^{\alpha\beta}$ , is calculated according to:

$$\mathbf{r}_{aff}^{\alpha\beta}(t + \tau) = \mathbf{F}_\tau \mathbf{r}^{\alpha\beta}(t), \quad (2.22)$$

where  $\mathbf{F}_\tau$  is the globally applied deformation gradient from time  $t$  to  $t + \tau$ . By definition,  $\delta u^* = 0$  when the network deformation is affine and  $\delta u^* \rightarrow 0$  in the limit  $\tau \rightarrow 0$ .

In this framework, network connectivity is modulated through the total number of tethers as opposed to by changing the bonds' attachment or detachment rates. As such, a network with more tethers will have more total bond reactions per unit volume within a given time interval and undergo a greater degree of configurational change. Therefore, to isolate the degree of non-affine deformation due to conformational effects (e.g., floppy modes [68]), as opposed to network restructuring, we normalize  $\delta u^*$  by the total number of network tethers  $\mathcal{N}n$ , which scales proportionately to the density of bond reactions. Indeed, observing **Fig. 2.10**, we see that non-affine deformation due to conformational change increases in time, but is negligible in the limit  $\tau \rightarrow 0$ , which is consistent with the instantaneously affine assumption. We also see that non-affine deformation is amplified for networks with lower connectivities. Since non-affine deformation modes allow networks to reduce their free energy (thus softening their mechanical responses) [63], [68], this is the likely explanation for the underestimation of network stress by the continuum model at low chain concentrations. In the remainder of this work, we examine a modification to the continuum approach (through the phantom network theory [68], [98]) that is meant to correct for non-affine softening effects.

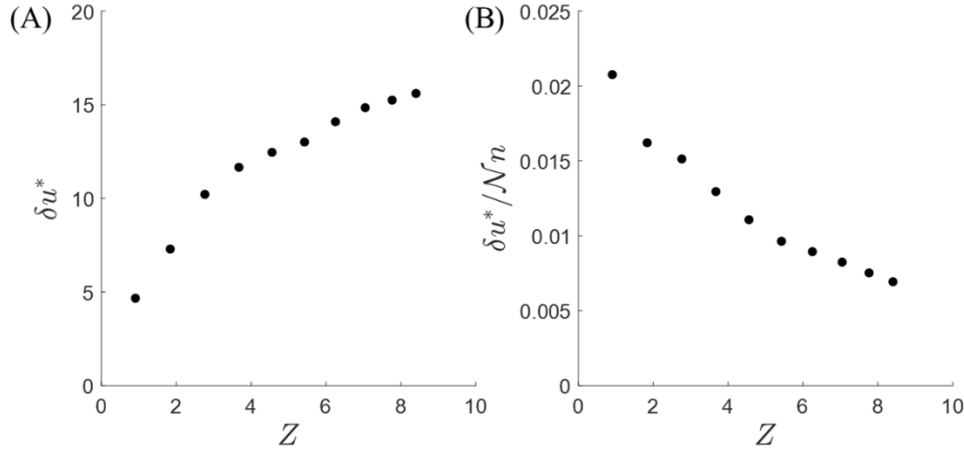


**Figure 2.10. Micromechanical study of non-affine deformation.**  $\delta u^*/(\mathcal{N}n)$  is plotted with respect to time interval,  $\tau$ , for networks in which  $\bar{Z} \approx 1.8$  (solid cyan),  $\bar{Z} \approx 3.7$  (dashed teal),  $\bar{Z} \approx 5.4$  (dotted-dashed grey),  $\bar{Z} \approx 7.0$  (dashed maroon), and  $\bar{Z} \approx 8.4$  (solid red).

**Correction to network stiffness through phantom network theory leads to under-prediction of the network stress by the continuum approach.** Through the conventional TNT, a network's shear modulus is taken as  $G = ckT$ . However, to adjust for non-affine effects the phantom network theory poses a correction to the instantaneous shear modulus as follows [68]:

$$G = \left(1 - \frac{2}{Z}\right) ckT, \quad (2.23)$$

for  $Z \geq 2$  and  $G = 0$  for  $Z < 2$ . The shear modulus of discrete networks is estimated according to the relation  $G = 2E(1 + \nu)$ , where  $E$  is the Young's modulus, and  $\nu$  is the Poisson's ratio ( $\nu = 0.5$ , given enforced incompressibility). For each network connectivity,  $E$  is taken as the initial tangent modulus of the stress-strain response ( $E \approx \partial\sigma/\partial\varepsilon$ ), based on the assumption that dissipative effects of networks near their stress-free configurations and over short timescales are negligible. This assumption is valid given that the networks begin at roughly stress-free states and the time interval over which  $E$  is measured ( $\sim \Delta t$ ) is much smaller than the timescale of bond dynamics ( $\bar{k}_d^{-1}$ ). Indeed, examining **Fig. 2.11.A** we see that this correction introduces good agreement between the shear modulus predicted by the TNT and discrete models. Nevertheless, as displayed in **Fig. 2.11.B**, applying this correction to the TNT leads to the ubiquitous under-prediction of network stress by the continuum approach

due to use of Langevin chains in the discrete model. Furthermore, a finite modulus remains measurable for discrete networks even below the percolation threshold of  $Z = 2$ .

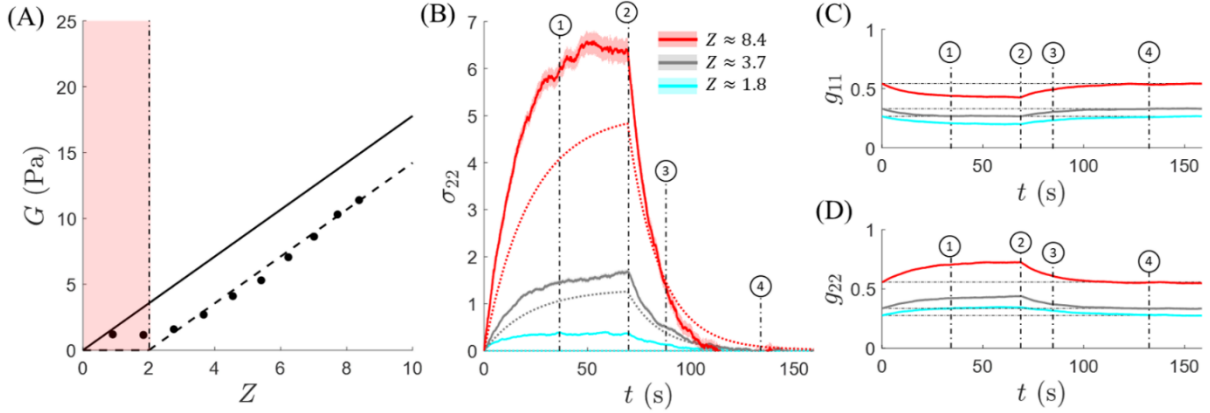


**Figure 2.11. Phantom chain theory and chain conformation.** (A) network stiffness,  $G$ , is plotted with respect to  $Z$  for the numerical model as discrete data, and the continuum theory as a continuous black curve for the unadjusted model ( $G = ckT$ ) and a dashed black curve for the adjusted model ( $G = (1 - 2/Z)ckT$ ). The region shaded in red represents the non-percolated regime in which the adjusted TNT predicts no finite modulus. (B) The stress response predicted by the discrete model (continuous curves with shaded regions to represent standard error) and TNT (dashed curves) corrected through Eqn. (2.23), are plotted with respect to time. (C-D) The normal components of  $\mathbf{g}$  in direction (C)  $\mathbf{e}_1$  and (D)  $\mathbf{e}_2$  are plotted with respect to time. (B-D) Results from networks with average connectivities of  $Z \approx 1.8$  (cyan),  $Z \approx 3.6$  (grey), and  $Z \approx 8.4$  (red) are provided.

**A small tensile stress can exist below the percolation threshold.** The correction from the phantom network theory dictates that no network stress will exist for networks below the percolation threshold of  $Z = 2$ . However, as displayed in **Fig. 2.11.A**, the discrete model indicates that a finite tensile stress remains present even when  $Z < 1$  (or  $n = 1$ ). In such cases the measured stress cannot be the result of percolation, rather it is due to the alignment of disconnected chains. To better understand this effect, we revisit the computation of virial stress through Eqn. (2.18). Recalling that pairwise volume exclusion forces occur between all neighboring units, we recognize that this produces a roughly isotropic contribution to the stress. As such, any preferential alignment of the chains, which can only carry tension, culminates in a finite normal stress that is not balanced by the isotropic volume exclusion. To

quantitatively gauge chain alignment, we computed the ensemble average metric tensor of  $\mathbf{r}$ ,  $\mathbf{g}$ , defined as:

$$g_{ij} = \frac{1}{V_{ct}} \sum_{\alpha}^{\mathcal{N}} \sum_{\beta} r_i^{\alpha\beta} \otimes r_j^{\alpha\beta}. \quad (2.24)$$

The diagonal components of  $\mathbf{g}$  indicate the degree to which chains are aligned with the components of the orthonormal basis  $\{\mathbf{e}_1, \mathbf{e}_2\}$ , where  $g_{11} > g_{22}$  indicates that chains are more aligned with  $\mathbf{e}_1$  than  $\mathbf{e}_2$ , and  $g_{11} \approx g_{22}$  indicates no preferential alignment. Examining  $g_{11}$  and  $g_{22}$  in **Fig. 2.11.C-D**, it is clear that even when the networks are below the percolation threshold ( $Z < 2$ ), the chains align with the direction of applied extension (i.e.,  $g_{22}$  increases during loading, while  $g_{11}$  decreases). Chain alignment is the origin of measurable stress for networks below the percolation threshold in this model, and is perhaps comparable to the stress evolution which occurs in dilute solutions of dumbbell-like polymers (e.g., dimers or finitely-extensible nonlinear elastic polymers) or viscoelastic fluids undergoing shear flows [99], [100]. However, unlike these dilute systems, the discrete model is representing compactly confined nodes. Furthermore, the current iteration does not capture the solute-solvent interactions which are often critical to the hydrodynamic effects of such systems [99], [101]. Therefore, while commenting on the effects observed below the percolation threshold, here we primarily focused on the findings of these models in the regime  $Z > 2$ .

## 2.5 Summary and concluding remarks

Ultimately, we have introduced a coarse-grained, discrete numerical model that allows us to directly investigate topological changes in transient networks without the high computational cost stemming from modeling the elemental constituents. To better represent the set of networks that can be examined through this model, we incorporated nonlinear Langevin chains [86], probabilistic slip-bond detachment through Eyring's [65] or Bell's [72] model, and probabilistic bond reattachment based on Rouse diffusion of tethered chains [80], thereby capturing the energetic penalty

associated with highly stretched networks. Despite these features, we find that the idealized TNT approach [1], which assumes linear chains and constant bond dynamics, provides excellent agreement with the numerical model when low strain rates are applied and network connectivity is high. Therefore, this discrete method may be feasibly incorporated into a quasicontinuum [75]–[77] framework in which regions exhibiting low stretch and heterogeneity are efficiently modeled through the TNT [60], while regions of high local stretch, such as those near crack tips or other stress concentrations, are modeled through the newly introduced approach. While quasicontinuum models have recently been developed for irregular networked materials undergoing rate-dependent, permanent damage [76], [77], to our knowledge no framework has been developed for fully dynamic, self-healing networks. Yet, as recently discussed by Ghareeb and Elbanna (2021) [77], quasicontinuum modeling also lends itself to comparable investigation in such materials. This model constitutes one possible discrete modelling component of such an approach for networks with fully reversible bond dissociation.

Whether a quasicontinuum or purely discrete framework is used, our results suggests that network discretization remains crucial in regions of high stretch for a couple of reasons. First, the finite length of true entropic chains (here captured using the Langevin chain model) consistently serves to stiffen the network and its effects become significant when the rate of deformation exceeds that of relaxation. Second, we find that force-dependent bond dynamics induce steady state creep in the discrete model, at high strain rates for which elastic behavior is predicted by the TNT. This same force-dependent bond detachment also induces non-exponential stress decay. Indeed, the numerical approach appears to capture two key features that the continuum model does not: variability of bond kinetics and heterogenization of network topology. Despite variability in the detachment rate, the discrete model predicts conservation of overall mean network connectivity, indicating that the networks, while not enforceably or locally associative, behave macroscopically as such. One might expect that conservation of connectivity precludes the loss of

mechanical strength; yet, the discrete model also predicts the occasional nucleation of voids whose dimensions are too large for chains to reattach across. The formation of such voids induces loss of mechanical strength and it is believed that void nucleation likely precedes the onset of fracture or “damage” in dynamic networks despite the reversibility of their bonds [95].

### 2.5.1 Limitations of the discrete model.

A number of simplifications exist in the current numerical framework that limit the generality of this approach. Firstly, we assume monodispersity in chain lengths; however, given polydispersity's effects on network mechanics [87], it may be included in future work. Regarding the force-extension of single chains, we include no enthalpic bending contribution and the cross-links are modeled as freely attached pin joints [68], limiting this current iteration of the model to networks of flexible chains. Since no energetic penalty is incurred for bending, chains can attach with equiprobability in any direction. Therefore, to mitigate directional biases in attachment between nearest neighbors and facilitate homogenization of network topology, neighboring units are not permitted to attach more than once. However, this simplification is not intrinsically gotten from the underlying physics. Finally, the effects of solvent-solute interactions are neglected, which suspends considerations such as depletion [102] or drag forces [101] from the current framework. Although these limitations do not impact the findings of this work, they must be addressed for the study of specific considerations in future work.

For the extension of this model to damage and self-healing, several limitations must be addressed. Firstly, here network incompressibility is enforced through the condition  $\det \mathbf{F} = 1$  rather than being an outcome of the underlying physical interaction potentials between nodes. In future work, compressible uniaxial tension with traction free bounds may be conducted on networks whose Poisson's ratio is dictated by their inter-unit potentials. Given some attractive regime (e.g., that of



Lennard-Jones potentials [103]), these interactive potentials will introduce an effective surface tension that governs compressibility (or the lack thereof). Secondly, irreversible damage of chains that are overly stretched is omitted from the current framework, but is needed for the prospective study of permanent damage [73], [74], [104], which can impact the number of available chains for reattachment. Lastly, the positions of individual stickers are not tracked in the current framework. Although this does not impact detachment kinetics, it may influence the timescale and bias the direction of reattachment once heterogeneities in the distribution of nodes (i.e., through damage) develop. Tracking the diffusion-driven positions of free stickers in a manner that more directly reflects the work of Stukalin, et al. (2013) [80] would mitigate these concerns and also eliminate the need for restrictive simplifications such as the prohibition of double connections between neighboring nodes.

**Future work.** In future work, we aim to explore a number of additional considerations that restrict the application of continuum theory, including the effects of compressible deformation and its influence on phenomena such as void nucleation (or cavitation), and void coalescence [2], [105]. Cavitation, especially in regions of highly localized stress (e.g., ahead of crack tips) [106], has been observed as the cause of mechanical failure of soft materials loaded under not only hydrostatic, but also uniaxial tension [107]. Yet, much remains uncertain about when cavities form, how they grow (or coalesce), and how this leads to mechanical failure. More importantly, it remains unclear how the evolution of damage phenomena relates to the underlying chain properties of networks. Availability of experimental data for such considerations remains sparse [107]. However, in forthcoming work the discrete model introduced here will allow us to explore these features through controlled, *in silico* experimentation. Specifically, this model will permit direct observation of the damage zone near a crack tip, wherein both damage and viscoelastic deformation contribute to energy dissipation and failure onset. Such detailed exploration could elucidate the size of the damage zone and nature of the dissipative mechanisms, thereby revealing the intrinsic fracture toughness of the network.

## CHAPTER III

### MICROSCALE, COMPUTATIONAL INVESTIGATION OF DYNAMIC POLYMERS WITH MULTIPLE TIMESCALES INFORMS TNT

This chapter serves to exhibit one useful function of the discrete network model: its ability to inform physically motivated appendages to TNT. In this case, discrete networks containing multiple bond types with distinct kinetic dissociation rates attached in series are investigated, revealing that a standard rule of mixture is insufficient to describe the coupled stress response occurring in such networks. Microstructural investigation of the discrete network model predictions motivates the inclusion of a single parameter,  $\xi$ , that characterizes the extent to which more stable bond types in the network relax due to the faster bonds' dynamic reconfiguration. Finally, treating  $\xi$  as a fitting parameter, the updated TNT is used to reproduce the stress relaxation response of gels containing multiple reversible bond types [13] and to infer micromechanical phenomena within this material.

#### 3.1 Introduction

Networked polymeric materials containing multiple bond types have become increasingly investigated for their exemplary combinations of mechanical strength and toughness [47], [73], [108], [109]. For example, many state-of-the-art polymers contain both relatively stable covalent bonds and dynamic physical bonds (e.g., metallo-ligand interactions, ionic bonds, hydrogen bonding, etc.) in series [13], [21], [22], [46], [48], [110]. In such networks, the stable bonds (SBs) often form a scaffold that supports the dynamic bonds (DBs) interstitially throughout the material. Under these conditions, the SBs may preserve suitably high moduli, while incorporation of the sacrificial or reversible DBs introduces tunable viscoelasticity [13], [111]–[115] and even the ability to self-heal [55], [110], [116].

In designing such materials, researchers often employ physically motivated constitutive modeling techniques through which the properties of individual bonds (e.g., polymer force-extension, bond exchange rates, etc.) may be used to predict the globally emergent responses of the networks [1], [85], [117], [118]. However, real-time experimental characterization of the microstructure in such materials remains exceedingly challenging and is relatively limited to techniques such as small angle neutron scattering [119], or inference using diffusion and rheology data [120]. Therefore, gauging the degree of phenomenology in such models or interpreting their parameters is somewhat difficult, thus limiting the confidence in extrapolations made about microstructure via these approaches.

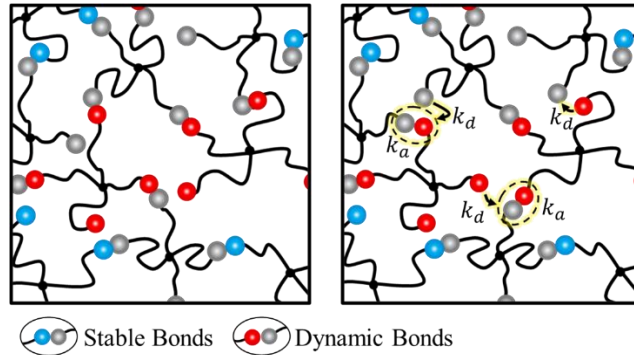


**Figure 3.1 Hybrid network schematic.** A schematic of a dynamic network including both stable (blue-to-grey) and dynamic (red-to-grey) bonds is displayed before (left) and after (right) a set of dissociation and attachment events.

To address this limitation, many researchers have resorted to network-scale modeling techniques for the exploration of polymeric microstructure [3], [73], [74], [121], [122]. We here employ one such recently developed model [3] to investigate the percolation threshold of SBs in 2D networks containing interstitial DBs (**Fig. 3.1**). Through this model, we examine the mechanical stress response of networks containing different fractions of stable and DBs, and then relate the clustering and geometric percolation of SBs to the emergence of a long-term elastic modulus. We find that under some topological conditions, a long-term modulus may emerge without SB percolation due to the jamming of clustered SBs. Inversely, under some conditions, a

portion of SBs that are fully percolated may relax non-affinely due to the reconfiguration of neighboring DBs. Equipped with this information we establish a coupled rule of mixture (ROM) for hybrid networks using transient network theory (TNT) [1]. This rule introduces just one additional parameter,  $\xi \in [0,1]$ , that defines the degree to which SBs can relax.

### 3.2 Discrete network model.

The network model used here was introduced by Wagner, et al. (2021) [3] and simulates discrete networks in 2D, periodic volume elements (VEs) to which deformations may be applied. For detailed modeling methods, see the Supporting Information (SI) Section I. The networks are comprised of  $\mathcal{N} = 400$ , four- ( $z = 4$ ) or eight-armed ( $z = 8$ ), star-shaped macromers whose central junctions represent permanent crosslinks or “nodes”. Either stable or dynamic telechelic bonds may form between neighboring nodes, the latter of which are assigned some constant dissociation kinetic rate,  $k_d$ . The association kinetic rate,  $k_a$ , is determined via a scaling law introduced in Wagner, et al. (2021) [3]. For simplicity, attached chains are treated as ideal entropic springs that impart pairwise tensile forces on the nodes to which they are attached. These tensile forces are balanced by repulsive forces deriving from volume exclusion interactions between neighboring nodes or polymer chains. Nodes’ positions are iteratively updated to equilibrate unbalanced forces originating from bond reactions or applied loading at every timestep. After equilibration, the network stress is computed through the virial formation according to:

$$\boldsymbol{\sigma} = \frac{1}{2V} \sum_{\alpha}^{\mathcal{N}} \sum_{\beta} \mathbf{r}^{\alpha\beta} \otimes \mathbf{f}^{\alpha\beta}, \quad (3.1)$$

where  $V$  is the VE volume,  $\mathbf{r}^{\alpha\beta}$  is the end-to-end vector between node  $\alpha$  and its attached neighbor  $\beta$ , and  $\mathbf{f}^{\alpha\beta}$  denotes the pairwise tensile and repulsive force between said nodes.

Parameters used in this study were preserved from Wagner, et al. (2021) [3] unless specified otherwise in Appendix B.6 However, here distinct fractions of stable and DBs ( $f$  and  $1 - f$ , respectively) were introduced randomly and uniformly throughout the networks. All networks were deformed under incompressible uniaxial tension via a constant velocity gradient,  $\mathbf{L} = \text{diag}(-\dot{\epsilon}, \dot{\epsilon})$  to a stretch of  $\lambda = 2$ , where  $\dot{\epsilon}$  is the applied strain rate. Strain rate was set such that even DBs behaved elastically during loading (i.e.,  $\dot{\epsilon}/k_d \gg 1$ ). Once  $\lambda = 2$ , networks were held in the deformed state to permit stress relaxation for four relaxation timescales (i.e.,  $t^* = tk_d = 4$  where  $t$  is time), which corresponds to relaxation within 2% of the steady state value predicted by exponential decay.

### 3.3 Review of TNT.

While this discrete model permits direct observation of microscale statistics in networks, its relatively high computational expense motivates the development of equally suitable continuum approaches, such as TNT. TNT predicts the Cauchy stress of a dynamic network comprised entirely of linear entropic springs as [1], [3]:

$$\boldsymbol{\sigma} = ck_b T \boldsymbol{\mu} + \pi \mathbf{I} \quad (3.2)$$

where  $c$  is the attached chain concentration,  $k_b$  is the Boltzmann constant,  $T$  is the ambient temperature,  $\pi \mathbf{I}$  is the isotropic pressure enforcing incompressibility, and  $\boldsymbol{\mu}$  is the conformation tensor that defines the instantaneous principal components and magnitudes of mean chain stretch. The conformation tensor evolves according to [1], [3]:

$$\dot{\boldsymbol{\mu}} = \mathbf{L}\boldsymbol{\mu} + \boldsymbol{\mu}\mathbf{L}^T - k_d(\boldsymbol{\mu} - \mathbf{I}). \quad (3.3)$$

Eqns. (3.2) and (3.3) return the Neo-Hookean model when  $k_d = 0$  (i.e., SBs):

$$\boldsymbol{\sigma} = ck_b T \mathbf{b} + \pi \mathbf{I}, \quad (3.4)$$

where  $\mathbf{b} = \mathbf{F}\mathbf{F}^T$  is the left Cauchy-Green tensor and  $\mathbf{F} = \partial \mathbf{x} / \partial \mathbf{X}$  is the deformation gradient that maps material points' reference spatial coordinates,  $\mathbf{X}$ , to current coordinates,  $\mathbf{x}$  (see Fig. B.1 for loading history).

### 3.4 Standard rule of mixture.

In modeling networks containing both stable and DBs, we postulate a general ROM whereby stable and DBs introduce elastic and dissipative components of stress ( $\sigma^e$  and  $\sigma^d$ ), respectively, and the total stress is given by:

$$\boldsymbol{\sigma} = k_b T (c^s \mathbf{b} + c^d \boldsymbol{\mu}) + \pi \mathbf{I}, \quad (3.5)$$

where  $c^s$  and  $c^d$  are the attached fraction of stable and DBs, respectively, and we have substituted Eqns. (3.2) and (3.4) for the two components of stress. We may further write that  $c^s = p^s f c$  and  $c^d = p^d (1 - f) c$  where  $c$  is the total chain concentration, and  $p^s$  and  $p^d$  are the respective probabilities that a given SB or DB are attached. Note that while  $p^s$  requires some *a priori* knowledge about the conversion ratio of activated SBs in a polymer,  $p^d$  may be estimated by the ratio  $k_a/(k_a + k_d)$  [1]. Substituting these definitions into Eqn. (3.5), solving for  $\pi$ , and dividing by the peak stress (see Appendix B.2.a-b for details) gives the normalized stress in the principal direction of loading as:

$$\sigma^* = P^{-1} [p^s f + p^d (1 - f) e^{-k_d t}], \quad (3.6)$$

where  $p^s f$  is the combined probability that a bond is both stable and attached,  $p^d (1 - f)$  is the probability that a bond is dynamic and attached, and  $P = p^s f + p^d (1 - f)$ .

Ensemble averaged ( $n = 10$ ) stress relaxation results from the discrete model, as well as those predicted by Eqn. (3.6) are presented in **Fig. 3.2.A** for a bond functionality of  $z = 4$ ,  $k_d = 1$  (in arbitrary units of inverse time), and multiple values of  $f^s$ . Notably,  $p^s$  and  $p^d \approx k_a/(k_a + k_d)$  were both found to be upwards of 0.9 for the parameters used. See Fig. B.2 for the measured values of  $k_a$  and  $k_d$ , as well as Fig. B.3 for  $P^s = p^s f$ ,  $P^d = p^d (1 - f)$ , and  $P$  in the extended parameter space. While Eqn. (3.6) provides good agreement with *in silico* predictions for purely dynamic networks when  $P^s = 0$  ( $f = 0$ ) or permanent networks when  $P^s \rightarrow 1$  ( $f = 1$ ), it significantly overpredicts the long-term stress at intermediate values of  $f$  (hybrid networks). To

elucidate the origins of this disagreement, we utilize the discrete model to examine the isolated SB and DB network topologies.

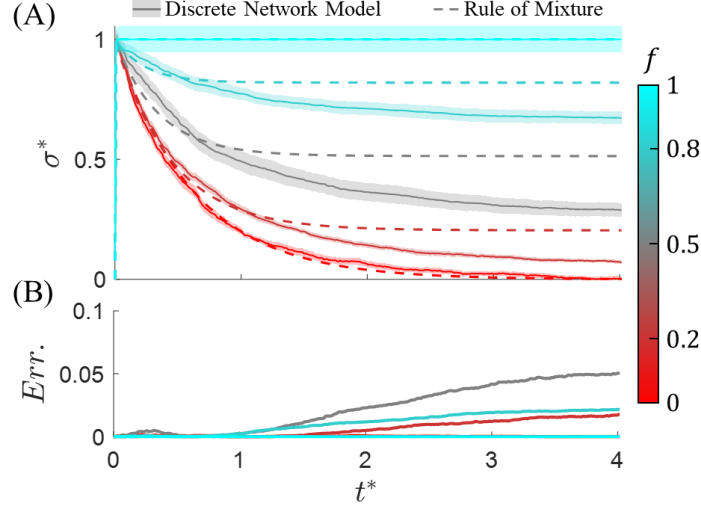


**Figure 3.2. Fitting the general ROM.** (A) Normalized stress,  $\sigma^*$ , is plotted with respect to normalized time,  $t^*$ , for the ensemble average of  $n = 10$  discrete network simulations (solid curves with shaded regions representing standard error, S.E.) and as predicted by Eqn. (9) (dotted curves) when  $k_d^* = 1$ . (B) Absolute errors between the models'  $\sigma^*$  are plotted with respect to  $t^*$ . (A-B) Results are shown for  $f = 0\%$  (red),  $f = 20\%$  (maroon),  $f = 50\%$  (grey),  $f = 80\%$  (teal), and  $f = 100\%$  (cyan).

We first investigate the independent probabilities that the dynamic and SBs form independently percolated networks [68] ( $X^s$  and  $X^d$ , respectively). **Fig. 3.3.A-C** display undeformed networks with  $f = 0.2, 0.5$  and  $0.8$  when  $z = 4$ , while **Fig. 3.3.D-F** display networks at the same stable bond fractions when  $z = 8$ . For all parameters investigated, the overall networks form percolated domains, however when  $f < 0.2$ , the SBs rarely, if ever, formed continuous networks (i.e.,  $X^s \sim 0$ ) (Fig. 3G-H). Instead, the SBs formed clustered regions suspended in a matrix of DBs (Fig. 3A,D). Likewise, at high  $f$  ( $f > 0.6$  for  $z = 4$  and  $f > 0.8$  for  $z = 8$ ), the SB networks was always continuous, but the DBs failed to percolate and instead formed clusters in a stable matrix. The probability that the DBs percolate also decreases as the fraction  $k_a/(k_a + k_d)$  decreases (Fig. S2-S4). Notably, regardless of network degree, there exists transition regions at intermediate values of  $f$  wherein both SBs and DBs can independently percolate (i.e.,  $X^s$  and  $X^d > 0$ ) and form an interpenetrating and

mutually bonded mesh, although this region is far more prominent for networks with higher functionality (where  $X^s \approx X^d \approx 1$  from  $f \sim 0.4 - 0.5$ ).

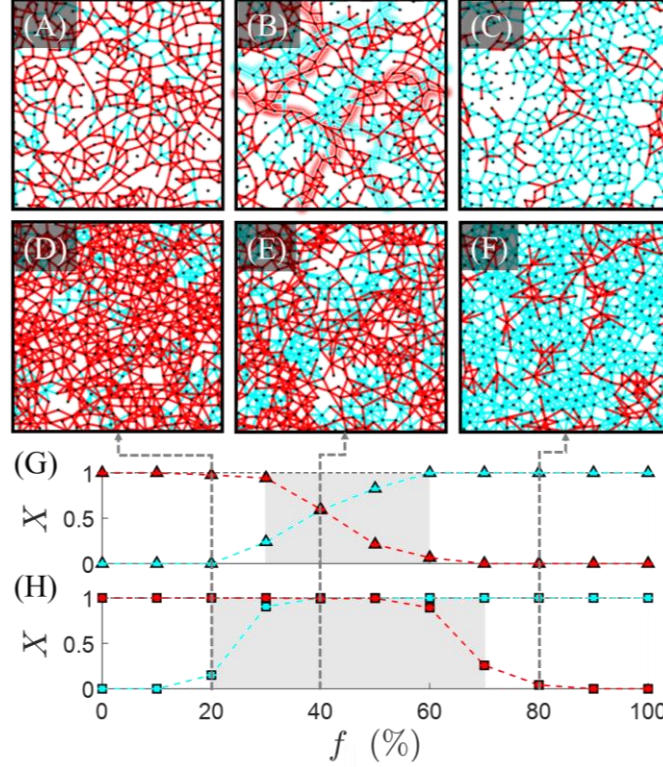


**Figure 3.3. Network percolation with respect to SB fraction and crosslink functionality.** (A-C) Sample discrete networks with  $z = 4$  when (A)  $f = 20\%$ , (B)  $f = 50\%$ , and (C)  $f = 80\%$ , illustrate the clustering of (A) SBs and (C) DBs (see circled regions). (B) Paths highlighted by red and blue shading illustrate how given certain inputs, both dynamic and SBs, respectively, can form percolated load paths. (D-F) Comparable schematics to (A-C) for  $z = 8$  reveal comparable clustering formations. (G) The probability that the stable (cyan) and dynamic (red) bonds independently form geometrically percolated networks ( $X^s$  and  $X^d$ ) are plotted with respect to  $f$  for (G)  $z = 4$  and (H)  $z = 8$ . (G-H) The regions shaded grey demark transition zones wherein simultaneous percolation of both bond types is possible ( $X > 0$ ).

One might expect that when the SBs percolate, they will store stress purely elastically, and that Eqn. (3.6) will provide good agreement with the predicted discrete network stress. Yet we see from Fig. 2A that when  $f = 0.8$  ( $X^s = 1$  for  $f \geq 0.8$ , **Fig. 3.3.G-H**) the long-term stress is overpredicted by the ROM, Eqn. (3.6) (e.g., Fig. 3A,  $f = 0.8$ ), suggesting that the SBs undergo some degree of relaxation. Since no relaxation is observed when  $f = 1$ , it must stem from DB reconfiguration. Furthermore, one might also expect that whenever the SBs do not percolate, the



clusters they form have sufficient conformational degrees of freedom to relax completely such that no long-term stress persists. Yet the discrete network predicts that non-negligible long-term stress exists when  $f = 0.2$  (**Fig. 3.3.A**), implicating that the SBs clusters are conformationally jammed by the surrounding DB matrix. Both phenomena indicate coupling between the stable and dynamic components of network stress, motivating amendment of the decoupled ROM.

### 3.4 Coupled rule of mixture.

To amend the ROM, Eqn. (3.6), we posit that some fraction,  $\xi$ , of SBs can relax at rate  $k_d$  due to reconfiguration of adjacent DBs, whereas the fraction  $1 - \xi$  cannot relax because they are bound within a network of SBs, jammed by steric interactions, or some combination of both. Incorporating  $\xi$  into Eqn. (3.5), gives a coupled ROM for hybrid networks:

$$\boldsymbol{\sigma} = ck_b T [P^s \xi \mathbf{b} + P^s (1 - \xi) \boldsymbol{\mu} + P^d \boldsymbol{\mu}] + \pi \mathbf{I} \quad (3.7)$$

where we use  $P^s = p^s f$  and  $P^d = p^d (1 - f)$  for brevity. Solving for  $\pi$ , and normalizing as before (see Appendix B.2.c) gives the normalized stress in the principal loading direction as:

$$\sigma^* = P^{-1} [(1 - \xi) P^s + \xi P^s e^{-k_d t} + P^d e^{-k_d t}]. \quad (3.8)$$

When  $\xi = 1$ , all the SBs relax completely, and the stress response is effectively dynamic whereas when  $\xi = 0$ , none of the SBs relax and Eqn. (3.8) returns the decoupled ROM. The stresses predicted by the discrete model and Eqn. (3.8) are in excellent agreement for all  $f$  when  $\xi$  is treated as a fitting parameter (**Fig. 3.4.A**). Significantly, the isolated stress contributions from the SBs (**Fig. 3.4.B**) and DBs (**Fig. 3.4.C**) also agree between models.

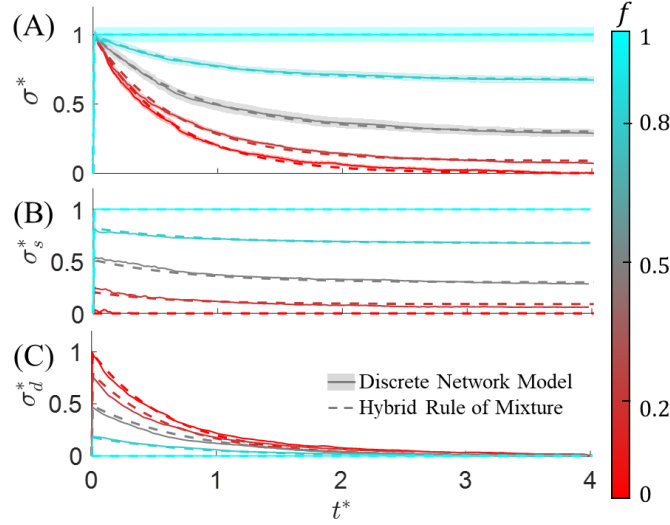


**Figure 3.4. Fitting the coupled ROM.** (A) Normalized stress,  $\sigma^*$ , is plotted with respect to normalized time,  $t^*$ , for the ensemble average of  $n = 10$  discrete simulations (solid curves with shaded S.E.) and as predicted by Eqn. (11) (dotted curves) when  $k_d = 1$ . Stress is decoupled into the contribution from (B) SBs,  $\sigma_s^*$ , and (C) DBs,  $\sigma_d^*$ . Error between models is consistently  $< 5\%$  at all values of  $t^*$  and  $f^s$ .

### 3.5 On the mechanisms of SB relaxation

**Fig. 3.4.C** confirms that the DB stress from both models decays exponentially to near-zero stress at a rate of  $k_d$ , indicating that only the SB stress response is significantly affected by coupling. This justifies the way in which the coupled stress (term two of Eqn. (3.8)) depends only on the SB concentration. Furthermore, it supports the presumption that faster relaxation timescales in networks with multiple bond types dominate relaxation response [115]. That SB stress predictions agree between models, confirms that  $\xi$  characterizes the degree to which SBs conform non-affinely into lower energy states at a rate of  $k_d$  (**Fig. 3.4.B**). However, it is not immediately clear whether  $\xi$  defines a fraction of the SBs that relax entirely, the degree to which all SBs relax, or some combination of both. To elucidate the meaning of  $\xi$ , we leverage topological information from the discrete network model.

**Fig. 3.5.A-B** illustrate the probability mass functions (PMFs) of SBs' and DBs' end-to-end stretches,  $\lambda = \mathbf{r}/(\sqrt{N}b)$ , in the principal direction of loading at the start and

end of stress relaxation ( $f = 0.5$ ). The insets display the 2D PMFs of chain stretch, as well as isolated network snapshots at the start and end of relaxation. As evidenced by the axisymmetric 2D PMF of **Fig. 3.5.B** ( $t^* = 4$ ), the DBs reconfigure to an isotropic state, whereas the elongated shape and negligible reduction in variance of the 2D and 1D PMFs, respectively, in **Fig. 3.5.A** confirm that SB relaxation is only partial. To quantify the modes of SB relaxation, as well as their distribution amongst the chain population, **Fig. 3.5.C** presents the distributions of single-chain relaxation strains,  $\epsilon^r$ , in the principal directions of the orthonormal basis  $\{\mathbf{e}_1, \mathbf{e}_2\}$ , as well as the change in end-to-end norms,  $\|\epsilon^r\|$ . Most SBs relax to lower energy states (see predominantly negative values of  $\|\epsilon^r\|$ ), however some chains elongate, indicating that thermal fluctuations stochastically move a minority of SBs to temporarily higher energy states. Nevertheless, most SBs shorten in the direction of principal stretch,  $\mathbf{e}_2$ , during loading (i.e., the PMF of  $\epsilon_{22}^r$  is skewed right). In contrast, SBs undergo roughly equiprobable shortening or lengthening in direction  $\mathbf{e}_1$  (i.e., the PMF of  $\epsilon_{11}^r$  nearly uniform). Positive  $\epsilon_{11}^r$  can occur due to chain lengthening but is confirmed to occur predominantly due to chain reorientation.

### 3.6 Interpreting the relaxation parameter, $\xi$

The finite variances of the PMFs in **Fig. 3.5.C** indicate that most SBs relaxed, but to a variable degree. Therefore, while  $\xi$  generally characterizes the extent of SB relaxation, it likely cannot be mapped to a single, physical value. Rather, it lumps the effects of SB shortening and reorientation into some effective value. However, over the range of  $k_d \in \{0.1, 1, 10\}$  and  $f \in [0, 1]$  for  $z = 4$ , we find that  $\xi$  reliably evolves according to:

$$\xi \sim 1 - \sqrt{\eta^2 + f^2(1 - \eta^2)}, \quad (3.9)$$

where  $\eta$  is the fraction of SBs that are immobilized even at very low SB fractions ( $f \rightarrow 0$ ) (**Fig. 3.5.D**). Note that Eqn. (3.9) returns linear scaling ( $\xi \sim f$ ) when no SBs become jammed (i.e.,  $\eta = 0$ ) and satisfies the condition that no SBs can relax for permanent networks (i.e.,  $\xi(f = 1) = 0$ ). Generally, **Fig. 3.5.H** depicts the fraction of jammed SBs

and reveals that as the fraction of SBs increases, the degree to which said bonds may relax decreases, implying that percolation of SBs is a contributor to SB immobilization. Indeed, networks with higher coordination exhibit lesser degrees of SB relaxation at low  $f$  (as indicated by higher values of  $\eta$  in **Fig. B.5**) supporting this notion. However, although networks in which chain length is doubled are well represented by Eqn. (3.8) (**Fig. B.6**) and exhibit improved percolation of SBs at low  $f$  (**Fig. B.7**), they do not exhibit a significant increase in  $\eta$  (**Fig. B.8**) suggesting a limited effect of SB percolation on immobilization. Another factor influencing connectivity is the reaction rates. **Fig. 3.5.D** reveals that networks with higher  $k_d$  generally appear to have fewer SBs immobilized in the limit  $f \rightarrow 0$  ( $\eta = 0.52$  for  $k_d = 0.1$  whereas  $\eta = 0.22$  for  $k_d = 10$ ). Since all networks were allowed to relax for the same normalized time ( $t/k_d = 4$ ), one might expect identical relaxation behavior regardless of  $k_d$ . However, the parameters governing  $k_d$  are preserved across simulations so that the emergent steady state fraction of attached DBs ( $p^d \approx k_a/(k_a + k_d)$ ), decreases as  $k_d$  increases. This indicates that  $\eta$  is correlated with  $p^d$  and suggests that networks in which  $k_a \gg k_d$  mitigate conformational change of SBs to a greater extent.

Another factor that undoubtedly influences SB relaxation is material density. As seen in studies of granular media, networks with exclusively repulsive interactions between members jam at high packing fractions or pressures [123], [124]. However, we have here tuned the network model's density and pairwise repulsive potential such that – without tensile chains – the crosslinks exists below the jamming transition [125]. This reveals that without sufficient network connectivity (e.g., for networks particularly short chains, **Fig. B.6**), the hybrid ROM cannot accurately predict SB relaxation, as relaxation becomes dominated by floppy modes of deformation at much shorter timescales. Nevertheless, the hybrid ROM is applicable to sufficiently percolated networks (here,  $z \gtrsim 3.8$ ) even without significant steric interactions, as in the case of swollen gels whose polymer packing is on the order of 0.01-0.1 [49].

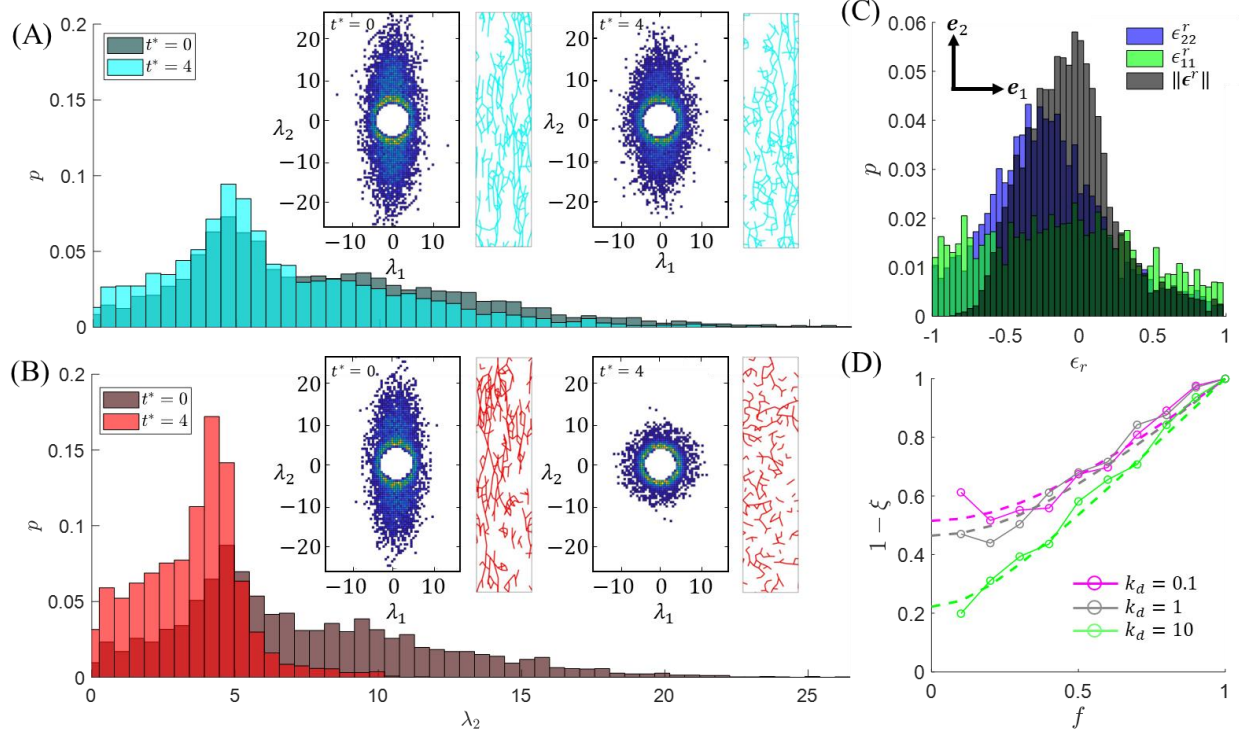


**Figure 3.5. Micromechanical chain relaxation.** (A-B) Topological relaxation data. The joint PMFs of SB end-to-end stretch,  $\lambda$ , at (A)  $t^* = 0$  and (B)  $t^* = 4$ . (C-D) The joint PMFs of DB  $\lambda$  at (C)  $t^* = 0$  and (D)  $t^* = 4$ . (E-F) The PMFs of (E) stable and (F) DB stretch in the principal direction of loading,  $\lambda_2$ , at  $t^* = 0$  (teal, maroon) and  $t^* = 4$  (cyan, red). Insets display the visually isolated stable and DB networks at both times. (G) The PMFs of  $\epsilon_{22}^r = (r_2 - r_2^0)/r_2^0$  (blue),  $\epsilon_{11}^r = (r_1 - r_1^0)/r_1^0$  (green), and  $\|\epsilon^r\| = (|\mathbf{r}| - |\mathbf{r}_0|)/|\mathbf{r}_0|$  (black) are presented where  $r^0$  and  $r$  are the end-to-end lengths of SBs at time  $t^* = 0$  and  $t^* = 4$ , respectively. (H) Fitted values of the immobilization factor,  $1 - \xi$ , are plotted with respect to  $f$  for three different values of  $k_d$ . Discrete circles represent the results of the network model, while dashed curves represent fitted functions per Eqn. (3.8) where  $\eta = 0.52$  for  $k_d = 0.1$  (magenta,  $R^2 = 0.94$ ),  $\eta = 0.46$  for  $k_d = 1$  (grey,  $R^2 = 0.96$ ), and  $\eta = 0.22$  for  $k_d = 10$  (magenta,  $R^2 = 0.99$ ).

### 3.7 Applying the coupled rule of mixture

To validate the hybrid ROM against experimental data, while demonstrating its applicability to materials with negligible steric jamming, we apply it to the stress relaxation data for a hydrazone covalently adaptable hydrogel, as reported by Richardson, et al. (2019) [13] (**Fig. 3.6.A**). Here, rather than there being SBs and DBs, there exists “slower” benzyl-hydrazone bonds (aHz) and “faster” alkyl-hydrazone (aHz) bonds with kinetic dissociation rates of  $k_s$  and  $k_d$ , respectively. Thus, we may rewrite Eqn. (3.8) (see Appendix B.4 for details) to estimate normalized shear stress as:

$$\tau^* = P^{-1}[\xi P^b e^{-k_s t} + P^b(1 - \xi)e^{-k_d t} + P^a e^{-k_d t}]. \quad (3.10)$$

where  $P^b = f p^b$  and  $P^a = (f - 1)p^a$ ;  $f$  is the fraction of bHz; and  $p^b$  and  $p^a$  are the attached fractions of bHz and aHz, respectively ( $p^b = p^a \sim 0.9$  assuming much faster attachment than detachment kinetics). Here we postulate that the hybrid stress (the second term from Eqn. (3.10)) relaxes at the faster of the two kinetic rates,  $k_d$ .

As indicated by Richardson, et al. (2019) [13], and as evidenced by non-exponential relaxation curves when  $f = 0$  and  $f = 1$  (red and cyan data in Fig. 6A, respectively), both bHz and aHz bonds exhibit shear-sensitive slip bond behavior. To capture this effect, dissociation kinetic constants are updated according to a modified Eyring's theorem [65], [72]:

$$k_i = k_i^0 \exp\left(\frac{\tau_i^*}{\tau_i^*}\right), \quad (3.11)$$

where  $i \in \{a, b\}$  denotes either aHz or bHz;  $k_a^0$  and  $k_b^0$  are the stress-free kinetic dissociation rates of aHz and bHz, respectively; and  $\tau_a^*$  and  $\tau_b^*$  are these bonds' respective sensitivities to bulk shear stress (where  $\tau_i^* \rightarrow \infty$  implies no sensitivity). Through Eqns. (3.10) and (3.11), stress relaxation responses were computed in discretized time using a forward Euler approach. First, the experimental stress response of the purely aHz ( $f = 0$ ) network was fitted, while treating  $k_a^0$  and  $\tau_a^*$  as fitting parameters, revealing that  $k_a^0 \sim 0.5 \text{ hrs}^{-1}$ , which is in reasonable agreement with the aHz relaxation rate estimated by Richardson, et al. (2019) of  $\sim 0.6 - 1.2 \text{ hrs}^{-1}$ , and  $\tau_a^* \sim 0.9$  (for  $f = 0$ ). Similarly, the experimental stress for the purely bHz ( $f = 1$ ) network was fitted to find that  $k_b^0 \sim 8 \times 10^{-7} \text{ hr}^{-1}$ , and  $\tau_b^* \sim 0.08$  (for  $f = 1$ ) indicating that bHz are relatively stable but are also highly sensitive to force. Using the fitted values of  $k_a^0$  and  $k_b^0$ , the stress responses of the hybrid networks were then fitted while treating  $\xi$ ,  $\tau_a^*$  and  $\tau_b^*$  as fitting parameters. Results are reported in **Fig. 3.6.A-C**.

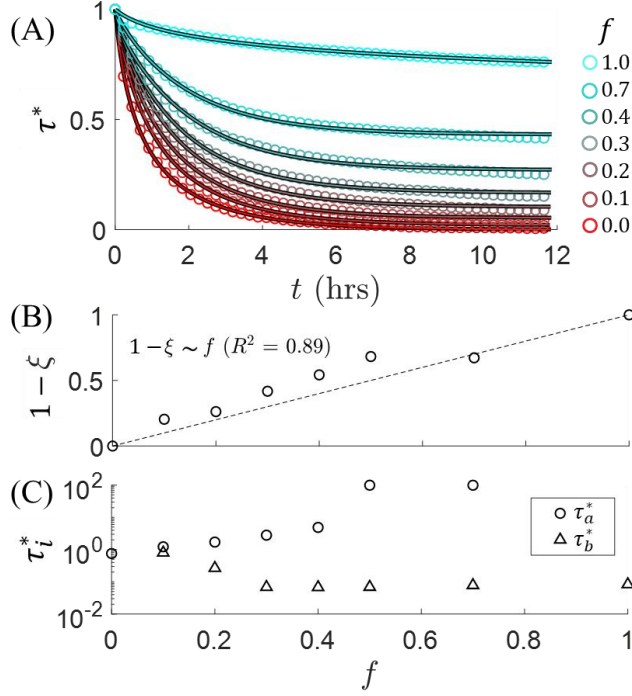


**Figure 3.6. Experimental validation.** (A) The force-sensitive coupled ROM (solid curve) is fit to the experimental stress relaxation data (circles) for hydrazone covalently adaptable network with  $f \in \{0, 10, 20, 30, 40, 70, 100\}\%$  bHz.  $f = 0$  is represented by red and  $f = 1$  is represented by cyan.  $R^2 > 0.99$  for all values of  $f$ . (B) The fitted jamming parameter,  $\xi$ , (black circles) is plotted with respect to  $f$ . The dotted curve represents the scaling relation  $\xi \sim f$ . (C) The fitted sensitivity parameters for aHz,  $\tau_a^*$ , and bHz,  $\tau_b^*$ , are plotted with respect to  $f$ .

Eqn. (3.10) is consistently able to predict the stress response of the gels (**Fig. 3.6.A**,  $R^2 > 0.99$  for all values of  $f$ ). Furthermore, **Fig. 3.6.B** reveals that there is a direct correlation between  $\xi$  and  $f$  (i.e., that  $\eta \sim 0$  from Eqn. (3.9)), indicating that very few of the SBs remain jammed in the limit of  $f \rightarrow 0$ . This supports the notion that, without significant steric interactions between crosslinks (as in the case of a swollen gel), unpercolated SBs undergo negligible immobilization. Besides revealing information about jamming, the inclusion of force sensitivities in Eqn. (3.11) allows for inference about load sharing in the networks. The shear threshold of bHz decreases as  $f$  increases, and plateaus at  $\tau_b^* \sim 0.1$ , predicting that higher fractions of bHz beget greater sensitivity of said bonds to the overall network stress (**Fig. 3.6.C**). One possible explanation for this is that with greater fractions of bHz, the relative fraction of stress carried by these bonds becomes higher and so their effective stress sensitivity is increased. Likewise, the shear threshold of aHz increases monotonically

with respect to bHz fraction (note that  $\tau_a^*$  was capped at 100 for plotting purposes), suggesting that in networks with predominantly bHz, the detachment kinetics of aHz become less stress-sensitive for the same reason. While isolated investigation of in-network chain kinetics and verification of stress-sensitivity is difficult to accomplish experimentally, we may simulate hydrazone covalently adaptable networks containing aHz and bHz using the discrete network model in future work.

### 3.8 Conclusion

Here we have utilized the discrete network model to explore coupled stress response of hybrid networks containing SBs and DBs (or multiple DB types). In doing so, we discovered that at low SB concentrations (below percolation) a long-term modulus subsists due to conformational immobilization of said bonds. Additionally, we discovered that even when the fraction of SBs is above the percolation threshold, SBs may undergo stress relaxation due to non-affine, conformational changes induced by DB reconfiguration. Together, these effects motivated the introduction of a novel fitting parameter,  $\xi$ , that characterizes the extent of SB relaxation and correlates with the attached SB fraction. Incorporating this parameter into TNT, we then developed a coupled rule of mixing for hybrid dynamic networks.

While  $\xi$  characterizes some mean approximation of the extent to which SBs relax, treating it as a fitting parameter does not elucidate any detailed distribution of bond relaxation. Furthermore, although we found that  $\xi$  reliably scales with  $f$  according to Eqn. (3.9) for both the network model and the gels of Richardson, et al. (2019), it likely depends on several factors not explored directly in the scope of this work. For example, as expected from studies of granular matter, SBs in denser networks with higher degrees of steric interactions (e.g., the network model) appear to be more susceptible to jamming than those in dilute networks (e.g., the gels of Richardson, et al. (2019)). Additionally, while not explored here, highly entangled networks likely experience a greater degree of SB jamming than their less entangled counterparts.



Finally, the degree of jamming is likely strain, strain rate, and damage-dependent [126]. While these features were not examined through this iteration of the numerical framework their incorporation is compatible with the coupled ROM through TNT, and they may be explored in future work.

Nevertheless, this model has here proved applicable to not only discretely modeled networks containing stable and DBs in series, but also physical gel networks comprised of two bond types with distinct relaxation timescales. Furthermore, this approach is demonstrably compatible with features such as stress-dependent bond dynamics and has here been used to infer microstructural traits that are difficult to characterize experimentally (i.e., degree of jamming shear stress sensitivity). Ultimately, the simplicity and robustness of this approach may render it useful in the predictive design of a diverse set of hybrid networks including elastomers or gels with charge interactions [114], [127], [128], vitrimers [13], and metallopolymers [22], [110].

## CHAPTER IV

### A MESOSCALE MODEL FOR THE MICROMECHANICAL STUDY OF GELS

This chapter is tasked with exemplifying the applicability of the discrete network model to physical materials. Here, stable poly(ethylene glycol) (PEG) based gels are chosen as a first model material due to their relatively ideal network structure with minimum chain entanglement, low polydispersity, and the reduced significance of steric interactions between adjacent crosslinks in these materials (since their polymer packing fraction is less than the order of 10%). Nonetheless, in the absence of existing pairwise potentials between crosslinks in gels with various solvent qualities (i.e., effective repulsion or depletion forces between polymer segments), we here first introduce a novel scaling law that defines the local polymer concentration as a function of the current gel topology. We then utilize this concentration to define local osmotic pressure gradients through Flory-Huggin’s [129] theory from which effective mixing forces are computed and used to update discretely modeled crosslink positions. Implementing this model such that all input parameters mirror experimentalists’ controls, we then demonstrate its ability to reproduce mixing or phase separation, the topological defect trends in PEG gels, the swelling mechanics of Flory-Rehner [130] theory, and the experimentally measured mechanical response of a 10kDa tetra-PEG gel. Finally, we utilize the model to predict and explain trends in the failure response of gels over a wide parameters space.

#### 4.1 Introduction

Gels generally consists of a skeletal network of high molecular weight polymer chains interpenetrated by low molecular weight solvent. This two-state composition imparts

gels with complex mechanical response that depends on the topological evolution of the skeleton, transport properties of the solvent, and the interactions between them. The entropic stiffness of the polymer network and time-dependent transport of fluid impart gels with elastic and poroelastic responses, respectively, while non-affine network deformation, entanglements, and the intrinsic viscosity of the solvent introduce various sources of viscous dissipation. Furthermore, inclusion of sacrificial bonds [73], [74], [90], [91]; bonds that break and reform without damage [112], [131]; or irreversible chain rupture [121] induce topological evolution in gels that may improve toughness [48], [132], and introduce stress relaxation or self-healing [133]. These mechanical traits render gels especially suitable candidates in applications such as tissue engineering wherein they are often used as cell scaffolds [13]. In such applications, gels' moduli and stress relaxation rates influence stem cell differentiation and in-growth of new tissue [15], [16], [134]. Thus, this exemplifies a case in which understanding the mechanical properties of a gel as a function of its fabrication parameters would greatly aid researchers. Indeed, modeling techniques that accurately predict the microstructural evolution and globally emergent mechanical properties of gels are highly sought after. However, the hierarchical structure of gels renders it difficult to formulate computationally tenable, non-phenomenological models that track topological changes in gels across length scales.

Gels are inherently multiscale materials, whose pertinent constituents (i.e., solvent particles and mers) are on the atomistic scale, yet whose characteristic chain and pore sizes are on the scale of nanometers [119] (**Fig. 4.1**). Furthermore, defects on the order of  $10^1$  to  $10^3$  nm may exist in the network, which grow due to local stress concentrations. Understanding the emergence, evolution, and propagation of these defects, as well as their cause, is imperative to understanding the failure and strength

of gels [135], [136]. These pore sizes and defects suffuse gels with intrinsic property gradients and heterogeneity at the network scale. The size of these features limits the resolution with which continuum approaches may be applied since such models typically invoke smoothing assumptions and require homogenous materials.

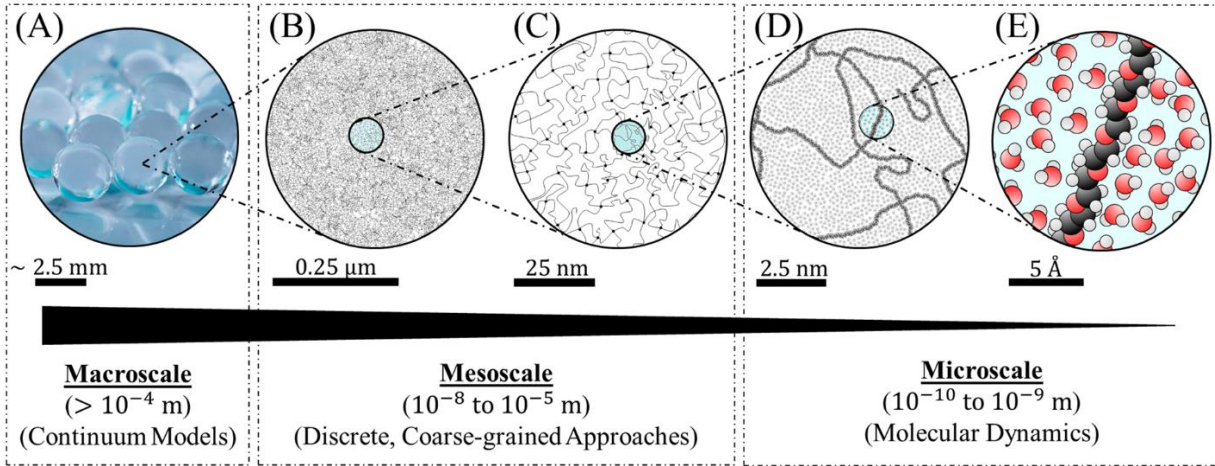


**Figure 4.1. Hierarchical length scales of gels.** A gel at (A) the macroscale ( $> \sim 10^{-4} \text{ m}$ ) is depicted with schematic illustrations of its topological structure at (B-E) diminishing length scales. (A) At the macroscale, smoothing assumptions permit application of continuum approaches, but these methods prohibit detailed study of damage or the influence of defects. (B-C) The discrete methods introduced here represent gel structures at intermediate length scales or the “mesoscale” by coarse-graining polymer chains as nonlinear mechanical springs. In modeling individual polymer chains, mesoscale approaches are equipped to capture the mechanical effects of topological defects and damaged regions, with reduced computational expense. (D-E) The most detailed models track constituents (either atoms, molecules, or Kuhn segments) utilizing discrete MD approaches. However, capturing defects on the order of  $10^1 \text{ nm}$  to  $10^{-1} \mu\text{m}$ , or conducting large ensembles of repeated *in silico* experiments becomes computationally untenable using these fine-grained approaches. The gel topology shown is meant to loosely represent a tetra-PEG hydrogel whose mesh size is on the order of  $10^{-8} \text{ m}$  and which has 4 functional arms per macromer.

However, the length scale of these features also ensures that within a representative element on the order of cubic micrometers,  $10^9 - 10^{12}$  constituents would need to be modeled in fine-grained approaches, thus also limiting the efficacy of methods such as molecular dynamics (MD) [137]. As such, many MD studies focus on the interaction of just one or a few macromers [138]–[140]. Even employing coarse-graining practices to MD, such as those of [141] (e.g., the use of Kuhn segments for bead-spring chains

and smoothing of the solvent), such approaches require large computational time and resources. Therefore, a tertiary class of explicit, mesoscopic models are needed to bridge the microstructural-to-global mechanical property response of gels. Such approaches may capture the length scale of heterogeneities and local topological traits while leveraging statistical representations of features such as individual entropic chains or mixing effects.

Towards this aim, researchers such as [121] have used mesoscale models to study the mechanics of gels. Indeed, these researchers and much of the existing literature have focused on perhaps the most idealized polymeric networks observed in gels to date – those of tetra-polyethylene glycol (PEG) based gels. In fact, such gels are under strong consideration in bioengineering applications for their biocompatibility and the ease with which their mechanical properties may be tuned. These networks are formed through the gelation of star-shaped macromers with functional arms that bind to one another telechelically (i.e., at their terminal ends), and achieve high conversion rates [137], with relatively few defects [142] and high homogeneity [119], [143]. The relative homogeneity of these networks has allowed researchers such as [121] to initiate modelled gels as ideal diamond lattices from which bonds are stochastically and retroactively removed, while still accurately predicting their mechanical response. However, this phenomenological gelation approach is empirically motivated, and the correct topologies are set according to experimental results rather than emerging because of the underlying physics. As such, these idealized approaches are ill-suited to capture the local microstructures of gels with transient bonds, dangling chains, or post-chain-rupture landscapes. In reality, the local positions of dangling chains and the distribution of crosslinks in a gel are heavily dependent on local solute-solvent interactions and resulting osmotic pressure gradients [130],

[139], [144], [145]. Furthermore, existing mesoscopic approaches are limited in predicting the initial topologies of gels as a function of macromer functionality (governing the number of potential crosslinking interactions), as-prepared solution concentration [137], [142], molecular weight, or solvent quality. Yet these are the types of parameters which experimentalists may control during gel fabrication.

To address these limitations, we here adapt a recently developed mesoscale numerical framework [3], to the case of PEG-based gels. The current work is novel two significant ways. Firstly, it considers the effects of osmotic pressure on global swelling of traction boundaries. While previous works enforced volumetric deformation through the empirically motivated displacement of network boundaries [121], [146], we here compute the degree of swelling based on the competition between global osmotic pressure (as predicted via Flory-Huggins theory) and the hydrostatic component of polymer network stress. Secondly, we introduce a scaling law to estimate the local polymer concentration as a function of the average mesh size, and spatial crosslink distribution. Previous works have employed more general methods of homogenization such as "explosion-contraction" Monte Carlo (MC) algorithms with Lennard-Jones potentials between nodes [146]. However, the distribution of polymer in a gel depends significantly on solute-solvent interactions [138]–[140], [145], [147]. Therefore, we introduce a physically motivated method in which the spatial arrangement of macromers is governed by solute-concentration dependent gradients in osmotic pressure that introduce effective mixing forces. Thus, this model considers first-order physics that enable the *ab initio* simulation of gel networks, thereby requiring less a priori knowledge of gel microstructure over previous approaches and instead enabling predictive design of gels with certain topologies. To support *ab initio* predictive design, input parameters to this model correspond directly to typical

control parameters during gel fabrication – namely, macromer molecular weight ( $M_w$ ), solvent type (whose effects are coarsely captured through the Flory-Huggins mixing parameter,  $\chi$ ), normalized pre-gelation polymer concentration ( $\phi^*$ ), and macromer functionality ( $f$ ) [119], [137], [142], [143], [148].

The remainder of this work is structured as follows. In Section 4.2, we briefly overview the continuum mechanics approach commonly used to model global swelling mechanics of gels. This introduces readers to the significant concepts of osmotic pressure (governed by the free energy of mixing between polymer and solvent) and network stress (governed by strain energy of the polymer network). We then examine these features’ counterparts at the network scale. In Section 4.3, we introduce the novel scaling law that relates local osmotic pressure gradients to microstructural crosslink distribution, and the single-chain force extension relation that drives global network stress. We also describe the numerical implementation of not only these features, but also the macro-scale theory discussed in Section 4.2. In Section 4.4, we demonstrate that this model accurately predicts topological and mechanical characteristics of sol-gels (i.e., polymer suspensions turned to gels) during mixing, gelation, equilibrium swelling, and elastic deformations under plane stress boundary conditions. Finally, Section 4.5 concludes by exploring the effects of network topology on damage onset in permanent gels.

## 4.2 Flory-Rehner theory for global equilibrium of gels

Polymeric gels are comprised of networks of high molecular weight chains crosslinked to one another. When these networks are submersed into a low molecular weight solvent there is an entropic increase associated with the interstitial penetration of

liquid into the polymeric network. Additionally, in cases where there is energetic favorability between solvent-polymer interactions (as opposed to interpolymer or solvent-solvent interactions), there is also an enthalpic contribution to mixing. Together, these contributions lead to some effective osmotic pressure that induces transport of solvent into the network, inducing swelling. In this work, we consider the effects of osmotic pressure on not only the global mechanics (i.e., equilibrium swelling and traction boundary positions), but also local topology (i.e., the spatial distribution of crosslinks). In this section, we briefly outline the Flory-Rehner continuum mechanics theory used to predict the global swelling mechanics of gels [130].

The Flory-Rehner approach treats gels as a two-state solution in which the polymer network represents solute, while the interstitial fluid that causes swelling represents solvent (**Fig. 4.2**). Through this approach the Helmholtz free energy of the mixture is taken as the sum of the elastic strain energy ( $\psi_{el}$ ) stored in the polymeric chains, and the free energy of mixing ( $\psi_{mix}$ ) between solute and solvent as:

$$\psi = \psi_{el}(\mathbf{F}) + \psi_{mix}(\phi). \quad (4.1)$$

Here,  $\mathbf{F} = \partial \mathbf{x} / \partial \mathbf{X}$  is the elastic deformation gradient (where  $\mathbf{X}$  and  $\mathbf{x}$  represent the reference and current crosslink positions of the network, respectively, as depicted in **Fig. 4.2**), and  $\phi = V_p / V$  is the volume fraction of polymer (where  $V_p$  is the total volume of the polymer in the network and  $V$  is the total volume enveloped by the gel).

At mechanical equilibrium in the absence of body forces, the Cauchy stress state ( $\boldsymbol{\sigma}$ ) of the gel must obey the differential equation:

$$\nabla \cdot \boldsymbol{\sigma} = 0 \quad (4.2)$$



where  $\nabla$  is the differential operator in the current configuration, and  $\boldsymbol{\sigma} = \boldsymbol{\sigma}_{el} + \boldsymbol{\sigma}_{mix}$  may be decomposed into its elastic network ( $\boldsymbol{\sigma}_{el}$ ) and mixing ( $\boldsymbol{\sigma}_{mix}$ ) components. It can be shown that the forms of these stresses arise from the minimization of the free energy and may therefore be directly derived from Eqn. (4.1). The Cauchy stress is thus expressed as:

$$\boldsymbol{\sigma}_{el} = 2J^{-1}\mathbf{B} \cdot \frac{\partial \psi_{el}}{\partial \mathbf{B}}, \quad (4.3)$$

where  $\mathbf{B} = \mathbf{F}\mathbf{F}^T$  is the left Cauchy-Green or finger deformation tensor, and  $J = \det(\mathbf{F})$  denotes the relative change of volume of the gel (i.e.,  $J = V/V_0$  given a reference volume of  $V_0$ ). The mixing stress emerges as an isotropic pressure (i.e., osmotic pressure) of the form:

$$\boldsymbol{\sigma}_{mix} = \pi \mathbf{I}. \quad (4.4)$$

To compute  $\pi$  we consider that the solute consists of long chains of  $N$  bonded mers or Kuhn segments. The mixing entropy of a Kuhn segment may be written as  $N^{-1}\phi \ln \phi$  and  $\psi_{mix}$  is given by [149]:

$$\psi_{mix} = \frac{k_b T}{v} \left[ \frac{\phi}{N} \ln \phi + (1 - \phi) \ln(1 - \phi) + \chi \phi(1 - \phi) \right]. \quad (4.5)$$

where  $k_b$  is the Boltzmann constant,  $T$  is the ambient temperature,  $v$  is the volume of a Kuhn segment, and  $\chi$  is the Flory-Huggins solubility parameter ( $\chi = 0.5$  for theta solvent in which polymers behave ideally as freely jointed chains, and  $\chi \leq 0.5$  indicates that mixing will occur). Through Eqn. (4.5), we may compute the amount of mixing work needed to expand or contract the gel by some incremental amount  $dV$  as:

$$\pi dV = -d(V\psi_{mix}), \quad (4.6)$$

where osmotic pressure,  $\pi$ , constitutes the pressure needed to maintain a given volume. Differentiating the right-hand side of Eqn. (4.6) with respect to  $V$  gives  $\pi$  as:

$$\pi = \frac{k_b T}{v} \left[ \frac{\phi}{N} - \ln(1 - \phi) - \phi - \chi \phi^2 \right]. \quad (4.7)$$

For detailed derivations of Eqns. (4.5) to (4.7), readers are encouraged to read *Soft Matter Physics* by Masao Doi [149]. From Eqn. (4.7), we see that osmotic pressure is zero when  $\phi = 0$ , and pressure increases monotonically with respect to  $\phi$  for good solvent in which mixing is favored ( $\chi \leq 0.5$ ). This drives solvent from regions of lower- to-higher solute concentration.

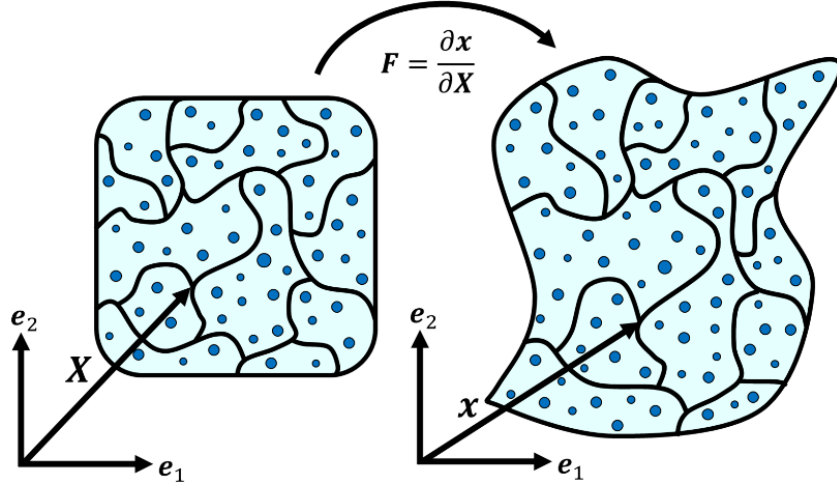


**Figure 4.2. Deformation of a gel.** An arbitrary gel network is illustrated in its reference (left) and current (right) configurations after undergoing some compressible deformation  $\mathbf{F}$ . Polymer chains are depicted as black curves, while solvent is represented by the blue background and blue circles. The position of an arbitrary crosslink is illustrated in its reference ( $\mathbf{X}$ ) and current ( $\mathbf{x}$ ) positions with respect to the orthonormal basis.

Eqn. (4.7) will prove useful in tracking the local osmotic pressure of the network model as described in Section 3.1. However, to consider the effects of osmotic pressure on global swelling, let us instead express Eqn. (4.7) in terms of the volumetric change,  $J$ , of the overall gel as measured with respect to its dry state. Assuming the amount of polymer in the gel is conserved and that all volumetric change is driven by flux of solvent, then  $J = \phi_0/\phi$  where  $\phi_0$  is the polymer volume fraction of the dry network. Substituting this into Eqn. (4.7) gives:

$$\pi = \frac{k_b T}{v} \left[ \frac{1}{JN} - \ln \left( 1 - \frac{1}{J} \right) - \frac{1}{J} - \frac{\chi}{J^2} \right]. \quad (4.8)$$

Note that the first term in Eqn. (4.8) drops out with the assumption that  $N \rightarrow \infty$ , as appropriate for the case of gels containing large polymer networks. Eqns. (4.2), (4.3), and (4.8) collectively define the global equilibrium condition of a gel. While Flory-Rehner theory provides the governing equilibrium equations for a gel at the macro-scale, it neglects any local evolutions of spatial crosslink distribution. In the following sections we demonstrate how the concepts of local osmotic pressure gradients and single-chain elastic strain energy may be leveraged to update topology in the discrete network model.

### 4.3 The network model

The numerical framework adopted here was introduced by [3]. The chronological stages modeled by this framework are meant to mimic the *ab initio* processes of gel fabrication and mechanical experimentation as illustrated in **Fig. 4.3**. First, representative volume elements (RVEs) are initiated as square domains with periodic boundary conditions, centered at the Cartesian origin. The sizes of RVEs were set based on the convergence of stress response for increasingly large domains (see Appendix C.I). Star-shaped macromers or “nodes” are then seeded at coordinates  $\mathbf{x}^\alpha$  using a Poisson’s point process where the index  $\alpha$  denotes the node number ( $\alpha \in [1, \mathcal{N}]$ ) (**Fig. 4.3.A**). Once initially seeded, the positions of nodes are equilibrated as governed by osmotic mixing forces (**Fig. 4.3.B**). Nodes may remain unattached to model polymer suspensions, or their chains may be telechelically bonded to one another to mimic gelation (**Fig. 4.3.C**). The RVEs are then prescribed some combination of traction and displacement boundaries to mimic experimental conditions such as equilibrium swelling (**Fig. 4.3.D**) and applied deformations (**Fig. 4.3.E**). In this section, we detail the effective mixing forces that act on macromers in

star-shaped polymer suspensions or crosslinks in gel networks. We then review the chain attachment algorithm used to mimic gelation and describe the entropic chain forces that act on nodes in the crosslinked networks. Next, we describe how nodes' positions are iteratively equilibrated and network stress is computed at each discrete deformation or network reconfiguration step. Finally, we overview the various boundary conditions used over the course of this work and list the input parameters associated with the network model.

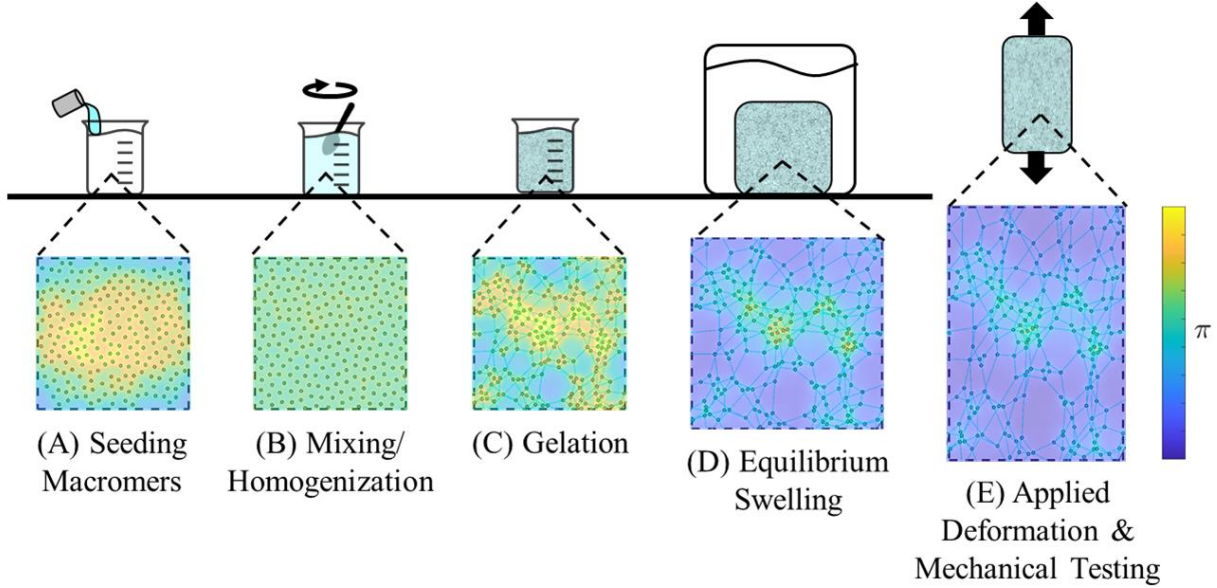


**Figure 4.3. Chronological steps of numerical model.** (A) An RVE is seeded with macromers (or “nodes”) whose centers are depicted as circles. (B) The macromers are positionally equilibrated by effective osmotic mixing forces. (C) The macromers are bonded to form a gelated network. (D) The network expands, decreasing the osmotic pressure, until the condition of Eqn. (2) is met. (E) Deformation is applied to the boundaries of the RVE. The heat map represents normalized, local osmotic pressure. Dangling chains are not explicitly modeled and are therefore not shown in figures throughout this work.

#### 4.3.1 Local effects of osmotic pressure

We begin by examining the local effective mixing forces, as these are relevant for both the initial polymer suspensions and post-gelation networks. In this subsection we introduce the novel scaling law used to estimate spatial solute concentration

gradients, which in turn govern effective pressure-gradient mixing forces. We then detail the numerical methods used to compute said forces.

**Local scaling of solute concentration and effective mixing forces.** In many polymeric materials such as dry elastomers [150], [151] volume exclusion (i.e., repulsive contact potentials) will dominate the effective macromer or crosslink distributions. However, in this work and in the broader context of gels, polymer packing fractions are generally on the order of 0.01 to 0.1, such that the separation distances between macromers or crosslinks are significantly larger than the size of a mer ( $\sim b$ ) or length scale of volume exclusion interactions. As such, network topology of gels or radial distribution of polymer in suspensions [139], [152] is instead governed by the effective mixing forces ( $f^\pi$ ) introduced by gradients in osmotic pressure [153]. Osmotic pressure, as described by Eqn. (4.7), depends on both the local solute concentration (through  $\phi$ ) and favorability of solute-solvent interactions (characterized by  $\chi$ ). At the mesoscale,  $\phi$  evolves locally as a function of the positions,  $x^\alpha$ , of macromers or crosslinks (i.e., “nodes”). While scaling laws such as that introduced by [145] or [154], [155] have been developed to predict the concentration gradient surrounding star-shaped polymers in solvent of varying quality, discrete numerical investigation of these relationships has called their ability to predict local swelling into question [156]. A great deal of research has been conducted through Monte Carlo and molecular dynamics simulations on the effective interactions between star shaped polymers, as well [138]–[140], [147], [152], [156], [156]. These include the study of both dilute and concentrated systems. Nevertheless, few (if any) such studies have been conducted in the context of percolated gels comprised of star-shaped polymers, despite the fact that tetra-PEG macromers in solution have verifiably different concentration gradients than those in a percolated network [119],

[143]. Indeed most of the literature on the structure of such gels is empirically-gotten [142], [143], [148], [157], [158], and appropriate scaling laws for solute concentration gradients are, to our knowledge, not available in existing works. Therefore, for our purposes we begin by introducing a simple scaling law for solute concentration specific to the case of star-shaped crosslinkers in the low functionality regime (here,  $f \in [3,10]$ ).

Consider an arbitrary, 2D network such as that depicted in **Fig. 4.4.A**, which has an average nearest crosslink-to-crosslink separation or “mesh size”  $\bar{\xi}$ , and in which each crosslink has a functionality of  $f$ ; each arm has  $N$  Kuhn segments; and each Kuhn segment has a length of  $b$  and width of  $w$ . Let us first examine the solute concentration function due to a single node at position,  $\mathbf{x}^\alpha$ , as we move radially outwards from its center to some position  $\mathbf{r}$ . Here we temporarily treat  $\mathbf{x}^\alpha$  as our reference position and we denote the solute concentration function due to this isolated node as  $\varphi^\alpha(\mathbf{r})$ . To estimate  $\varphi^\alpha(\mathbf{r})$ , we envision an infinitesimal ring of width  $\delta r$ , at distance  $r = |\mathbf{r}|$  from  $\mathbf{x}^\alpha$ , as illustrated in **Fig. 4.4.B-C**. In 2D, the local polymer packing fraction within this ring is defined as the area of polymer residing within it ( $\delta A$ ) divided by the total ring area ( $2\pi r \delta r$ ):

$$\varphi^\alpha(\mathbf{r}) = \frac{\delta A}{2\pi |\mathbf{r}| \delta r}. \quad (4.9)$$

The area of polymer inside the ring may be written as:

$$\delta A = (fbw)\delta N, \quad (4.10)$$

where  $bw$  represents the area of a single mer and  $\delta N$  represents the number of mers inside the ring belonging to a single chain (so that  $f\delta N$  represents the contribution from all chains). For simplicity, we posit that a polymer chain remains evenly coiled and distributed in the space between the crosslinks it spans (**Fig. 4.4.B**). We also coarsely impose that it is equiprobable to find polymer at any azimuthal position

around the crosslink (i.e., radial symmetry). Under these conditions,  $\delta N$  scales proportionately with the number of Kuhn segments per chain ( $N$ ), and the ring thickness ( $\delta r$ ), and is inversely related to the average mesh size ( $\bar{\xi}$ ):

$$\delta N \sim N \bar{\xi}^{-1} \delta r. \quad (4.11)$$

This notion assumes that at low functionality, steric interactions between adjacent chains are minimal so that the chains may coil freely. Combining Eqns. (4.9), (4.10) and (4.11) gives the estimated solute area at distance  $r$  in 2D as:

$$\delta A \sim f N b w \bar{\xi}^{-1} \delta r. \quad (4.12)$$

Substituting Eqn. (4.12) into (4.9) provides that the local solute fraction scales with  $|\mathbf{r}|$  according to:

$$\varphi^\alpha(\mathbf{r}) \sim \begin{cases} 1, & |\mathbf{r}| < \frac{f N b w}{2\pi} \bar{\xi}^{-1} \\ \frac{f N b w}{2\pi |\mathbf{r}|} \bar{\xi}^{-1}, & \frac{f N b w}{2\pi} \bar{\xi}^{-1} < |\mathbf{r}| \end{cases} \quad (4.13)$$

with the added condition that  $\varphi^\alpha(\mathbf{r})$  cannot exceed unity. To compute  $\bar{\xi}$ , we consider that many of the chains are fully attached to the network so that their end-to-end separation is governed by the average mesh size of the system. Meanwhile, the average length of dangling chains depends instead on their tethered diffusion in the solvent. Taking  $c$  and  $1 - c$  as the relative fractions of attached and dangling chains, respectively, then we may estimate the mean mesh size as the sum of weighted contributions from each population:

$$\bar{\xi} \approx c \bar{\xi}_a + (1 - c) \bar{\xi}_d, \quad (4.14)$$

where  $\bar{\xi}_a$  and  $\bar{\xi}_d$  are the average measured end-to-end distance of an attached and dangling chain, respectively (**Fig. 4.4.B**). While the average end-to-end length of attached chains,  $\bar{\xi}_a$ , may be measured explicitly, we impose that dangling chains behave ideally (since we are primarily concerned with gels in good solvent) and therefore have a mean end-to-end length of  $\bar{\xi}_d = \sqrt{N}b$ .

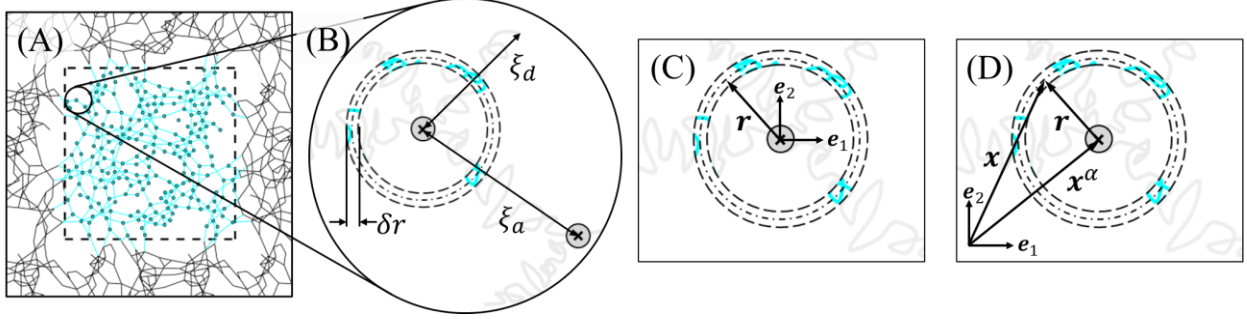


**Figure 4.4. Solute concentration scaling in a gel.** (A) An RVE containing an arbitrary network is displayed. (B) A close-up schematic of an arbitrary crosslink from (A) is shown. A differential ring of width  $\delta r$  is enclosed by dashed lines. A dangling chain is depicted and posited to have an approximate end-to-end length of  $\xi_d \approx \sqrt{N}b$ . An attached chain is also depicted and posited to have an approximate end-to-end length,  $\xi_a$ , that is the same as the network's average attached chain length. (C) A differential ring at radial distance  $|r|$  with respect to the local reference frame (i.e., crosslink position) is displayed. (D) The same differential ring from (C) is displayed, with the material point  $\mathbf{x} = \mathbf{x}^\alpha + \mathbf{r}$  denoted in the global reference frame. (B-D) The segments of polymer chain residing within the differential ring are shaded cyan.

Eqn. (4.13) provides  $\varphi^\alpha(\mathbf{r})$  as a function of radial distance with respect to the reference position  $\mathbf{x}^\alpha$  (**Fig. 4.4.C**). However, with respect to the global reference frame, we instead write:

$$\varphi^\alpha(\mathbf{x}) \sim \begin{cases} 1, & |\mathbf{x} - \mathbf{x}^\alpha| < \frac{fNb\omega}{2\pi} \bar{\xi}^{-1} \\ \frac{fNb\omega}{2\pi|\mathbf{x} - \mathbf{x}^\alpha|} \bar{\xi}^{-1}, & \frac{fNb\omega}{2\pi} \bar{\xi}^{-1} < |\mathbf{x} - \mathbf{x}^\alpha| \end{cases} \quad (4.15)$$

where  $\mathbf{x} = \mathbf{x}^\alpha + \mathbf{r}$  (**Fig. 4.4.D**). In a system of  $\mathcal{N}$  macromers, the overall solute concentration function may then be taken as the sum of  $\varphi^\alpha(\mathbf{x})$  for  $\alpha \in [1, \mathcal{N}]$  as:

$$\phi(\mathbf{x}) = \Phi^{-1} \sum_{\alpha=1}^{\mathcal{N}} \varphi^\alpha(\mathbf{x}). \quad (4.16)$$

where  $\Phi = \int_V \phi(\mathbf{x}) dV / (VJ\phi_0)$  is a normalization scalar that enforces conservation of mass (i.e., that the average value of  $\phi(\mathbf{x})$  equals the globally computed solute fraction,  $J\phi_0$ ).

Given  $\phi(\mathbf{x})$  the spatial osmotic pressure function,  $\pi(\mathbf{x})$ , may be computed directly using Eqn. (4.7). To compute the effective force,  $\mathbf{f}^\pi(\mathbf{x})$ , imposed by local gradients in  $\pi(\mathbf{x})$ , we invoke that the amount of work,  $\mathbf{f} \cdot d\mathbf{x}$ , needed to move a solute particle by a displacement of  $d\mathbf{x}$  must be equal and opposite to the consequential change in the



local free energy of mixing,  $-Vd\pi$  [149], [159]. Thus, we may write the pressure gradient force relation as:

$$\mathbf{f}^\pi \cdot d\mathbf{x} = -Vd\pi, \quad (4.17)$$

where  $V$  is the approximate volume of solvent displaced by the movement of a macromer ( $V \approx fNb w^2$ ). Solving Eqn. (4.16) for  $\mathbf{f}^\pi$  gives the local driving force of solute due to mixing as:

$$\mathbf{f}^\pi(\mathbf{x}) = -\frac{N}{2}fbw^2\nabla\pi(\mathbf{x}). \quad (4.18)$$

where  $\nabla\pi$  denotes  $d\pi/d\mathbf{x}$ , or the spatial pressure gradient in the current configuration. Although the scaling relation of Eqn. (4.15) is presented for 2D networks, an analogous relation may be derived to apply this method to 3D networks. Eqns. (4.16) and (4.18) remain applicable, regardless of dimensionality (i.e., whether spatial vectors are one, two, or three dimensional).

**Numerical implementation of mixing force.** As discussed in the previous section, osmotic mixing forces depend on local gradients in osmotic pressure, which in turn depend on the local solute concentration,  $\phi(\mathbf{x})$ . To approximate a differentiable landscape of osmotic pressure within the numerical framework,  $\phi(\mathbf{x})$  is computed on a discretized, Eulerian grid, whose node positions are defined by the vector set  $\mathbf{x}^q$ . This Eulerian grid and the numerical methods described in this subsection are illustrated schematically through **Fig. 4.5** for a simple 1D, two-node system. The solute packing fraction at each  $q^{th}$  query point on the Eulerian grid as a function of its distance from each  $\alpha^{th}$  node in the domain,  $\phi(\mathbf{x}^{q\alpha})$ , is calculated using Eqn. (4.15) (**Fig. 4.5.A-B**). Note that here,  $\mathbf{x}^{q\alpha} = |\mathbf{x}^q - \mathbf{x}^\alpha|$  is the distance between node  $\alpha$  and query point  $q$  and is synonymous with  $|\mathbf{x} - \mathbf{x}^\alpha|$  in continuous space from Eqn. (4.15). The solute concentration functions due to each crosslink,  $\phi(\mathbf{x}^{q\alpha})$ , are then summed over all nodes per Eqn. (4.16) to get the overall solute concentration function on the

Eulerian grid,  $\phi(\mathbf{x}^q) = \Phi^{-1} \sum_{\alpha=1}^{\mathcal{N}} \varphi(\mathbf{x}^{\alpha q})$ . To compute  $\Phi$  in the numerical framework, the overall solute concentration is taken as  $\phi_0 J = A_p / A_{RVE}$ , where  $A_p = \mathcal{N} f N b w$  is the total solute area in the RVE and  $A_{RVE}$  is the total RVE area. The solute concentration function,  $\phi(\mathbf{x}^q)$ , is then used to compute the osmotic pressure function  $\pi(\mathbf{x}^q)$  on the Eulerian grid through Eqn. (4.7) (**Fig. 4.5.C**). Given  $\pi(\mathbf{x}^q)$ , the spatial gradient in pressure is linearly interpolated at position  $\mathbf{x}^q$  using a central difference approximation:

$$\nabla \pi(\mathbf{x}^q) \approx \frac{\pi(\mathbf{x}^{q+1}) - \pi(\mathbf{x}^{q-1})}{2\Delta x}, \quad (4.19)$$

where  $\Delta x \sim \bar{\xi} \times 10^{-1}$  is the grid spacing, which is set less than an order of magnitude smaller than the network's mesh size to approximate smooth crosslink motion. Finally,  $\nabla \pi(\mathbf{x}^q)$  is substituted into Eqn. (4.18) to compute the effective mixing force function,  $\mathbf{f}^\pi(\mathbf{x}^q)$ , which is then linearly interpolated at the positions of the crosslinks in the network (**Fig. 4.5.E**).

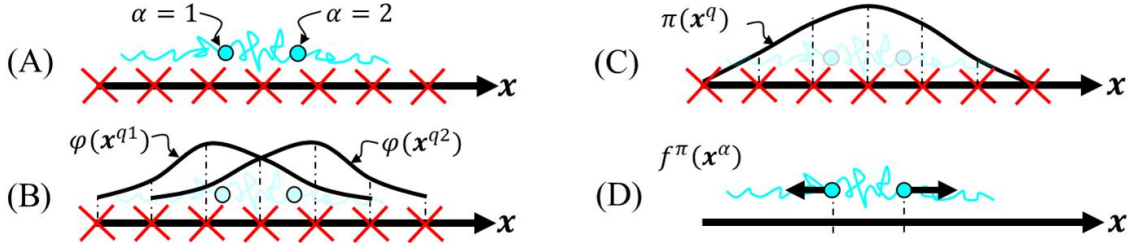


**Figure 4.5. Numerical implementation of effective mixing forces in 1D.** (A) A two-node ( $\alpha \in [1,2]$ ) system is displayed in 1D along spatial dimension  $x$ . The nodes are depicted as blue circles with blue chains connecting them, and the underlying Eulerian grid is depicted as red exes. (B) The local solute concentration function due each node,  $\varphi(\mathbf{x}^{\alpha q})$ , is estimated using Eqn. (4.15) and illustrated at the positions of the Eulerian query points,  $\mathbf{x}^q$ . (C) The combined local solute concentration function,  $\phi(\mathbf{x}^q) = \sum_{\alpha=1}^2 \varphi(\mathbf{x}^{\alpha q})$  is computed and then used to calculate  $\pi(\mathbf{x}^q)$  through Eqn. (4.7), which is displayed at the positions  $\mathbf{x}^q$ . (D) The effective mixing forces,  $\mathbf{f}^\pi(\mathbf{x}^q)$ , are computed through Eqns. (4.17) and (4.18) and then interpolated at the positions of the nodes to get  $\mathbf{f}^\pi(\mathbf{x}^\alpha)$ , which is illustrated as black vectors at positions  $\mathbf{x}^\alpha$ . The sizes of the arrows indicate the relative magnitudes of effective forces. (B-C) The functions  $\varphi(\mathbf{x}^{\alpha q})$  and  $\pi(\mathbf{x}^q)$  are smoothly interpolated between query points for illustrative purposes, although actual interpolation takes place between (C) and (D).

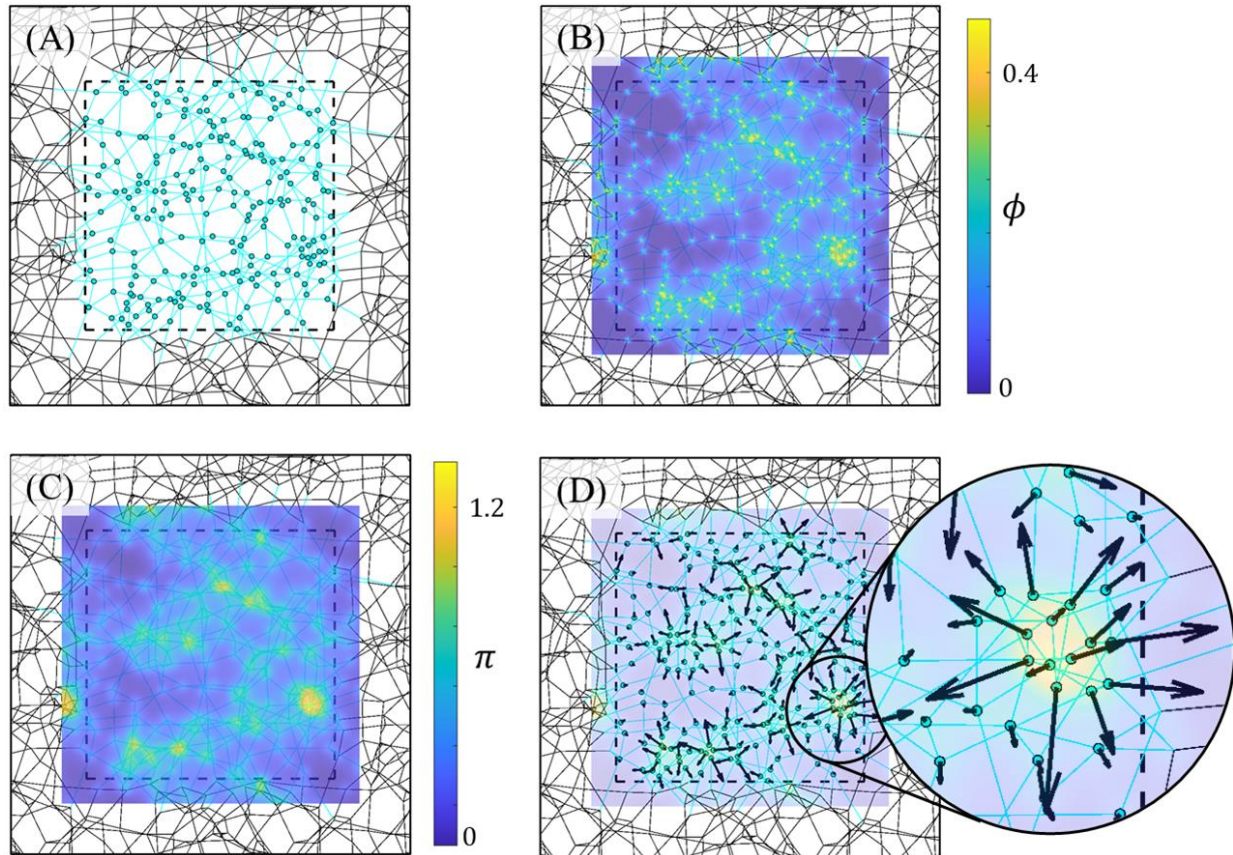


**Figure 4.6. Outcomes of numerical implementation in 2D.** (A) An equilibrated numerical gel network is displayed. (B) The estimated polymer packing fraction function ( $\phi(\mathbf{x}^q)$ ) is displayed at the query points ( $\mathbf{x}^q$ ) of the Eulerian grid. (C) The corresponding local osmotic pressure function ( $\pi(\mathbf{x}^q)$ ) is displayed. (D) The pressure gradient force ( $\mathbf{f}^\pi(\mathbf{x}^\alpha)$ ) is computed and interpolated at the positions of crosslinks (black arrows). The heat map of  $\pi(\mathbf{x}^q)$  from (C) remains faintly displayed in (D) to visually illustrate how forces follow the local osmotic pressure gradient. A close-up of osmotic pressure forces around a cluster of nodes is also depicted for clarity. (B-D) The heat maps of  $\phi(\mathbf{x}^q)$  and  $\pi(\mathbf{x}^q)$  are interpolated between query positions for illustrative purposes.

**Fig. 4.6** illustrates the outcome of this numerical implementation via snapshots of the network model. **Figs. 4.6.A** and **4.6.C-D** are 2D analogues to the 1D schematics of **Figs. 4.5.A** and **4.5.C-D**, respectively. Again, while the framework adapted here is 2D, this method could also be incorporated into 3D frameworks. **Fig. 4.6.D** displays a close-up view of the effective mixing forces at the crosslink positions,  $\mathbf{f}^\pi(\mathbf{x}^\alpha)$ , around a higher density cluster, thus demonstrating how this method drives crosslinks away from regions of higher solute concentration for good solvent (here  $\chi = 0.5$ ), thus fulfilling the role of an effective pairwise repulsion between neighboring crosslinks.

Significantly,  $\mathbf{f}^\pi(\mathbf{x})$  induces homogenization of simulated macromers in good solvent ( $\chi \leq 0.5$ ) prior to gelation. In homogenizing the solution before nodes are attached to one another, mixing forces mitigate any boundary effects introduced by the way in which nodes are seeded into the periodic RVE. In effect, through  $\mathbf{f}^\pi(\mathbf{x}^\alpha)$ , the model mimics the mixed conditions of solutions prior to crosslinker polymerization.

#### 4.3.2 Gelation and entropic chain forces

Once macromers are seeded and initial homogenization due to effective mixing forces is completed, the system may be gelated without biased formation of defects near the RVE's boundaries. This is achieved using the Rouse diffusion-based chain attachment introduced by [3]. Within a given timestep, the probability of attachment between two chains belonging to neighboring nodes is defined according to the Poisson's process:

$$dP_a = k_a e^{-k_a t} dt, \quad (4.20)$$

where  $k_a$  is the rate of attachment. Given that the chains are tethered to their permanent crosslinks, we define  $k_a$  according to a scaling law based on Rouse diffusion to define  $k_a$  as [3]:

$$k_a = \frac{1}{\tau_0} \left( \frac{b}{d} \right)^4. \quad (4.21)$$

where  $d$  is the distance between neighboring nodes and  $\tau_0$  is the time it takes a chain's tip to diffuse the length of one of a Kuhn segment,  $b$ . For simplicity, nodes are not allowed to attach to themselves. However, nodes may attach to each other more than once to capture the double, triple and quadruple-link defects observed by [137] and [157] and discussed in Section 4.4.2. Attachment events are checked iteratively until the network achieves greater than 95% connectivity.

Note that the introduction of bonded chains mandates computation of single-chain forces derived from the entropic penalty of polymer extension. The strain energy function of entropic chains is suitably modeled using the Padé approximation [160] of Langevin chains given by [3]:

$$\psi_c = k_b T \left[ \frac{\lambda^2}{2} - N \log(N - \lambda^2) \right], \quad (4.22)$$

where  $\lambda$  is the chain stretch given by  $\lambda = r/\sqrt{N}b$  and  $r$  is the chain's end-to-end length.

This yields a force-stretch relation of the form:

$$f = \frac{3k_b T}{\sqrt{N}b} \lambda \left( \frac{\lambda^2 - 3N}{\lambda^2 - N} \right). \quad (4.23)$$

As in the case of polymers [161] the force in this model diverges for chains extended near their full contour lengths (or  $\lambda \rightarrow \sqrt{N}$ ), thus also capturing the enthalpic effects of bond stretching [162].<sup>2</sup> Chain forces always act in tension and remain aligned with their chains' end-to-end vectors,  $\mathbf{r}$ .

### 4.3.3 Force equilibration and stress formulation

Since macromers or crosslinks are seeded stochastically, they do not begin at equilibrium. Additionally, processes such as bond attachments, equilibrium swelling, applied deformation, and bond rupture also drive the crosslinks out of equilibrium. However, equilibrium is assumed throughout this work based on the assumptions that solvent may move freely into or out of the networks as needed to maintain thermodynamic equilibrium, and any loading rates are applied significantly slower than the rate of solvent transport. Therefore, nodes are iteratively equilibrated to their lowest energy state at every network reconfiguration or deformation step (i.e.,

---

<sup>2</sup> Where indicated, Gaussian (i.e., ideal or linear) chains are used in lieu of Langevin chains. The force-extension of a Gaussian chain is given by  $f = 3k_b T \lambda / (\sqrt{N}b)$  and does not diverge in the limit  $\lambda \rightarrow \sqrt{N}$ .

“timestep”). This is done using the overdamped method detailed in [3], which updates the positions of the nodes from iteration  $k$  to  $k + 1$  according to:

$$\mathbf{x}_{k+1}^\alpha = \mathbf{x}_k^\alpha + \nu^{-1} \mathbf{f}_k^\alpha. \quad (4.24)$$

Here,  $\nu$  is a numerical overdamping coefficient and  $\mathbf{f}^\alpha$  is the net force acting on node  $\alpha$  given by:

$$\mathbf{f}^\alpha = \sum_\beta \mathbf{f}^{\alpha\beta} + \mathbf{f}^\pi. \quad (4.25)$$

where  $\sum_\beta \mathbf{f}^{\alpha\beta}$  is the sum of node  $\alpha$ 's pairwise interaction forces with its neighboring nodes,  $\beta$ , and  $\mathbf{f}^\pi$  is the osmotic pressure-dependent force of mixing detailed in Section 4.3.1. Since osmotic pressure-dependent forces,  $\mathbf{f}^\pi$ , depend on the local solute concentration and osmotic pressure, these scalar fields are also iteratively updated throughout equilibration. Pairwise interaction forces,  $\mathbf{f}^{\alpha\beta}$ , consists of the tensile forces carried by attached polymer chains described in Section 4.3.2. For simplicity, monomer interactions between crossing chains (e.g., volume exclusion, entanglement, etc.) are here omitted and do not affect the forces of Eqn. (4.25). Again, this is because effective osmotic pressure forces (as opposed to short-range monomer interactions) are taken as the first-order phenomenon affecting polymer distribution in gels [145]. This treatment is justified by the relatively ideal network structure and minimized entanglement in low polydispersity (i.e., low molecular weight variance) PEG-based gels [121], [143]; the dilution of swollen gels in good solvent (which reduces the frequency of short-range monomer interactions); and the finding that the effects of intra-chain monomer volume exclusion diminish for longer polymer chains [163].

Eqns. (4.24) and (4.25) are iterated until the mean and maximum unbalanced forces on the nodes move below 0.05 pN and 0.1 pN, respectively. These residual thresholds constitute roughly 0.2 and 0.4% of the force carried by a linear chain stretched to its full contour length, and thus sufficiently approximate the minimum energy state for

the purposes of this work. Once equilibration is completed after each timestep, the entropic chain forces,  $\mathbf{f}^{\alpha\beta}$ , may be used to compute the instantaneous network stress through the virial formulation according to:

$$\boldsymbol{\sigma}_p = \frac{1}{2V} \sum_{\alpha}^{\mathcal{N}} \sum_{\beta} \mathbf{r}^{\alpha\beta} \otimes \mathbf{f}^{\alpha\beta}, \quad (4.26)$$

where  $V$  is the RVE volume<sup>3</sup>, and  $\mathbf{r}^{\alpha\beta} = \mathbf{x}^{\alpha} - \mathbf{x}^{\beta}$  is the end-to-end vector between node  $\alpha$  and its bonded neighbor  $\beta$  [3]. Note that  $\boldsymbol{\sigma}_p$  through Eqn. (4.26) gives only the polymer network stress, which is counteracted by osmotic pressure  $\pi$  such that the overall material stress  $\boldsymbol{\sigma}$  in the equilibrated swollen state is given by  $\boldsymbol{\sigma}_p + \pi \mathbf{I} = 0$  when  $\mathbf{F} = \mathbf{I}$ .

#### 4.3.4 Equilibrium swelling and applied deformations

Once the networks are fully gelated, deformation is typically applied in two stages. First the gel network is permitted to swell isotropically and unconstrainedly from its initial arbitrary size to its equilibrated state (**Fig. 4.7.A**). At this stage all four of the RVE's periodic edges are traction boundaries. In the second stage we apply mixed boundary conditions to the RVE to enforce a prescribed uniaxial tensile deformation of the gel (**Fig. 4.7.B**). In both stages, stepping of the traction-free boundaries is conducted to satisfy the Flory-Rehner, global equilibrium condition from Eqn. (4.2). While only the central RVE is depicted in images throughout this work, all RVEs are 2D periodic. Both displacement and traction boundaries are updated by stepping the position of the RVE edges, however the former are stepped to enforce some prescribed strain, while the latter are stepped to achieve some prescribed stress on the boundary.

---

<sup>3</sup> Since the RVE is 2D, its volume is taken as  $V = \ell_1 \ell_2 \zeta$  where  $\zeta$  represents the thickness of the domain. Thickness is treated as a fitting parameter when comparing  $\boldsymbol{\sigma}$  between 3D experimental results and the 2D model predictions.

During initial swelling, the dimensions of the RVE boundaries are updated iteratively according to:

$$\ell_1^{k+1} = \ell_1^k + \nu^{-1}[\ell_2^k(\pi - \sigma^h)], \quad (4.27)$$

$$\ell_2^{k+1} = \ell_2^k + \nu^{-1}[\ell_1^k(\pi - \sigma^h)], \quad (4.28)$$

where  $\ell_1^k$  and  $\ell_2^k$  represent the length of the horizontal and vertical traction boundaries at iteration  $k$ , respectively, and  $\nu$  is again some numerical overdamping coefficient. Eqns. (4.27) and (4.28) ensure that if the osmotic pressure exceeds the hydrostatic network stress ( $\pi > \sigma^h$ ), then the domain increases in size and swelling continues. These equations are iterated until the residual difference between  $\pi$  and  $\sigma^h$  is below  $0.004 \text{ kPa}$ , which constitutes less than 1% of the overall hydrostatic network stress typically observed and provides ample convergence in the swollen equilibrium state.

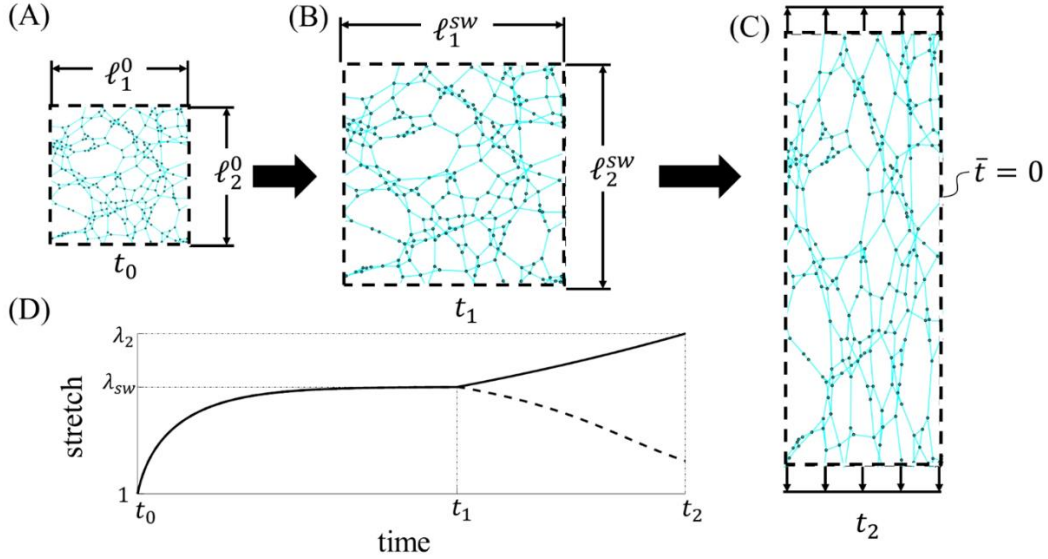


**Figure 4.7. Applied boundary conditions.** (A-B) Stage I: A sample numerical gel network, which begins at (A) time  $t_0$  with the dry, square dimensions  $\ell_1^0 = \ell_2^0$ , is depicted undergoing initial, unconstrained equilibrium swelling. (B-C) Stage II: From the (B) swollen state at time  $t_1$ , the network is then (C) stretched in the vertical direction at a constant strain rate of  $L_{22}$ . During this applied deformation, the RVE width is governed by the balance between  $\sigma_{11}$  and  $\pi$ . (D) A sample loading history ( $\lambda$  with respect to time) is depicted with  $t_0$ ,  $t_1$  and  $t_2$  corresponding to the times of (A), (B), and (C), respectively. Dotted lines denote periodic boundaries.



Both Eqns. (4.27) and (4.28) are carried out during stage one of deformation (i.e., isotropic swelling). However, during the second stage of deformation, displacement of the vertical boundary is governed by the condition that:

$$\ell_2(t) = \ell_2^{sw} \exp(L_{22}t), \quad (4.29)$$

where  $\ell_2^{sw}$  is the height of the RVE after isotropic equilibrium swelling is completed,  $L_{22}$  is the constant applied strain rate and  $t$  denotes time. During this stage, the Flory-Rehner condition (i.e., a traction-free condition) is maintained for the horizontal boundaries through the traction-free equilibrium condition that  $\sigma_{11} + \pi = 0$ . Therefore, the horizontal boundary is iteratively stepped via a displacement condition that is analogous to Eqn. (4.28), given by:

$$\ell_1^{k+1} = \ell_1^k + v^{-1}[\ell_2^k(\pi - \sigma_{11})]. \quad (4.30)$$

Again, the physicality of this boundary condition is contingent on the unhindered influx of solvent into the gel, as needed, and is therefore based on the assumption that the loading rate,  $L_{22}$ , is significantly smaller than the rate of solvent diffusion. After every step of boundary deformation during either stage, the network's crosslink positions are iteratively equilibrated using Eqns. (4.24) and (4.25).

#### 4.3.5 Free parameters

Despite gels' complexity, this model requires the input of just four free parameters, as listed in **Table 4.1**. These parameters are the functionality ( $f$ ), macromer molecular weight ( $M_w$ ), solute-solvent interaction parameter ( $\chi$ ), and as-prepared solute concentration ( $c^*$ ). Solute concentration is taken as the solute volume fraction ( $\phi$ ) normalized by the overlap volume fraction ( $\phi_{ol}$ ) at which the star-shaped macromers' radii of gyration inter-penetrate one another. Note that the number of nodes is held constant across simulations such that  $\phi^*$  is mediated by the initial size

of the RVE during gelation. Both  $M_w$  and  $f$  are coupled with the chain length ( $L$ ) of a single arm. Therefore,  $f$  and  $M_w$  are often paired, as indicated throughout the text, to fix  $L$  as  $f$  is swept.

**Table 4.1.** Primary model parameters

Parameter	Value, Range	Units
Functionality, $f$	[3,10]	NA
Molecular Weight, $M_w$	[10,200]	kDa
Mixing Parameter, $\chi$	0.5	NA
As-prepared Solute Fraction, $c^*$	$\sim 2$	NA

For details on domain length scale and concentration calibration, see Appendix C.II. There are no relevant timescales included in this work since deformations are presumed to occur at a rate much slower than the diffusion rate of solvent and no rate-dependent bond detachments are included. However these timescales can and will be included in future works through the swelling kinetics theory of [164], force-dependent bond detachment rates [65], [72], and/or diffusion-dependent re-attachment rates [3], [165]. Nonetheless, without any pertinent timescale, the deformation rate,  $L_{22}$ , is arbitrary and the more important consideration is how many steps in which the deformation is carried out. To achieve adequate sampling frequency, and properly isolate the effects of discrete bond rupture events, the deformation was applied in approximately 550 steps per simulation.

#### 4.4 Gel topology and elastic response

The networks examined in this work are modeled after PEG-based gels for which there exists an abundance of experimental data, and which display exceptional

spatial homogenization and high yield ( $> 90\%$  chain connectivity) [158]. Macromer functionality is specified throughout this section, but is most commonly set to  $f = 4$  due to the large number of experimental studies on tetra-PEG<sup>4</sup> gels [142], [143], [158], [166], [167]. Unless specified otherwise, gels undergoing deformations are treated as if suspended in a solvent bath at thermodynamic equilibrium with the ambient environment. Additionally, all applied deformation rates are considered slower than the rate of solvent diffusion through the network such that rate-dependent solvent transport effects may be ignored. Together, these assumptions allow us to invoke that solvent moves into and out of the gel as needed to maintain equilibrium.

#### 4.4.1 Homogenization and phase separation of polymer suspensions

Here we demonstrate the model’s ability to predict homogenization or phase separation of polymer suspensions without the explicit inclusion of any repulsive or attractive pairwise potentials between nodes. A novelty of this approach is that it does not take homogenization of macromer’s for granted before or after gelation, as in the case of other comparable approaches. Instead, the distribution of macromers is governed by the physics of solute-solvent interactions characterized by  $\chi$ . **Fig. 4.8.A-B** displays suspensions in which the centers of tetra-functional macromers are depicted. Two suspensions (for  $\chi = 0.5$  and  $\chi = 2$ , respectively) are displayed as initiated (**Fig. 4.8.A-B**, left) and after they have achieved the prescribed equilibrium criteria (**Fig. 4.8.A-B**, right). To demonstrate that the local osmotic pressure, and not the initial macromer distribution is what causes phase separation, all networks are

---

<sup>4</sup> Gels constituting a specific molecular weight and functionality are referenced using the convention “ $\langle M_w \rangle$  k <Greek numerical prefix>-PEG”. For example, a gel comprised of 4-arm macromers with  $M_w = 10$  kDa is referred to as a 10k tetra-PEG gel throughout the text.

initiated with relatively high homogeneity using a pairwise Poisson’s point process. Again, neither attractive nor repulsive pairwise potentials are included.

To characterize macromer distribution, we investigate the radial distribution function (RDF),  $g(r)$ , which quantifies the probability of finding two macromers at a given end-to-end distance. Peaks in  $g(r)$  indicate correlation length scales (i.e., that there is a higher probability of finding two particles at a given pairwise separation distance). In contrast, values of  $g(r)$  near or below unity indicates that particles are less correlated with one another and more correlated with empty space at a given length scale. When  $\chi = 0.5$  (**Fig. 4.8.A**) mixing and homogenization occur whereby the macromers evenly distribute and  $g(r)$  appears periodic (**Fig. 4.8.C**), indicating a degree of long-range order like that observed in concentrated colloidal and star-polymer suspensions [168], [169]. Despite only accounting for solute-solvent interactions (as opposed to volume exclusion effects), such homogenization is consistent with the statistical mechanics predictions of [170], the MC studies of [171], or the higher fidelity MD results of [45] and [172] for suspensions in good solvent. However, when  $\chi = 2.0$  this method predicts unstable phase separation that cannot be modeled using only volume exclusion interactions (**Fig. 4.8.B**). Indeed, setting  $\chi > 0.5$  effectively introduces depletion forces between solute particles. While it is tempting to phenomenologically introduce such forces via attractive regimes in effective pairwise potentials, it is well demonstrated that such forces vary locally with solute concentration [138], [152], [173], [174] and should therefore not be treated monolithically across a spatial domain. This method avoids such treatment and constitutes a more physically motivated method in which any effective depletion forces automatically evolve with local topological gradients.

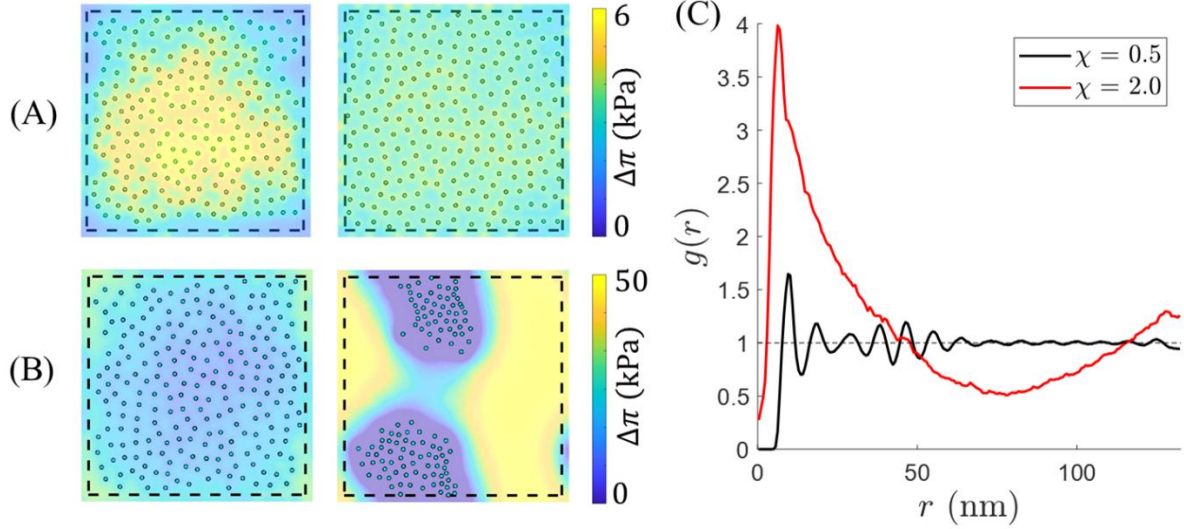


**Figure 4.8. Phase separation of polymer suspensions.** (A-B) The evolution of macromer suspensions (10k tetra-PEG macromer) is displayed. The initial solutions (left) were forced into a relatively homogenous state using a Poisson’s point process such that the more equilibrated systems (right) could evolve as governed solely by the local gradient in osmotic pressure. Evolutions are depicted for solvent qualities of (A)  $\chi = 0.5$  (theta solvent), and (B)  $\chi = 2$ , resulting in full homogenization and phase separation, respectively. (C) The corresponding RDFs are displayed for both solvent qualities with  $\chi$  as indicated in the legend.

While we have neglected the effects of volume exclusion interactions, Brownian diffusion, or entanglements between interpenetrating macromers, in the future these features could be easily combined with the methods introduced here. This would enable detailed studies of polymer suspensions in applications such as colloidal photonic crystals [175], [176]. However, in the remainder of this work – unless specified otherwise – we focus on sol-gels in theta solvent ( $\chi \approx 0.5$ ) based on experimental evidence that for tetra-PEG gels in the molecular weight range  $M_w \in [5,40]$  kDa, the effective mixing parameter is within the tight range of  $\chi \in [0.46,0.49]$  [119]. For such sol-gels, homogenization prior to gelation is reasonably assumed.

#### 4.4.2 Gelation and as-prepared network topology

Here we demonstrate the model’s *ab initio* reproduction of 10k tetra-PEG gel topologies based on as-prepared conditions. Initial gelation was carried out via the implementation outlined in Section 4.3.2 for networks swept across a range of as-prepared polymer concentrations (Fig. 9A,C), here characterized by  $\phi^* = \phi/\phi_{ol}$ , where  $\phi_{ol}$  is the 2D overlap concentration of macromers estimated by  $\phi_{ol} = fNbw/(2\pi R_g^2)$ , and  $R_g \sim Nf^{1/2}b^2$  is a star-shaped macromer’s radius of gyration (see Appendix C.II for details). Bond attachment events were allowed to take place until the fraction of attached chains reached 0.95, tantamount to a high conversion during gelation as seen in experimental studies on tetra-PEG networks [158]. **Fig. 4.9.B-C** depicts the fraction of chains comprising single links and double links with respect to concentration. Here a “single link” is defined as a connection between crosslinks that share only one chain, while a “double link” or “triple link” (fraction not shown in **Fig. 4.9.C**) indicates that the pair shares two or three chains, respectively. Such defects are critical in the accurate prediction of network mechanics and failure [177]. Therefore, accurate replication of initial experimental gel topologies is crucial.

The trends in defect prevalence with respect to as-prepared concentrations strongly agree between the model and experiments. Higher as-prepared concentrations consistently result in networks with higher fractions of single links and fewer defects (e.g., double or triple links). While at a given as-prepared concentration the predicted fraction of single links is slightly higher (and the fraction of attached double links is lower) for the *in silico* experiments (**Fig. 4.9.C**) than for experimental results (**Fig. 4.9.B**) [137], [178], this mismatch occurs primarily at higher concentrations and may be decreased by adjusting the timescale of Kuhn segment diffusion,  $\tau_0$  through Eqn.

(4.21). Additionally, the 2D overlap concentration estimated for simulations, is not synonymous with the rheologically extrapolated 3D overlap concentration cited by [137], thereby rendering direct quantitative comparison between the horizontal axes of **Fig. 4.9.B,C** uncertain. Ultimately, for the eventual purposes of predictive design, it is the relative trends in emergent topologies and mechanical properties that will guide fabrication parameters. Notably, at low concentrations a crossover region occurs for both simulations and experiments in which the fraction of double links becomes statistically consistent with that of single links, each representing between 40-50% of the overall population. However, for simulated gels prepared at  $\phi^* \leq 0.5$ , no networks formed (i.e., gelation was not observed), which is not consistent with the observations of [137]. As such, this iteration of the framework is limited to the study of sol-gels prepared at relatively high initial concentrations ( $\phi^* > 0.5$ ). In future work this limitation may be overcome by introducing Brownian diffusion of entire macromers to emulate intervention mixing, however here we focus on the case of gels fabricated at  $\phi^* \sim 1.5$  (as depicted in the rightmost schematic from **Fig. 4.9.A**).

For simulated gels prepared at  $\phi^* \sim 1.5$  the mean end-to-end length of an attached chain is  $\langle r \rangle = 12.1 \pm 0.1 \text{ nm}$ , or 28% of the overall contour length (**Fig. 4.9.D**). Of note is that  $\langle r \rangle$  changes little at lower concentrations ( $\langle r \rangle = 13.6 \pm 0.1 \text{ nm}$  for  $\phi^* \sim 0.8$  and  $\langle r \rangle = 12.9 \pm 0.1 \text{ nm}$  for  $\phi^* \sim 0.5$ ) (**Fig. 4.9.D**) despite an obvious increase in effective mesh size as visually seen in **Fig. 4.9.A**. This suggests that at lower concentrations, chains still relax to approximately the same lengths, but that crosslinks are generally more clustered (as indicated by the higher degree of double link defects from **Fig. 4.9.C-B**), which is what enables a larger pore structure. Unlike the distributions of attached chain length, the RDF of crosslinks,  $g(r)$ , elucidates information about clustering (**Fig. 4.9.E**). As expected, the RDFs universally indicate that the gels are

amorphous, with high structural noise and no long-range order (**Fig. 4.9.E**). However, at all three concentrations observed, there exists a length scale ( $\sim 10 \text{ nm}$  for  $\phi^* \sim 1.5$ ,  $\sim 15 \text{ nm}$  for  $\phi^* \sim 0.8$ , and  $\sim 20 - 25 \text{ nm}$  for  $\phi^* \sim 0.5$ ) below which the positions of crosslinks are highly correlated. This is consistent with the findings of [143] and indicates the presence of clusters whose characteristic sizes are on the same order as these correlation lengths, suggesting that lower as-prepared concentrations beget larger clusters. Clustering is further characterized with respect to  $\phi^*$  by the average clustering coefficient,  $\langle C \rangle = \mathcal{N}^{-1} \sum_{\alpha} C_{\alpha}$  where  $C_{\alpha} = 2T_{\alpha}/[k_{\alpha}(k_{\alpha} - 1)]$ ,  $k_{\alpha}$  is the number of uniquely attached neighbors to crosslink  $\alpha$ ,  $T_{\alpha}$  is the number of shared chains between said neighbors, and  $k_{\alpha}(k_{\alpha} - 1)/2$  constitutes the number of possible shared connections between said neighbors [179].  $\langle C \rangle$  characterizes the extent to which attached neighbors of crosslinks are attached to one another thereby quantifying the degree of clustering. **Fig. 4.9.F** demonstrates that  $\langle C \rangle$  decreases as the as-prepared network concentration increases, supporting the interpretation that lower density networks exhibit greater clustering. Clusters are visible in **Fig. 4.9.A** as the high osmotic pressure regions for  $\phi^* \sim 1.5$  or the regions of high crosslink density for  $\phi^* \sim 0.8$  and  $\phi^* \sim 0.5$ .

As an aside, below the length scale of  $1.3 \text{ nm}$  (for  $\phi^* \sim 1.5$ ),  $g(r)$  diverges suggesting that overlap of crosslinks occurs at the length scale of a Kuhn segment, which is a consequence of omitting any hard bodied repulsive potentials between nodes. While effective soft repulsion is introduced through the gradient in osmotic pressure, these forces are evidently overcome by the entropic tension of chains in some instances. Regardless, omitting hard body exclusion improves the numerical stability of the framework and only influences the displacement of crosslinks for gels by on the order



of 1% of the contour length of a chain. Therefore, it has negligible effect on emergent network mechanics as revealed in the following sections.

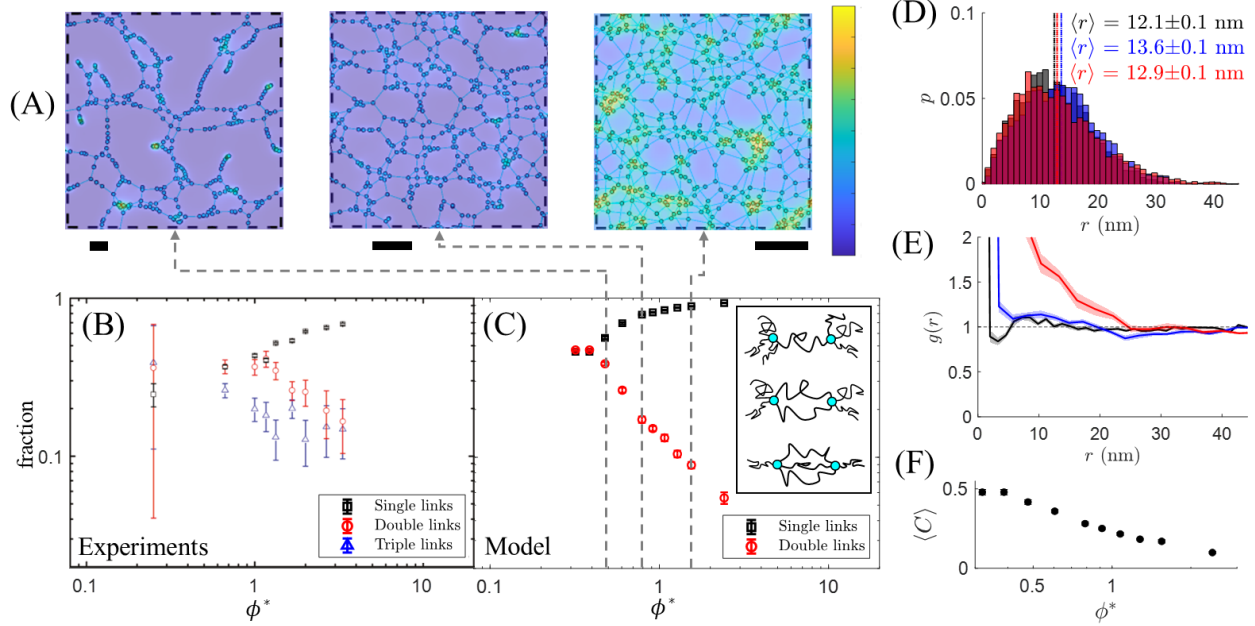


**Figure 4.9. Validation of the model's predicted *ab initio* topologies.** (A) Sample networks gelled from low (left) to high (right) as-prepared concentration are depicted. The rightmost sample represents the network topology used for *in silico* experimentation throughout this work. All scale bars represent the contour length of a single chain (44 nm). The color bar indicates the local osmotic pressure,  $\pi \in [0,10]$  kPa. (B) The experimentally measured fractions of single links (black squares), double links (red circles), and triple links (blue triangles) are plotted with respect to the normalized as-prepared concentration depicted for a 10k tetra-PEG gel. Adapted with permission from [137]. Copyright 2011 American Chemical Society. (C) The fraction of single links (black squares) and double links (red circles) is plotted with respect to the normalized as-prepared concentration for the ensemble average of ten simulated 10k tetra-PEG gel samples. The normalization concentration,  $\phi_{ol}$  was taken as the 2D overlap concentration based on the estimated radius of gyration in theta solvent. Error bars represent standard error (S.E.) of the mean. The inset in (C) graphically depicts the definition of single (top), double (center), and triple (bottom) links between two crosslinks. (D) The probability distribution function (PDF) of attached chains' end-to-end lengths is shown for  $\phi^* = 0.48$  (red),  $\phi^* = 0.79$  (blue), and  $\phi^* = 1.58$  (black) corresponding to the snapshots depicted in (A) from left to right, respectively. The mean lengths  $\langle r \rangle$  are denoted by the vertical dotted lines of the same respective colors. (E) The RDFs of crosslink positions,  $g(r)$ , from the model are shown for  $\phi^* = 0.48$  (red),  $\phi^* = 0.79$  (blue), and  $\phi^* = 1.58$  (black). (F) Mean clustering coefficient,  $\langle C \rangle$ , is plotted with respect to  $\phi^*$ .

#### 4.4.3 Equilibrium swelling mechanics of gels

Having ensured that the initial topological features for the case of 10k tetra-PEG gels match available experimental data, we next examine the equilibrium swelling of percolated gels to ensure that their initial swelling behavior matches that predicted by the Flory-Rehner theory discussed in Section 4.2. For the purposes of this section, we use Gaussian (i.e., linear) chains and omit deterministic fracture of bonds. This allows us to use the relatively simple elastic strain energy density function of a compressible Neo-Hookean material given by:

$$\psi_{el} = \frac{\mu}{2}(\bar{I}_1 - 2) + \frac{\kappa}{2}(J - 1)^2, \quad (4.31)$$

where  $\mu$  is the shear modulus,  $\kappa$  is the bulk modulus,  $J$  is the Jacobian ( $J = \det \mathbf{F} = \lambda_1 \lambda_2$ ), and  $\bar{I}_1 = (\lambda_1^2 + \lambda_2^2)/\lambda_1 \lambda_2$  is the first invariant of the isochoric component of the left stretch tensor ( $\bar{\mathbf{I}}_1 = \text{tr } \bar{\mathbf{B}} = \text{tr } [J^{-1} \mathbf{F} \mathbf{F}^T]$  for symmetric deformation gradients). The maximum number of attachments per crosslink is relatively low ( $f = 4$ ), so we set  $\mu = (1 - 2/f)ck_bT$  in accordance with phantom chain theory for networks with low connectivity [3], [68]. Here  $c$  is the network's attached chain concentration [3], [180], which evolves from the dry chain concentration ( $c_0$ ) as the network undergoes volumetric deformation according to  $c = J^{-1}c_0$ . For reasons examined in Appendix C.III, we also posit that the bulk modulus,  $\kappa$ , evolves as  $\kappa = 3\mu/2$  in 2D. To be consistent with the analysis of osmotic pressure, the reference state for  $J$  is taken as that of the dry polymer network.

Invoking the definition of Cauchy stress through Eqn. (4.3), simplifying, and writing stress in terms of the principal stretch components gives:

$$\boldsymbol{\sigma} = \frac{2}{J} \left\{ \begin{bmatrix} \lambda_1/\lambda_2 & 0 \\ 0 & \lambda_2/\lambda_1 \end{bmatrix} - \frac{\lambda_1^2 + \lambda_2^2}{2\lambda_1 \lambda_2} [\mathbf{I}] \right\} + \frac{\kappa_0}{J} (\lambda_1 \lambda_2 - 1) [\mathbf{I}]. \quad (4.32)$$

where  $\kappa_0 = \frac{3}{2}(1 - 2/f)c_0k_bT$  is the dry state bulk modulus. For the case of unconstrained (and therefore isotropic) swelling ( $\lambda_1 = \lambda_2 = \lambda$ ), Eqn. (4.32) reduces simply to  $\boldsymbol{\sigma} = \sigma^h \mathbf{I}$  where:

$$\sigma^h = \frac{\kappa_0}{J}(J - 1), \quad (4.33)$$

which represents the hydrostatic component of network stress,  $\sigma^h = \text{tr}(\boldsymbol{\sigma})/3$ , and is plotted in **Fig. 4.10.A** (black curve). Examining **Fig. 10A**, we see that  $\sigma^h$  increases monotonically with respect to  $J$ , and approaches a value of  $\kappa_0$  in the limit  $J \rightarrow \infty$ . Notably, the form of  $\sigma^h$  presented through Eqn. (4.32) is synonymous with that of the phenomenological, modified Ogden free energy functional introduced for rubberlike solids [181], [182]. This free energy formulation gives the hydrostatic stress as:

$$\sigma^h = \frac{\kappa}{J\beta}(1 - J^{-\beta}), \quad (4.34)$$

where  $\kappa$  is considered an invariant bulk modulus (i.e., is not a function of material density) and  $\beta$  is a material parameter governing the linearity of the system. Eqn. (4.33) and Eqn. (4.34) are identical when  $\beta = -1$ . The invariance between  $\sigma^h$  and  $J$  for each of these formulations at high volumetric strains is perhaps intuitive if stress is contextualized as the free energy density of the elastic network. The free energy stored in the system increases proportionately to the stretch of the chains in each dimension ( $\propto \lambda_1\lambda_2 = J$ ), however the material density also decreases proportionately to volume ( $\propto J^{-1}$ ), such that these two effects cancel one another. Indeed, the analytical virial formulation of network stress predicts complete invariance of  $\sigma^h$  with respect to  $J$  such that:

$$\sigma_{vir}^h = \kappa_0, \quad (4.35)$$

for networks whose only pairwise interactions are linear and tensile, even at low volumetric strains (Appendix C.III). Therefore, as illustrated in **Fig. 4.10.A**, there is a notable discrepancy between  $\sigma_{vir}^h$  and  $\sigma_h$  at low values of  $J$  (e.g., approximately 40% difference when  $J \approx 3$ ). Despite this, we find that numerically predicted values of  $\sigma^h$

are in good agreement with Eqn. (4.35) for all values of  $J$ . This is likely due to the omission of volume exclusion interactions in the numerical model. At low volumetric strains, the hydrostatic stress response of a true material most likely increases more rapidly with respect to  $J$  due to the alleviation of repulsive forces between neighboring constituents as the material density declines. A reduction in repulsive forces corresponds to a reduction of pressure (not to be confused with “osmotic pressure”) at the continuum scale. In turn, this drop in pressure amounts to an increase in hydrostatic stress as entropic chain forces become the dominant phenomenon. Thus, the modified Ogden model likely remains an accurate phenomenological predictor of materials’ true stress responses and mismatch here derives from our deliberate choice to neglect volume exclusion interactions for simplification. Volume exclusion interactions may be easily included in future iterations of this model concerned with materials at higher densities.

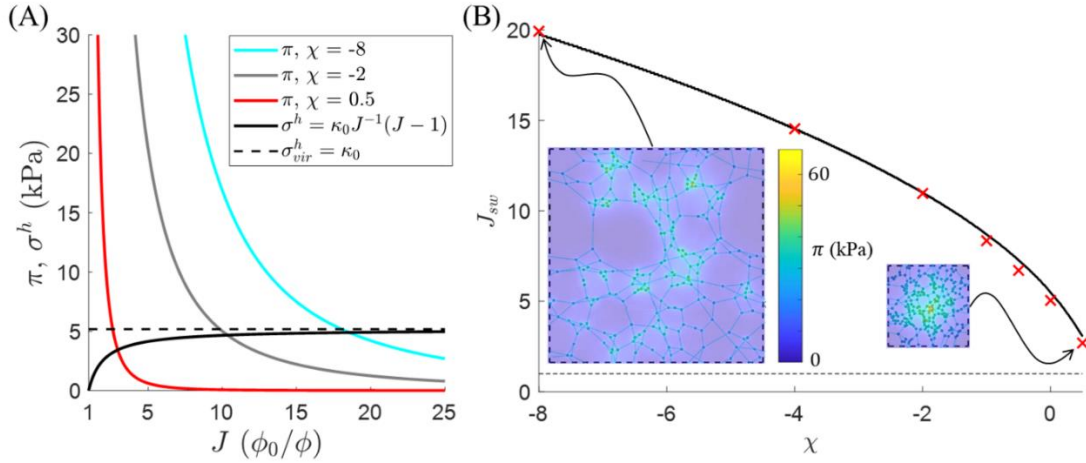


**Figure 4.10. Validation of the model’s predicted swelling mechanics.** (A) Osmotic pressure,  $\pi$ , is plotted as colored curves with respect to  $J$  for  $\chi = 0.5$  (red),  $\chi = -2$  (grey), and  $\chi = -8$  (cyan). The hydrostatic component of network stress,  $\sigma^h$ , is also depicted for the modified Ogden model (black curve) in which  $\kappa \propto J^{-1}$  [182] and based on the virial formulation (dotted black curve). Where the colored curves and black curve intersect represents the equilibrium swell state per Flory-Rehner theory. (B) The continuous set of equilibrium swelling ratios from (A) are plotted with respect to  $\chi \in [-8, 0.5]$ . Discrete equilibrium swelling ratios (averaged over ten networks of linear springs with a functionality of  $f = 8$ ) are plotted as red exes for the set  $\chi \in \{-8, -4, -2, -1, -0.5, 0, 0.5\}$ . S.E. of the mean constitutes less than 0.5% (or less than the marker size).

To assess the effect of osmotic pressure on gel swelling, the mixing parameter was numerically swept over the arbitrary set,  $\chi \in \{-8, -4, -2, -1, -0.5, 0, 0.5\}$ , where  $\chi < 0$  indicates that there is an effective repulsive potential between solute particles when placed in solvent [149]. **Fig. 4.10.B** depicts the swelling ratios  $J$  with respect to the mixing parameter  $\chi$ , as predicted by Flory-Rehner theory (using the modified Ogden strain energy) and the discrete model (red scatterplot). The continuous curve in **Fig. 4.10.B** may be graphically interpreted as the horizontal coordinates at which the  $\chi$ -dependent osmotic pressure curves intersect the hydrostatic stress curve in **Fig. 4.10.A**. Regardless of whether the virial formulation or modified Ogden model is used to predict  $\sigma^h$ , the numerical model predicts equilibrium swelling characteristics in good agreement with Flory-Rehner theory, even at low volumetric strains. This is because relatively large discrepancies in the equilibrium stress value (i.e., vertical axis intersection of curves in **Fig. 4.10.A**) amount to relatively small changes in  $J$  at low strains. Given the accurate prediction of swelling mechanics demonstrated here, in future studies, this model feature may be utilized in conjunction with force-sensitive bond dissociation to predict and avoid fabrication parameters that result in reverse gelation.

#### 4.4.4 Elastic response of a gel undergoing external load

While this model predicts swelling ratios in agreement with the predictions of Flory-Rehner theory for networks of ideal chains, it is also important to validate its prediction of mechanical response against nonlinear experimental results. We here demonstrate that the model's prediction of stress-stretch response ( $\sigma - \lambda$ ) is in agreement with the experimental results presented by [183] for 20k tetra-PEG gels undergoing uniaxial extension (**Fig. 4.11**). 20k tetra-functional networks comprised

of Langevin chains were generated per the methods of Section 3, however equilibrium swelling was not conducted. Instead, after percolation (i.e., continuous network formation), the initial RVE domain size was adjusted until the initial mean attached chain length  $\langle r \rangle$  was within 5% of the initial chain length ( $r_0 = 7.1 \text{ nm}$ ) reported experimentally, thereby ensuring that  $\lambda$  is reported with respect to the same reference state for both numerical and experimental results. To match experimental loading conditions, incompressible uniaxial tension was applied through the deformation gradient  $\mathbf{F} = \text{diag}(\lambda^{-1}, \lambda)$ . To fit the model's 2D predicted stress-stretch behavior against 3D experimental results, we invoke plane stress boundary conditions (i.e., stress-free boundaries on the faces whose norms are out-of-plane), for which a tertiary dimension (i.e., the RVE thickness,  $\zeta$ ) is needed to meaningfully compute the virial stress.

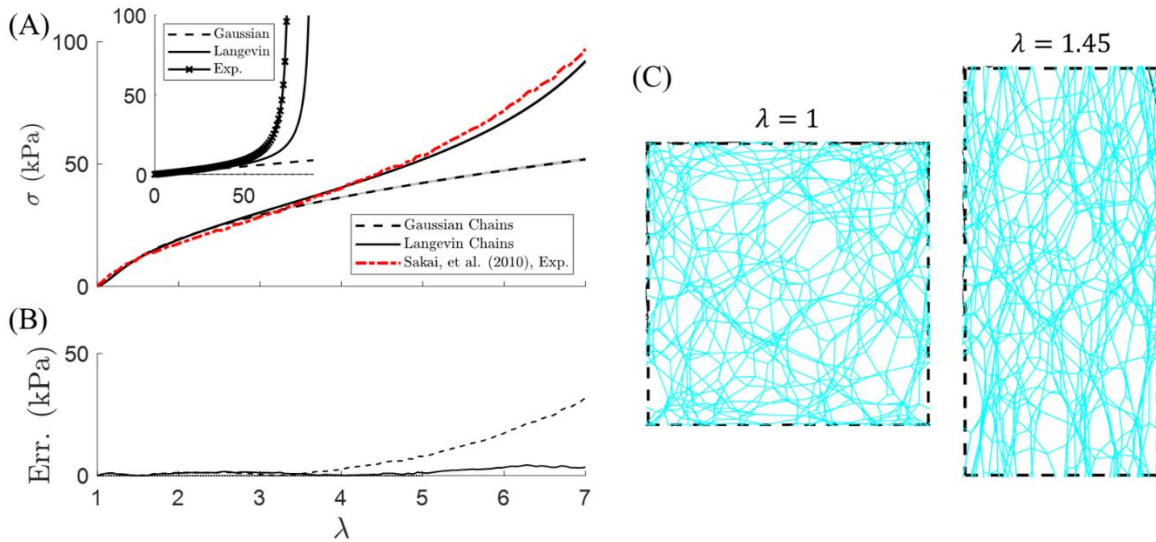


**Figure 4.11. Validation of the model's predicted stress response.** (A) The principal component of nominal network stress in the direction of uniaxial extension is plotted with respect to stretch for 20k tetra-PEG gels. The experimental results (red dashes) of Sakai, et al. (2010), are plotted against model predictions for networks of Gaussian (dotted black) and Langevin (solid black) chains. The shaded regions for numerical results denote S.E. of the mean. The inset displays the force (pN) versus extension (nm) relationships for the Gaussian and Langevin chains ( $L = 88 \text{ nm}$ ) of the model, as well as the inversely derived experimental force-extension reported by Sakai, et al. (2010) ( $L = 76 \text{ nm}$ ). (B) Root mean square error (RMSE) is plotted with respect to stretch. (A-B) Share a horizontal axis. (C) Snapshots of a numerical network at stretches of  $\lambda = 1$  and  $\lambda = 1.45$  are depicted for reference.

As illustrated in **Fig. 4.11.A**, the results of our model agree reasonably well with the experimental results when said thickness is set to  $\zeta = 7.4 \text{ nm}$ , which approximately coincides with the initial mean chain end-to-end length of  $\langle r \rangle \approx 7.5 \text{ nm}$ , suggesting that the numerical RVE represents one layer of crosslinks. To emphasize the importance of finite chain extensibility, **Fig. 4.11** includes predicted results using both linear (Gaussian) and nonlinear (Langevin) chains. We see that for linear networks the model quickly deviates from the experimental stress-stretch behavior reported, whereas low error (RMSE < 1.5 kPa) is achieved when Langevin chains are used in the regime  $\lambda \leq 5$  (**Fig. 4.11.B**). Error reaches up to RMSE  $\approx 6 \text{ kPa}$  or  $\sim 6\text{-}10\%$  of the overall network stress for  $\lambda > 5$ . However, this is attributed to earlier divergence of the force-extension relation (occurring when  $r \rightarrow L$ ) reported by [183], than that used in the model. The single chain force-extension relations of both works are displayed in the inset of **Fig. 4.11.A**. Note that for the number of macromers modeled ( $\mathcal{N} = 625$ ) the domain width became smaller than that of a single chain's contour length above  $\lambda = 7$ , hence the upper limit of stretch reported.

#### 4.5. Damage and the role of heterogeneities

Given the accurate predictions of network topology, swelling mechanics, and stress response for 10k and 20k tetra-PEG gels thus far, the remainder of this work is devoted to using the model to extrapolate predicted mechanical properties of gels across a range of functionalities and molecular weights (or chain contour lengths). It is well documented that the damage of polymeric materials, including gels is sensitive to defects and thus topology [33], [74], [184], [185]. Therefore, in Section 4.5.1, we examine the predicted mechanical properties and failure mechanics of four network types (representing two functionalities and two chain lengths). We then quantify

topological properties and visually inspect the network configurations to explain the observed trends. In Section 4.5.2, we conduct a larger parameter sweep and introduce a set of structure-property function plots that aid in understanding the role of topology on mechanical failure.

#### 4.5.1 Mechanical and topological properties of *ab initio* tetra-PEG gels

**Fig. 4.12** presents the predicted stress-stretch response and mechanical properties of tetra-PEG gels with the combinations of  $M_w$  (or  $L$ ) and  $f$  indicated in **Table 4.2**. Damage was introduced using the deterministic failure criteria used by [121], whereby scission occurs for chains whose end-to-end lengths reach 95% of their contour lengths. Although enthalpic bond stretching becomes a significant effect influencing the failure of polymer chains at high strains [126], it demonstrably increases the stiffness of PEG chains in water by multiple orders of magnitude [162], [186]. As such, the exact stretch at which carbon-carbon binding energy is exceeded (i.e., rupture occurs) will reside near  $\lambda \rightarrow \sqrt{N}$ , hence the use of this coarse failure criteria for our purposes. As one would expect, from **Fig. 4.12.A** we see that increasing the contour lengths of chains resulted in softer networks (i.e., lower Young's moduli,  $E$ , **Fig. 4.12.B**) that therefore reach larger equilibrium swelling ratios ( $J_{eq}$ , **Fig. 4.12.C**) and higher deformations prior to yield (**Fig. 4.12.D**) and failure (**Fig. 4.12.E**). Perhaps unexpectedly, these networks absorbed less energy prior to fully fracturing (i.e., exhibited lower toughness,  $U_t$ , taken as  $U_t = \int \sigma(\epsilon) d\epsilon$  in the limits  $\epsilon_{eq}$  to  $\epsilon_t$ ) (**Fig. 4.12.F**). However, this is partially realized by the fact that longer chains store less mechanical energy at a given stretch, thus reducing the strain energy density of the overall network. Furthermore, here  $\epsilon$  was measured from the swollen equilibrium state, as opposed to the dry state or ideal chain end-to-end length



$\langle r \rangle = b\sqrt{N}$ ). Since the networks made from longer chains begin at a higher swelling ratios, their chains begin at higher effective stretches. Visually, this is illustrated by both the inset depictions of the initial networks in **Fig. 4.12.A**, which are all depicted at the same length scale, as well as the close-up snapshots of these same networks from **Fig. 4.12.G-J**, whose scale bars all represent 50 nm. Despite significant differences in initial chains stretch in the equilibrated swollen states, the lower limit used to compute  $U_t$  was always taken as  $\varepsilon_{eq} = \sqrt{J_{sw}} - 1$ . This lower limit choice also explains why the networks with chains that are roughly four times longer (177 nm versus 44 nm) are not four times as extensible (**Fig. 4.12.E**).

Also as expected, increasing the functionality of networks with the same length chains stiffened them (i.e., increased  $E$ ), thereby decreasing  $J_{eq}$  and increasing yield stresses ( $\sigma_y$ ) (**Fig. 4.12.A**). This is because introducing a higher crosslink density to the network ensures that more chains may effectively carry load in parallel. However, less intuitively, as seen from **Fig. 4.12.D-F**, increasing functionality also resulted in a decrease of the strain at peak force ( $\varepsilon_y$ , taken as the average strain at which stress peaks), fracture strain ( $\varepsilon_t$ ), and therefore toughness ( $U_t$ ) of the networks, indicating more brittle behavior. To explain this behavior from a micromechanical perspective, we must understand how the chains in these respective networks are oriented and stretched prior to and during deformation.

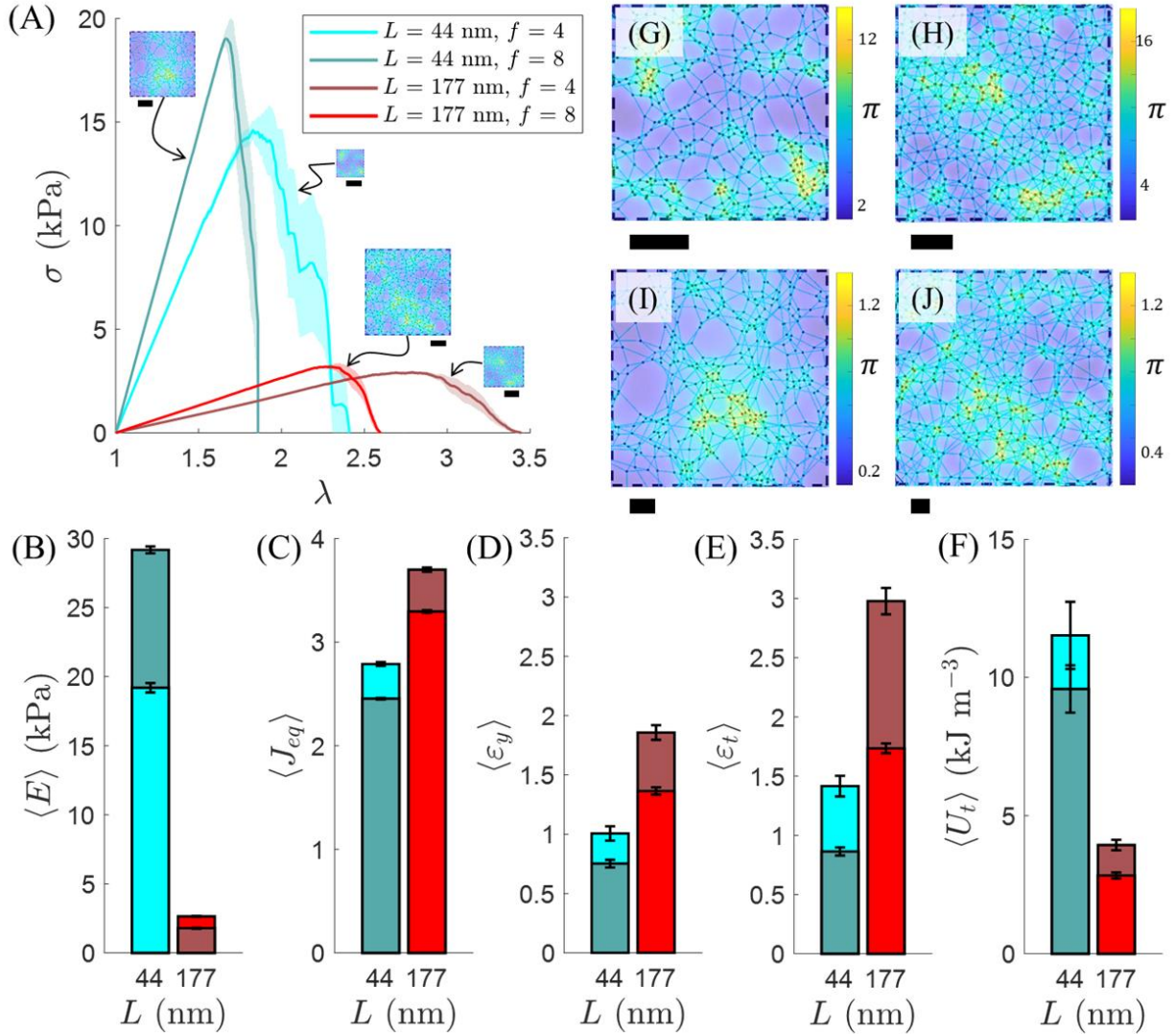


**Figure 4.12. Mechanical predictions of gels with different functionalities and chain lengths.** (A) The ensemble averaged principal component of Cauchy network stress in the direction of uniaxial extension from ten simulations ( $n = 10$ ) is plotted with respect to stretch measured from the equilibrated swollen state. This relation is shown for four types of tetra-PEG gels with varying chain contour lengths  $L$  and functionalities  $f$  as indicated by the legend. The inset snapshots depict sample networks for each combination of  $L$  and  $f$ , all at the same length scale to emphasize the different degrees of initial chain stretch, which results from different dry macromer densities (based on functionality) and initial swelling ratios. The average (B) tangent modulus  $\langle E \rangle$ , (C) equilibrium swell ratio  $\langle J_{eq} \rangle$ , (D) strain at peak force  $\langle \epsilon_y \rangle$ , (E) failure strain  $\langle \epsilon_t \rangle$ , and (F) toughness  $\langle U_t \rangle$  are displayed for each chain contour length and functionality. Colors correspond to the legend from (A). (G-J) Close-up views of the snapshots from (A) are depicted for the networks with (G)  $L = 44$  nm and  $f = 4$ ; (H)  $L = 44$  nm and  $f = 8$ ; (I)  $L = 177$  nm and  $f = 4$ ; and (J)  $L = 177$  nm and  $f = 8$ . All shaded regions or error bars represent S.E. of the mean. All scale bars represent 50 nm. Heat maps represent osmotic pressure.

**Table 4.2.** Macromer inputs for the networks of **Fig. 4.12**.

Network No.	Molecular Weight, $M_w$ (kDa)	Chain Contour Length <sup>5</sup> , $L$ (nm)	Functionality, $f$
1 (Blue)	10	44	4
2 (Teal)	20	44	8
3 (Maroon)	40	177	4
4 (Red)	80	177	8

**Figs. 4.13.A** and **4.13.C** depict the joint probability distribution functions of the normalized chain end-to-end lengths  $r^* = r/L$  for 10k tetra- and octa-PEG gels, respectively. Examining **Fig. 4.13.A-E**, it is immediately apparent that a greater fraction of the chains in the octa-PEG network exists at higher values of  $r^*$ , even prior to deformation. Plotting the average value of  $r^*$  in the principal direction of extension,  $\langle r_2^* \rangle$ , against  $\lambda$  for each network (**Fig. 4.13.F**) confirms that the mean end-to-end length of chains in the octa-PEG gel is almost universally higher in the stretch regime  $1 < \lambda < 1.8$  than those in the tetra-PEG gel. Indeed,  $\langle r_2^* \rangle$  is only lower for the octa-PEG network in this range of  $\lambda$  after the gel fully fractures ( $\lambda > 1.83$ ). Visually investigating the networks at their initial state immediately elucidates an obvious cause of this. **Fig. 4.14.A** and **4.14.B**, illustrates samples of simulated 10k tetra-PEG and 20k octa-PEG gels, respectively, at various uniaxial stretches up to full fracture.

---

<sup>5</sup> Note that while  $M_w$  serves as the primary control variable influencing chain length in both experiments and this numerical framework, we are here interested in isolating the effects of chain length on mechanical response. As such, in this section we investigate four values of  $M_w$  that result in just two values of  $L$  for the given functionalities.

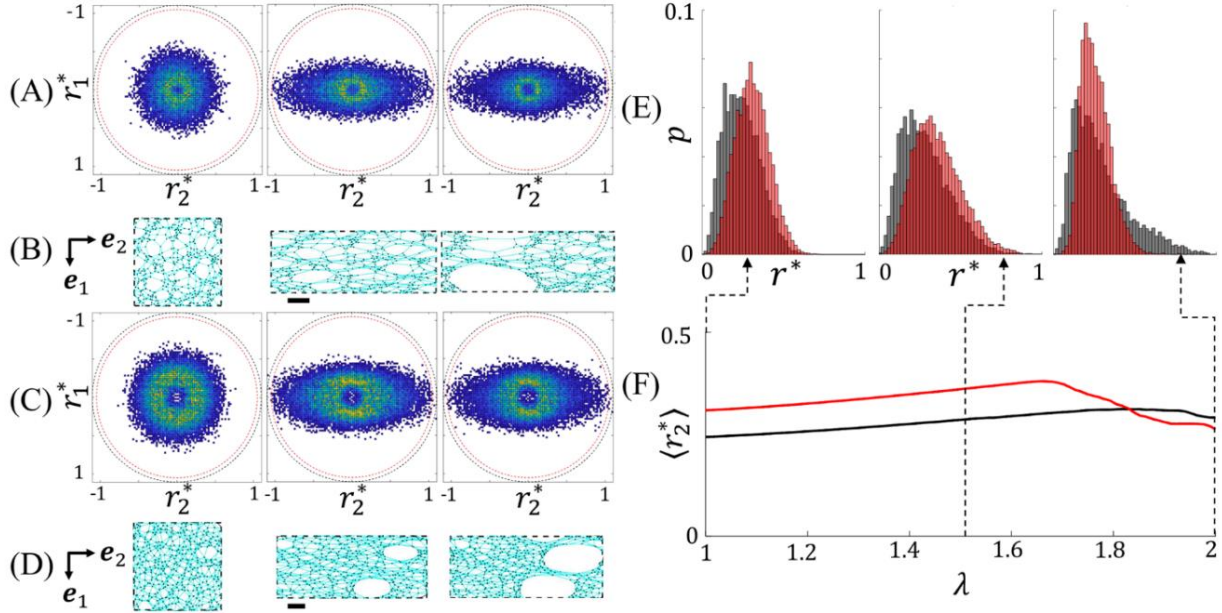


**Figure 4.13. Chain distribution functions of gels with  $L = 44 \text{ nm}$  and different functionalities.** (A) The joint PDF of  $r^*$  is shown for the ensemble of ten ( $n = 10$ ) 10k tetra-PEG gels at  $\lambda = 1$  (left), the measured yield stretch  $\lambda = 2.00$  (center), and the measured failure stretch  $\lambda = 2.16$  (right). (B) Snapshots of a sample 10k tetra-PEG network at the stretches from (A) are depicted. The network depicted did not reach absolute failure by the average failure stretch of  $\lambda = 2.16$ . (C) The joint PDF of  $r^*$  is shown for the ensemble of ten 20k octa-PEG gels at  $\lambda = 1$  (left), the measured yield stretch  $\lambda = 1.75$  (center), and the measured failure stretch  $\lambda = 1.83$  (right). (D) Snapshots of a sample 20k octa-PEG network at the stretches from (C) are depicted. The network depicted did not reach absolute failure by the average failure stretch of  $\lambda = 1.83$ . (A-D) The extensile direction,  $e_2$  is oriented horizontally. Scale bars in (B) and (D) represent  $L = 44 \text{ nm}$ . Dashed black circles in (A) and (C) indicate the chain contour length, while dashed red circles represent the deterministic scission length for chains. (E) The radial PDFs of  $r^*$  are shown for the 10k tetra- and 20k octa-PEG gels as grey and red histograms, respectively. For direct comparison, these histograms are depicted at  $\lambda = 0$  (left),  $\lambda = 1.5$  (center), and  $\lambda = 2.0$ . Note that the chains in these two networks have the same contour length. (F) The average component of normalized chain end-to-end length in the principal direction of extension is plotted with respect to stretch. End-to-end lengths are normalized as  $r^* = r/L$  such that  $r^* \geq 0.95$  prompts chain scission.

Each network was generated from the same number of macromers ( $\mathcal{N} = 400$ ), and we know from **Fig. 4.12.C** that the 10k tetra-PEG network has swelled more from its initial dry state to the references state shown. Despite this, the scale bar (which represents  $L$ ) is 38% larger for the 10k tetra-PEG gel (**Fig. 4.14.A**) than it is for the 20k octa-PEG gel (**Fig. 4.14.B**). This is because the 20k octa-PEG gel occupies more space per macromer in its dry state than the 10k tetra-PEG gel, simply because it has a greater number of chains, a notion made visually apparent by the macromer

illustrations in **Fig. 4.14**. Were the topological features of these networks (such as coordination number and variance of the end-to-end length) equal, then this difference in swelled dimensions would immediately imply that the chains in the 20k octa-PEG gel begin at a 38% greater stretch prior to deformation, closely reflecting the average 39.8% greater extensibility of the 10k tetra-PEG gels.

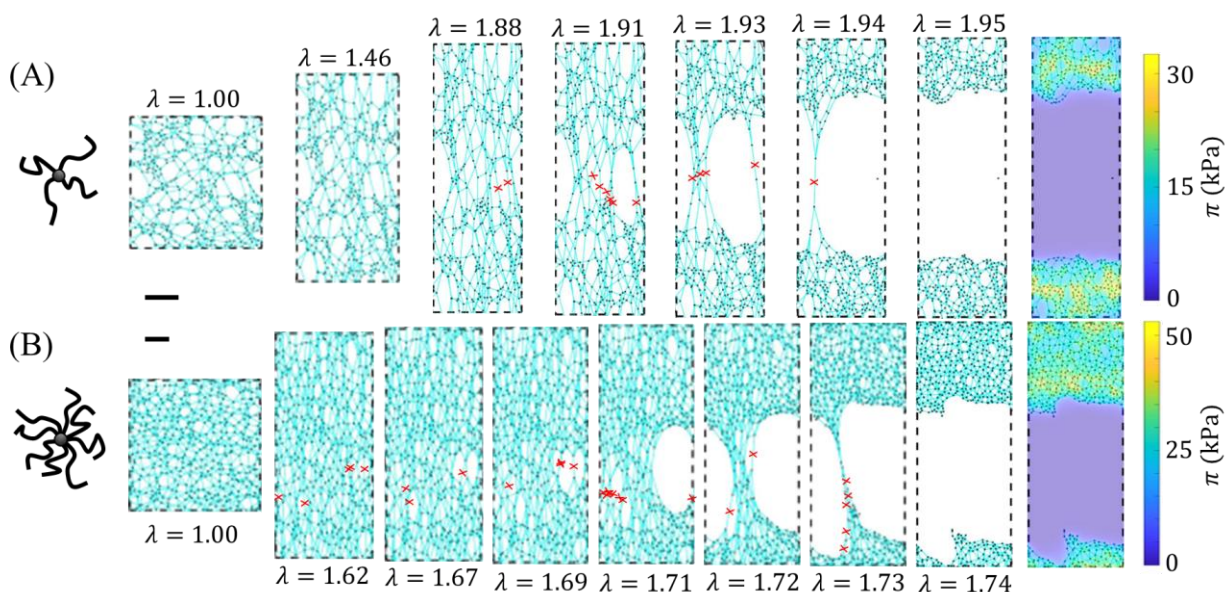


**Figure 4.14. Fracture of gels with of gels with  $L = 44$  nm and different functionalities.** (A) A schematic of a tetra-functional macromer is depicted, alongside snapshots of a simulated 10k tetra-PEG gel as it undergoes uniaxial extension. (B) A schematic of an octa-functional macromer is depicted, alongside snapshots of a simulated 20k octa-PEG gel as it undergoes uniaxial extension. The macromer schematics are depicted at the same scale, whereas the sizes of the gel snapshots are indicated by their respective scale bars, each representing  $L$ . Red crosses in the gel snapshots demark which chains rupture before the next displayed snapshot. The rightmost snapshots depict the osmotic pressure landscapes of the domains at initial fracture.

However, the topological properties in these two gels are not the same, with the 20k octa-PEG gel appearing more homogenized (**Fig. 4.15A-B**). This is reflected in the radial distribution functions (RDFs) at  $\lambda = 1$  displayed in **Fig. 4.15.C**, which reveal that the 10k tetra-PEG gel displays just one correlation length scale around  $d^* = 0.15$  followed by an inversely correlated region from  $d^* \approx 0.3$  to  $d^* \approx 1$  (i.e.,  $g(0.3 \leq d^* \leq 1) < 1$ ). The single correlation peak indicates that crosslinks in the lower

functionality network are relatively clustered in regions wherein the most common pairwise separation is approximately 15% of  $L$ . The inversely correlated regime indicates that clusters are separated by vacant regions with a characteristic size on the order of  $L$ . This is visually supported by the network depicted in **Fig. 4.15.A**. In contrast, the RDF of the 20k octa-PEG gel displays two correlation length scales (i.e., peaks) around  $d^* = 0.29$  and  $0.65$ , indicative of more ordered crosslink distribution below  $d^* = 1$  and greater homogeneity of the higher functionality gel. One clear, inversely correlated region exists for the 10k tetra-PEG gel in the approximate range  $0.4 < d^* < 0.6$ , indicating a smaller characteristic size of vacant regions, which is visually illustrated by **Fig. 4.15.B**. While one might assume that this results in greater resistance to damage, it merely promotes the nucleation of more numerous, but smaller voids as bond scissions begin. This is somewhat reflected by the red crosses in the network snapshots **Fig. 4.14**, which demark the bonds that rupture in each subsequent frame. We see that the first discrete rupture events occur in wholly separate regions of the 20k octa-PEG gel (see  $\lambda = 1.62$  or  $1.67$ ), whereas the first rupture events of the 10k tetra-PEG gel (see  $\lambda = 1.88$ ) are localized to one region that already exhibited low chain density.

To gain a quantitative understanding of damage onset, we utilize image analysis to measure and plot the RDF of void centroids, as well as the average number of voids and void area with respect to stretch for the gels with  $L = 44 \text{ nm}$  (**Fig. 4.16**). To remove noise and filter out pores occurring in highly clustered regions, we define “voids” simply as pores in the network whose areal size is greater than  $A_v = 0.25\pi\rho^2$  where  $\rho = 0.15$  is the shortest correlation peak length scale measured from **Fig. 4.15.C**. The RDFs of **Fig. 4.16.A** reveal that void positions are not correlated in either network above a lengths scale of  $d^* \sim 0.5$ . However, the voids in the tetra-functional

network are demonstrably more clustered with some small correlation existing around  $d^* \sim 0.3$  and a non-negligible population of voids within less than  $d^* \sim 0.2$  of one another. This supports the greater homogeneity of the octa-functional gels and is made visually clear by the black and white network depictions in **Fig. 4.16.B** both without (left) and with (right) filtration of small pores. Examining the statistics of voids during deformation, **Fig. 4.16.C-D** indicate that the average number of voids per crosslink  $\langle N_v^* \rangle$  and average void area  $\langle A_v^* \rangle$  (normalized as  $A_v^* = A_v/0.25\pi L^2$ , where  $0.25\pi L^2$  is the maximum envelope of a single macromer) are both consistently higher for the tetra-PEG gel than the octa-PEG gel, which is perhaps trivial. Of note though is that the first observed instances of rupture events (denoted by the vertical dotted lines in **Fig. 4.16.C-D**) are closely followed by steep declines and spikes in  $\langle N_v^* \rangle$  and  $\langle A_v^* \rangle$ , respectively, quantifying the rapid void coalescence illustrated through **Fig. 4.14**. Note that subsequent drops in  $\langle A_v^* \rangle$  are due to elastic energy in the network causing local retraction around highly damaged regions, thus restoring a smaller average pore size. However, it must be noted that without inclusion of a fluid transport timescale, the rate of this elastic retraction is likely misrepresented by this iteration of the model, as reflected by the high disparity in osmotic pore pressure between the fractured and intact network domains (see the rightmost panels of **Fig. 4.14**). Poroelastically slowed retraction around damage zones may mitigate the onset of stress risers that result from heightened strain of one or a few intact chains, thus perhaps also delaying the rate of crack propagation in true gels. In future iterations of this approach, we will incorporate poroelasticity via a fluid transport timescale and investigate this likelihood. Nonetheless, this iteration of the model is still revealing regarding damage initiation as it relates to the *ab initio* inputs.



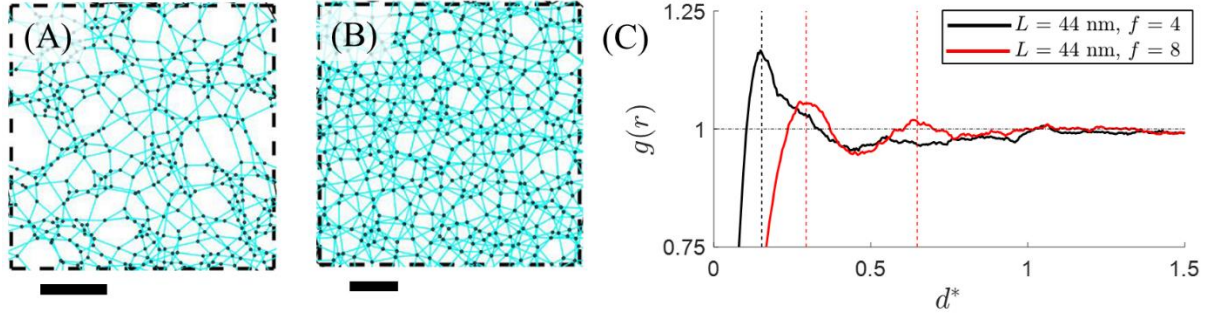


**Figure 4.15. RDFs of gel's crosslinks with  $L = 44 \text{ nm}$  and different functionalities.** (A-B) Samples of a (A) 10k tetra-PEG and (B) 20k octa-PEG networks are shown at  $\lambda = 1$  for visual reference. Scale bars represent  $L = 44 \text{ nm}$ . (C) The RDFs of ensembles of ten ( $n = 10$ ) 10k tetra-PEG (black) and ten 20k octa-PEG (red) gels' crosslinks are displayed. The distance between crosslinks is normalized as  $d^* = d/L$ . Dotted lines denote correlation length scales or peaks in  $g(r)$ .

No statistically significant difference was measured between the average rate at which voids initiate ( $\partial\langle N_v^* \rangle / \partial\lambda$ ), nor the rate at which their average area increases ( $\partial\langle A_v^* \rangle / \partial\lambda$ ) prior to damage onset ( $\lambda < 1.5$ ). Nevertheless, it is clear from this analysis that the higher functionality leads to a more homogenous domain with fewer and smaller voids. Thus, while the lower failure strains of higher functionality networks are attributed primarily to the higher initial stretch of the chains therein, it is also likely that brittle behavior is exacerbated by a higher degree of load sharing and homogeneity between chains as they approach their failure criteria (here,  $r^* \rightarrow 0.95$ , but governed by bond dissociation energy in true polymer chains [65]) This culminates in greater homogeneity of the subsequent failure domains and rapid void coalescence. This analysis holds true in comparing the 40k tetra-PEG gels to 80k octa-PEG gels (both of which have  $L = 177 \text{ nm}$ ), as well (see Appendix D for extended data).



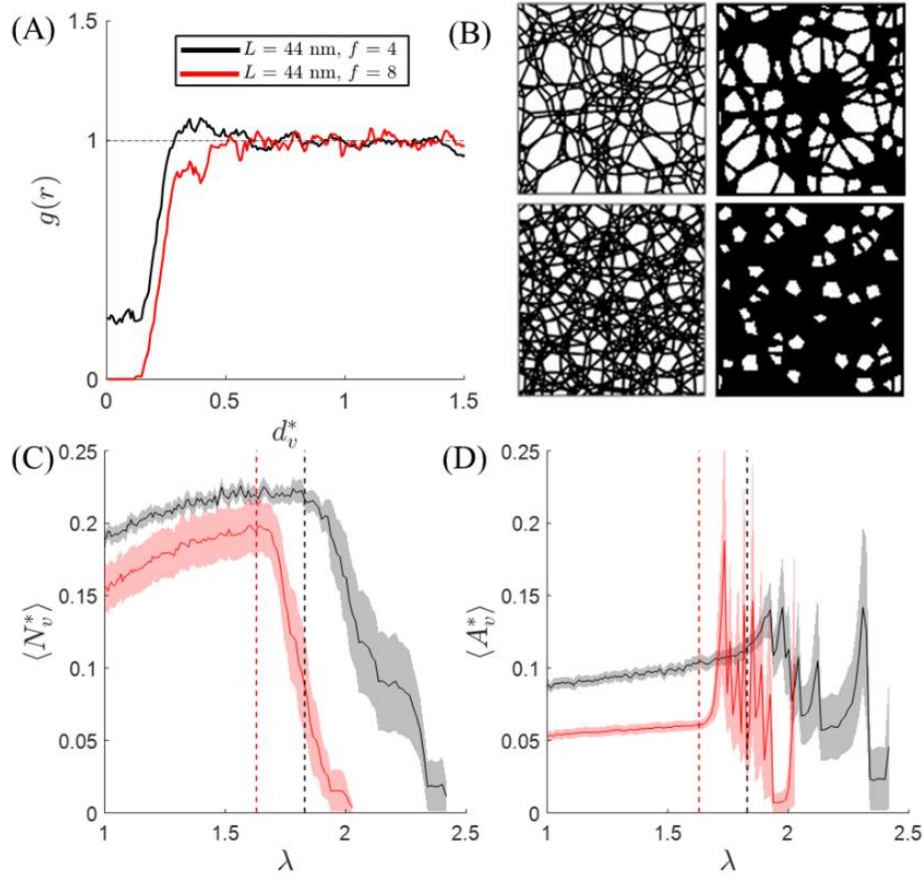


**Figure 4.16. Void characteristics of gels with  $L = 44$  nm and different functionalities.** (A) The RDFs of ensembles of ten ( $n = 10$ ) 10k tetra-PEG (black) and ten 20k octa-PEG (red) gels' void centroids are displayed at  $\lambda = 1$ . The distance between void centroids is normalized as  $d_v^* = d_v/L$ . (B) Black-white snapshots of sample networks are displayed. The left column displays the black-white network configurations of a 10k tetra-PEG gel (top) and 20k octa-PEG gel (bottom) prior to deformation. The right column displays the same respective networks with pores below the prescribed threshold filtered out (to reduce noise). (C) The average number of voids per macromer is plotted with respect to stretch. (D) The average void area (normalized as  $A_v^* = A_v/\pi L^2$ ) is plotted with respect to stretch. (C-D) Shaded regions represent S.E. of the mean. The vertical dotted lines denote the approximate stretches at which bond rupture events were first detected through Fig. 5.14 ( $\lambda \approx 1.85$  – black,  $\lambda \approx 1.6$  – red).

#### 4.5.2 Predictive mapping as functions of $M_w$ and $f$

Having postulated micromechanical causes of observed trends in emergent properties, we here conduct a broader parameter sweep to predict high order mechanical trends in PEG-based gels. Fig. 4.17 plots mean values of Young's

modulus ( $E$ ), yield stress ( $\sigma_y$ ), swell ratio at initial equilibrium ( $J$ ), yield strain ( $\epsilon_y$ ), failure strain ( $\epsilon_t$ ), and toughness ( $U_t$ ) with respect to  $f \in [3,10]$ , for five different molecular weights ( $M_w \in \{10,20,30,40,50\}$  kDa). While PEG-based copolymers with  $f \in \{2,4,8\}$  are perhaps most typical, we include uncommon functionalities to highlight the mechanical trends and with the recognition that intermediate effective functionalities are attainable contingent on network composition [187]. We exclude systems in which  $f = 2$  as these are below the percolation threshold. Note that we no longer set  $M_w$  to fix the chain length based on functionality, as we are now interested in examining the effects of typical control parameters used by experimentalists.

The mechanical trends are in general agreement with existing literature [119], [188], [189]. Greater  $M_w$  typically decreases the elastic modulus (**Fig. 4.17.A**) and yield stress (**Fig. 4.17.B**) of the networks due to the increased length and decreased stiffness of the chains (thereby increasing the equilibrium swelling ratio – **Fig. 4.17.C**). In contrast, greater  $M_w$  increases the yield (**Fig. 4.17.D**) and failure strains (**Fig. 4.17.E**) of networks due to the increased extensibility of the underlying chains. It appears that the decreases in moduli robustly outpace the increases in extensibilities and result in an overall decrease in dissipated energy upon failure (i.e., toughness) with respect to  $M_w$  (**Fig. 4.17.F**). Regarding network connectivity, greater  $f$  generally increases modulus (**Fig. 4.17.A**) and yield stress (**Fig. 4.17.B**) thereby decreasing equilibrium swelling ratio (**Fig. 4.17.C**), due to the increased stiffness associated with higher chain concentrations. Given increased network homogeneity and initial chain stretch at (as discussed in Section 4.5.1), greater  $f$  also generally decreases the yield and failure strains (**Fig. 4.17.C-D**). Interestingly, the toughness (**Fig. 4.17.F**) appears to either decrease or increase with respect to  $f$  depending on  $M_w$ . Specifically, the toughness of networks generated using  $M_w = 10$  kDa increases

as  $f$  decreases, whereas toughness appears positively correlated with  $f$  for all other values of  $M_w$  investigated. Notably, the toughness of gels with intermediate functionalities ( $5 \leq f \leq 8$ ) and low molecular weights ( $M_w \leq 30 \text{ kDa}$ ) does not vary significantly with respect to  $f$  given the number of samples ( $n = 10$ ) observed. Despite the significance of functionality's impact on mechanics, existing experimental literature examining its specific effects on star-polymer-initiated networks' mechanical properties was not identified in the context of PEG gels (unless significant compositional changes were involved as in the studies of Schultz, et al. 2008 [187]). Nevertheless, further investigation is justified, and functionality will be central to the scope of forthcoming studies in which we probe the mechanical properties of both tetra and octa-functional macromers comprising a covalently adaptable gel [13].

While the overall trends observed here are largely in agreement with those observed by experimentalists, the limitations of extrapolated predictions are perhaps highlighted by the outlier case in which  $M_w = 10 \text{ kDa}$  and  $f = 10$ . A precipitous drop in modulus, yield stress, and therefore toughness is observed for networks with these inputs. We see from Eqn. (4.15) that the solute concentration (with respect to radial distance from a crosslink) scales proportionately to the functionality and inversely with the mesh size in the model ( $\phi(r) \sim f/\bar{\xi}$ ). As such, through Eqn. (4.18), high effective osmotic repulsive forces occur between macromers with these properties despite their short chain lengths (of  $35 \text{ nm}$ ). Hence, during gelation, a high fraction of defects emerges as – at the as-prepared concentration – each macromer is more likely to double or triple link to a few nearest neighbors rather than bond equiaximthally with its surroundings. This yields gel topologies with high defect fractions as depicted in the inset of **Fig. 4.17.C**. These defects soften the networks' mechanical responses [137]. In truth, adequate mixing during gelation is generally

facilitated in experiments by Brownian diffusion and stirring intervention [158], neither of which were modeled here. Therefore, future application of this method for the predictive design of experimental systems should commence with multiple model calibration experiments, preferably at the extreme ends of the relevant parameter space.

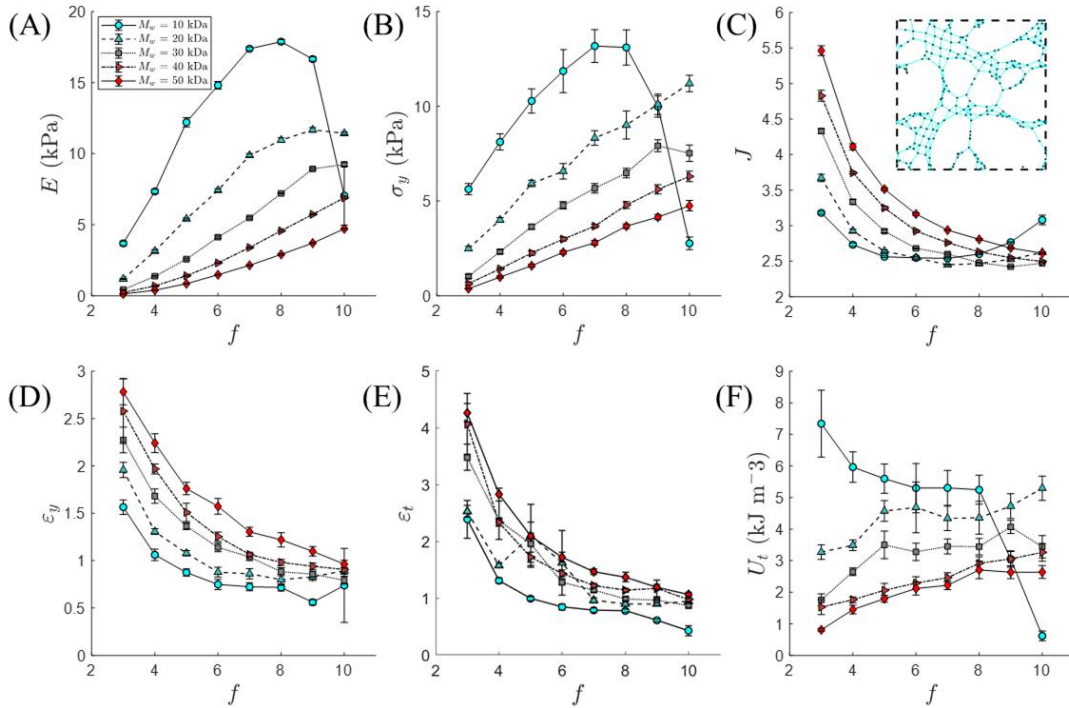


**Figure 4.17. Mechanical predictions for extended parameter sweep.** Mean (A) Young's modulus, (B) yield stress, (C) equilibrium swell ratio, (D) yield strain, (E) failure strain, and (F) toughness are plotted with respect to functionality for  $M_w = 10$  kDa (blue circles),  $M_w = 20$  kDa (teal triangles),  $M_w = 30$  kDa (grey squares),  $M_w = 40$  kDa (sideways maroon triangles), and  $M_w = 50$  kDa (red diamonds). Ten ( $n = 10$ ) samples of each network type were modeled. Error bars represent S.E. of the mean. The inset of (C) displays the anomalous topology of a gel with  $M_w = 10$  kDa and  $f = 10$ , as discussed in the main body text.

#### 4.6. Concluding remarks

In this work we have introduced a theoretical and computational framework for modeling the spatial distribution of macromers in sol-gels, based on the nm-scale

solute-concentration landscape and its effect on the local osmotic pressure gradient as dictated by Flory-Huggins mixing theory. The method constitutes a more physically motivated approach than the phenomenological, effective pairwise potentials often employed at the network scale to capture inter-polymer repulsion and depletion interactions. While the methods introduced here may be incorporated into 3D models, for simplicity, we initially incorporated them into a 2D, discrete numerical framework adopted from our previous work [3]. Indeed, both topological and mechanical properties may be affected by network dimensionality. For example, both network connectivity and degree of non-affine deformation tend to be larger in 3D networks [68], and so in future efforts we will apply these methods to 3D domains. Nevertheless, we here demonstrated this initial framework’s prediction of mixing and phase separation as a function of the Flory mixing parameter,  $\chi$ , thereby exhibiting its potential for use modeling polymer suspensions. As the primary focus of this work, we then demonstrated this framework’s accurate *ab initio* prediction of the topological and mechanical properties of tetra-PEG gels as functions of their as-prepared polymer concentration, molecular weight, and functionality. Finally, we utilized the framework to extrapolate predicted mechanical properties of gels, further exploring the effects of molecular weight and functionality.

We found that increasing molecular weight generally decreased the moduli, yield stresses and toughness of gels. In contrast, it reliably increased their equilibrium swelling ratio, and their extensibility with respect to the swollen reference state. As expected, increasing the functionality of crosslinks also increased stiffness of the emergent gels; however, less intuitively increased functionality (given the same chain length and as-prepared concentration) decreased mechanical toughness and failure strains (as measured from the swollen state). We found that this was due primarily

to higher initial stretch of the polymer chains for gels with higher chain concentration, emphasizing that the effects of initial swelling must be accounted for when designing the mechanical properties of gels. This greater initial swelling imposes residual stresses that result directly from increased functionality. This finding is consistent with that of [74] who reported that increasing crosslink density in mesoscopically modeled polymer networks reduced overall network extensibility due to higher pre-stressing of the chains. However, the approach introduced here is novel in its ability to explain such phenomena as governed by the *ab initio* sample preparation conditions that experimentalist can control. Nonetheless, there are two major advantages introduced through mesoscopic frameworks such as these. Firstly, they allow for the direct, detailed observation of local topological traits in a way that is unattainable through existing experimental characterization techniques or continuum models. Secondly, they do so while mitigating much of the computational cost associated with modeling every polymer chain explicitly. Therefore, these methods are inherently more scalable than conventional coarse-grained MD models. Moving forward, the *ab initio* approach of this model may be used both to inversely investigate the micromechanical origins of globally emergent mechanical properties (as was done here) or supplement experimental studies by facilitating predictive design of gels with desired mechanical traits, based on controllable inputs. Nonetheless, this iteration of the model may be improved upon in several ways.

Features such as polydispersity, variability in the local mixing parameter, rate-dependent effects of solvent transport, and inclusion of reversible bonds are all compatible with this model and may be incorporated in future iterations. For example, the current model assumes a constant Flory parameter despite the demonstrable effects of both temperature and solute concentration on this statistical

value [138], [139], [152], [173], [174], [190], [191]. While treating  $\chi$  as a constant did not affect agreement between the model’s predicted mechanical properties and those of experimental results for gels in theta solvent, solute-solvent interactions may play a more potent effect on the damage mechanics of gels in poor solvent or containing local pockets of effectively poor solvent quality. In such systems, we hypothesize that clustering of polymer chains may reduce their conformational degrees of freedom, thereby increasing their stored free energy and reducing the effective crosslink separation or network stretch at which chains begin to rupture. In gels with dynamic bonds, poor solvent may also increase the effective bond dissociation rate per [65]. In future work, we may incorporate these physics via another layer of the Eulerian mesh that tracks  $\chi$  as a function of solute concentration. However, this addition is contingent on *a priori* knowledge of the  $\chi - \phi$  relationship, which likely requires further molecular-scale investigation.

Another pertinent effect to consider is dissipation due to entanglement. Entanglements are ubiquitously hypothesized to play a part in the viscoelastic response of gels, particularly gels with high polydispersity (e.g., poly(acrylamide)) or chain length [192]. Researchers such as [193] have previously introduced coarse-grained models in which entanglements are captured as slip links through which the passage of polymer depends on the entropic tension and density gradients of the chains on either side. Notably, this introduces sliding friction and dissipation that likely depend on the modes of entanglement. Yet, it remains unclear how to quantify the types and relative fractions of said modes experimentally. Therefore – inspired by [193] – in future work we will incorporate slip links into an iteration of this framework to instead model slide-ring gels whose crosslink characteristics (e.g., density and distribution) may be tuned and characterized empirically [194], or

inferred via continuum approaches [195]. More immediately, this iteration of the model will be improved by accounting for rate-dependent poroelastic effects and dynamic bonds. The former will be introduced and mediated by mesh-size-dependent transport of solvent through Darcy’s law and incorporation of viscous drag [196]–[198]. This will allow for investigation of dynamic loading rates and time-dependent swelling inhomogeneity. Rate-dependence is also highly influenced by inclusion of reversible bonds, which imbue networks with viscous response and the ability to relax. In forthcoming work we incorporate reversible, telechelic bonds to investigate and predictively tune the properties of covalently adaptable networks that have potential applications as extracellular scaffolds in osteochondral tissue engineering [13], [199], [200]. For gels containing such reversible bonds, any *a priori* knowledge about initial topology quickly loses significance as the networks reconfigure, particularly during applied loading. Therefore, methods that relate local crosslink distribution to underlying first-order physics are of great importance [201], [202].



## CHAPTER V

### TREADMILLING AND PROTRUSION GROWTH IN FIRE ANT RAFTS

Moving away from purely numerical studies limited to thermally driven systems, this chapter is purposed with introducing the reader to an active system in which the constituents store chemical energy and convert it to mechanical work. The system in question is the rafts formed by the workers of red imported fire ants (*Solenopsis invicta*). Here we illustrate how this active system comprised entirely of ants morphs ceaselessly over hour timescales through the process of treadmilling. We then illustrate and quantify how treadmilling enable the ants to form long, tether-like protrusions that they sometimes use as land bridges for the escape of flooded environments. Finally, we adapt a statistical model of self-propelled particles in confinement, along with a physically motivated edge growth rule to explain factors that lead to the runaway growth of the observed protrusions. However, in doing so, we emphasize the inherent need for discrete approaches (e.g., the network model developed in Chapter I) when exploring the emergent behaviors in systems driven by activity and subject to discrete size effects such as these ant rafts.

#### 5.1 Introduction

Collective emergent behavior is a remarkable and omnipresent feature of living systems that often results in functions like motility of aggregations, self-healing of tissues, and morphing of swarms [4], [5], [203]. Cooperatively behaving living systems are of interest to a wide variety of researchers ranging from biologists [204] and physicists [205] to engineers [206] and roboticists [17], because they elucidate the local-to-global relationship in complex ecologies or physical systems, and may inspire

a broad class of functional metamaterials that adapt their mechanical properties or autonomously self-assemble. One category of organisms, favorably studied for their macroscopic size and ease of observation, is insect aggregations [207], [208], including those of the red imported fire ant (*Solenopsis invicta*). Fire ants condense into buoyant rafts comprised of worker ant bodies when their habitats are flooded. These cohesive swarms are crosslinked by reversible ant-to-ant bonds [209]–[211] which may dissociate from highly stressed states and re-associate into lower energy configurations without sustaining damage. In the last 10 years, researchers have begun to investigate the mechanical properties of these aggregated swarms, which demonstrate nonlinear viscoelastic responses due to the reversibility of their inter-ant bonds [208], [212], [213]. However, another remarkable feature of fire ants that contributes to their complex response is activity [214], [215].

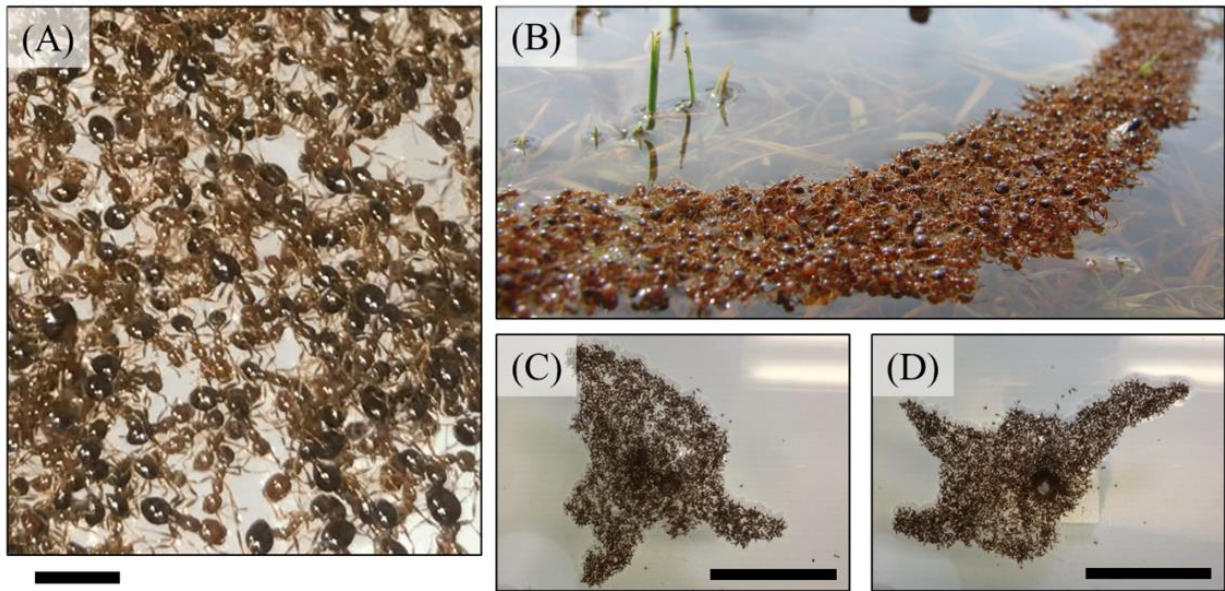


**Figure 5.1. Networked fire ant rafts form dynamic structures.** (A) The floating, structural network of ant rafts is crosslinked by ant-to-ant bonds. The scale bar represents  $1 \ell$  or one average ant body length. (B) Fire ants in nature form rafts that, under various boundary conditions, create tether-like protrusions and bridges. (C-D) A top view of an experimental raft anchored to an acrylic rod is depicted at the (C) start and (D) end of a roughly 60 min duration to illustrate the cyclical protrusion growth that occurs over hour timescales. Scale bars represent  $20 \ell$ .

Individual ants convert chemical energy into mechanical work, including both locomotion and – as with many active systems [216], [217] – active contraction. This activity endows unperturbed fire ants with the ability to dynamically change their raft shapes [218] and even form complex, 3D structures such as towers nucleated about substrates [219]. While the behavior and flow of 3D ant towers has been examined [42], [219], questions remain regarding the long-term dynamics of roughly 2D rafts. Mlot, et al. (2011) reported that upon being placed into the water as roughly 3D spheroids, ant rafts spread out rapidly. Confirming these observations and those of Adams, et al. (2011) we see that ant rafts consists of a bounded network of interconnected structural ants that floats on the water (**Fig. 5.1.A**). On top of this network, a dispersed state of free ants walks freely. Mlot, et al. studied initial raft expansion over short timescales (up to 200 s) experimentally [210], and intermediate timescales (up to  $10^3$  s) numerically [218] and reported that free ants walk on the surface of the structural raft until they encounter the edge at which point they either bank off said edge, pause, or deposit into the structural layer. This deposition of free ants into the structural network drives outwards raft expansion [210], [218]. However, here we observe over longer timescales ( $> 10^3$  s) that ant rafts under specific boundary conditions undergo cyclical and sustained dynamic shape changes including the formation of 2D tether-like instabilities that protrude from the rafts' edges (**Fig. 5.1.B**). These protrusions have, to our knowledge, neither been documented nor explained in existing literature. Edge deposition, alone, cannot explain the initiation, growth, and complete reclamation of protrusions observed (**Fig. 5.1.C-D**). Without any cyclic mechanism(s) of turnover or dynamic properties in the structural network itself, one would expect the shape of the raft to become static once the population of free ants is exhausted. That this is not the case implies either

the population of free ants is replenished, the structural network morphs, or some combination of both.

Indeed, here we report that the structural networks of ant rafts anchored to vertical rods contract in a process that counteracts edge deposition-driven expansion. Furthermore, this contraction occurs simultaneously with the exiting of some ants from the structural layer, which replenishes the population of free ants. These competing mechanisms balance rafts into a pseudo-steady state of torus-like treadmilling that vaguely resembles the phenomena observed in cytoskeletal systems of actin filaments [220]. As in the case of cytoskeletal systems [221], this treadmilling leads to the cyclical turnover of constituents that facilitates sustained shape change, which in ant rafts includes cycles of unstable protrusion growth. In the remainder of this work, we detail our experimental and data-processing methods. We then report on the dynamic properties of both free and structural ants, including the rates of transition between these respective states. Finally, we examine the local properties of self-propelled free ants on protrusions to reveal that directed motion occurs in these strongly confined regions. Employing a model for strongly confined self-propelled particles (SPPs), we interpret that both density gradients along the rafts' edges and confinement-induced directed motion of ants on protrusions likely contribute to the runaway growth of instabilities.

## **5.2 Methods**

### **5.2.1 Experimental design**

To conduct experiments, we collected anywhere from 3 to 10 *g* of worker ants (or roughly 3,000 to 10,000 ants) and placed them into a container of water where they

enveloped and nucleated to a stationary acrylic rod protruding vertically from the waterline. Both  $\varnothing 6\text{ mm}$  and  $\varnothing 16\text{ mm}$  rods were tested with and without talcum powder coating to prohibit climbing. The degree to which rods protruded from the water's surface was varied from  $< 1$  to  $15\text{ cm}$ . Treadmilling and instabilities were observed under all boundary conditions over the span of several hours until many of the free ants became inactive and clustered near the rod. In the scope of this work, sampling was performed sufficiently far from the rod so that inactive free ants were not characterized since they did not contribute to raft dynamics. Additionally, sampling was only conducted while enough ants remained active to sustain relatively steady raft dynamics. To mitigate potential temperature effects on activity, air temperature in the room was maintained between  $20^\circ$  and  $24^\circ\text{ C}$ . The water temperature was monitored and remained between  $17.9^\circ$  and  $19.0^\circ\text{ C}$ . Cameras were positioned above the rafts to capture footage. Time-lapse footage, captured throughout the entirety of select experiments, was used to characterize structural ants and raft dynamics. Real-time footage, captured every 10 minutes throughout the duration of the experiments (to ensure representative temporal sampling), was used to characterize free ants. Reference length scales were placed horizontally in the frame, at the water line. Footage was imported into and processed using ImageJ [222]–[224]. Data post-processing was achieved using MATLAB 2019b [225].

### 5.2.2 Planar density

Planar density of the structural ants comprising the floating layer of the raft ( $\rho_r$ ) was estimated by counting the number of structural ants residing within regions of known area. Planar density of free ants that walk on top of the raft was difficult to measure due to heterogeneity and clustering. The mean packing fraction of free ants ( $\bar{\phi}$ ) was

estimated according to  $\bar{\phi} = (N_{tot} - A\rho_r)/A\rho_r$ , where  $N_{tot}$  is the total number of ants,  $A$  is the total raft area, and  $A\rho_r$  is the number of structural ants given that  $\rho_r$  is conserved (**Fig. D.1**).  $\bar{\phi}$  varied greatly due to the accumulation of inactive free ants near the rod at long timescales. However, it is freely active ants which contribute to raft dynamics. Therefore, the local packing fraction,  $\phi$ , was also estimated by manually counting the number free ants in images of regions far from the rods, with sufficient visual contrast. Free ants were distinguished from structural ants by toggling between these images and their adjacent frames to identify which ants were active.

### 5.2.3 Free ant trajectories

Free ants were image-tracked using ImageJ's manual image tracking plugin. To prevent selection bias, footage was partitioned into regions of interest wherein the petiole of every free ant that entered the region was tracked frame-to-frame. Free ant position data,  $\mathbf{x}_i(t)$ , were used to compute velocities ( $\mathbf{v}$ ), mean speed ( $v_0$ ) (**Fig. D.2**), mean square displacement ( $\langle x^2 \rangle$ ) (**Fig. D.3.E-F**), and the local normalized order parameter ( $|\phi|$ ) (**Fig. 5.2.F**) according to:

$$\mathbf{v}_i = [\mathbf{x}_i(t + \Delta t) - \mathbf{x}_i(t)]/\Delta t, \quad (5.1)$$

$$v_0 = \langle |\mathbf{v}_i| \rangle_N, \quad (5.2)$$

$$\langle x^2 \rangle = \langle |\mathbf{x}_i(t + \tau) - \mathbf{x}_i(t)|^2 \rangle_N, \quad (5.3)$$

and,

$$|\phi| = |\langle \mathbf{v}_i(t) \rangle_N / \langle |\mathbf{v}_i(t)| \rangle_N|, \quad (5.4)$$

respectively. Here the index  $i$  denotes a single ant,  $\Delta t$  is the time between frames,  $\tau$  is a time interval that can span multiple frames, and  $\langle \rangle_N$  denotes ensemble-averaging over all  $N$  ants.  $|\phi|$  was measured in successively smaller domains of square

dimension  $L$  to determine the length scale over which order occurred ( $|\varphi| = 1$  and  $|\varphi| \rightarrow 0$  for aligned and random motion, respectively [226]). Regions containing only one ant (where  $\varphi = 1$  by default) were excluded. Persistence length ( $l_p$ ), defined as the travel distance ( $l_c$ ) at which correlation in an ant's trajectory is lost with itself, was also estimated according to [227]:

$$\langle \hat{\mathbf{v}}_{i,0} \cdot \hat{\mathbf{v}}_{i,\tau} \rangle_{N_\tau} = \exp[-l_c/l_p], \quad (5.5)$$

where  $\hat{\mathbf{v}}_{i,\tau} = \mathbf{v}_{i,\tau}/|\mathbf{v}_{i,\tau}|$  is the direction of the  $i^{th}$  ant's travel at time  $\tau$ , and  $\langle \rangle_{N_\tau}$  denotes ensemble averaging over all  $N_\tau$  observations. For ideal trajectories of fixed step size and turning angle,  $\langle \hat{\mathbf{v}}_{i,0} \cdot \hat{\mathbf{v}}_{i,\tau} \rangle_{N_\tau}$  decays exponentially with respect to  $l_c$  [227], hence the form of Eqn. (5.5). Although free ants do not walk ideally, a least-squares regression fit to Eqn. (5.5) provides a rough estimate of  $l_p$  useful for our purposes (see **Fig. D.3.B** for extended data of  $\langle \hat{\mathbf{v}}_{i,0} \cdot \hat{\mathbf{v}}_{i,\tau} \rangle_{N_\tau}$ ). Edge-encountering ants were excluded from sampling.

#### 5.2.4 Structural contraction

We observed that the structural network contracts visibly, with structural ants appearing to flow inwards towards the stationary rod, when viewed in time-lapsed footage at 240-900x speed. To quantify the contractile strain rate of the structural layer, we identified sets of structural ants originally located at the rafts' outermost edge such that the perimeter was traced with a spatial resolution of roughly 2 to 5  $\ell$ . These ants were image-tracked as they flowed inwards due to contraction (**Fig. 5.3.A-B**). The area circumscribed by these ants ( $A_r$ , outlined red in **Fig. 5.2.A-C** and **D.4.A-C**) decayed exponentially in time ( $t$ ) according to:

$$A_r = A_r^0 e^{-2\dot{\epsilon}t}, \quad (5.6)$$

where  $A_r^0$  represents the initial reference area and  $\dot{\epsilon}$  is the linear strain rate assuming isotropic contraction.  $\dot{\epsilon}$  was estimated from the coefficient of the exponential least-squares fit to (5.6). To verify isotropic contraction,  $\dot{\epsilon}$  was also estimated radially with respect to the anchoring rod as the coefficient of the linear least-squares fit to  $\dot{R}(R)$  (*i.e.*,  $\dot{\epsilon} = d\dot{R}/dR$ ), where  $R$  and  $\dot{R}$  are the structural ants' distances from the rod and speeds towards it, respectively.  $\dot{R}$  was computed as  $\mathbf{v} \cdot \hat{\mathbf{R}}$  where  $\mathbf{v}$  was calculated via (5.2) or collected via particle image velocimetry (PIV), and  $\hat{\mathbf{R}}$  is the unit vector directed towards the anchoring rod. PIV was conducted via PIVlab [228], [229] on a continuous region of interest on the largest experimental raft over a 13-minute duration (**Fig. 5.3.D**). Noise due to movement of dispersed free ants on top of the structural layer was easily filtered out since free ants travel on the order of  $1 \ell s^{-1}$ , while structural contraction occurs at the order of  $0.01 \ell s^{-1}$ . Note that the free ant noise was also utilized to qualitatively illustrate the positions and clustering of free ants (**Fig. D.5**). See **Fig. D.6** for extended  $\dot{\epsilon}$  data ( $\dot{\epsilon} > 0$  represents contraction).

#### 5.2.4 Structural exit and edge deposition rates

To quantify raft dynamics, we leveraged image-tracked data of structural ants. Given roughly conserved  $\rho_r$  the rate of structural ant exits into the free layer is:

$$\delta = -2\rho_r\dot{\epsilon}, \quad (5.7)$$

where  $\delta$  is measured as the number exit events per minute per unit raft area. Through (5.7),  $\delta$  is measured in the bulk of the structural network. Since free ants primarily bind to the structural layer at the rafts' perimeter, this measure occurs independently of the effects of edge deposition.



We calculated the edge deposition rate per unit perimeter length ( $\gamma$ ) using the newly deposited growth area ( $A_g$ , shaded cyan in **Fig. 5.2.A-C** and **D.4.A-C**), taken as  $A_g \approx A - A_r$ . Although ants may exit the structural layer in the growth zone, this was not observed to occur frequently at the perimeter amongst the ants that had recently transitioned, and so this estimate of  $A_g$  is relatively unaffected by  $\delta$  if the image-tracked structural ants that define  $A_r$  are periodically updated (so that  $A_g \ll A$ ). The areal growth rate was calculated via  $\dot{A}_g = [A_g(t) - A_g(t - \Delta t)]/\Delta t$ . Given constant  $\rho_r$ ,  $\gamma$  is:

$$\gamma = \dot{A}_g \rho_r / P, \quad (5.8)$$

where  $P$  is the updated raft perimeter. See **Fig D.4.D-F** for extended  $\alpha$  and  $\delta$  data, where  $\alpha = \gamma P / A$  is the edge deposition rate per unit raft area. Note that if  $A$  is normalized by average area of one structural ant ( $\rho_r^{-1}$ ), then  $\alpha$  and  $\delta$  may be thought of as the areal expansion and decay rates, respectively.

### 5.2.5 Instabilities

Instability growth rates ( $V$ ) and widths ( $W$ ) were measured using ImageJ. Since the structural networks perpetually contract (including within protrusions) a pair of reference structural ants near the tip, but on opposite flanks of each protrusion were image-tracked (**Fig. D.7**). The distance between the mean position of these reference ants and the protrusion tip ( $L$ ) was used to calculate  $V = [L(t + \Delta t) - L(t)]/\Delta t$ . Note that local contraction was an order of magnitude smaller than tip growth ( $L\dot{\epsilon} \ll V$ ) while  $L \sim 10 \ell$ .  $W$  was approximated via  $W \approx A_p / L_c$  where  $A_p$  and  $L_c$  are the total protrusion area and length, respectively.

## 5.3 Results

### 5.3.1 Treadmilling

Planar density of the structural network was roughly conserved throughout experiments at  $\rho_r = 0.304 \pm 0.018 \text{ ants mm}^{-2}$ , which is consistent with the value of  $0.34 \pm 0.02 \text{ ants mm}^{-2}$  reported by Mlot et al. (2011) [210]. The mean free ant packing fraction,  $\bar{\phi}$ , as estimated by areal image analysis, was anywhere between 0.56 and 2.6 free ants per structural ant depending on the time of measurement and experiment. Indeed,  $\bar{\phi}$  could exceed unity indicating that ants in the free layer(s) were more numerous than those in the structural layer, consistent with the findings of Mlot, et al. (2011). However, here this was due to local clustering of inactive ants near or on the anchoring rod. These inactive ants did not contribute to the raft dynamics reported here and even when  $\bar{\phi}$  exceeded one, raft dynamics were still observed (**Fig. D.1.C**). Manual measurements confirmed that free ants in regions far from the rod remained relatively dispersed with an average density of  $\rho_s = 0.072 \pm 0.006 \text{ ants mm}^{-2}$ , and a local free ant packing fraction of  $\phi \approx 0.240$  free ants per structural ant. This estimate of  $\phi$  demonstrates that far from the anchoring rod, free ants may exist in a dispersed state, however even within these regions free ant density is heterogeneous, as ants form transient clusters analogous to those arising in self-propelled colloidal suspensions when  $\phi \sim 0.3$  [6]. Regardless of density heterogeneities, we measured that free ants deposit into the edges at an average rate of  $\alpha \approx 0.02 \text{ deposition events min}^{-1}$  per structural ant (or  $\gamma \approx 0.29 \text{ deposition events min}^{-1}$  per unit body length of perimeter). If the raft expanded unchecked this would correspond to areal raft growth on the order of  $\alpha \approx 2\% \text{ min}^{-1}$  until the number of free ants was depleted, and a static raft area was reached. Therefore, this mechanism alone explains neither instability formation, nor the dynamic

treadmilling that recycles these formations over the span of hours. To better understand the full scope of what drives these features, we first examine the transport of free ants.

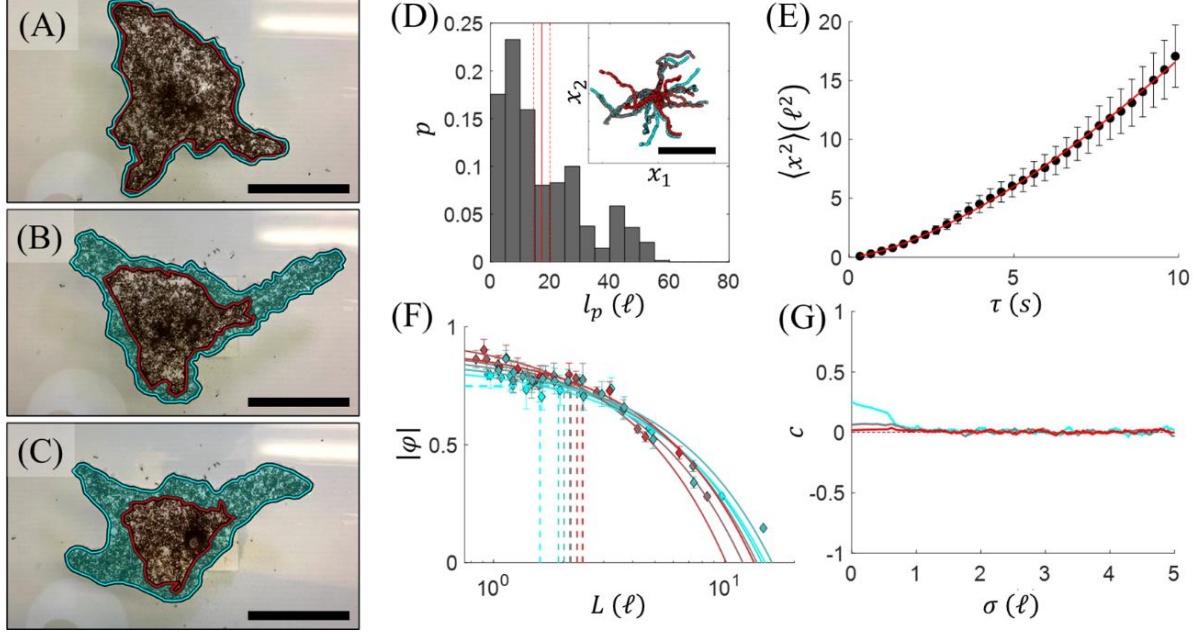


**Figure 5.2. Trajectory analysis of non-edge-encountering surface ants.** (A-C) An ant raft is depicted at the (A) start, (B) middle, and (C) end of a 54-minute duration. The red outline demarks ants that were originally in the edge of the raft at the start of the timespan and the region shaded in cyan highlights newly deposited area. Scale bars represent  $20 \ell$ . (D) The probability distribution of  $l_p$  measured for 105 distinct free ants that traveled a distance of at least  $5 \ell$  is displayed, with the solid and dotted vertical red lines representing the mean value and standard error, respectively ( $l_p = 17.3 \pm 2.7 \ell$ ). The inset displays the end-to-end trajectories of 38 free ants image-tracked over a duration of roughly 30 seconds to visually illustrate isotropic movement. The start of each trajectory has been centered at the origin for visual clarity and the scale bar represents  $10 \ell$ . (E) Mean  $\langle x^2 \rangle$  of all samples is plotted with respect to the time interval of measurement ( $\tau$ ) for free ant trajectories tracked at least 10 s. The red curve represents the least-squares regression fit of the form  $\langle x^2 \rangle = 4D\tau^\xi$ . (F)  $|\phi|$  is plotted with respect to the rectilinear domain size ( $L$ ) in which it was measured for seven samples of ants over four experimental rafts. The dotted lines denote the length scales at which  $|\phi| \geq 0.75$ . (E-F) Error bars represent standard error. (G) The moving average of  $c(\sigma, \tau)$  is plotted with respect to separation distance for  $\tau = 0$  s (cyan),  $\tau = 1$  s (grey), and  $\tau = 10$  s (red). The moving average window was set to  $1 \ell$  to reduce noise for transparency.

Previous studies modeled free ants as Brownian particles that deposit into the structural layer with constant probability upon every edge encounter, leading to isotropic raft expansion [218]. In actuality, the motion of freely active ants is not

ambiently driven, rather free ants are SPPs that actively locomote. Therefore, we characterize their trajectories in the context of Active Brownian Particles. First, we confirm that free ants that do not encounter the raft edges walk isotropically [210] (**Fig. 5.2.D**) with  $l_p$  on the order of  $\sim 20 \ell$  and  $v_0 = 0.59 \pm 0.01 \ell s^{-1}$ , suggesting a correlation time ( $\tau_r = l_p/v_0$ ) on the order of  $\sim 34 s$  [230]. Although our approximation of  $l_p$  affirms that free ants can sustain self-correlated trajectories over the order of  $10 \ell$ , our methods of estimating  $l_p$  are extrapolatory and assume that self-correlation decays exponentially. To better characterize ants' trajectories, we also examine mean square displacement,  $\langle x^2 \rangle$ . We find that surface ants have an average measured diffusion coefficient ( $\bar{D}$ ) in the range of  $0.01 \ell^2 s^{-1}$  to  $0.16 \ell^2 s^{-1}$  ( $0.1 \times 10^{-6}$  to  $1.3 \times 10^{-6} m^2 s^{-1}$ ) depending on the experiment and sample, placing the order of free ants' diffusivity near that of gaseous particles. Significantly, the ants do not diffuse randomly as previously modeled [210], [218]. Instead, they diffuse anomalously according to a power law  $\langle x^2 \rangle = 4D\tau^\xi$ , where the average scaling coefficient is  $\bar{\xi} \approx 1.48$ , indicating super-diffusive behavior ( $\xi > 1$ ) [231] (**Fig. 5.2.E**). Worth noting though is that  $\bar{D}$  appears to vary in both time and space for a given trajectory (hence the wide range reported here) and ants undergo interstitial periods of super and sub-diffusive behavior ( $\xi < 1$ ) (see **Fig. D.3.C**), comparable to those which occur in the “run-and-tumble” motion of swimming bacteria [232] and plankton [233], or the Lévy walks of foraging spider monkeys [234]. Such anomalous diffusion is common amongst motile organisms whose trajectories are influenced by both internal decisions and external stimuli. In fire ants sub-diffusive zones are likely caused by factors such as clustering due to volume exclusion between ants (*i.e.*, the inability of two ants to occupy the same space) [230]. Regardless, the prevailing behavior is that of super-diffusivity [235], [236]. Super-diffusivity is not inherent to SPPs, rather it is generally indicative of field or current-induced drift [236]–[238]. In this case it is

plausible that local fluxes of synchronously moving ants emerge over some length scale due to ant-to-ant (i.e., local) or ant-to-raft edge (i.e., confinement) interactions providing early evidence that ants exhibit some degree of directed motion.

To evaluate the degree and length scale over which order in ant trajectories exists, we examine  $|\varphi|$  within successively smaller square domains of length  $L$  (**Fig. 5.2.F**). Across seven different sets of free ants,  $|\varphi|$  scales linearly with respect to  $L^{-1}$ . Between these samples, the length scale over which strongly ordered trajectories emerge ( $|\varphi| \geq 0.75$ ) ranges from roughly  $L \leq 1.5$  to  $2.4 \ell$ . While some degree of synchronized motion exists within domains on the order of one to two ant body lengths, it is evident that free ants on the bulk of rafts generally move isotropically above the length scale of a single ant. To further identify whether there exists any trajectory correlation between two neighboring free ants (designated by indices  $i$  and  $j$ ), and whether this correlation persists in time, we also examine the pair-wise directional correlation between their velocities (separated by time span  $\tau$ ), according to:

$$c(\sigma, \tau) = \langle \hat{\mathbf{v}}_i(t) \cdot \hat{\mathbf{v}}_j(t + \tau) \rangle, \quad (5.9)$$

where  $c \rightarrow 1$  indicates strong correlation (**Fig. 5.2.G**),  $c \approx 0$  suggests no correlation, and  $c < 0$  indicates negative correlation or that the ants are walking in opposite directions. Here,  $\mathbf{v}_i(t)$  and  $\mathbf{v}_j(t + \tau)$ , are the velocities ( $\mathbf{v} = \partial \mathbf{x} / \partial t$ ) of ant  $i$  (at time  $t$ ) and ant  $j$  (at time  $t + \tau$ ), respectively, and  $\sigma$  is their ant-to-ant separation distance defined by  $\sigma = |\mathbf{x}_i(t) - \mathbf{x}_j(t + \tau)|$ . Delay in directional correlation is commonly used to identify leaders and followers in systems with established pairwise alignment interactions, but here  $c(\sigma, \tau)$  is used to identify the length and time scales above which ants lose mutual alignment of motion [203]. Examining the spatial moving average of  $c(\sigma, \tau)$  (over a window of  $1 \ell$  to reduce noise), there appears to be no significant correlation above a length scale of  $\sim 1 \ell$ , regardless of  $\tau$ . Also, for timespans of  $\tau \geq 1$  s,

there appears to be no correlation in direction of ants. Therefore, the only spatiotemporal separation for which any directional correlation occurs is  $\sigma < 0.75 \ell$  and  $\tau < 1 \text{ s}$ , suggesting that correlated movement only occurs between ants in (or nearly in) contact, and even then, it is weak with ( $c < 0.5$ ). The lack of correlation for  $\sigma > 1 \ell$ , despite ants' relatively long  $l_p$ , suggests that ants, experience no significant pairwise alignment interactions. Despite the lack of evidence for alignment interactions, we see later in this work (through measurement of  $c(\sigma, \tau)$  for free ants on protrusions) how directional motion occurs in highly confined regions (wherein the dimensions of the raft are smaller than the free ants' persistence lengths), likely contributing to the runaway growth of protrusions; however, first we examine the remaining scope of mechanisms that contribute to the treadmilling dynamics which permit sustainable shape evolution. Simply reexamining **Fig. 5.2.A-C**, it is immediately clear that the area circumscribed by the set of ants outlined in red depreciates in time, indicating that some contractile mechanism occurs within these systems.

Although ant rafts' structural networks may appear to be amorphous solids at first glance, examination of time-lapsed footage reveals that these networks flow visibly. Specifically, the structural network robustly contracts throughout the bulk at rate  $\dot{\epsilon}$ . Given the fixed rod in the experimental setup, this causes visible raft contraction towards said rod in time.  $\dot{\epsilon} \approx 1.75 \% \text{ min}^{-1}$  ( $R^2 = 1.00$ ) as estimated from the areal decay rate through (5.7) (**Fig. 5.3.C**). The radial contractile strain rate was calculated as  $\dot{\epsilon} = 1.82 \pm 0.03 \% \text{ min}^{-1}$  from manually image-tracked data (**Fig. 5.3.A-B,E**), and  $\dot{\epsilon} = 1.75 \pm 0.01 \% \text{ min}^{-1}$  ( $R^2 = 0.97$ ) from PIV-gotten data (**Fig. 5.3.D-E**). The former value is within 2 % of  $\dot{\epsilon}$  coarsely estimated through (5.6), while the latter value agrees with it, which suggests that the circumferential component of contraction must also

be on the order of  $1.8 \% \text{ min}^{-1}$  and that there is no significant directional bias in contraction. Notably, measured values of  $\dot{\epsilon}$  correspond to maximum contractile speeds on the order of just  $0.01 \ell \text{ s}^{-1}$ , while free ants on top of the structural layer walk with speeds on the order of  $1 \ell \text{ s}^{-1}$ . Therefore, structural contraction has negligible effect on the previously reported trajectories of free ants.

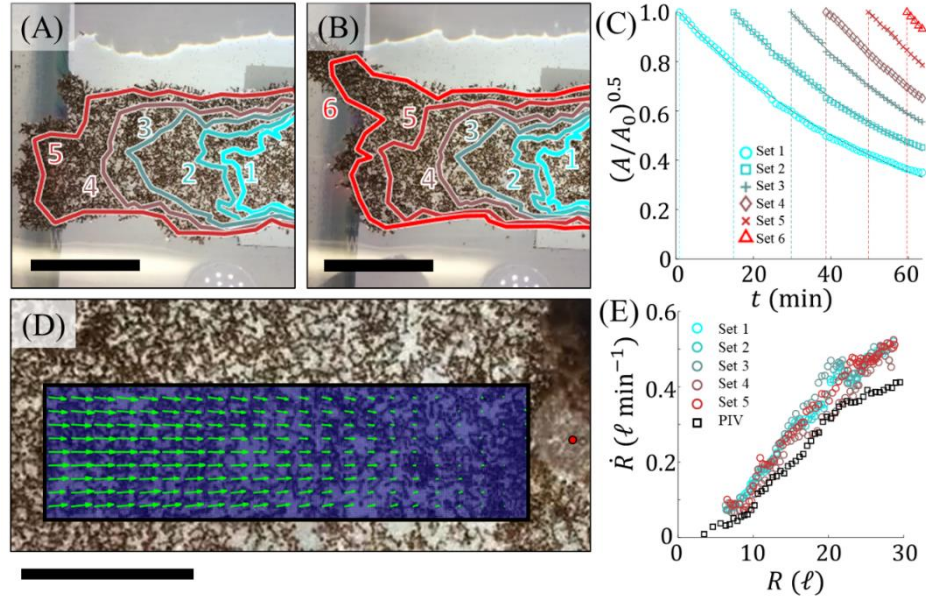


**Figure 5.3. Quantifying structural retraction.** (A-B) A top view of an experimental raft is illustrated at the (A) start and (B) end of a roughly 8 min duration. The perimeter is traced every 15 minutes and outlined by numbered, colored contours (1 represents the oldest set of ants and 6 represents the newest). The scale bars represent  $20 \ell$ . (C) The square root of the ratio  $A/A_0$  is plotted with respect to time and used to estimate  $\dot{\epsilon}$  according to  $(A/A_0)^{0.5} = e^{-\dot{\epsilon}t}$ . The data from each of six separately tracked sets of ants are shown, with the vertical dotted lines denoting the time at which image tracking began.  $\dot{\epsilon}$  is estimated to be  $1.7$  to  $1.8 \% \text{ min}^{-1}$  ( $R^2 = 1.00$ ) for all six data sets, indicating that strain rate is roughly conserved in time. (D) The velocity field obtained from PIV is shown within the region of interest. To eliminate noise due to raft spin, only the radial component of the velocity (*i.e.*, that vectored towards the anchor point of the raft denoted by a red dot) is shown. The field depicted is averaged over the full analysis duration (roughly 13 min) to reduce temporal noise. The scale bar represents  $10 \ell$ . (E)  $\dot{R}$  from manual image tracking (circles in a cyan-to-red color gradient) and PIV (black squares) is plotted with respect to  $R$ . Data from manual tracking represents the contractile speed of every ant sampled (*i.e.*, the full image tracked edge). Data from PIV is presented from every point measured in the region of interest.

There exists no significant correlation between  $\dot{\epsilon}$  and distance from the rod,  $R$  (**Fig. D.6.A-C**) implying that  $\dot{\epsilon}$  is constant throughout the bulk. That contraction is both

spatially constant and roughly isotropic indicates that the primary mechanism of contraction originates within the bulk structural network as opposed to entirely at a specific interface (e.g., the junction between the raft and the rod). Interestingly, despite contraction structural density,  $\rho_r$  was roughly conserved throughout experiments, mandating that there exists a flux of ants out of the structural layer. Upon closer examination, we indeed observed instances of ants bound to the raft network exiting and becoming part of the free layer. We quantified the exit rate,  $\delta$ , through (5.7) to find that across experiments, ants unparked at a rate of  $\delta \approx 2 - 3\% \text{ min}^{-1}$ , counteracting and nearly balancing the global expansion rate  $\alpha \approx 2\% \text{ min}^{-1}$  measured earlier.

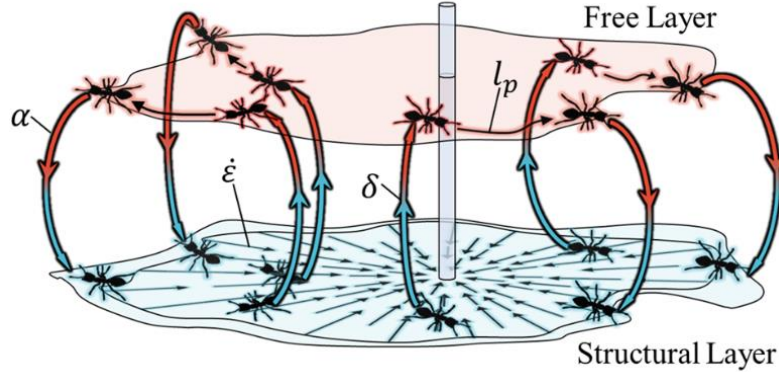


**Figure 5.4. Treadmilling of fire ant rafts.** Contraction of the structural layer (at rate  $\dot{\epsilon}$ ) perpetually pulls ants in the structural network (blue) inwards given the anchored boundary condition. Structural ants exit from the network at a rate of  $\delta$  in the bulk and become part of the free layer of ants (red). Free ants walk directly on top of the structural network until they encounter the perimeter of the raft. Edge-encountering ants either bank off the edge of the raft or deposit into the structural network at its perimeter at a rate of  $\alpha$ . Note that free ants (denoted by the red layer) have been vertically offset from the structural ants (of the blue layer) purely for visual clarity, but these two layers maintain direct contact in ant rafts.

Global raft expansion (due to edge-deposition of free ants into the structural layer) and structural contraction (concurrent with bulk dislocation of structural ants into the free layer) define the global treadmilling illustrated schematically in **Fig. 5.4**. This treadmilling sustains ant rafts' ability to change their shape by recycling the



populations of both structural and free ants, thus also permitting the recurring formation (*i.e.*, initiation, growth, and complete retraction) of instabilities. However, the detailed causes of unstable protrusion growth remain unclear. To unveil these mechanisms, we revisit the properties of freely active ants.

### 5.3.2 Instabilities

Before examining the contributing factors to protrusion formation, we first quantified their characteristic growth rates and widths. Protrusions grow at an average rate of  $\langle V \rangle = 0.74 \pm 0.05 \ell \text{ min}^{-1}$  with an average width of  $\langle W \rangle = 5.85 \pm 0.06 \ell$  (**Fig. 5.5.A-B**) suggesting that the areal tip growth rate per unit edge length is on the order of  $\langle V \rangle \langle W \rangle = 4.33 \pm 0.08 \ell^2 \text{ min}^{-1}$  (or  $11 \text{ ants min}^{-1}$ ) given that  $\rho_r \approx 0.3 \text{ ants mm}^{-2}$ . Normalizing this value by the approximate width of the leading tip (taken as  $\langle W \rangle$ ) we see that the average tip growth rate is roughly  $\gamma_{tip} \approx 1.9 \text{ min}^{-1} \ell^{-1}$ , which is an order of magnitude higher than that of the overall raft ( $\gamma \approx 0.29 \text{ min}^{-1} \ell^{-1}$ ). This disproportionate growth rate could either be due to a higher flux of free ants to the tips of protrusions, a higher probability of free ant deposition into the structural network at these locations, or both. Whether the probability of edge deposition varies by location is difficult to measure directly for two reasons. Firstly, defining the length scale over which an ant detects the edge is not easily quantified, and so precisely recognizing edge encounters is exceedingly difficult. Secondly, edge accumulation effects [239] induce clustering of free ants near the edges (see **Fig. 5.5.H** and **Fig. D.5**) to the extent that they become visually indistinguishable from one another in these regions and image-tracking is implausible. However, characterization of free ants on the bulk of protrusions far from their tips proved feasible.

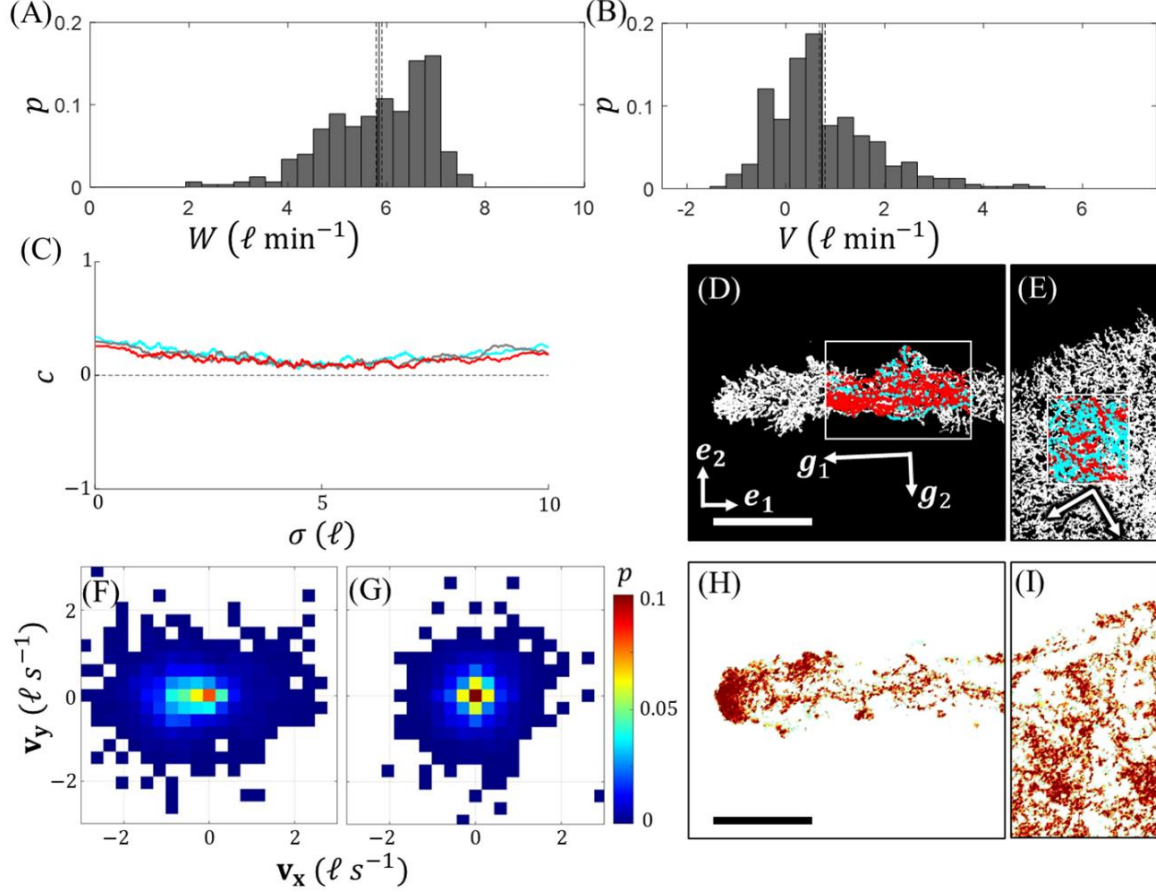


**Figure 5.5. Characterizing protrusion growth and directional motion.** (A) The distribution of 326 observations of  $W$ . (B) The distribution of 406 frame-to-frame observations of  $V$ . (A-B) Observations were taken over 13 distinct sample protrusions.  $\langle W \rangle$  and  $\langle V \rangle$  are represented by vertical lines with the dotted lines representing standard error. (C) The moving average of  $c(\sigma, \tau)$  is plotted with respect to separation distance for  $\tau = 0$  s (cyan),  $\tau = 1$  s (grey), and  $\tau = 10$  s (red). The moving average window was set to  $1 \ell$  to reduce noise for transparency. (D-E) All ant trajectories within domains (D) on and (E) off a protrusion were manually image tracked. Ants moving left and right were overlaid with red and cyan dots, respectively, to emphasize any net flux during this time span. The principal directions (eigenvectors) of  $g^v$  are shown as arrows labeled  $g_1$  and  $g_2$ , respectively. (F-G) 2D velocity probability ( $p$ ) distributions of free ants tracked in domains (F) on and (G) off a protrusion are displayed. (H-I) Visually isolated free ants (red) (H) on and (I) off a protrusion illustrate the degree and location of clustering. All scale bars represent  $10 \ell$ .

We discovered that free ants on protrusions display a high degree of directed motion as characterized by  $c(\sigma, \tau)$  from (3.1) (**Fig 5.5.C**). In fact, on protrusions, ants separated by more than  $10 \ell$  exhibit statistically the same directional correlation ( $c \sim 0.1 - 0.2$ ) as ants within the contact length scale. The mean value of  $c(\sigma, \tau)$  across all  $\sigma$  when  $\tau = 0$  s is  $0.170 \pm 0.003$ , which suggests that the ants are walking on average

with a nominal separation angle of roughly  $80^\circ$ . While this may seem like a large angular difference, it suggests that ants are walking on average within the same quadrant of directional orientation, indicating a net flux of ants in some direction. To confirm and identify the direction of flux we examine a multitude of measures for free ants on a protrusion whose longitudinal axis is aligned with the first principal direction of analysis,  $\mathbf{e}_1$ . Firstly, we examine the metric tensor of ant velocity defined by  $\mathbf{g}^v = \langle \hat{\mathbf{v}} \otimes \hat{\mathbf{v}} \rangle_N$  where  $\hat{\mathbf{v}}$  represents the direction of motion of a single ant,  $\otimes$  denotes the tensor product, and the operator  $\langle \rangle_N$  denotes averaging over the sample size,  $N$ . This tensor is represented by a symmetric, positive definite matrix, whose principal directions, here denoted  $\mathbf{g}_1$  and  $\mathbf{g}_2$ , indicate the directions in which ant traffic is a maximum and minimum (**Fig. 5D**). Thus, isotropic traffic is represented by the principal matrix  $\mathbf{g}^v = \text{diag}(0.5, 0.5)$ , while strongly directional traffic will be represented by eigenvalues with distinct values. Examining  $\mathbf{g}^v$  in the reference coordinate axes  $\{\mathbf{e}_1, \mathbf{e}_2\}$ , indeed we find that  $g_{11}^v = 0.66$  while  $g_{22}^v = 0.34$ , indicating that the ants are traveling faster in the direction  $\mathbf{e}_1$  (which aligns with the longitudinal axis of the protrusion) than the direction  $\mathbf{e}_2$ . We also find that  $g_{12}^v = g_{21}^v = 0.01$ , suggesting that the longitudinal axis is close to free ants' principally fastest direction (with the principal components of  $\mathbf{g}^v$  displayed in **Fig. 5D** to illustrate alignment). For further visual transparency, both the 2D velocity distribution and isolated traffic of surface ants are presented in **Fig. 5.5.F** and **Fig. 5.5.H**, respectively. Examining the 2D velocity distribution, the maximum longitudinal component exceeds that of the transverse component. Observing **Fig. 5.5.H**, the ants on the protrusion generally move longitudinally, with little transverse motion. For comparison, the metric tensor, velocity distribution and visually isolated free ant traffic far from the raft edge are depicted in **Fig. 5.5.E**, **Fig. 5.5.G** and **Fig.**

**5.5.I**, respectively and reaffirm that free ants in weak confinement move randomly ( $g_{11}^v \approx g_{22}^v \approx 0.5$ ).

Although  $\mathbf{g}^v$  indicates that free ants move primarily in-line with protrusions, it reveals nothing about the sense of this movement. To identify the direction of this bias, we examine the 2D velocity distribution (**Fig. 5.5.F**) and observe a slightly higher probability of ants moving towards the tip than the base at speeds up to  $1 \ell \text{ s}^{-1}$  (*i.e.*, the distribution is skewed slightly left). To emphasize this flux illustratively, **Fig. 5.5.D** includes red and cyan points wherever an ant was recorded moving left ( $\hat{v}_1 < 0$ ) or right ( $\hat{v}_1 > 0$ ), respectively. Both the velocity distribution and binary plot from **Fig. 5.5.D** indicate that within the recorded timeframe, more ants moved from the base-to-tip of the protrusion. We hypothesize that both local tip clustering (**Fig. 5.5.H**) and directional motion (**Fig. 5.5.C**, **5.5.D** and **5.5.F**) of free ants on protrusions contribute to their unstable growth. To interpret experimental observations we employ a simple model for SPPs under strong confinement, introduced by Fily, et al. (2014) [240]. This model prescribes that the SPPs move with some overdamped velocity and a rotational diffusion rate synonymous with  $v_0$  and  $\tau_r^{-1}$ , respectively. “Strong confinement” mandates that  $l_p$  of SPPs must be larger than their confining dimensions, which is satisfied by fact that the mean persistence length of free ants is roughly three times greater than the average width of protrusions ( $l_p \sim 20 \ell > \langle W \rangle \sim 6 \ell$ ) [240], [241], and roughly 83% of measured ants have persistence lengths greater than  $\langle W \rangle$  (**Fig. 5.2.D**). In purely convex domains the model predicts that SPPs glide along their confining boundaries and accumulate at regions of high local curvature [240], [241].

We implement Fily's model into a numerical framework in which half of an elliptically shaped protrusion (with a minor-axis of  $2.5 \ell$  and major-axis of  $5 \ell$ ) is initiated. According to Fily's model, given the entirely convex domain and assuming a quasistatic state, the local density of free ants per unit edge length may be estimated by  $\rho_s = \kappa/2\pi$ , where  $\kappa = \partial\psi/\partial s$  is the local edge curvature,  $\psi$  is the orientation of the local edge normal ( $\hat{\mathbf{n}}$ ), and  $s$  denotes curvature space along the boundary [240], [241] (**Fig. 5.6.A**). We impose that the local rate of directional edge deposition,  $\boldsymbol{\gamma}(s)$ , scales linearly with the local free ant density  $\rho_s$ , according to:

$$\boldsymbol{\gamma} = \left( a \frac{\rho_s}{\rho_0} + \gamma_0 \right) \hat{\boldsymbol{\gamma}} \quad (5.10)$$

where  $a/\rho_0$  defines the deposition rate's sensitivity to  $\rho_s$ ,  $\rho_0$  is a sensitivity parameter (in units of  $\ell^{-1}$ ),  $a = v_0/\ell^2$  is a normalization constant (in units of  $\text{min}^{-1} \ell^{-1}$ ),  $\gamma_0$  is the nominal global deposition rate (also in units of  $\text{min}^{-1} \ell^{-1}$ ), and  $\hat{\boldsymbol{\gamma}}$  is the direction of edge deposition. Increasing  $\rho_0$  decreases the effects of  $\rho_s$  on  $\boldsymbol{\gamma}$ , and increasing  $\gamma_0$  increases the overall edge deposition rate. We posit that  $\hat{\boldsymbol{\gamma}}$  has components aligned with both  $\hat{\mathbf{n}}$  and some directional bias ( $\hat{\boldsymbol{\phi}}$ ) such that (5.10) becomes::

$$\boldsymbol{\gamma} = \left[ \frac{v_0}{\ell^2} \left( \frac{\rho_s}{\rho_0} \right) + \gamma_0 \right] \frac{\hat{\mathbf{n}} + \beta \hat{\boldsymbol{\phi}}}{|\hat{\mathbf{n}} + \beta \hat{\boldsymbol{\phi}}|}, \quad (5.11)$$

where  $\boldsymbol{\gamma}$  is computed in units of deposition events per minute per unit edge length ( $\text{min}^{-1} \ell^{-1}$ ).  $\beta$  is a weighting parameter that determines the extent of directional bias in edge deposition. Without bias ( $\beta = 0$ ) deposition occurs normal to the edge, while high bias ( $\beta \gg 0$ ) skews this deposition in the direction of  $\hat{\boldsymbol{\phi}}$ . Inclusion of  $\hat{\boldsymbol{\phi}}$  was initially motivated by the observed directional motion of free ants on protrusions and was set accordingly (flux of free ants occurs from base-to-tip such that  $\hat{\boldsymbol{\phi}} = [0,1]$ ).  $\gamma_0$  was set to  $0.29 \text{ min}^{-1} \ell^{-1}$  based on experiments. Reasonable comparison with areal experimental growth rates was coarsely achieved when  $\rho_0 = 0.9 \ell^{-1}$  (see **Table D.1** for a summary of parameter values). The boundary mesh was stepped in time according to  $\boldsymbol{\gamma} = \rho_r d\mathbf{x}/dt$  using the forward Euler method. Note that since the

observed speed of free ants ( $v_0 \sim 1 \ell s^{-1}$ ) is two orders greater than that of protrusion growth ( $\langle V \rangle \sim 0.02 \ell s^{-1}$ ), we posit that the steady state assumption employed by Fily, *et al.* (2014) remains viable.

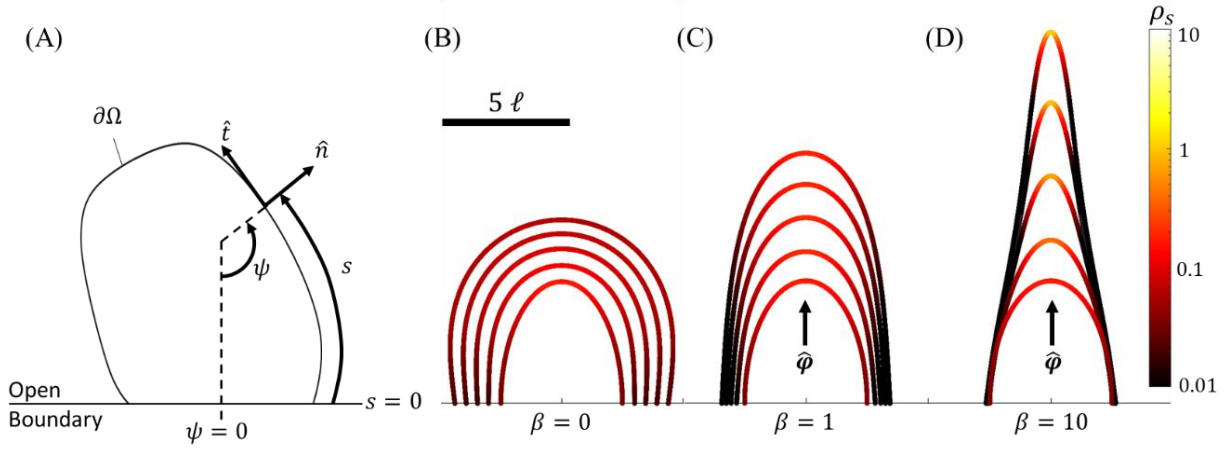


**Figure 5.6. Numerical model results.** (A) A schematic illustrates an arbitrary, convex boundary,  $\partial\Omega$ .  $\psi$ ,  $s$ ,  $\hat{n}$  and  $\hat{t}$  are all denoted at an arbitrary point along  $\partial\Omega$  to convey sign convention. (B-D) The numerical mesh is displayed from  $t = 0 s$  (innermost curves) to  $480 s$  (outermost curves) in  $120 s$  intervals for the cases of (B)  $\beta = 0$ , (C)  $\beta = 1$ , and (D)  $\beta = 10$ . The color scale represents  $\rho_s$  ( $\ell^{-1}$ ). The scale bar represents  $5 \ell$ .

In the absence of biased edge deposition (**Fig. 5.6.B**,  $\beta = 0$ ) this model does not produce the type of protrusion growth observed for fire ants, instead predicting exaggerated outwards growth with relatively diminished tip growth ( $\dot{L} < 0.5 \ell min^{-1}$ ) and edge curvature ( $\kappa < 0.5 \ell^{-1}$ ). This suggests that tip-clustering alone does not fully explain the runaway protrusion growth observed experimentally. We found that as bias increases,  $\dot{L}$  and  $\kappa$  also increase with reasonable comparison to experiments occurring at  $\beta = 1$  ( $\dot{L} \sim 1 \ell min^{-1}$  and  $\kappa \sim 1 \ell^{-1}$ ) (**Fig. 5.6.C**). As bias is increased further (*e.g.*, **Fig 5.6.D**,  $\beta = 10$ ),  $\kappa$  eventually exceeds  $1 \ell^{-1}$  implying that the tip is less than two ants wide, which was never observed experimentally, indicating an upper limit to any biasing effects. While  $\hat{\phi}$  was initially inspired by directional motion, this model cannot specifically affirm directional motion as a first order cause

of runaway growth. Rather, it simply reveals that a bias in edge deposition, whatever its cause, significantly improves agreement.

#### **5.4 Discussion and concluding remarks**

Our experimental results reveal that dynamic shape and area changes of fire ant rafts are sustained by competing mechanisms of structural contraction and outwards expansion, which together define global treadmilling. The structural network's planar density is conserved (despite contraction and any consequential areal change) due to a flux of structural ants into the freely active surface layer. Counteracting this flux is the deposition of free ants primarily into the edge of the structural layer, driving outwards expansion. That the rate of contraction slightly exceeds the rate of expansion is reflected in the eventual shrinking of overall raft areas observed after several hours due to accumulation of free, yet inactive ants near the anchoring rod, which slowed edge deposition. Perhaps this less active state relates to the activity cycles observed in confined, 3D aggregations of fire ants [214], [215]. Ant raft evolution over longer timescales and in the context of activity may be worth examining in future work. Additionally, further consideration is warranted regarding the effects of boundary conditions on the treadmilling and instabilities observed. It remains unclear, what influences, if any, the vertical rod and the height it protrudes above the water have on either of these behaviors, and a systematic sweep of this height must be conducted in order to attribute any causal relationships with raft dynamics. Furthermore, variables that may influence behavior, such as season, the locations of ant collection, and the time of day were not considered in the scope of this study. As such, a control study may be conducted in future work to evaluate the robustness of raft dynamics under various conditions. However, here we simply

report the ant properties, treadmilling dynamics, and instability characteristics as observed under the boundary conditions specified.

Similar looking finger-like instabilities (e.g., Rayleigh-Taylor [242], Kelvin-Helmholtz, Saffman-Taylor [243], etc.) are regularly observed at fluid interfaces, due to local property gradients (e.g., fluid density, viscosity, etc.). Although these phenomena look like fire ant protrusions, ant aggregations are distinct in several ways. Firstly, they exist as a multistate system whose outwards expansion is driven by transport of a dispersed surface layer of free ants, as opposed to diffusion of particles through a homogenous bulk. Secondly, the dispersed layer is comprised of SPPs as opposed to thermally diffusing constituents. Finally, the size of individual fire ants is comparable to the size of the instabilities they form, rendering the system far from the continuum limit and introducing potential discrete size effects. Given the first two considerations, this system is perhaps better compared to other systems of active particles in confinement. It is well-demonstrated that SPPs in strong confinement accumulate in regions of local convex edge curvature [230], [239], [241] and sometimes phase transition into directed motion depending on the confining geometry [244]. The persistence length of ant trajectories was estimated to be on the order of  $20 \ell$ . This likely explains why free ants far from protrusions, where the confining dimensions are on the order of 20 to  $50 \ell$ , display roughly isotropic behavior, while ants on protrusions (where  $W \sim 6 \ell$ ) exhibit directional motion (**Fig. 5.5.C-E**) and significant tip clustering (**Fig. 5.5.H**). It is for this reason that we adopted the model for SPPs under strong confinement introduced by Fily, et al. (2014) [241].

This model provides a conceptual picture of the instabilities driving protrusion initiation and growth. Citing both the model and experiments, we see that



imperfections in ant rafts' edges (*i.e.*, regions of higher edge curvature) generally host higher densities or clusters of free ants (**Fig. D.5.A-F**) [241]. We posit that this drives an increase in the local edge deposition rate, which then strengthens the locally high curvature, introducing a positive feedback loop. Perhaps compounding this effect are factors such as the directional motion of free ants on protrusions most likely caused by the relatively small width of these features as compared to the trajectory persistence length of free ants (**Fig. 5.5.C-E**). Observing experiments (**Fig. D.5.C-F**) we see that directional motion promotes additional tip clustering, thus indirectly also encouraging tip growth. While local clustering appears to accentuate growth wherever local edge symmetry is broken, it does not explain the elongated shape of some protrusions. We see from the model that if there exists a bias in the direction of edge deposition (**Fig. 5.6.C-D**,  $\beta > 0$ ), then the tip growth rates and curvatures of experimental protrusions are reasonably-well replicated. One potential cause for this bias is some first order effect from the directional motion of free ants. Indeed, where directional motion was measured experimentally (**Fig. 5.5.H**), the direction of instability growth appears in-line with said motion. Examining the model, local directional motion may also result from boundary evolution (*i.e.*, local changes in the boundary's normal orientation,  $\psi$ ) as growth occurs. In this case, the local orientation of SPPs,  $\theta$ , do not necessarily align normal to the edge. According to Fily's model, this introduces a local glide speed along the boundary that depends on the difference between the ant's orientation and that of the local boundary norm according to,  $\dot{s} = v_0 \cos(\theta - \psi)$ . Assuming negligible change in  $\theta$  since the persistence lengths of ants are relatively large, then this glide speed coincides with the direction of tip growth for the given boundary conditions (see **Fig. D.8**) and provides one possible explanation for the bias in directional tip growth observed. Besides bulk directional motion seen in experiments and local directional gliding predicted by the model, we

also observed cases of protrusion initiation in regions of low boundary curvature that seemingly occurred when many ants approach the local edge simultaneously (**Fig. D.5.G-H**). In these cases, spontaneous directional motion appears to antecede locally strong confinement and wall accumulation, suggesting that directional motion may sometimes be the original cause of asymmetric growth. Similar systems of SPPs in confinement display tether-like growths attributed to local cooperative effects. For example, Vutukuri, et al. (2020) revealed that Janus particles inside 3D lipid vesicles initiate protrusions when multiple Janus particles undergo spontaneous synchronous motion and applying a cooperative local force on the vesicle wall [245]. Remarkably, these growths emerge in the absence of centralization or external gradients. Whether this is also the case in fire ants remains to be seen, as other potential causes of biased edge deposition, such as environmental cues or local pheromone signals (analogous to chemotactic agents [205]) have not been ruled out.

While the model employed here helps interpret possible first and second order effects driving instabilities, it still possesses limitations in the context of fire ants. For example, it assumes a dilute system without local interactions. This presupposes that jamming does not occur and SPPs in strong confinement congregate entirely at the boundaries. Furthermore, this model assumes that density gradients reach a quasistatic state. However, this is not the case for fire ants, which exist at packing fractions anywhere between  $\sim 0.2$  and  $0.8$  free ants per structural ant, with local concentrations evolving ceaselessly. At these concentrations, ants appear to cluster and jam at certain locations, reflecting the phases that evolve in systems of SPPs with volume exclusion interactions [230]. Furthermore, this model steps the boundary continuously to preserve smooth functions in curvature space ( $\psi$ ,  $\kappa$  and  $\partial\kappa/\partial s$ ) despite the acknowledged potential for discrete size effects in real ants. Finally, it coarse

grains directional deposition bias through  $\hat{\phi}$  and cannot elucidate its underlying cause(s). This motivates future work in which we will employ discrete, agent-based modelling to better understand the physics of this biological system, while also providing swarm roboticists and engineers with distilled, ant-inspired rules that may achieve complex functional tasks.

## CHAPTER VI

### COMPUTATIONAL EXPLORATION OF TREADMILLING AND PROTRUSION GROWTH OBSERVED IN FIRE ANT RAFTS

In this penultimate chapter, we retrofit an iteration of the discrete network model to include the active features – monostructural raft layer contraction and outwards surface growth – that define ant raft treadmilling. Through this model, we unveil a set of stochastically occurring mechanisms that may explain the spontaneous emergence of protrusion growth for a treadmilling system such as the ant rafts, despite the omission of any long-range interactions, external gradients, or centralized control in the system. In doing so, we demonstrate the discrete network approach’s ability to elucidate possible origins of emergent functions and collective behaviors in active systems.

#### 6.1 Introduction

Cooperative living systems can achieve a wide range of complex functional tasks well beyond the capabilities of the individuals that comprise them. Perhaps chief amongst such organisms are social insects, which can operate collectively with other members of their colonies to more efficiently construct nests [246], [247], thermoregulate [248], [249], and forage for food [250], [251]. Another fascinating example of cooperative behavior by social insects is the formation of rafts by fire ants (*Solenopsis invicta*) [210], [211]. During floods, fire ants condense into buoyant rafts made entirely of worker ant bodies, thereby keeping their colonies unified and bolstering chances of survival [210], [211]. Recently, we discovered and reported that rafts can maintain

the ability to explore, even in flooded environments, through cooperative morphogenesis [11].

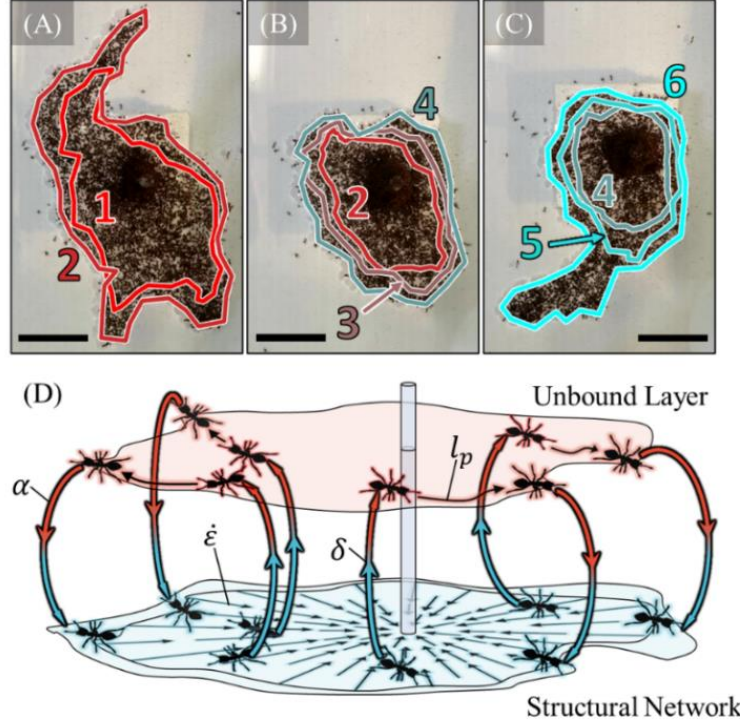


**Figure 6.1. Treadmilling review.** (A-C) A top view of the same experimental raft is illustrated at the (A) start, (B) middle, and (C) end of a roughly 106 min duration. To visually illustrate treadmilling, a set of structural ants at the perimeter is selected every 22 minutes. These ants are then image-tracked as they flow inwards due to network contraction and the geometry defined by these ants is traced by a distinctly colored and numbered outline. The set of ants labeled “2” in (B), for example, corresponds to the same set of ants labeled “2” in (A), but roughly 53 min later. The label “1” represents the oldest set of ants while “6” represents the newest. The shrinking of these contours indicates retraction of the raft structure, while the existence of new layers indicates outwards expansion. Periods of raft expansion and coinciding protrusion emergence (A,C) were interrupted by interstitial spans of decreased activity and less eccentric morphologies (B). All scale bars represent  $10 \ell$  where  $\ell = 2.93 \pm 0.60$  mm is the approximate average body length of 1 ant. (D) A schematic visually illustrates the four concurrent mechanisms of treadmilling: (1) structural raft contraction at a global rate  $\dot{\epsilon}$ , (2) transition of structural ants to freely active ants in the bulk at a nominal rate  $\delta$ , (3) transport of the free ants on top of the raft with a mean persistence length  $l_p$ , and (4) binding of free ants back into the structural network at the edges of the raft at nominal rate  $\alpha$ . The schematic is taken from Wagner, et al. (2021). The freely active layer is offset from the structural layer for illustrative purposes only, as it resides directly on top of the structural network in real ant rafts. Furthermore, note that the freely active layer, while shaded continuously, is comprised of dispersed ants while the structural layer is relatively homogeneous and condensed.

In our previous work [11], we observed ant rafts containing on the order of 3,000-10,000 worker ants. When introduced to water in which a vertical rod stemmed from the surface, these ants formed dynamic raft structures comprised of a floating layer of structural ants on top of which a layer of freely active ants walked [11]. While the structural network constituted a single, condensed layer of ants with roughly conserved planar density, the freely active layer was dispersed, heterogenous and transient on the timescale of seconds. Under these conditions, these rafts display the ability to sprout tether-like protrusions that emerge and recede perpetually over the span of hours [11]. The sustained emergence of these growths relies on treadmilling dynamics in which the structural network comprising the raft continually contracts, while freely active ants on the surface of the raft deposit into the structural network's edges and drive outwards expansion (**Fig. 6.1**). The population of free ants that fuels outwards expansion is continually replenished by unbinding or “exit” of structural ants from the bulk of the raft and their subsequent transition into the freely active layer. We note that although the presence and dimensions of the anchoring rod may impact the behavior of fire ants in experiments, we here focus on how the experimentally measured, local behavior (e.g., trajectory properties, local interactions, *etc.*) of ants drives the treadmilling and formation of dynamic protrusions observed.

In some cases, the ants utilized protrusions as floating bridges to reach the edge of and collectively escape their containers, demonstrating that they serve an adaptive advantage. Comparable cellular systems, such as cytoskeletal walls [252]–[254] and cellular aggregates [8], [255], display protrusion growth that, as in the case of fire ant rafts, facilitates motility and collective migration. While these cellular systems are understood to utilize chemotaxis [256], durotaxis [257] or other gradient-driven

mechanisms [258] to initiate migration, it is not entirely clear whether such external stimuli are necessary to drive protrusion growth in fire ant rafts. This raises the question; do fire ants deliberately work to create these protrusions or do these features emerge spontaneously in the absence of targeted signals or external gradients? Indeed, spontaneous behaviors such as flocking of plant-animal worms [259] or ordered motion of California blackworms [260] have been demonstrated in other condensed biological systems. However, the specific circumstances and adaptive advantages, under which these behaviors occur, differ greatly from the exploratory or escape function displayed by floating fire ant rafts.

Spontaneous ordering is also well-documented in non-living active matter systems and indicates that no agent-intent is necessary to spur comparable formations [6], [241], [261]. Perhaps most similarly, Janus particles entrapped by lipid membranes have been shown to generate remarkably analogous geometries to these ant rafts due solely to stochastic, synchronous motion [245]. This occurs when a few neighboring Janus particles simultaneously apply force to the boundary that causes an acute increase in local edge curvature and runaway tether growth. Along these lines, in our previous work we treated freely active fire ants as decentralized self-propelled particles in confinement. We demonstrated that the trajectory persistence length of freely active ants is greater than the dimensions of the rafts they walk on. Under these “strongly confined” conditions, it is known that self-propelled particles cluster near the convex edges of their containment geometries [240], [241]. Employing a coarse-grained continuum model of ants on protrusions based on the work of Fily, et al. (2014) [241], we postulated a mechanism through which local breaks in convex symmetry at the rafts’ edges may induce a runaway feedback loop whereby the locally higher curvature causes clustering of free ants, and the higher concentration of free

ants causes a higher local edge deposition rate. Yet, we also demonstrated that a higher concentration of free ants alone does not lead to the elongated morphologies observed in the experimental system and there must exist some mechanism that biases the direction in which ants bind into the structural network [11]. While the hypothesized source of this bias is a first or second-order effect of the directional motion of free ants on protrusions [11], its true origins remain unclear and whether such protrusion may form in ant rafts due solely to local interaction rules alone is uncertain. However, further exploration through the continuum model is limited by smoothing assumptions that prohibit the investigation of phenomena such as individual ant behavior, heterogeneities, and discrete size effects. Additionally, exploration of this bias through experimentation is limited by factors such as small sample sizes (since protrusions must be allowed to occur spontaneously without interference), difficulty in image-tracking the position of free ants, and the inability to measure variables such as ant self-propulsion force. For these reasons, a discrete modeling approach such as that taken by Vutukuri, et al. (2020) [245] or other researchers in the study of ant species [262]–[267] is warranted.

We here develop and employ a 2D, ant-inspired, agent-based, numerical model in which the behavior of every single ant in the structural and freely active layer is discretely captured. In matching the statistical behavior of agents to ants in both layers, we use this model to demonstrate that a set of local interaction rules predicts the emergence of spontaneous protrusion growth in the absence of any long-range communication or external gradients. These rules confirm that biased motion of free agents occurs on protrusions given the condition of strong confinement and local alignment interactions, and this directional motion facilitates the runaway growth of said protrusions, as hypothesized previously [11]. Furthermore, we use this model to



investigate another unexplored phenomenon: oscillatory phase changes in fire ant rafts between highly eccentric periods of outwards expansion accompanied by protrusion growth, and recessive periods in which the rafts assume more rounded or elliptical shapes (**Fig. 6.1.A-C**). Comparable cyclical changes in the mechanical properties of 3D aggregations of fire ants have been documented and attributed to shifts in the activity level of the overall population [214], [215]. We find here that morphological phases of ant rafts may similarly be modulated through the activity level of freely active ants on their surface as characterized by a dimensionless activity parameter  $\mathcal{A}$ . This parameter represents the competition between ants' self-propulsion force, and their effective repulsion from the raft edge due to their dislike of water. In the remainder of this work, we introduce the model and confirm that it replicates the treadmilling dynamics observed experimentally. We then demonstrate that it predicts the spontaneous formation and runaway growth of protrusions, despite initially circular raft geometries. Finally, we explore how modulating activity induces phase transitions between periods of outwards, exploratory growth, and contractile withdrawal, as seen in experiments.

## 6.2 Results

### 6.2.1 Modeling ant rafts

Here we overview the discrete numerical model used in this work to contextualize the results presented. Detailed derivations and implementation methods are provided, as needed, in Appendix E. We see in our previous work that treadmilling of ant rafts is driven by four concurring mechanisms: (1) perpetual contraction of the floating, structural ant network, (2) exit of structural ants out of the network into the freely active layer, (3) self-propulsion of the free ants on top of the raft, and (4) deposition

of free ants into the structural layer at the raft’s edges (**Fig. 6.1.D**) [11]. To capture these mechanisms, the model represents ants as discrete agents whose motions are confined to a lattice of water nodes. To represent the two-state nature of ant rafts, the model consists of a population of structural agents representing the raft’s structural network, on top of which a population of freely active agents moves dispersedly. These respective populations are denoted by the colors cyan and red throughout this text unless specified otherwise. The positions of structural agents and water nodes are updated in continuous space to capture the mechanism of structural network contraction. However, the movement of free agents is constrained to the lattice defined by the structural agents, thus naturally ensuring that free agents can only occupy the spatial domain of the raft. An illustrative schematic of two hypothetical free ants in continuous space is depicted in **Fig. 6.2.A**, while the corresponding conception of free agents in the lattice-based model is shown in **Fig. 6.2.B**. Although the respective states of structural and free ants may consist of multiple layers distributed in the  $z$ -axis (depending on the time of inspection) [11], [210], we here choose to model each as a single layer of agents based on the experimental observation that during phases of protrusion growth, the structural network generally spread into a monolayer (with a planar density of  $0.304 \text{ ants mm}^{-1}$ ) and the freely active layer was – on average – dispersed with a mean packing fraction of approximately 0.24 free ants per structural ant [11]. **Fig. 6.2.C-E** depicts snapshots of a simulated raft in which the monolayered structural network is represented by cyan lattice sites, and the dispersed active layer on top is depicted by red free agents. While these two states behave independently in the model, agents transition between them according to a set of ant-inspired rules.

### 6.2.2 Modeling structural agents.

Based on experimental evidence we find that raft contraction is relatively constant in time [11]. In contrast the deposition of free ants that drives outwards raft expansion varies significantly over hours, with some free ants clustering near the rod in an inactive state. Therefore, in the scope of this work, our primary aim is to explore the local, free agent behavior that drives phase changes in these systems. Naturally, the model must still replicate the global treadmilling dynamics that are prerequisite to sustained shape change and for which global contraction is an essential mechanism. We found previously that the structural layer contracts uniformly throughout the network and that its density is roughly conserved even over long time frames [11]. To capture this uniform global contraction without introducing mechanisms that would require long-range cooperation, we introduce spatially continuous pairwise contraction between neighboring structural agents at a constant strain rate of  $\dot{d}$  [% min<sup>-1</sup>]. It remains unclear if structural ants contract towards all of their nearest neighbors or if they only contract to fill in voids originating at sites where ants recently exited the structural layer. Regardless, that global contraction is observed mandates that there exists microstructural contraction at some length scale, which we here enforce between all pairwise nearest neighbors for simplicity. This ensures that the mechanisms driving global contraction could feasibly be achieved by agents working through exclusively local interactions. Setting  $\dot{d}$  to 1.2 times the globally measured contractile strain rate ( $\dot{\epsilon}$ ) led to good agreement between experiments and simulations (**Fig. 6.3.A-C**) [11] (see Appendix E.2 for details). The fact that  $\dot{d}$  does not equal  $\dot{\epsilon}$  generally indicates that the local rate of contraction between nearest neighbors is higher than the emergent global rate, which is expected in a network due to non-affine effects [268].

To avoid hindering contraction, volume exclusion between structural agents is not enforced. However, unconstrained network contraction would lead to a ceaseless increase in structural ant concentration, which was not observed experimentally [11]. To ensure conserved planar network density structural agents are unbound and converted to freely active agents wherever their local quantity per unit area (i.e., their density) exceeds a prescribed threshold. This allows for robust exit of structural ants throughout the bulk, as observed in experiments [11]. To match experiments, this threshold was set to 1 agent per  $\zeta^2$ , where  $\zeta^2$  is the area occupied by one experimental, structural ant ( $\zeta = \rho_r^{-0.5} = 1.81 \pm 0.30$  mm, where  $\rho_r$  is the planar structural network density). Consequently, a numerical rate of structural unbinding,  $\delta \sim 2 \% \text{ min}^{-1}$ , naturally emerged and matched experimental estimates (**Fig. 6.3.F**) [11], suggesting that 2 % of structural agents convert to freely active agents every minute. Thus, through this pairwise contraction, both global network contraction and flux of ants from the structural network to the freely active layer were achieved. Note that the structural agents provide a continuously updated lattice on which the freely active agents move, such that structural layer contraction also induces contraction of the free layer. However, active agents walk at speeds two orders of magnitude greater than that of the structural contraction such that the effect of contraction is negligible on free agents.

### 6.2.3 Modeling freely active agents.

While global contraction and bulk structural unbinding are essential in replenishing the population of freely active ants, it is ultimately the deposition of these free ants into the edge of the structural network that governs global shape evolution. This

deposition is largely dependent on the distribution of free ants at the edge, and therefore the transport of free ants on the surface of the raft. To model surface traffic, we begin with the qualitative observations that free ants are self-propelled agents whose trajectories under weak confinement are isotropic but correlated below the length scale of one ant body length ( $1 \ell$ ), indicating some degree of local alignment interactions [11]. To capture this local alignment, the phenomenological Vicsek model [261] is used to predict the preferred direction of motion of self-propelled agents as they traverse the structural lattice. Through this model, the preferred angle of motion of free agent  $i$  at time  $t + \Delta t$  is updated according to [269]:

$$\theta_i(t + \Delta t) = \langle \theta_j(t) \rangle_i + \xi_i(t), \quad (6.1)$$

where  $\langle \theta_j(t) \rangle_i$  is the average orientation,  $\theta$ , of all neighboring freely active agents (including agent  $i$ ) at time  $t$ . Neighboring agents are denoted by the index  $j$  and defined as free agents residing within some detection distance,  $R$ , of agent  $i$ . Note that raft agents exert no influence on active force since they reside beneath the plane of active agents and move at considerably slower speeds. The scalar value  $\xi_i$  induces a random change in agents' directions within the uniformly distributed range  $[-\pi\eta, \pi\eta]$ , thus coarsely capturing decision-based noise in ants' trajectories. Here  $\eta \in [0,1]$  is the noise parameter introduced by Vicsek, et al. (1995) [261] (**Fig. 6.2.A**), whereby if  $\eta = 0$  there is no noise and if  $\eta = 1$  the movement of agents is completely random. The Vicsek model is a minimalist model for active particle motion that may capture a full spectrum of phases from fully isotropic motion (at low densities or high noise) to completely uniform movement (at high densities or low noise), and which depends on just three parameters: particle density, the radius of influence ( $R$ ) and noise ( $\eta$ ) [261]. Therefore, it is favored for its versatility, simplicity and is applied here given the experimental evidence that there exists mutual interactions between free ants, albeit only at the contact length scale [11]. Although this model is commonly used to capture

collective motion driven by non-local interactions between self-propelled particles, it is not exclusive to collision-avoiding particles, and we here set  $R$  such that only neighbors in contact may directly influence one another. In this lattice-based framework,  $\eta$  and  $R$  are taken as 0.2 and 0.9  $\ell$ , respectively, in order to replicate the experimentally measured persistence length,  $l_p$ , of free ant trajectories far from rafts' edges [261] (see the Appendix E.3 for details).

At every timestep, Eqn. (6.1) is used to define the preferred direction of motion for each free agent. However, since free agents are constrained to the lattice of structural agents, Eqn. (6.1) is not used to step their positions continuously. Instead, each agent is assigned (at most) 18 movement degrees of freedom (DOF) that may consist of either structural agents or water nodes, but which must exist within some distance  $R_{DOF}$  of agent  $i$  (see Appendix E.3 for selection of  $R_{DOF}$ ). Note that  $R_{DOF}$  naturally constrains the maximum speed of free agents to  $v_{max} = R_{DOF}/\Delta t$ , and defines some mean distance,  $\langle d \rangle$ , between agent  $i$  and its neighboring DOF. Indeed, this permits that the time step be set to according to  $\Delta t \approx \langle d \rangle / v_0$ , where  $v_0$  is the experimentally measured mean free ant speed, thereby calibrating the timescale of this model. Once  $\theta_i$  is computed, agent  $i$  is then stepped to the position of the “eligible” DOF whose relative orientation most closely matches  $\theta_i$  (see Appendix E.3 for details). Eligibility is defined by a set of ant-inspired criteria. Firstly, structural DOF are ineligible if they are already occupied by a free agent. This mimics volume exclusion interactions between free ants (i.e., that two ants cannot occupy the same space) and naturally enforces that the freely active agents occupy a monolayer and remain relatively dispersed as in experiments [11]. Secondly, eligible DOF must exist within the confines of some turning limit ( $\pm\pi/2$  radians) with respect to  $\theta_i$ . This turning limit was included due to the observation that it takes free ants greater than  $\Delta t$  to turn

more than approximately  $\pi/2$  radians, thereby limiting the turning rate of agents using an approach similar to that of Couzin and Franks (2003) in their investigation of army ants (*Eciton burchelli*) [267]. Finally, if the preferred DOF is a water node then an additional rule of edge deposition must be satisfied to allow movement, as discussed in the following section. If a free agent has no eligible movement DOF, it pauses before re-evaluating its preferred direction of motion according to the algorithm described in Appendix E.3.

#### **6.2.4 The rule of edge deposition.**

To properly model edge deposition, we again begin with experimental observations. Active ants appear to “encounter” the raft’s edge when they walk directly towards it and contact the water. These ants avoid binding into the raft’s edge (which requires moving into the water) unless pressured by neighboring active ants and adequately surrounded by structural ants upon deposition into the network. Together, these observations indicate competition between some effective active force  $\mathbf{F}_i^a$  due to a free ant’s self-propulsion combined with that of its nearest neighbors, and some effective edge repulsion force  $\mathbf{F}_i^r$  that occurs at the perimeter of the raft. Here,  $\mathbf{F}_i^r$  is not a physical force, but rather an embodiment of ants’ motivation to stay on dry substrates and is akin to the “social forces” employed by Helbing and Molnár (1995). Whether or not it is due to free ants’ affinity to the raft, aversion to water, or both is not immediately clear or relevant. Nevertheless, there is a clear observational tendency for individual ants to avoid moving into the water under their own volition.

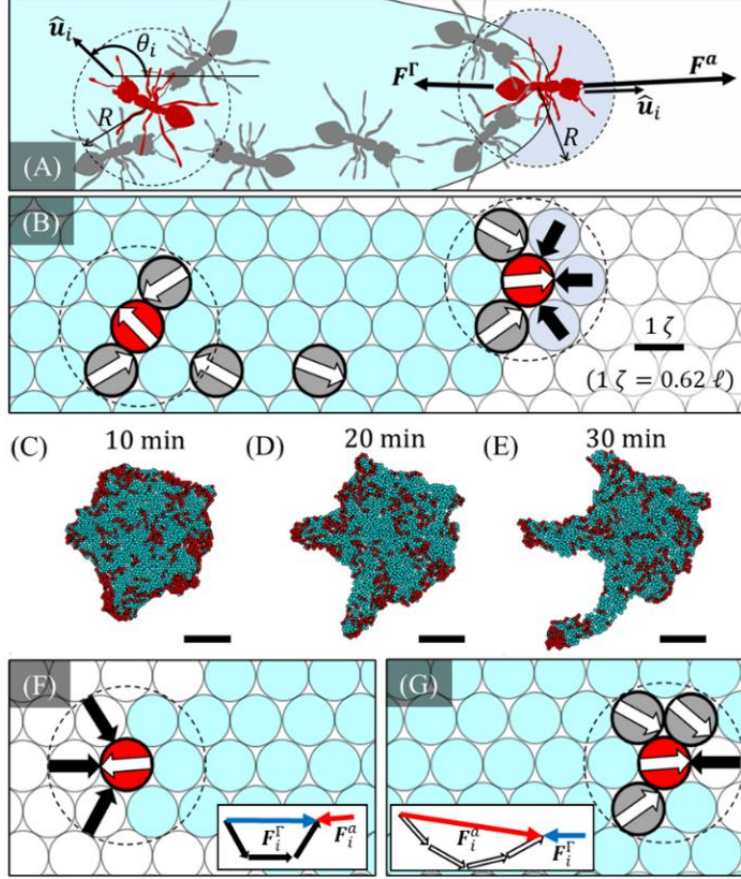


**Figure 6.2. Agent-based model schematic.** (A) Two free ants of interest (red) are schematically illustrated on a structural section of raft (shaded cyan) in continuous space. Other free ants are shaded grey. The direction of motion ( $\hat{u}_i = [\cos \theta_i, \sin \theta_i]$ ) of the ant far from the edge of the raft (left) is predicted entirely by the Vicsek model. In contrast, whether the ant encountering the edge of the raft (right) moves into the water, depends not only on  $\hat{u}_i$ , but also on the competition between active force  $F_i^a$  and the effective edge repulsion force  $F_i^r$ .<sup>6</sup> Each of these forces is governed by the motion of free ants and relative position of water within detection distance  $R$  of the ants. (B) A corresponding schematic envisions how these continuous scenarios are coarse-grained into the lattice-based framework of the numerical model. The motion of the free agents of interest (red) remains governed by the direction of travel (white arrows) of neighboring free agents, and effective pairwise repulsion (black arrows) from neighboring water nodes within distance  $R$ . However, free agent movement is updated by stepping the free agents to the adjacent structural agents (cyan) or water nodes (white) whose relative direction most closely matches the preferred direction,  $\theta_i$ . Nodes are displayed in a hexagonal, close-packed lattice for illustrative purposes only, but are initially offset in both directions of the horizontal plane by some amount in the range  $[-1/6, 1/6]\zeta$  and are further randomized by stochastic structural unbinding events as the simulation progresses. (C-E) The shape evolution of a simulated raft over a duration of 20 min (of virtual time), illustrates the implementation of the lattice-

<sup>6</sup> In the remainder of this work the indices, (as depicted in **Fig. 6.2.A**) and denote the agent of interest and its influencing neighbors, respectively, rather indicating vector values. Vectors are instead denoted by bold text. Where indicated, index  $i$  is replaced by  $j$ ,  $s$ , or  $w$  to specify neighboring free (surface) agents, structural (raft) agents, or water nodes, respectively. Combined indices (e.g., “”) are used to denote pairwise values or values from  $i$  to  $j$ , rather than second order tensors.



based conceptualization from (B) into the numerical model. Shape change is governed by the transition of free agents (red) into the structural network (cyan) at the raft's edge. The raft depicted was initiated as a circle and all scale bars represent  $10 \ell$ . (F-G) Agents encountering water in regions of (F) high and (G) low edge curvature are depicted. These respective agents experience high and low values of  $\mathbf{F}^r$  due to the pairwise contributions of repulsion force from detected water nodes (black arrows). The agent in (F) has no freely active neighbors such that the only contribution to its value of  $\mathbf{F}^a$  is its own self-propulsion force (white arrow), whereas the agent in (G) has many freely active neighbors moving in similar directions towards the water such that it has a high value of  $\mathbf{F}^a$  oriented off the raft. (F-G) Insets display the vectorial sums that define the effective forces  $\mathbf{F}^a$  (red) and  $\mathbf{F}^r$  (blue) for the respective agent configurations, thus illustrating how the agent in (G) is more likely to edge-deposit based on Eqn. (6.2).

To mimic these experimental observations, we define an edge encounter as occurring when a free agents' preferred movement DOF is a water node. We then compute  $\mathbf{F}_i^a$  and  $\mathbf{F}_i^r$ , and simply define an edge deposition event as occurring when the magnitude of active force driving the agent off the raft is greater than the magnitude of effective edge force repelling it from the water, in the direction of agent motion ( $\hat{\mathbf{u}}_i = [\cos \theta_i, \sin \theta_i]$ ). Mathematically, this is given by:

$$(\mathbf{F}_i^a + \mathbf{F}_i^r) \cdot \hat{\mathbf{u}}_i > 0. \quad (6.2)$$

To compute  $\mathbf{F}_i^a$  we coarsely assume that self-propulsion forces are fully transmitted between in-contact free agents such that:

$$\mathbf{F}_i^a = N f^a \boldsymbol{\varphi}_i^\sigma, \quad (6.3)$$

where  $f^a$  is the magnitude of a single agent's self-propulsion force and  $N$  is the number of neighboring free agents ( $\sigma \in [1, N]$ , inclusive of  $i$ ) residing within the contact radius  $R$ . Here,  $\boldsymbol{\varphi}_i^\sigma$  is the local order vector in free agent motion defined by  $\boldsymbol{\varphi}_i^\sigma = N^{-1} \sum_{\sigma}^N \hat{\mathbf{u}}_\sigma$  where  $\hat{\mathbf{u}}_\sigma$  is the direction of motion ( $\hat{\mathbf{u}}_\sigma = [\cos \theta_\sigma, \sin \theta_\sigma]$ ) of neighboring free agent  $\sigma$ . The local order vector is  $\mathbf{1}$  when all local free agents are moving in the same direction, and approaches  $\mathbf{0}$  when the local movement is completely disordered [226]. Therefore,  $\mathbf{F}_i^a$  scales with the degree of local synchronization (or cooperation) between free agent motion through  $\boldsymbol{\varphi}_i^\sigma$ , and is bound by the number of locally detected neighbors,  $N$ .

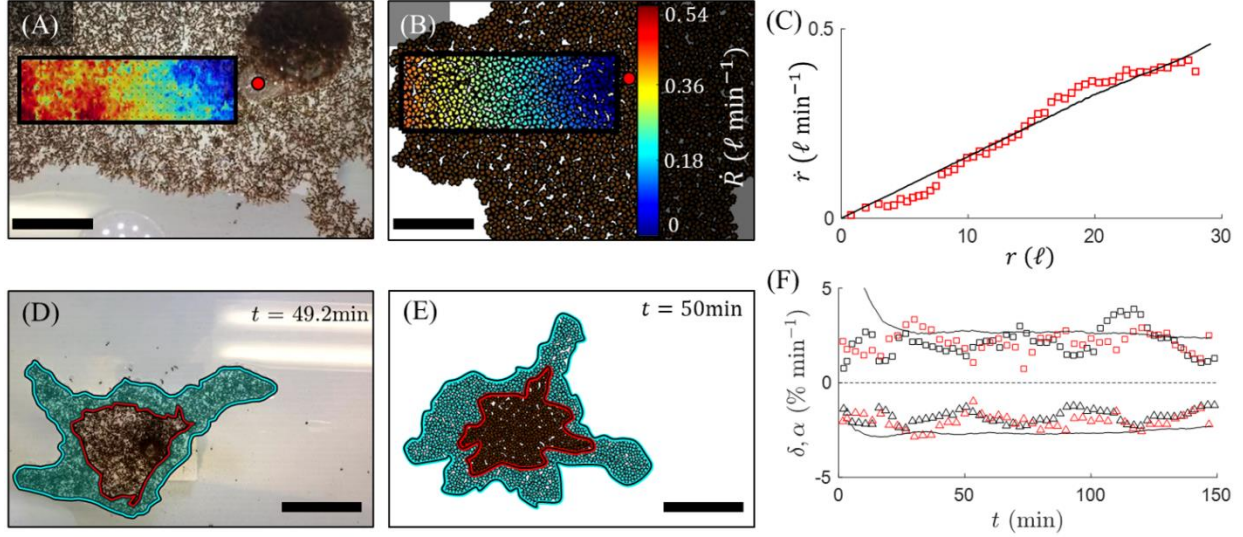


**Figure 6.3. Comparing treadmilling dynamics.** (A-B) The gradient of contractile speed,  $\dot{r}$ , towards the anchor point of the rafts (red dot) is illustrated via heat maps within defined regions of interest (ROIs) for both (A) an experimental and (B) simulated raft.  $\dot{r}$  was computed as the component of speed moving towards the stationary reference frame (i.e., the acrylic rod) and was measured for every point within these 2D ROIs, then averaged over durations exceeding 13 minutes. Scale bars represent  $10 \ell$ . (C)  $\dot{r}$  is plotted with respect to distance from the anchor point,  $r$ , for both the experiment (discrete red squares) and simulation (solid black curve). The slopes of the least-squares regression lines are taken as the average contractile strain rate  $\dot{\epsilon}$ . The experimental strain rate ( $\dot{\epsilon} = 1.63 \pm 0.01 \% \text{ min}^{-1}$ ,  $R^2 = 0.96$ ) agrees with the numerical value ( $\dot{\epsilon} = 1.62 \% \text{ min}^{-1}$ ,  $R^2 = 0.99$ ). (D-E) The growth zones of both (D) an experimental and (E) simulated raft after roughly 50 min are shaded in cyan. Scale bars represent  $15 \ell$ . The bound ants that occupied the perimeter of the raft at reference time,  $t_0 = 0$ , are outlined in red and were traced through time. (F) The time-evolution of the edge binding rate,  $\alpha$ , and bulk unbinding rate,  $\delta$ , as a percentage per unit raft area are shown for two sets of experiments (squares for  $\alpha$  and triangles for  $\delta$ ; red and black for two different experiments) along with the averaged results of 12 simulations (continuous black curves). Note that the initial drops in both  $\alpha$  and  $\delta$  for the simulation data occur since the raft was not initiated at steady state, whereas experimental data was only sampled at pseudo-steady state. (A,C,D,F) Experimental results are courtesy of Wagner, et al. (2021). All simulated rafts were initiated as circles and shape was allowed to evolve stochastically.

To compute  $\mathbf{F}^r$  we consider that there exists some effective pairwise repulsive force,  $\mathbf{f}_{i\omega}^r$ , acting on agent  $i$  due to each of its  $N$  adjacent water neighbors ( $\omega \in [1, N]$ ) within distance  $R$ . Treating this force as the negative gradient in potential energy between the positions of node  $\omega$  and agent  $i$  (i.e.,  $\mathbf{f}_{i\omega}^r = -\nabla_{\mathbf{r}} U$ ), assuming the simplest case of a linear energy gradient between these sites, and recognizing that detection distance  $R$  is the contact length scale (i.e.,  $R/\ell \sim 1$ ) then we may take the magnitude of  $\mathbf{f}_{i\omega}^r$  as a constant,  $f^r$  (see Appendix E.3 for details). Assuming a linear superposition of the

pairwise forces then the net repulsive force on  $i$  may be computed as the sum of discrete contributions [270] from all  $N$  water neighbors as:

$$\mathbf{F}_i^r = -Nf^r\boldsymbol{\varphi}_i^\omega, \quad (6.4)$$

where  $\boldsymbol{\varphi}_i^\omega$  is a local order vector ( $\varphi_i^\omega \in [0,1]$ ) indicating the relative position of water nodes with respect to  $i$ . Mathematically,  $\boldsymbol{\varphi}_i^\omega = N^{-1} \sum_{\omega} \hat{\mathbf{r}}_{i\omega}$  where  $\hat{\mathbf{r}}_{i\omega} = (\mathbf{X}_\omega - \mathbf{X}_i)/|\mathbf{X}_\omega - \mathbf{X}_i|$  is the direction vector from the position of  $i$  ( $\mathbf{X}_i$ ) to the position of  $\omega$  ( $\mathbf{X}_\omega$ ), which points towards the average location of detected water nodes. The magnitude of  $\boldsymbol{\varphi}_i^\omega$  increases as the relative orientation of these water nodes becomes more tightly grouped with respect to  $i$  (e.g., if all detected water nodes are approximately in-line with and on one side of  $i$ , then  $\boldsymbol{\varphi}_i^\omega \rightarrow \mathbf{1}$ ). As a result,  $\mathbf{F}_i^r$  scales proportionately to the amount of water detected through  $N$  and acts approximately in the direction normal to (and inwards from) the raft's boundary through  $-\boldsymbol{\varphi}_i^\omega$ .

Substituting Eqns. (6.3) and (6.4) into (6.2) provides a normalized condition for edge deposition:

$$\frac{f^a}{f^r} \left( \frac{N^\sigma \varphi^\sigma}{N^\omega \varphi^\omega} \right) > 1 \Leftrightarrow \text{Deposit}, \quad (6.5)$$

where  $\varphi^\sigma = \boldsymbol{\varphi}_i^\sigma \cdot \hat{\mathbf{u}}_i$ ,  $\varphi^\omega = \boldsymbol{\varphi}_i^\omega \cdot \hat{\mathbf{u}}_i$ , and we have distinctly labeled the number of neighboring free agents and water nodes as  $N^\sigma$  and  $N^\omega$ , respectively. Scalars  $N^\sigma \varphi^\sigma$  and  $N^\omega \varphi^\omega$  are numerically measured values that characterize the respective magnitudes of the active and repulsive forces in the direction of motion, and which depend only on the local configuration of the discrete system as illustrated through examples in Fig. 6.2.F-G. Therefore, the only parameter introduced through this edge deposition rule is the dimensionless ratio  $\mathcal{A} = f^a/f^r$ , which characterizes the competition between a free agent's self-propulsion force and its effective repulsion from water. As such,  $\mathcal{A}$  is the parameter that mediates global expansion and shape change of the rafts. Supposing that an ant's aversion to water is relatively consistent

(i.e., that  $f^T$  is constant), then  $\mathcal{A}$  is representative of the active force or “activity” of free ants, where high activity is synonymous with high  $f^a$ . Increasing  $\mathcal{A}$  results in an increase in the left-hand side of Eqn. (6.5), thereby escalating the overall edge deposition rate per free agent. With the edge deposition rule implemented, a mean expansion (or edge binding) rate of  $\alpha \sim 2 \% \text{ min}^{-1}$  naturally emerged for the overall rafts and automatically matched the experimentally measured values once pseudo-steady state treadmilling occurred ( $\alpha \approx \delta$ ) (**Fig. 6.3.D-F**). This rate may be interpreted as the percentage of structural agents that are newly added to the network’s edge each minute.

### 6.2.5 Protrusions emerge spontaneously.

To model experiments, we ran simulations with 2,250 agents for up to 4.5 hours of simulation time, letting the rafts reach quasi-steady state treadmilling (defined by  $\alpha \approx \delta$ ). To roughly mimic the dense, spheroidal shapes of the experimental ant aggregations when initially placed into water and to assure that protrusions form stochastically, all simulated rafts were originated as circles with a free agent packing fraction of  $\phi = 1$  freely active agent per structural agent (**Fig. 6.5**). To provide a still reference frame and mimic the anchored boundary conditions of experimental rafts, a permanent structural agent was located at the center of the domain and fixed in place. With both the pairwise contraction rate ( $\dot{d} = 1.9 \% \text{ min}^{-1}$ ) and Vicsek model parameters ( $R = 0.9 \ell$  and  $\eta = 0.2$ ) independently calibrated to match experimental treadmilling and free ant trajectories, respectively, ant activity ( $\mathcal{A}$ ) remained the only free parameter driving freely active agent behavior and global shape evolution.

Despite the initially circular shape of each raft, when  $\mathcal{A}$  was on the order of 1.25 to 1.47 the model consistently predicted the unstable growth of protrusions. For the purposes of this work, we define a protrusion as any elongated region of structural network branching from the raft whose width is less than half of the mean ant persistence length ( $0.5 \times l_p \approx 10 \ell$ ), and whose length is greater than or equal to its width (i.e., aspect ratio  $\geq 1$ ). In contrast, bulk sections of raft are defined as continuous regions of structural network whose dimensions exceed  $l_p$  in all directions, and which exists at least a distance of  $2 \ell$  from the raft's boundary to account for the correlated trajectory length scale of free ants ( $\sim 1 \ell$ ). To determine if the predicted protrusions had the same characteristic length scale and dynamics as experimental protrusions, we measured their average widths,  $W$ , and growth rates,  $V$ , over time. The widths of simulated protrusions ranged from roughly 2 to  $9 \ell$ , with a mean value of  $5.95 \pm 0.05 \ell$  that agrees with the experimental value of  $5.85 \pm 0.06 \ell$  (**Fig. 6.4.A**) [11]. Similarly, the tip-growth rates of the model-predicted protrusions ranged from roughly -1 to  $3 \ell \text{ min}^{-1}$ , with a mean value of  $0.46 \pm 0.02 \ell \text{ min}^{-1}$  (**Fig. 6.4.B**). While not exactly matching the experimental mean of  $0.74 \pm 0.05 \ell \text{ min}^{-1}$  [11], these growth rates are on the same order and are adjustable through  $\mathcal{A}$ . The model also allowed us to easily quantify the distinct behaviors of freely active agents, enabling us to confirm the factors leading to spontaneous protrusion initiation and runaway growth.

We confirmed that protrusion initiation is driven by stochastic nucleation of transient ant clusters, which occurred frequently near the rafts' convex edges, and are primarily attributed to wall-accumulation effects [239]–[241], [269], [271]–[273]. These clusters often caused concentrated edge-deposition of freely active ants resulting in local regions of high edge curvature that served as proto-protrusions. Following this, the model predicted directional flow of freely active ants along

protrusions' lengths consistent with what was observed previously in experiments and which is largely attributed to the strong confinement of particles in these regions wherein their persistence lengths exceed that of the protrusions' confining widths [11], [240], [241]. While similar clustering is predicted by the continuum model previously adapted and modified [11] from Fily et al. (2014), several limitations exist for said model, such that the causes of clustering and directional motion in the case of ant rafts are likely better captured by this discrete approach. First, the continuum approach requires a smoothly differentiable raft boundary and predicts that particles will “slide” directly along the edge of confinement until they reach a local minimum in the convex radius of curvature or hit a concave region of edge curvature (at which point they will “jump” tangentially across the domain and back to the opposite boundary) [240].

This smoothing prohibits the study of edge defects whose sizes are on the order of single ants (e.g., vacancies or small protuberances of just a few ants), as the continuum model would predict that these defects simply interrupt sliding along the edge. However, in this coarse-grained lattice model, the raft's edge defects naturally occur at the length scale of an agent. These defects sometimes interrupted free agent motion along the edge given the movement and edge deposition rules implemented here, causing agents to pause temporarily and then reorient. Despite these defects, the discrete model still predicted directional alignment (**Fig. 6.4.C-F**) and tip clustering (**Fig. 6.4.K-L**) on protrusions, exemplifying robustness in these features, as seen in physical experiments [11]. One possible explanation is that, on protrusions, agents jammed at edge defect sites, were influenced, and frequently realigned with the motion of uninterrupted agents nearby on the bulk such that directional motion resumed. Thus, the effects of volume exclusion, alignment interactions, and bulk

movement – none of which could be examined through the continuum approach – propagated the effects of strong confinement inwards (away from the rafts’ edges) and facilitated directional motion.

Visually, directional motion on a protrusion is represented in **Fig. 6.4.C-F** wherein the trajectories of free ants or agents are depicted in regions of interest both on protrusions (**Fig. 6.4.C** and **6.4.E**) and bulk sections far from the rafts’ edges (**Fig. 6.4.D** and **6.4.F**). The direction of motion is represented by a spectrum of colors per the color wheel in **Fig. 6.4.E**, which is oriented such that leftwards movement is depicted by shades of orange. For both experiments and the model, a bias in directional travel is clearly illustrated on protrusions from their bases to their tips, as indicated by the prevailing orange hues of trajectories (here entailing leftwards motion). In contrast, on the bulk it is more difficult to assign a single predominant hue, indicative of more isotropic movement. However, clusters of synchronous motion still appear to occur in all regions of interest on the order of  $1\ell$  (consistent with the findings of Wagner, et al. (2021)), making an objective visual analysis difficult. To instead quantify differences in directional motion, we compared the normalized velocity order parameter of free ants and agents (members) on protrusions, defined by  $\varphi = \langle \mathbf{v}(t) \rangle_N / \langle |\mathbf{v}(t)| \rangle_N$  where  $\mathbf{v}$  is the velocity of a particle and  $\langle \rangle_N$  denotes taking the ensemble average over all  $N$  members [226]. This parameter is zero when motion is completely isotropic but approaches 1 when movement is perfectly unidirectional. We found that in both experiments and simulations,  $\varphi$  was on average higher for freely active members on protrusions than on the bulk of the raft. For the experimental raft depicted in **Fig. 6.4.C-D**,  $\varphi = 0.65 \pm 0.02$  on the protrusion versus  $\varphi = 0.57 \pm 0.02$  on the bulk [11]. Similarly, for the simulated raft depicted in **Fig. 6.4.E-F**,  $\varphi = 0.64 \pm 0.12$  on the protrusion versus  $\varphi = 0.33 \pm 0.06$  on the bulk. In both

cases, comparably sized domains were used to compute  $\varphi$  and the relatively larger values of  $\varphi$  on protrusions confirms that the confinement of protrusions induces higher directional motion than that observed on the bulk. However,  $\varphi$  does not indicate the orientation or sense of said directional motion.

To further examine in which orientation freely active members preferentially traveled, we also investigated their velocity distributions on and off protrusions, from both experiments (**Fig. 6.4.G-H**) [11] and an ensemble of 11 *in silico* protrusions (**Fig. 6.4.I-J**). The elongation of velocity distributions along the length of protrusions confirms that traffic moves primarily along these structures' longitudinal axes, whereas the velocity distributions on the bulk (**Fig. 6.4.H** and **6.4.J**) appear uniform, indicating isotropic motion, thus supporting the interpretations of **Fig. 6.4.C-F**. Furthermore, the biased sense of motion is also exemplified by the velocity distributions on protrusions, which are slightly skewed left for both experiments (**Fig. 6.4.G**) and simulations (**Fig. 6.4.I**), implying motion from the bases-to-tips of protrusions. When directional traffic occurred towards the tips of protrusions, it induced jamming of freely active agents at their ends (**Fig. 6.4.K-L**) and high magnitudes of  $\mathbf{F}^a$ , similar to the locally high pressures exerted by confined Active Brownian Particles on highly convex regions of confinement curvature [241], [274]. This locally high active force accentuated edge binding and tip growth. Ultimately, runaway protrusions result from a positive feedback loop wherein cluster formations initiate protrusions that in turn promote directional traffic, spurring further tip clustering and growth. Indefinite growth of protrusions is checked by both the perpetual raft contraction and finite population of freely active agents, such that within an appropriately large domain the protrusions did not reach the simulation's boundaries.



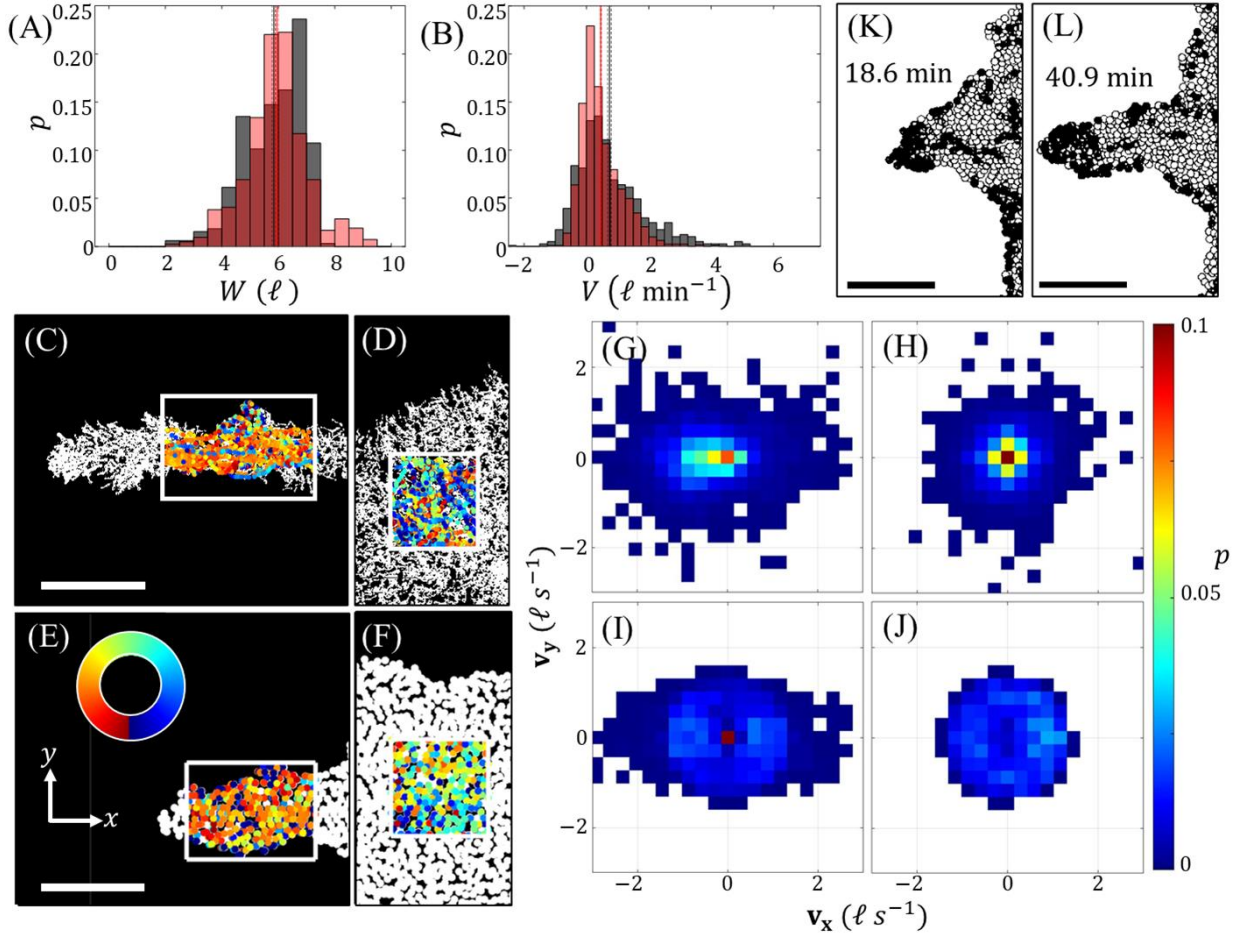


**Figure 6.4. Comparing protrusion dynamics.** (A-B) Probability mass functions are shown for (A) the average protrusion widths,  $W$ , and (B) growth rates,  $V$  of more than 400 experimental observations (grey) and numerical observations (light red) each. Here,  $R = 0.9 \ell$ ,  $\eta = 0.2$  and  $\mathcal{A} \in [1.25, 1.47]$ . (C-D) The direction of motion of free ants on experimental sections of (C) a protrusion and (D) the bulk of a raft are visually illustrated with the color of a free agent representing its direction of travel during one frame-to-frame observation. (E-F) The same visual analysis is made for sections of (E) a protrusion and (F) the bulk of a simulated raft, where the direction of travel is measured between one timestep. (C-F) Colors are assigned according to orientation based on the color wheel depicted in (E). (G-J) 2D velocity distributions are shown, courtesy of Wagner, et al. (2021). (G-H) correspond to (C-D), respectively, while (I-J) are the ensembled results from 11 *in silico* protrusions and on the order of 100,000 discrete velocity observations, each. A simulated protrusion at the start (K) and end (L) of a roughly 21 min duration exhibits how directional motion on protrusions culminates in clustering of freely active agents (black circles) at the tip and rapid, anisotropic growth. (A-B, C-D, G-H) Experimental results are courtesy of Wagner, et al. (2021). Scale bars in (C, E, K, L) represent  $10 \ell$ . All simulated rafts were initiated as circles such that the *in silico* protrusion growths depicted (and from which data were collected) occurred stochastically.

### 6.2.6 Activity level modulates shape.

Having confirmed that local-level agent interactions can lead to spontaneous instabilities, we then sought to understand the local behavioral changes that could lead to long-term variation in experimentally observed raft shapes by exploring the effects of  $\mathcal{A}$  over the range of 0.81 to 3.23. Results are summarized in **Fig 6.5** and **Fig. 6.6.A** where we visually present the effects of activity on the raft configurations during and after 1.5 hours of simulated time, respectively. From **Fig. 6.5**, we see that no protrusions emerged when  $\mathcal{A} = 1.08$ , whereas protrusions emerged within the first 30 *min* and 2 *min* when  $\mathcal{A} = 1.80$  and 2.31, respectively. Similarly, while there are numerous protrusions stemming from the rafts in **Fig. 6.6.A** when  $\mathcal{A} \geq 1.47$ , there were no distinct protrusions on the rafts when  $\mathcal{A} \leq 1.16$ , based on the definition provided earlier (i.e., width  $\leq 10 \ell$  and length  $\geq$  width). This is illustrated in **Fig. 6.6.B** by samples of the local edge curvature, each of which displays roughly the smallest geometric edge feature of its respective raft. Generally, these results indicate that higher  $\mathcal{A}$  promotes higher edge deposition rates that induced more frequent protrusion growth and more eccentric global shapes.

To quantitatively characterize global shape, we introduce a dimensionless parameter called surface excess defined by  $S = C/(2\sqrt{A\pi})$ , where  $C$  and  $A$  are a raft's perimeter length and area, respectively.  $S = 1$  for a circle and increases with a shape's eccentricity, thus higher  $S$  indicates the presence of more numerous or more elongated protrusions. Maximum surface excess and mean surface packing fractions of model results are presented in **Fig. 6.6.C**. Maximum (as opposed to mean) surface excess is presented to transparently indicate the peak degree of eccentricity achieved by the raft and exclude the inherently low surface excess of the initially circular rafts.

Moving from left to right in **Fig. 6.6.C** there is a continuous phase transition in the activity range of  $\mathcal{A} = 0.95$  to  $2.02$  indicated by the smooth curve of surface excess from low ( $S \approx 1.2$ ) to high ( $S \approx 2.8$ ). Likewise, there is a smooth transition of free active agent packing fraction from high ( $\phi \approx 1$  implying almost no edge binding, whatsoever) to low ( $\phi \approx 0.06$ , indicating relatively high edge binding rates) as  $\mathcal{A}$  increases. These phases are analogous to those observed in **Fig. 6.1.A** and **Fig. 6.1.B**, respectively.

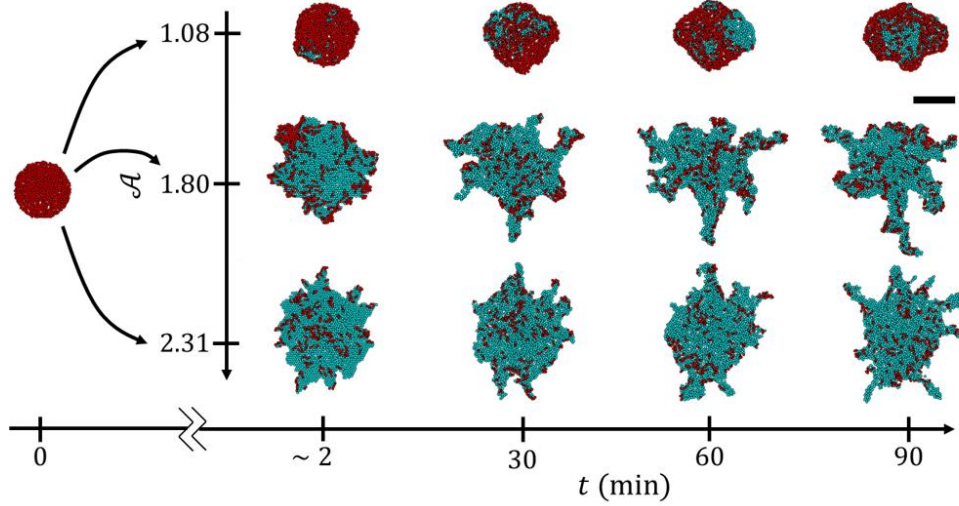


**Figure 6.5. Dynamic effects of activity level.** Snapshots of modelled rafts at different simulation times ( $t$ ) and activity levels ( $\mathcal{A}$ ) are depicted to illustrate the effect of  $\mathcal{A}$  on raft development. The raft on the far left depicts the initial conditions which were the same for each simulation throughout this work (a circular raft with  $\phi = 1$ ). On the right each row depicts a single raft as it evolves in time (moving from left to right along the horizontal axis). For all simulations shown,  $\eta = 0.2$  and  $R = 0.9 \ell$ . Structural agents are depicted in cyan, while dispersed free agents are depicted in red. The scale bar in the top right is universal to all snapshots and represents  $14 \ell$ .

Besides dictating the global presence of protrusions,  $\mathcal{A}$  also impacts the local shape of these tethers. Specifically, higher  $\mathcal{A}$  diminishes the characteristic widths and tip radii of growths as illustrated in **Fig. 6.6.B**. To quantify this, the mean protrusion tip radius,  $\langle R_K \rangle$ , (or convex edge radius for rafts in which no protrusions emerged) is plotted with respect to  $\mathcal{A}$  in **Fig. 6.6.D**. Examining **Fig. 6.6.D**,  $\mathcal{A} \leq 0.95$

distinguishes a region in which  $\langle R_\kappa \rangle \approx 10 \ell$ , which is approximately the same as the initial raft radius and is exemplary of the lack of growth at low activities. However, for  $\mathcal{A} > 0.95$ ,  $\langle R_\kappa \rangle$  decreases monotonically, indicating that regions of lower convex edge radius (or higher curvature,  $\kappa \equiv R_\kappa^{-1}$ ) begin to emerge as activity is increased. However, **Fig. 6.6.D** confirms that when  $\mathcal{A} \leq 1.16$ , the edge radii of growths were typically greater than  $5 \ell$ , suggestive of widths greater than  $10 \ell$  and mandating that growths such as those depicted in **Fig. 6.6.B** for  $\mathcal{A} \leq 1.16$  are not classifiable as protrusions given our prescribed definition. In the region defined by  $\mathcal{A} > 1.16$ ,  $\langle R_\kappa \rangle$  appears to approach and eventually reach the limit  $\langle R_\kappa \rangle \rightarrow 0.5 \ell$ , which represents a protrusion tip whose width is just one agent ( $\sim 1 \ell$ ) and is therefore the limit in this discrete system.

Mlot, et al. (2011) estimated the capillary length of ant rafts on the order of  $10 \ell$ . However, from these results we see that raft edge curvature is dependent on activity, and therefore relatable to the length scale,  $L = \ell/\mathcal{A}$ . When  $\mathcal{A}$  is low ( $L$  is high), we see smoother raft geometries (higher capillary length) with lower surface excess and edge curvature. In contrast, when  $\mathcal{A}$  is increased,  $L$  diminishes permitting the emergence of more, but narrower, protrusions. In essence, higher free agent activity reduces effective surface tension of the overall rafts, warranting a comparison of  $\mathcal{A}$  to temperature [275] in non-active materials whose surface tensions generally diminish as temperature increases [276]. Worth noting is that when  $\mathcal{A}$  is sufficiently large, the rate and azimuthal homogeneity of edge binding are high enough that expansion appears to approach an isotropic state. This is reflected by the reduction in the number and size of protrusions displayed by the raft in **Fig. 6.6.A** when  $\mathcal{A} = 3.23$ . It is likely that as  $\mathcal{A}$  increases, the propulsion force of a single agent  $f^a$  eventually becomes sufficient to cause edge binding anywhere along the raft's edge,

reducing the relative significance of local raft geometry and cooperative force  $F^a$ . Significantly, this suggests that there is, in fact, an optimal surface activity level for inducing an exploratory phase in systems that obey this model, which occurs when  $1.16 < \mathcal{A} < 3.23$ .

To demonstrate how  $\mathcal{A}$  may alter the phases of protrusion growth and non-growth, we modulated  $\mathcal{A}$  within a given model experiment to a value above ( $\mathcal{A} = 1.6$ ) and below ( $\mathcal{A} = 1.1$ ) the phase transition threshold (see **Fig. 6.6.E-K**). Indeed, this effectively toggled the raft between exploratory phases of high surface excess (e.g., **Fig. 6.6.H** and **6.6.J**) and low surface excess wherein no protrusions were present (e.g., **Fig. 6.6.I**), comparable to what was observed in experiments when free ants ceased activity. Worth noting is that the second phase of experimental protrusion growth (**Fig. 6.6.G**) did not reach the same magnitude of surface excess as the initial phase (**Fig. 6.6.E**), suggesting that either the activity level did not fully recover to its original state or not enough time was spent in this more active state to resume  $S \approx 2$ . Consequently, surface excess of the second simulated phase of protrusion growth (**Fig. 6.6.J**), exceeds that of the experimental surface excess. It is reasonable to assume that  $\mathcal{A}$  evolves roughly continuously for a real ant raft of thousands of individuals, however  $\mathcal{A}$  in the model was modulated via a binary step function, thus likely contributing to the abrupt resumption of high  $S$ . Regardless, activity level's effect on raft shape is made clear.

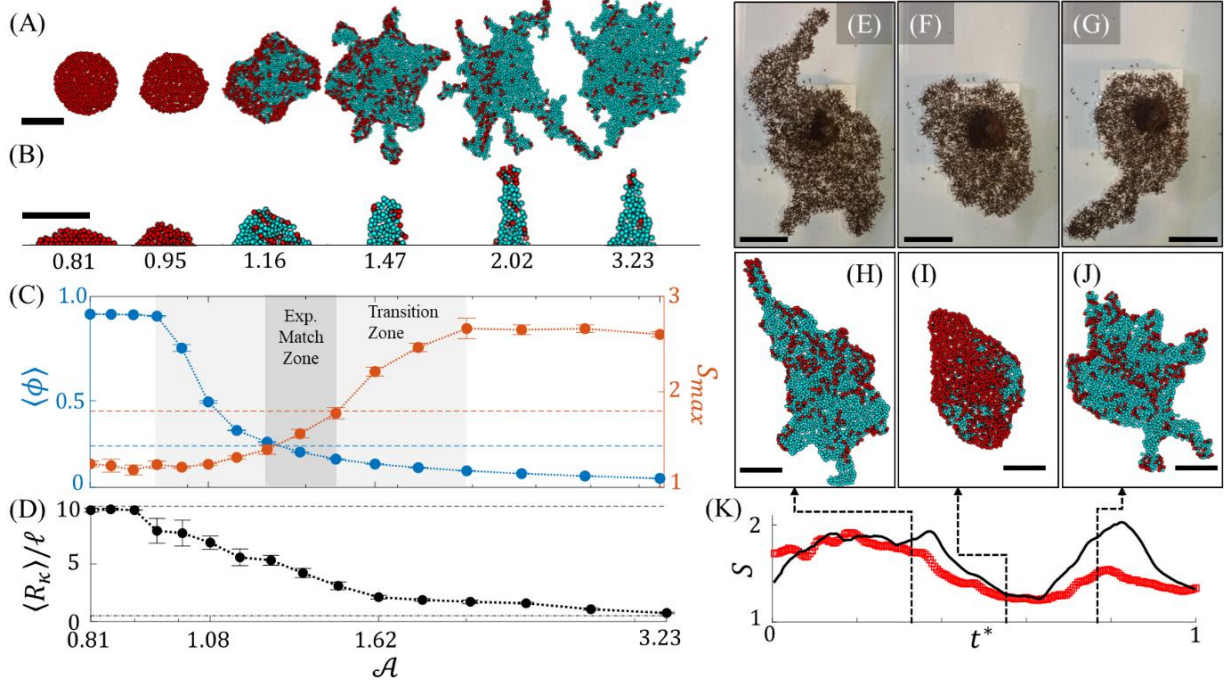


**Figure 6.6. Ant activity phases.** (A) Snapshots of initially circular, simulated rafts are shown after 1.5 hours of simulation time. Here,  $\eta = 0.2$ ,  $R = 0.9 \ell$  and  $\mathcal{A} \in [0.81, 3.23]$ . (B) Snapshots of protrusions, each representing the minimum observed radius of tip curvature from its raft at final simulation time, are depicted for each of the respective values of  $\mathcal{A}$ . The black line cropping each snapshot at its bottom is an open border to the remainder of the raft. The values of  $\mathcal{A}$  yielding each morphology for (A-B) are denoted beneath each snapshot in (B). (C) Mean freely active agent packing fraction,  $\langle\phi\rangle$ , (blue) and maximum surface excess,  $S_{max}$ , (red) are plotted with respect to  $\mathcal{A}$ , and averaged over 5 simulations at each value of  $\mathcal{A}$ , with error bars presenting standard error of the mean. Horizontal dotted lines in (C) represent the experimentally measured values of  $\phi = 0.24$  and  $S_{max} \approx 1.8$ . The bounds of the parameter space that matches experiments are marked where these respective lines intersect the numerical data (see “Exp. Match Zone” between  $\mathcal{A} = 1.25$  and  $1.47$ ). There exists a zone between roughly  $\mathcal{A} = 1.0$  and  $2.0$  of continuous phase transition between rafts with minimal-to-no growth whatsoever ( $\phi \approx 1$  and  $S \sim 1.2$ ) at low activity levels and frequent protrusion growth (low  $\phi$  and  $S > 2$ ) at high activity levels. (D) Mean protrusion tip radius ( $R_k$ ) is plotted with respect to  $\mathcal{A}$ . Anywhere from four (in the case of no growth) to forty-one observations were ensemble averaged depending on protrusion frequency. Where no protrusions were available ( $\mathcal{A} \leq 1.16$ ) the mean convex edge radius is reported instead. The top dotted line represents the initial raft diameter of  $10 \ell$ , while the bottom dotted line represents the limit of  $R_k \rightarrow 0.5 \ell$ , corresponding to the radius of one agent. (C-D) share a horizontal axis. (E-G) Three chronological snapshots of an experimental ant raft exhibiting different phases of protrusion growth are compared to (H-J) three chronological snapshots of a simulated raft when  $\mathcal{A}$  was modulated between  $1.1$  and  $1.6$ . (K) The time evolution of surface excess as measured from one experiment (red circles) and ensemble averaged over 28 numerical simulations (black curve with a negligible shaded region representing standard error of the mean) are displayed. Note that the simulations start close to  $S = 1$  given the initially circular raft shape. Time,  $t^*$ , is normalized by the experiment duration for a more direct comparison. Structural agents are depicted in cyan, while dispersed free agents are depicted in red. All scale bars represent  $10 \ell$ . All simulated rafts displayed were initiated as circles such that protrusions emerged stochastically.

### 6.3 Discussion

Our results indicate that fire ant rafts may exhibit spontaneous protrusion growth in the absence of external gradients or long-range interactions. While cueing factors such as pheromones have not been ruled out and should be tested for in future experimental studies, this model generally poses local mechanisms through which fire ants may achieve treadmilling and protrusion growth without centralized control or purposeful intent. Nevertheless, protrusions may sometimes serve the adaptive purpose of helping fire ants escape flooded environments, perhaps illustrating an example in which spontaneous cooperative behavior benefits a collective organism. Through the model, we find that the global shape of these rafts and their display of protrusions is highly dependent on the activity parameter  $\mathcal{A}$ , which characterizes the competition between an ant's self-propulsion and its aversion to water. Supposing free ants' aversion to water does not vary significantly, then  $\mathcal{A}$  may be interpreted as the normalized force with which free ants self-propel. Inversely, if self-propulsion force is conserved, then increased  $\mathcal{A}$  may be thought of as a reduced inhibition to structural edge deposition by ants. In either case, the model suggests that a behavioral change by solely the freely active ants may significantly impact the size and shape of ant rafts observed. Tennenbaum and Fernandez-Nieves (2020) demonstrated that temporal activity cycles in fire ants on the order of hours also impact the rheological properties of 3D aggregations. Based on our model, we suspect that this same oscillation of ant behavior between inactive and active states is responsible for the morphological variation in ant rafts. Indeed, in our previous work, we experimentally observed that the clustering of inactive, yet free ants near the centers of their rafts preceded the overall reduction in raft area and reduction in

surface excess [11]. During this time, the contraction of the structural layer remained relatively constant.

This model also offers an explanation regarding the directional bias in edge deposition that our previous work indicated is necessary for the evolution of elongated protrusions [11]. We see that strong confinement of active agents on protrusions promotes their directional motion towards the protrusions' tips, whereas active agent motion is isotropic on the rafts' bulk sections. Since we enforce that freely active agents deposit into the water in a direction that is correlated with their movement and that of their nearest neighbors (as determined by the local active force,  $\mathbf{F}^a$ ), this directional motion then promotes local edge growth that is aligned with the longitudinal axis of the protrusions. Through this rule, the shapes and growth rates of model-predicted protrusions are in good agreement with those of experiments, thereby supporting the hypothesis that confinement-induced directional motion is a contributing second-order cause of runaway protrusion growth in ant rafts. Ultimately, these results do not nullify the potential influence of biological stimuli (e.g., morphogens or pheromones), rather they support the notion that physics-driven mechanisms may aid or provided a redundant pathway for emergent protrusion growth in ant rafts.

While this discrete model helps interpret potential causes of protrusion growth in ant rafts, there exists several limitations that could influence the accurate representation of free ants by free agent trajectories and therefore global raft evolution. First, free agent movement is restricted to a lattice defined by structural agents and water nodes, which simplifies the model in several ways. For example, it alleviates the need to interpolate a continuous raft boundary, and free agents' encounters with the water



are discretely defined as instances when their preferred movement DOF is a water node. It also renders interpolation of the energy landscape unnecessary at the location of free agents (when computing  $\mathbf{F}^I$ ) since each free agent is already located on a structural agent. Additionally, it permits easy mimicry of volume exclusion between neighboring free agents, by prohibiting two free agents from occupying the same structural site. Finally, it eliminates the need for explicit constraints on agents' speeds (e.g., frictional forces or inertia) since the agents can move, at most, a distance of  $R_{DOF}$  within a given timestep. However, this lattice naturally introduces a degree of error between the continuously predicted direction of motion from Eqn. (6.1) and the actual direction of discrete movement. This could potentially influence the global raft evolution since it impacts the direction of structural deposition for agents at the raft's edge. Another discrepancy that could potentially influence the predicted raft evolution is that we opt to treat the ants as particles whose orientational DOF is in-line with their direction of motion. Coupling the translational DOF with the rotational DOF significantly reduces model complexity, yet it effectively surmises that the timescale of alignment is considerably smaller than a discrete timestep. To preserve finite alignment and turning times, we instead restricted the maximum turning angle of an agent within a given step and introduced a pause time in the event that an agent is limited to movements outside this angular range. Additionally, we assume radial symmetry or that the agents have an aspect ratio of one. In reality, fire ants have an aspect ratio on the order of 3:1 [277], [278] and it is well-documented that aspect ratios can introduce alignment effects in self-propelled particles [279]. Indeed, in our previous work [11], we saw evidence of non-negligible ant-to-ant interactions that caused short-range correlation between the motion of nearest neighbors. However, to capture local alignment we opted to employ the relatively simple and phenomenological Vicsek model rather than explicitly modeling

an aspect ratio and repulsive interactions. A final limitation that may impact free agent trajectories is that agents were not allowed to walk over one another despite such behavior being regularly observed in freely active ants. This may have exaggerated the effects of volume exclusion between ants and consequently exacerbated any local alignment in velocity by limiting free agents' local movement degrees of freedom.

Despite these limitations and their potential effects on free agent trajectories, we found that the model sufficiently approximated continuous space when 18 DOF were given to each free agent and the lattice was stochastically updated due to unbinding events and contraction. This is demonstrated by the isotropic distribution of the agent velocities in **Fig. 6.4.J** and a general lack in any preferential direction for protrusion growths throughout this work. Furthermore, the mean persistence length of free agents' trajectories (on the bulk of the modeled rafts), as well as the degree of directional motion (on both bulk sections of the rafts and protrusions) (**Fig. 6.4.E-F**) were both reasonably matched to experiments. However, one ant trajectory feature that remained uncaptured by the model is the frequent jamming of free ants far from the edges of the rafts, as indicated by the peak of the velocity distribution at  $\mathbf{v} \approx [0,0] \ell s^{-1}$  in **Fig. 6.4.H**. While free agents in the model were prompted to move at every timestep unless they had no unoccupied DOF, free ants were regularly observed stopping to clean themselves or interact with other ants, regardless of whether their movement was inhibited by obstacles. This discrepancy also appears in the velocity distributions of free ants (**Fig. 6.4.G**) versus agents (**Fig. 6.4.I**) on protrusions, with simulated free agents generally displaying a much more homogenous distribution of velocities. It is likely that this heightened motility of free agents exaggerates their diffusivity over their ant counterparts; however, the instantaneous distributions of

free members – which more directly influence raft evolution – were in good agreement between experiments and simulations.

Another limitation of this model is that it does not currently accommodate inclusion of local cues or external gradients. Such stimuli could enhance the degree of order in the system and if they were introduced by the fire ants themselves (e.g., pheromone trails [262]–[265], [267]; memory over second timescales and centimeter length scales; or collective memory through propagated short range social interactions [280]) they would effectively serve as long-range interaction potentials. Indeed, a precursory study reveals high sensitivity to the pairwise influence length scale  $R$ , which if set slightly higher ( $R = 1.23 \ell$ ) leads to the prediction of longer, more ordered protrusion growth at low activities ( $\mathcal{A} = 0.81$ ), as depicted in the top right corner of **Fig. E.6.A** (see Appendix E.5.c for details). Moreover, the emergent structural network contraction and unbinding events were simply reproduced here via a homogenized, phenomenological model. Yet the underlying behavioral rules, mechanisms, and the sequence in which they occur are likely far more complex for raft contraction and will be investigated in future work. For both states of ants, there is likely more than one set of rules that results in treadmilling and protrusion growth. Here we have merely investigated a distilled set of local interactions which reproduced the observed raft evolutions, thereby reducing the number of variable considerations and isolating the effects of local ant activity level on global shape. Nevertheless, phenomena such as local pheromones or external temperature gradients, could be easily included in future iterations for the study of not only fire ants but also other constituents. Therefore, although this numerical implementation was inspired by fire ant rafts, we also expect that in future work it may be adapted or inspiration for the *in silico* investigation of other biological or synthetic systems driven by transport and binding

reactions. Additionally, this model permits the investigation of emergent phenomena and global characteristics outside the biologically observed parametric space, as occurred here for the purposes of fitting  $R$  and  $\eta$  (see **Fig. E.5** and **E.6**), and then investigating the effects of  $\mathcal{A}$  (see **Fig. 6.6** and **Fig. E.7**). Thus, this model may permit extrapolation of properties and potentially serve as a source of inspiration for the predictive design of engineered systems such as active gels or swarm robotics.

## CHAPTER VII

### SUMMARY AND FUTURE WORK

In this thesis, we introduced a discrete network modeling framework intended for the micromechanical study of dynamic polymers. We then utilized this model to update TNT via a coupled rule of mixture, applicable to dynamic networks containing multiple bond types with different dissociation timescales in series. To exhibit the applicability of this model in predictive mechanics, we then used it to reproduce the mechanical response of stable gels. Finally, we retrofit the model with active contraction and an agent-based modeling approach to reproduce and understand the origins of treadmilling and protrusion growth as experimentally observed in the rafts of fire ants. Together, these works demonstrate the broad applicability of this modelling approach while motivating its necessity for bridging the gap between local physical interactions and globally emergent mechanical responses in dynamic and active networks.

While the existing iteration of the modeling framework is written in MATLAB 2019b, in future work, the methodologies introduced here may be incorporated into an open-source, highly parallelized framework such as LAMMPS (written in a compiled language such as C++). Doing so would greatly improve the spatiotemporal scales that may be modeled through these methods, thus permitting broader investigation of materials with higher degrees of hierarchical microstructure and heterogeneity such as poly(acrylamide) gels. This may also facilitate this model's direct use in the predictive design of tetra-PEG based gels containing multiple telechelic bond types in series [13]. Such gels are prospects as mesenchymal stem cell scaffolds for osteochondral tissue engineering. However, the synthesis of gels with desired

mechanical properties (e.g., shear modulus) may be expedited by narrowing the parametric space explored by experimentalists through predictive use of the model. Additionally, other micromechanical physics may be implemented into this framework to broaden its applicability. With regards to polymeric systems, we next aim to develop ways to statistically represent and incorporate the effects of entanglement into the model at the mesoscale, which may allow for direct investigation of systems such as polymer melts. Pertaining to active networks, we next aim to leverage the iteration of the model applied to fire ants to study the formation of stress fibers and intrinsic mechanosensitivity emerging from the incorporation of catch bond mechanics and active contraction. Doing so may elucidate mechanistic origins of material reconstitution by living systems and eventually inspire comparably designed mechanisms in synthetic, self-optimizing, structural materials.

## Bibliography

- [1] F. J. Vernerey, R. Long, and R. Brighenti, “A statistically-based continuum theory for polymers with transient networks,” *Journal of the Mechanics and Physics of Solids*, vol. 107, pp. 1–20, Oct. 2017, doi: 10.1016/j.jmps.2017.05.016.
- [2] T. Shen and F. J. Vernerey, “Rate-dependent fracture of transient networks,” *Journal of the Mechanics and Physics of Solids*, vol. 143, p. 104028, Oct. 2020, doi: 10.1016/j.jmps.2020.104028.
- [3] R. J. Wagner, E. Hobbs, and F. J. Vernerey, “A network model of transient polymers: exploring the micromechanics of nonlinear viscoelasticity,” *Soft Matter*, Aug. 2021, doi: 10.1039/D1SM00753J.
- [4] D. L. Hu, S. Phonekeo, E. Altshuler, and F. Brochard-Wyart, “Entangled active matter: From cells to ants,” *Eur. Phys. J. Spec. Top.*, vol. 225, no. 4, pp. 629–649, Jul. 2016, doi: 10.1140/epjst/e2015-50264-4.
- [5] F. J. Vernerey *et al.*, “Biological active matter aggregates: Inspiration for smart colloidal materials,” *Advances in Colloid and Interface Science*, vol. 263, pp. 38–51, Jan. 2019, doi: 10.1016/j.cis.2018.11.006.
- [6] I. Buttinoni, J. Bialké, F. Kümmel, H. Löwen, C. Bechinger, and T. Speck, “Dynamical Clustering and Phase Separation in Suspensions of Self-Propelled Colloidal Particles,” *Phys. Rev. Lett.*, vol. 110, no. 23, p. 238301, Jun. 2013, doi: 10.1103/PhysRevLett.110.238301.
- [7] A. Czirók, H. E. Stanley, and T. Vicsek, “Spontaneously ordered motion of self-propelled particles,” *J. Phys. A: Math. Gen.*, vol. 30, no. 5, p. 1375, 1997, doi: 10.1088/0305-4470/30/5/009.
- [8] M. Poujade *et al.*, “Collective migration of an epithelial monolayer in response to a model wound,” *Proc. Natl. Acad. Sci. U.S.A.*, vol. 104, no. 41, pp. 15988–15993, Oct. 2007, doi: 10.1073/pnas.0705062104.
- [9] L. Atia *et al.*, “Geometric constraints during epithelial jamming,” *Nature Phys*, vol. 14, no. 6, pp. 613–620, Jun. 2018, doi: 10.1038/s41567-018-0089-9.
- [10] F. Posta and T. Chou, “A mathematical model of intercellular signaling during epithelial wound healing,” *Journal of Theoretical Biology*, vol. 266, no. 1, pp. 70–78, 2010, doi: 10.1016/j.jtbi.2010.05.029.
- [11] R. J. Wagner, K. Such, E. Hobbs, and F. J. Vernerey, “Treadmilling and dynamic protrusions in fire ant rafts,” *Journal of The Royal Society Interface*, Jun. 2021, doi: 10.1098/rsif.2021.0213.
- [12] R. J. Wagner and F. J. Vernerey, “Computational exploration of treadmilling and protrusion growth observed in fire ant rafts,” *PLOS Computational Biology*, vol. 18, no. 2, p. e1009869, Feb. 2022, doi: 10.1371/journal.pcbi.1009869.
- [13] B. M. Richardson, D. G. Wilcox, M. A. Randolph, and K. S. Anseth, “Hydrazone covalent adaptable networks modulate extracellular matrix deposition for cartilage tissue engineering,” *Acta Biomaterialia*, vol. 83, pp. 71–82, Jan. 2019, doi: 10.1016/j.actbio.2018.11.014.
- [14] L. R. Smith, S. Cho, and D. E. Discher, “Stem Cell Differentiation is Regulated by Extracellular Matrix Mechanics,” *Physiology*, vol. 33, no. 1, pp. 16–25, Jan. 2018, doi: 10.1152/physiol.00026.2017.

- [15] B. Choi *et al.*, “Stiffness of Hydrogels Regulates Cellular Reprogramming Efficiency Through Mesenchymal-to-Epithelial Transition and Stemness Markers,” *Macromolecular Bioscience*, vol. 16, no. 2, pp. 199–206, Feb. 2016, doi: 10.1002/mabi.201500273.
- [16] O. Chaudhuri *et al.*, “Hydrogels with tunable stress relaxation regulate stem cell fate and activity,” *Nat Mater*, vol. 15, no. 3, pp. 326–334, Mar. 2016, doi: 10.1038/nmat4489.
- [17] V. Trianni, S. Nolfi, and M. Dorigo, “Evolution, Self-organization and Swarm Robotics,” in *Swarm Intelligence: Introduction and Applications*, C. Blum and D. Merkle, Eds. Berlin, Heidelberg: Springer, 2008, pp. 163–191. doi: 10.1007/978-3-540-74089-6\_5.
- [18] J. T. Ebert, M. Gauci, and R. Nagpal, “Multi-Feature Collective Decision Making in Robot Swarms,” in *Proceedings of the 17th International Conference on Autonomous Agents and MultiAgent Systems*, Richland, SC, 2018, pp. 1711–1719. Accessed: Nov. 21, 2018. [Online]. Available: <http://dl.acm.org/citation.cfm?id=3237383.3237953>
- [19] M. Rubenstein, A. Cornejo, and R. Nagpal, “Programmable self-assembly in a thousand-robot swarm,” *Science*, vol. 345, no. 6198, pp. 795–799, Aug. 2014, doi: 10.1126/science.1254295.
- [20] M. Vigeliuss, B. Meyer, and G. Pascoe, “Multiscale Modelling and Analysis of Collective Decision Making in Swarm Robotics,” *PLOS ONE*, vol. 9, no. 11, p. e111542, Nov. 2014, doi: 10.1371/journal.pone.0111542.
- [21] Y. Vidavsky, S. Bae, and M. N. Silberstein, “Modulating metallopolymer mechanical properties by controlling metal ligand crosslinking,” *Journal of Polymer Science Part A: Polymer Chemistry*, vol. 56, no. 11, pp. 1117–1122, 2018, doi: 10.1002/pola.28994.
- [22] Y. Vidavsky *et al.*, “Tuning the Mechanical Properties of Metallopolymers via Ligand Interactions: A Combined Experimental and Theoretical Study,” *Macromolecules*, vol. 53, no. 6, pp. 2021–2030, Mar. 2020, doi: 10.1021/acs.macromol.9b02756.
- [23] X. Zhang *et al.*, “Bridging experiments and theory: isolating the effects of metal–ligand interactions on viscoelasticity of reversible polymer networks,” *Soft Matter*, vol. 16, no. 37, pp. 8591–8601, Sep. 2020, doi: 10.1039/D0SM01115K.
- [24] D. Helbing and P. Molnár, “Social force model for pedestrian dynamics,” *Phys. Rev. E*, vol. 51, no. 5, pp. 4282–4286, May 1995, doi: 10.1103/PhysRevE.51.4282.
- [25] N. Shiwakoti, M. Sarvi, G. Rose, and M. Burd, “Biologically Inspired Modeling Approach for Collective Pedestrian Dynamics Under Emergency Conditions,” *Transportation Research Record: Journal of the Transportation Research Board*, vol. 2196, no. 1, pp. 176–184, 2011, doi: 10.3141/2196-19.
- [26] R. T. Tranquillo, D. A. Lauffenburger, and S. H. Zigmond, “A stochastic model for leukocyte random motility and chemotaxis based on receptor binding fluctuations,” *J. Cell Biol.*, vol. 106, no. 2, pp. 303–309, Feb. 1988, doi: 10.1083/jcb.106.2.303.
- [27] R. M. Donovan *et al.*, “Unbiased Rare Event Sampling in Spatial Stochastic Systems Biology Models Using a Weighted Ensemble of Trajectories,” *PLOS Computational Biology*, vol. 12, no. 2, p. e1004611, Feb. 2016, doi: 10.1371/journal.pcbi.1004611.
- [28] J. E. Andrade, C. F. Avila, S. A. Hall, N. Lenoir, and G. Viggiani, “Multiscale modeling and characterization of granular matter: From grain kinematics to continuum mechanics,” *Journal of the Mechanics and Physics of Solids*, vol. 59, no. 2, pp. 237–250, Feb. 2011, doi: 10.1016/j.jmps.2010.10.009.
- [29] A. Gooneie, S. Schuschnigg, and C. Holzer, “A Review of Multiscale Computational Methods in Polymeric Materials,” *Polymers*, vol. 9, no. 1, Art. no. 1, Jan. 2017, doi: 10.3390/polym9010016.



- [30] L. A. A. Beex, P. Kerfriden, T. Rabczuk, and S. P. A. Bordas, “Quasicontinuum-based multiscale approaches for plate-like beam lattices experiencing in-plane and out-of-plane deformation,” *Computer Methods in Applied Mechanics and Engineering*, vol. 279, pp. 348–378, Sep. 2014, doi: 10.1016/j.cma.2014.06.018.
- [31] S. Ishihara, P. Marcq, and K. Sugimura, “From cells to tissue: A continuum model of epithelial mechanics,” *Phys. Rev. E*, vol. 96, no. 2, p. 022418, Aug. 2017, doi: 10.1103/PhysRevE.96.022418.
- [32] G. Hozapfel, *Nonlinear Solid Mechanics: A Continuum Approach for Engineering*. Wiley, 2000.
- [33] F. J. Vernerey, R. Brighenti, R. Long, and T. Shen, “Statistical Damage Mechanics of Polymer Networks,” *Macromolecules*, vol. 51, no. 17, pp. 6609–6622, Sep. 2018, doi: 10.1021/acs.macromol.8b01052.
- [34] S. G. Bardenhagen, M. G. Stout, and G. T. Gray, “Three-dimensional, finite deformation, viscoplastic constitutive models for polymeric materials,” *Mechanics of Materials*, vol. 25, no. 4, pp. 235–253, May 1997, doi: 10.1016/S0167-6636(97)00007-0.
- [35] C.-Y. Hui and R. Long, “A constitutive model for the large deformation of a self-healing gel,” *Soft Matter*, vol. 8, no. 31, pp. 8209–8216, Jul. 2012, doi: 10.1039/C2SM25367D.
- [36] M. R. Buche and M. N. Silberstein, “Statistical mechanical constitutive theory of polymer networks: The inextricable links between distribution, behavior, and ensemble,” *Phys. Rev. E*, vol. 102, no. 1, p. 012501, Jul. 2020, doi: 10.1103/PhysRevE.102.012501.
- [37] M. R. Buche and M. N. Silberstein, “Chain breaking in the statistical mechanical constitutive theory of polymer networks,” *Journal of the Mechanics and Physics of Solids*, vol. 156, p. 104593, Nov. 2021, doi: 10.1016/j.jmps.2021.104593.
- [38] S. N. Coppersmith, “Overdamped Frenkel-Kontorova model with randomness as a dynamical system: Mode locking and derivation of discrete maps,” *Phys. Rev. A*, vol. 36, no. 7, pp. 3375–3382, Oct. 1987, doi: 10.1103/PhysRevA.36.3375.
- [39] D. Rodney, M. Fivel, and R. Dendievel, “Discrete modeling of the mechanics of entangled materials,” *Phys. Rev. Lett.*, vol. 95, no. 10, p. 108004, Sep. 2005, doi: 10.1103/PhysRevLett.95.108004.
- [40] A. Mauri, R. Hopf, A. E. Ehret, C. R. Picu, and E. Mazza, “A discrete network model to represent the deformation behavior of human amnion,” *Journal of the Mechanical Behavior of Biomedical Materials*, vol. 58, pp. 45–56, May 2016, doi: 10.1016/j.jmbbm.2015.11.009.
- [41] H. Tao *et al.*, “Discrete element method modeling of non-spherical granular flow in rectangular hopper,” *Chemical Engineering and Processing: Process Intensification*, vol. 49, no. 2, pp. 151–158, Feb. 2010, doi: 10.1016/j.cep.2010.01.006.
- [42] G. K. J. Nave, N. T. Mitchell, J. A. Chan Dick, T. Schuessler, J. A. Lagarrigue, and O. Peleg, “Attraction, Dynamics, and Phase Transitions in Fire Ant Tower-Building,” *Front. Robot. AI*, vol. 7, 2020, doi: 10.3389/frobt.2020.00025.
- [43] M. N. Bannerman, R. Sargant, and L. Lue, “DynamO: a free  $\mathcal{O}(N)$  general event-driven molecular dynamics simulator,” *Journal of Computational Chemistry*, vol. 32, no. 15, pp. 3329–3338, 2011, doi: 10.1002/jcc.21915.
- [44] N. Jiang, H. Zhang, Y. Yang, and P. Tang, “Molecular dynamics simulation of associative polymers: Understanding linear viscoelasticity from the sticky Rouse model,” *Journal of Rheology*, vol. 65, no. 4, pp. 527–547, Jul. 2021, doi: 10.1122/8.0000218.

- [45] H. Lee and R. G. Larson, “Molecular Dynamics Study of the Structure and Interparticle Interactions of Polyethylene Glycol-Conjugated PAMAM Dendrimers,” *J. Phys. Chem. B*, vol. 113, no. 40, pp. 13202–13207, Oct. 2009, doi: 10.1021/jp906497e.
- [46] Z. Song, Z. Wang, and S. Cai, “Mechanics of vitrimer with hybrid networks,” *Mechanics of Materials*, vol. 153, p. 103687, Feb. 2021, doi: 10.1016/j.mechmat.2020.103687.
- [47] K. Mayumi, J. Guo, T. Narita, C. Y. Hui, and C. Creton, “Fracture of dual crosslink gels with permanent and transient crosslinks,” *Extreme Mechanics Letters*, vol. 6, pp. 52–59, Mar. 2016, doi: 10.1016/j.eml.2015.12.002.
- [48] X. Li *et al.*, “Mesoscale bicontinuous networks in self-healing hydrogels delay fatigue fracture,” *PNAS*, vol. 117, no. 14, pp. 7606–7612, Apr. 2020, doi: 10.1073/pnas.2000189117.
- [49] R. J. Wagner, J. Dai, X. Su, and F. J. Vernerey, “A mesoscale model for the micromechanical study of gels,” *Journal of the Mechanics and Physics of Solids*, p. 104982, Jun. 2022, doi: 10.1016/j.jmps.2022.104982.
- [50] H. Tabuteau, S. Mora, G. Porte, M. Abkarian, and C. Ligoure, “Microscopic mechanisms of the brittleness of viscoelastic fluids,” *Phys. Rev. Lett.*, vol. 102, no. 15, p. 155501, Apr. 2009, doi: 10.1103/PhysRevLett.102.155501.
- [51] S. Fürthauer *et al.*, “Self-straining of actively crosslinked microtubule networks,” *Nature Physics*, vol. 15, no. 12, Art. no. 12, Dec. 2019, doi: 10.1038/s41567-019-0642-1.
- [52] M. Tennenbaum, Z. Liu, D. Hu, and A. Fernandez-Nieves, “Mechanics of fire ant aggregations,” *Nature Materials*, vol. 15, no. 1, p. 54, Jan. 2016, doi: 10.1038/nmat4450.
- [53] F. J. Vernerey, T. Shen, S. L. Sridhar, and R. J. Wagner, “How do fire ants control the rheology of their aggregations? A statistical mechanics approach,” *Journal of The Royal Society Interface*, vol. 15, no. 147, p. 20180642, Oct. 2018, doi: 10.1098/rsif.2018.0642.
- [54] O. Peleg, J. M. Peters, M. K. Salcedo, and L. Mahadevan, “Collective mechanical adaptation of honeybee swarms,” *Nature Physics*, p. 1, Sep. 2018, doi: 10.1038/s41567-018-0262-1.
- [55] N. Roy, B. Bruchmann, and J.-M. Lehn, “DYNAMERS: dynamic polymers as self-healing materials,” *Chemical Society Reviews*, vol. 44, no. 11, pp. 3786–3807, May 2015, doi: 10.1039/C5CS00194C.
- [56] S. A. Rincon *et al.*, “Kinesin-5-independent mitotic spindle assembly requires the antiparallel microtubule crosslinker Ase1 in fission yeast,” *Nature Communications*, vol. 8, p. 15286, May 2017, doi: 10.1038/ncomms15286.
- [57] C. Shi *et al.*, “Investigating the Self-Healing of Dynamic Covalent Thermoset Polyimine and Its Nanocomposites,” *Journal of Applied Mechanics*, vol. 86, no. 101005, Jul. 2019, doi: 10.1115/1.4044088.
- [58] S. Lalitha Sridhar, J. Dunagin, K. Koo, L. Hough, and F. Vernerey, “Enhanced Diffusion by Reversible Binding to Active Polymers,” *Macromolecules*, vol. 54, no. 4, pp. 1850–1858, Feb. 2021, doi: 10.1021/acs.macromol.0c02306.
- [59] T. Koga and F. Tanaka, “Molecular origin of shear thickening in transient polymer networks: A molecular dynamics study,” *Eur. Phys. J. E*, vol. 17, no. 2, pp. 115–118, Jun. 2005, doi: 10.1140/epje/i2005-10010-2.
- [60] T. Shen, R. Long, and F. Vernerey, “Computational modeling of the large deformation and flow of viscoelastic polymers,” *Comput Mech*, vol. 63, no. 4, pp. 725–745, Apr. 2019, doi: 10.1007/s00466-018-1619-0.

- [61] Y. Yu, N. Bouklas, C. M. Landis, and R. Huang, “A Linear Poroelastic Analysis of Time-Dependent Crack-Tip Fields in Polymer Gels,” *Journal of Applied Mechanics*, vol. 85, no. 111011, Aug. 2018, doi: 10.1115/1.4041040.
- [62] P. L. Chandran and V. H. Barocas, “Affine Versus Non-Affine Fibril Kinematics in Collagen Networks: Theoretical Studies of Network Behavior,” *Journal of Biomechanical Engineering*, vol. 128, no. 2, pp. 259–270, Oct. 2005, doi: 10.1115/1.2165699.
- [63] Q. Wen, A. Basu, P. A. Janmey, and A. G. Yodh, “Non-affine deformations in polymer hydrogels,” *Soft Matter*, vol. 8, no. 31, pp. 8039–8049, Jan. 2012, doi: 10.1039/c2sm25364j.
- [64] R. Petrosyan, “Improved approximations for some polymer extension models,” *Rheol Acta*, vol. 56, no. 1, pp. 21–26, Jan. 2017, doi: 10.1007/s00397-016-0977-9.
- [65] Henry. Eyring, “The Activated Complex and the Absolute Rate of Chemical Reactions.,” *Chem. Rev.*, vol. 17, no. 1, pp. 65–77, Aug. 1935, doi: 10.1021/cr60056a006.
- [66] A. P. Tabatabai, D. S. Seara, J. Tibbs, V. Yadav, I. Linsmeier, and M. P. Murrell, “Detailed Balance Broken by Catch Bond Kinetics Enables Mechanical-Adaptation in Active Materials,” *Advanced Functional Materials*, vol. 31, no. 10, p. 2006745, 2021, doi: 10.1002/adfm.202006745.
- [67] A. Aksimentiev and R. Holyst, “Single-chain statistics in polymer systems,” *Progress in Polymer Science*, vol. 24, no. 7, pp. 1045–1093, Sep. 1999, doi: 10.1016/S0079-6700(99)00023-4.
- [68] R. C. Picu, “Mechanics of random fiber networks—a review,” *Soft Matter*, vol. 7, no. 15, pp. 6768–6785, Jul. 2011, doi: 10.1039/C1SM05022B.
- [69] H. Hatami-Marbini and R. C. Picu, “Scaling of nonaffine deformation in random semiflexible fiber networks,” *Phys. Rev. E*, vol. 77, no. 6, p. 062103, Jun. 2008, doi: 10.1103/PhysRevE.77.062103.
- [70] H. Hatami-Marbini and M. Rohanifar, “Mechanical properties of subisostatic random networks composed of nonlinear fibers,” *Soft Matter*, vol. 16, no. 30, pp. 7156–7164, 2020, doi: 10.1039/D0SM00523A.
- [71] S. Arbabi and M. Sahimi, “Mechanics of disordered solids. I. Percolation on elastic networks with central forces,” *Phys. Rev. B*, vol. 47, no. 2, pp. 695–702, Jan. 1993, doi: 10.1103/PhysRevB.47.695.
- [72] G. I. Bell, “Models for the specific adhesion of cells to cells,” *Science*, vol. 200, no. 4342, pp. 618–627, May 1978.
- [73] A. E. Elbanna and J. M. Carlson, “Dynamics of Polymer Molecules with Sacrificial Bond and Hidden Length Systems: Towards a Physically-Based Mesoscopic Constitutive Law,” *PLOS ONE*, vol. 8, no. 4, p. e56118, Apr. 2013, doi: 10.1371/journal.pone.0056118.
- [74] K. Kothari, Y. Hu, S. Gupta, and A. Elbanna, “Mechanical Response of Two-Dimensional Polymer Networks: Role of Topology, Rate Dependence, and Damage Accumulation,” *Journal of Applied Mechanics*, vol. 85, no. 3, Jan. 2018, doi: 10.1115/1.4038883.
- [75] K. Mikeš and M. Jirásek, “Quasicontinuum method extended to irregular lattices,” *Computers & Structures*, vol. 192, pp. 50–70, Nov. 2017, doi: 10.1016/j.compstruc.2017.07.002.
- [76] A. Ghareeb and A. Elbanna, “An adaptive quasicontinuum approach for modeling fracture in networked materials: Application to modeling of polymer networks,” *Journal of the Mechanics and Physics of Solids*, vol. 137, p. 103819, Apr. 2020, doi: 10.1016/j.jmps.2019.103819.

- [77] A. Ghareeb and A. Elbanna, “Modeling fracture in rate-dependent polymer networks: A quasicontinuum approach,” *Journal of Applied Mechanics*, pp. 1–22, Jul. 2021, doi: 10.1115/1.4051658.
- [78] Z. Yang, Q. Wang, and T. Wang, “Dual-Triggered and Thermally Reconfigurable Shape Memory Graphene-Vitrimer Composites,” *ACS Appl. Mater. Interfaces*, vol. 8, no. 33, pp. 21691–21699, Aug. 2016, doi: 10.1021/acsami.6b07403.
- [79] G. Singh and V. Sundararaghavan, “Modeling self-healing behavior of vitrimers using molecular dynamics with dynamic cross-linking capability,” *Chemical Physics Letters*, vol. 760, p. 137966, Dec. 2020, doi: 10.1016/j.cplett.2020.137966.
- [80] E. B. Stukalin, L.-H. Cai, N. A. Kumar, L. Leibler, and M. Rubinstein, “Self-Healing of Unentangled Polymer Networks with Reversible Bonds,” *Macromolecules*, vol. 46, no. 18, pp. 7525–7541, Sep. 2013, doi: 10.1021/ma401111n.
- [81] S. Tang, A. Habicht, S. Li, S. Seiffert, and B. D. Olsen, “Self-Diffusion of Associating Star-Shaped Polymers,” *Macromolecules*, vol. 49, no. 15, pp. 5599–5608, Aug. 2016, doi: 10.1021/acs.macromol.6b00959.
- [82] N. P. Thien and R. I. Tanner, “A new constitutive equation derived from network theory,” *Journal of Non-Newtonian Fluid Mechanics*, vol. 2, no. 4, pp. 353–365, Jul. 1977, doi: 10.1016/0377-0257(77)80021-9.
- [83] M. Doi and S. F. Edwards, “Dynamics of concentrated polymer systems. Part 4.—Rheological properties,” *J. Chem. Soc., Faraday Trans. 2*, vol. 75, no. 0, pp. 38–54, Jan. 1979, doi: 10.1039/F29797500038.
- [84] S. Q. Wang, “Transient network theory for shear-thickening fluids and physically crosslinked networks,” *Macromolecules*, vol. 25, no. 25, pp. 7003–7010, Dec. 1992, doi: 10.1021/ma00051a043.
- [85] F. Tanaka and S. F. Edwards, “Viscoelastic properties of physically crosslinked networks. 1. Transient network theory,” *Macromolecules*, vol. 25, no. 5, pp. 1516–1523, Mar. 1992, doi: 10.1021/ma00031a024.
- [86] A. Cohen, “A Padé approximant to the inverse Langevin function,” *Rheol Acta*, vol. 30, no. 3, pp. 270–273, May 1991, doi: 10.1007/BF00366640.
- [87] B. Li and N. Bouklas, “A variational phase-field model for brittle fracture in polydisperse elastomer networks,” *International Journal of Solids and Structures*, vol. 182–183, pp. 193–204, Jan. 2020, doi: 10.1016/j.ijsolstr.2019.08.012.
- [88] Y. Mao, B. Talamini, and L. Anand, “Rupture of polymers by chain scission,” *Extreme Mechanics Letters*, vol. 13, pp. 17–24, May 2017, doi: 10.1016/j.eml.2017.01.003.
- [89] S. Ahmadi, M. Schmidt, R. J. Spiteri, and R. K. Bowles, “The effect of soft repulsive interactions on the diffusion of particles in quasi-one-dimensional channels: A hopping time approach,” *J. Chem. Phys.*, vol. 150, no. 22, p. 224501, Jun. 2019, doi: 10.1063/1.5100544.
- [90] C. K. C. Lieou, A. E. Elbanna, and J. M. Carlson, “Sacrificial bonds and hidden length in biomaterials: A kinetic constitutive description of strength and toughness in bone,” *Phys. Rev. E*, vol. 88, no. 1, p. 012703, Jul. 2013, doi: 10.1103/PhysRevE.88.012703.
- [91] G. E. Fantner *et al.*, “Sacrificial bonds and hidden length dissipate energy as mineralized fibrils separate during bone fracture,” *Nature Mater*, vol. 4, no. 8, pp. 612–616, Aug. 2005, doi: 10.1038/nmat1428.
- [92] J. Adams, G. E. Fantner, L. W. Fisher, and P. K. Hansma, “Molecular energy dissipation in nanoscale networks of Dentin Matrix Protein 1 is strongly dependent on ion valence,”

- Nanotechnology*, vol. 19, no. 38, p. 384008, Sep. 2008, doi: 10.1088/0957-4484/19/38/384008.
- [93] J. C. Meza, “Steepest descent,” *WIREs Computational Statistics*, vol. 2, no. 6, pp. 719–722, 2010, doi: <https://doi.org/10.1002/wics.117>.
  - [94] A. K. Subramaniyan and C. T. Sun, “Continuum interpretation of virial stress in molecular simulations,” *International Journal of Solids and Structures*, vol. 45, no. 14, pp. 4340–4346, Jul. 2008, doi: 10.1016/j.ijsolstr.2008.03.016.
  - [95] Z. Song, T. Shen, F. J. Vernerey, and S. Cai, “Force-dependent bond dissociation explains the rate-dependent fracture of vitrimers,” *Soft Matter*, vol. 17, no. 27, pp. 6669–6674, Jul. 2021, doi: 10.1039/D1SM00518A.
  - [96] S. Kundu and A. J. Crosby, “Cavitation and fracture behavior of polyacrylamide hydrogels,” *Soft Matter*, vol. 5, no. 20, pp. 3963–3968, 2009, doi: 10.1039/B909237D.
  - [97] P. R. Onck, T. Koeman, T. van Dillen, and E. van der Giessen, “Alternative Explanation of Stiffening in Cross-Linked Semiflexible Networks,” *Phys. Rev. Lett.*, vol. 95, no. 17, p. 178102, Oct. 2005, doi: 10.1103/PhysRevLett.95.178102.
  - [98] T.-S. Lin, R. Wang, J. A. Johnson, and B. D. Olsen, “Revisiting the Elasticity Theory for Real Gaussian Phantom Networks,” *Macromolecules*, vol. 52, no. 4, pp. 1685–1694, Feb. 2019, doi: 10.1021/acs.macromol.8b01676.
  - [99] P. S. Doyle, E. S. G. Shaqfeh, G. H. McKinley, and S. H. Spiegelberg, “Relaxation of dilute polymer solutions following extensional flow” Dedicated to the memory of Professor Gianni Astarita.1,” *Journal of Non-Newtonian Fluid Mechanics*, vol. 76, no. 1, pp. 79–110, Apr. 1998, doi: 10.1016/S0377-0257(97)00113-4.
  - [100] D. Won and C. Kim, “Alignment and aggregation of spherical particles in viscoelastic fluid under shear flow,” *Journal of Non-Newtonian Fluid Mechanics*, vol. 117, no. 2, pp. 141–146, Feb. 2004, doi: 10.1016/j.jnnfm.2004.01.005.
  - [101] Q. Du, C. Liu, and P. Yu, “FENE Dumbbell Model and Its Several Linear and Nonlinear Closure Approximations,” *Multiscale Model. Simul.*, vol. 4, no. 3, pp. 709–731, Jan. 2005, doi: 10.1137/040612038.
  - [102] S. A. Egorov, “Effect of repulsive and attractive interactions on depletion forces in colloidal suspensions: A density functional theory treatment,” *Phys. Rev. E*, vol. 70, no. 3, p. 031402, Sep. 2004, doi: 10.1103/PhysRevE.70.031402.
  - [103] K. Koura and H. Matsumoto, “Variable soft sphere molecular model for inverse-power-law or Lennard-Jones potential,” *Physics of Fluids A: Fluid Dynamics*, vol. 3, no. 10, pp. 2459–2465, Oct. 1991, doi: 10.1063/1.858184.
  - [104] C. Nguyen, D. Peetz, A. E. Elbanna, and J. M. Carlson, “Characterization of fracture in topology-optimized bioinspired networks,” *Phys. Rev. E*, vol. 100, no. 4, p. 042402, Oct. 2019, doi: 10.1103/PhysRevE.100.042402.
  - [105] Z. Song and S. Cai, “Cavitation dynamics in a vitrimer,” *Acta Mech. Sin.*, Apr. 2021, doi: 10.1007/s10409-021-01078-y.
  - [106] J. Guo, A. T. Zehnder, C. Creton, and C.-Y. Hui, “Time dependent fracture of soft materials: linear versus nonlinear viscoelasticity,” *Soft Matter*, vol. 16, no. 26, pp. 6163–6179, 2020, doi: 10.1039/D0SM00097C.
  - [107] C. Creton and M. Ciccotti, “Fracture and adhesion of soft materials: a review,” *Rep. Prog. Phys.*, vol. 79, no. 4, p. 046601, Mar. 2016, doi: 10.1088/0034-4885/79/4/046601.

- [108] J. p. Gong, Y. Katsuyama, T. Kurokawa, and Y. Osada, “Double-Network Hydrogels with Extremely High Mechanical Strength,” *Advanced Materials*, vol. 15, no. 14, pp. 1155–1158, Jul. 2003, doi: 10.1002/adma.200304907.
- [109] E. Ducrot, Y. Chen, M. Bulters, R. P. Sijbesma, and C. Creton, “Toughening Elastomers with Sacrificial Bonds and Watching Them Break,” *Science*, vol. 344, no. 6180, pp. 186–189, Apr. 2014, doi: 10.1126/science.1248494.
- [110] L. Xu *et al.*, “Thermosensitive P(AAc-co-NIPAm) hydrogels display enhanced toughness and self-healing via ion-ligand interactions,” (*Under Review*).
- [111] G. Foyart, C. Liguore, S. Mora, and L. Ramos, “Rearrangement Zone around a Crack Tip in a Double Self-Assembled Transient Network,” *ACS Macro Lett.*, vol. 5, no. 10, pp. 1080–1083, Oct. 2016, doi: 10.1021/acsmacrolett.6b00516.
- [112] M. Gianneli, P. W. Beines, R. F. Roskamp, K. Koynov, G. Fytas, and W. Knoll, “Local and Global Dynamics of Transient Polymer Networks and Swollen Gels Anchored on Solid Surfaces,” *J. Phys. Chem. C*, vol. 111, no. 35, pp. 13205–13211, Sep. 2007, doi: 10.1021/jp0728959.
- [113] S. Lalitha Sridhar and F. J. Vernerey, “Mechanics of transiently cross-linked nematic networks,” *Journal of the Mechanics and Physics of Solids*, vol. 141, p. 104021, Aug. 2020, doi: 10.1016/j.jmps.2020.104021.
- [114] H. Chen, J. Zhang, W. Yu, Y. Cao, Z. Cao, and Y. Tan, “Control Viscoelasticity of Polymer Networks with Crosslinks of Superposed Fast and Slow Dynamics,” *Angewandte Chemie International Edition*, vol. 60, no. 41, pp. 22332–22338, 2021, doi: 10.1002/anie.202105112.
- [115] L. Porath, J. Huang, N. Ramlawi, M. Derkaloustian, R. H. Ewoldt, and C. M. Evans, “Relaxation of Vitrimers with Kinetically Distinct Mixed Dynamic Bonds,” *Macromolecules*, vol. 55, no. 11, pp. 4450–4458, Jun. 2022, doi: 10.1021/acs.macromol.1c02613.
- [116] G. I. Dzhardimalieva, B. C. Yadav, S. Singh, and I. E. Uflyand, “Self-healing and shape memory metallopolymers: state-of-the-art and future perspectives,” *Dalton Trans.*, vol. 49, no. 10, pp. 3042–3087, Mar. 2020, doi: 10.1039/C9DT04360H.
- [117] S. Mora, “The kinetic approach to fracture in transient networks,” *Soft Matter*, vol. 7, no. 10, pp. 4908–4917, 2011, doi: 10.1039/C0SM01203C.
- [118] T. Shen and F. J. Vernerey, “Rate-dependent fracture of transient networks,” *Journal of the Mechanics and Physics of Solids*, vol. 143, p. 104028, Oct. 2020, doi: 10.1016/j.jmps.2020.104028.
- [119] T. Matsunaga, T. Sakai, Y. Akagi, U. Chung, and M. Shibayama, “SANS and SLS Studies on Tetra-Arm PEG Gels in As-Prepared and Swollen States,” *Macromolecules*, vol. 42, no. 16, pp. 6245–6252, Aug. 2009, doi: 10.1021/ma901013q.
- [120] J. Karvinen, T. O. Ihalainen, M. T. Calejo, I. Jönkkäri, and M. Kellomäki, “Characterization of the microstructure of hydrazone crosslinked polysaccharide-based hydrogels through rheological and diffusion studies,” *Materials Science and Engineering: C*, vol. 94, pp. 1056–1066, Jan. 2019, doi: 10.1016/j.msec.2018.10.048.
- [121] A. Sugimura *et al.*, “Mechanical properties of a polymer network of Tetra-PEG gel,” *Polym J*, vol. 45, no. 3, pp. 300–306, Mar. 2013, doi: 10.1038/pj.2012.149.
- [122] N. Cohen, C. Du, and Z. L. Wu, “Understanding the Dissociation of Hydrogen Bond Based Cross-Links In Hydrogels Due to Hydration and Mechanical Forces,” *Macromolecules*, vol. 54, no. 24, pp. 11316–11325, Dec. 2021, doi: 10.1021/acs.macromol.1c01927.

- [123] R. P. Behringer, “Jamming in granular materials,” *Comptes Rendus Physique*, vol. 16, no. 1, pp. 10–25, Jan. 2015, doi: 10.1016/j.crhy.2015.02.001.
- [124] R. P. Behringer and B. Chakraborty, “The physics of jamming for granular materials: a review,” *Rep. Prog. Phys.*, vol. 82, no. 1, p. 012601, Nov. 2018, doi: 10.1088/1361-6633/aadc3c.
- [125] P. Mills, P. G. Rognon, and F. Chevoir, “Rheology and structure of granular materials near the jamming transition,” *EPL*, vol. 81, no. 6, p. 64005, Feb. 2008, doi: 10.1209/0295-5075/81/64005.
- [126] S. C. Lamont, J. Mulderrig, N. Bouklas, and F. J. Vernerey, “Rate-Dependent Damage Mechanics of Polymer Networks with Reversible Bonds,” *Macromolecules*, vol. 54, no. 23, pp. 10801–10813, Dec. 2021, doi: 10.1021/acs.macromol.1c01943.
- [127] S.-N. Li *et al.*, “Constructing dual ionically cross-linked poly(acrylamide-co-acrylic acid)/chitosan hydrogel materials embedded with chitosan decorated halloysite nanotubes for exceptional mechanical performance,” *Composites Part B: Engineering*, vol. 194, p. 108046, Aug. 2020, doi: 10.1016/j.compositesb.2020.108046.
- [128] T. L. Sun *et al.*, “Physical hydrogels composed of polyampholytes demonstrate high toughness and viscoelasticity,” *Nature Mater*, vol. 12, no. 10, Art. no. 10, Oct. 2013, doi: 10.1038/nmat3713.
- [129] P. J. Flory, “Thermodynamics of High Polymer Solutions,” *J. Chem. Phys.*, vol. 10, no. 1, pp. 51–61, Jan. 1942, doi: 10.1063/1.1723621.
- [130] P. J. Flory and J. Rehner, “Statistical Mechanics of Cross-Linked Polymer Networks II. Swelling,” *J. Chem. Phys.*, vol. 11, no. 11, pp. 521–526, Nov. 1943, doi: 10.1063/1.1723792.
- [131] T. Narita, K. Mayumi, G. Ducouret, and P. Hébraud, “Viscoelastic Properties of Poly(vinyl alcohol) Hydrogels Having Permanent and Transient Cross-Links Studied by Microrheology, Classical Rheometry, and Dynamic Light Scattering,” *Macromolecules*, vol. 46, no. 10, pp. 4174–4183, May 2013, doi: 10.1021/ma400600f.
- [132] X. Li *et al.*, “Effect of mesoscale phase contrast on fatigue-delaying behavior of self-healing hydrogels,” *Science Advances*, vol. 7, no. 16, p. eabe8210, Apr. 2021, doi: 10.1126/sciadv.abe8210.
- [133] R. Long, K. Mayumi, C. Creton, T. Narita, and C.-Y. Hui, “Time Dependent Behavior of a Dual Cross-Link Self-Healing Gel: Theory and Experiments,” *Macromolecules*, vol. 47, no. 20, pp. 7243–7250, Oct. 2014, doi: 10.1021/ma501290h.
- [134] C. Yang *et al.*, “Spatially patterned matrix elasticity directs stem cell fate,” *PNAS*, vol. 113, no. 31, pp. E4439–E4445, Aug. 2016, doi: 10.1073/pnas.1609731113.
- [135] C. Chen, Z. Wang, and Z. Suo, “Flaw sensitivity of highly stretchable materials,” *Extreme Mechanics Letters*, vol. 10, pp. 50–57, Jan. 2017, doi: 10.1016/j.eml.2016.10.002.
- [136] C. Yang, T. Yin, and Z. Suo, “Polyacrylamide hydrogels. I. Network imperfection,” *Journal of the Mechanics and Physics of Solids*, vol. 131, pp. 43–55, Oct. 2019, doi: 10.1016/j.jmps.2019.06.018.
- [137] F. Lange *et al.*, “Connectivity and Structural Defects in Model Hydrogels: A Combined Proton NMR and Monte Carlo Simulation Study,” *Macromolecules*, vol. 44, no. 24, pp. 9666–9674, Dec. 2011, doi: 10.1021/ma201847v.
- [138] A. Jusufi, M. Watzlawek, and H. Löwen, “Effective Interaction between Star Polymers,” *Macromolecules*, vol. 32, no. 13, pp. 4470–4473, Jun. 1999, doi: 10.1021/ma981844u.

- [139] S. Huissmann, R. Blaak, and C. N. Likos, “Star Polymers in Solvents of Varying Quality,” *Macromolecules*, vol. 42, no. 7, pp. 2806–2816, Apr. 2009, doi: 10.1021/ma8023359.
- [140] A. Johnner and N.-K. Lee, “The Daoud and Cotton blob model and the interaction of star-shaped polymers,” *Eur. Phys. J. E*, vol. 41, no. 7, p. 88, Jul. 2018, doi: 10.1140/epje/i2018-11698-3.
- [141] E. Wang and F. Escobedo, “Swelling and Tensile Properties of Tetra-Polyethylene glycol via Coarse-Grained Molecular Models,” *Macromolecular Theory and Simulations*, vol. 26, no. 3, p. 1600098, 2017, doi: 10.1002/mats.201600098.
- [142] Y. Akagi, T. Matsunaga, M. Shibayama, U. Chung, and T. Sakai, “Evaluation of Topological Defects in Tetra-PEG Gels,” *Macromolecules*, vol. 43, no. 1, pp. 488–493, Jan. 2010, doi: 10.1021/ma9019009.
- [143] T. Matsunaga, T. Sakai, Y. Akagi, U. Chung, and M. Shibayama, “Structure Characterization of Tetra-PEG Gel by Small-Angle Neutron Scattering,” *Macromolecules*, vol. 42, no. 4, pp. 1344–1351, Feb. 2009, doi: 10.1021/ma802280n.
- [144] P. J. Flory and J. Rehner, “Statistical Mechanics of Cross-Linked Polymer Networks I. Rubberlike Elasticity,” *The Journal of Chemical Physics*, vol. 11, no. 11, pp. 512–520, Nov. 1943, doi: 10.1063/1.1723791.
- [145] M. Daoud and J. P. Cotton, “Star shaped polymers : a model for the conformation and its concentration dependence,” *J. Phys. France*, vol. 43, no. 3, pp. 531–538, Mar. 1982, doi: 10.1051/jphys:01982004303053100.
- [146] A. Zhang, J. Ling, Y. Sun, and G. Fu, “Three-dimensional molecular geometry of PEG hydrogels by an ‘expansion-contraction’ method through Monte Carlo simulations,” *Chin J Polym Sci*, vol. 33, no. 5, pp. 721–731, May 2015, doi: 10.1007/s10118-015-1620-4.
- [147] Lue and Kiselev, “STAR POLYMERS IN GOOD SOLVENTS FROM DILUTE TO CONCENTRATED REGIMES: CROSSOVER APPROACH,” *Condens. Matter Phys.*, vol. 5, no. 1, p. 73, 2002, doi: 10.5488/CMP.5.1.73.
- [148] V. S. Sukumar and S. T. Lopina, “Network Model for the Swelling Properties of End-Linked Linear and Star Poly(ethylene oxide) Hydrogels,” *Macromolecules*, vol. 35, no. 27, pp. 10189–10192, Dec. 2002, doi: 10.1021/ma0213753.
- [149] M. Doi, *Soft Matter Physics*. OUP Oxford, 2013.
- [150] P. J. Flory, “Molecular Theory of Rubber Elasticity,” *Polymer Journal*, vol. 17, no. 1, pp. 1–12, Jan. 1985, doi: 10.1295/polymj.17.1.
- [151] J. S. Bergström and M. C. Boyce, “Deformation of Elastomeric Networks: Relation between Molecular Level Deformation and Classical Statistical Mechanics Models of Rubber Elasticity,” *Macromolecules*, vol. 34, no. 3, pp. 614–626, Jan. 2001, doi: 10.1021/ma0007942.
- [152] V. Krakoviack, J.-P. Hansen, and A. A. Louis, “Influence of solvent quality on effective pair potentials between polymers in solution,” *Phys. Rev. E*, vol. 67, no. 4, p. 041801, Apr. 2003, doi: 10.1103/PhysRevE.67.041801.
- [153] F. Horkay and D. C. Lin, “Mapping the Local Osmotic Modulus of Polymer Gels,” *Langmuir*, vol. 25, no. 15, pp. 8735–8741, Aug. 2009, doi: 10.1021/la900103j.
- [154] T. M. Birshtein and E. B. Zhulina, “Conformations of star-branched macromolecules,” *Polymer*, vol. 25, no. 10, pp. 1453–1461, Oct. 1984, doi: 10.1016/0032-3861(84)90109-5.
- [155] T. M. Birshtein and E. B. Zhulina, “Scaling theory of supermolecular structures in block copolymer-solvent systems: 2. Supercrystalline structures,” *Polymer*, vol. 31, no. 7, pp. 1312–1320, Jul. 1990, doi: 10.1016/0032-3861(90)90223-L.



- [156] H.-P. Hsu, W. Nadler, and P. Grassberger, “Scaling of Star Polymers with 1–80 Arms,” *Macromolecules*, vol. 37, no. 12, pp. 4658–4663, Jun. 2004, doi: 10.1021/ma0355958.
- [157] K. Schwenke, M. Lang, and J.-U. Sommer, “On the Structure of Star-Polymer Networks,” *Macromolecules*, vol. 44, no. 23, pp. 9464–9472, Dec. 2011, doi: 10.1021/ma202022q.
- [158] M. Shibayama, X. Li, and T. Sakai, “Precision polymer network science with tetra-PEG gels—a decade history and future,” *Colloid Polym Sci*, vol. 297, no. 1, pp. 1–12, Jan. 2019, doi: 10.1007/s00396-018-4423-7.
- [159] A. Salari, M. Karmozdi, R. Maddahian, and B. Firoozabadi, “Analytical study of single particle tracking in both free and forced vortices,” *Scientia Iranica*, vol. 20, no. 2, pp. 351–358, Apr. 2013, doi: 10.1016/j.scient.2013.02.011.
- [160] A. Cohen, “A Padé approximant to the inverse Langevin function,” *Rheol Acta*, vol. 30, no. 3, pp. 270–273, May 1991, doi: 10.1007/BF00366640.
- [161] F. Kienberger *et al.*, “Static and Dynamical Properties of Single Poly(Ethylene Glycol) Molecules Investigated by Force Spectroscopy,” *Single Molecules*, vol. 1, no. 2, pp. 123–128, 2000, doi: 10.1002/1438-5171(200006)1:2<123::AID-SIMO123>3.0.CO;2-3.
- [162] F. Oesterhelt, M. Rief, and H. E. Gaub, “Single molecule force spectroscopy by AFM indicates helical structure of poly(ethylene-glycol) in water,” *New J. Phys.*, vol. 1, pp. 6–6, Jan. 1999, doi: 10.1088/1367-2630/1/1/006.
- [163] P. J. Flory and S. Fisk, “Effect of Volume Exclusion on the Dimensions of Polymer Chains,” *J. Chem. Phys.*, vol. 44, no. 6, pp. 2243–2248, Mar. 1966, doi: 10.1063/1.1727029.
- [164] T. Tanaka and D. J. Fillmore, “Kinetics of swelling of gels,” *J. Chem. Phys.*, vol. 70, no. 3, pp. 1214–1218, Feb. 1979, doi: 10.1063/1.437602.
- [165] E. B. Stukalin, L.-H. Cai, N. A. Kumar, L. Leibler, and M. Rubinstein, “Self-Healing of Unentangled Polymer Networks with Reversible Bonds,” *Macromolecules*, vol. 46, no. 18, pp. 7525–7541, Sep. 2013, doi: 10.1021/ma401111n.
- [166] F. Horkay, K. Nishi, and M. Shibayama, “Decisive test of the ideal behavior of tetra-PEG gels,” *J. Chem. Phys.*, vol. 146, no. 16, p. 164905, Apr. 2017, doi: 10.1063/1.4982253.
- [167] L. Wang, K. Lei, Z. Li, X. Wang, H. Xiao, and Z. Zheng, “Tetra-PEG-Based Nano-Enhanced Hydrogel with Excellent Mechanical Properties and Multi-Functions,” *Macromolecular Materials and Engineering*, vol. 303, no. 11, p. 1800325, 2018, doi: 10.1002/mame.201800325.
- [168] P. S. Mohanty, D. Paloli, J. J. Crassous, E. Zaccarelli, and P. Schurtenberger, “Effective interactions between soft-repulsive colloids: Experiments, theory, and simulations,” *J. Chem. Phys.*, vol. 140, no. 9, p. 094901, Mar. 2014, doi: 10.1063/1.4866644.
- [169] J. T. Padding and W. J. Briels, “Momentum conserving Brownian dynamics propagator for complex soft matter fluids,” *J. Chem. Phys.*, vol. 141, no. 24, p. 244108, Dec. 2014, doi: 10.1063/1.4904315.
- [170] M. Watzlawek, H. Löwen, and C. N. Likos, “The anomalous structure factor of dense star polymer solutions,” *J. Phys.: Condens. Matter*, vol. 10, no. 37, pp. 8189–8205, Sep. 1998, doi: 10.1088/0953-8984/10/37/007.
- [171] P. Hebbeker, F. A. Plamper, and S. Schneider, “Aggregation of Star Polymers: Complexation versus Segregation,” *Macromolecular Theory and Simulations*, vol. 27, no. 6, p. 1800033, 2018, doi: 10.1002/mats.201800033.
- [172] I. Khoiroh, S. Y. Lee, M. Pirdashti, and M.-J. Lee, “Insight into structural properties of polyethylene glycol monolaurate in water and alcohols from molecular dynamics studies,” *RSC Adv.*, vol. 10, no. 37, pp. 21760–21771, Jun. 2020, doi: 10.1039/C9RA09688D.

- [173] P. G. Bolhuis, A. A. Louis, J. P. Hansen, and E. J. Meijer, “Accurate effective pair potentials for polymer solutions,” *J. Chem. Phys.*, vol. 114, no. 9, pp. 4296–4311, Feb. 2001, doi: 10.1063/1.1344606.
- [174] S. A. Egorov, “Effect of repulsive and attractive interactions on depletion forces in colloidal suspensions: A density functional theory treatment,” *Phys. Rev. E*, vol. 70, no. 3, p. 031402, Sep. 2004, doi: 10.1103/PhysRevE.70.031402.
- [175] I. D. Hosein, S. H. Lee, and C. M. Liddell, “Dimer-Based Three-Dimensional Photonic Crystals,” *Advanced Functional Materials*, vol. 20, no. 18, pp. 3085–3091, 2010, doi: 10.1002/adfm.201000134.
- [176] E. K. Riley and C. M. L. Watson, “Slab photonic crystals with dimer cylinder bases,” *J. Opt. Soc. Am. B, JOSAB*, vol. 31, no. 9, pp. 2084–2094, Sep. 2014, doi: 10.1364/JOSAB.31.002084.
- [177] J. W. Chung, A. Roos, J. Th. M. De Hosson, and E. van der Giessen, “Fracture of disordered three-dimensional spring networks: A computer simulation methodology,” *Phys. Rev. B*, vol. 54, no. 21, pp. 15094–15100, Dec. 1996, doi: 10.1103/PhysRevB.54.15094.
- [178] M. Asai, T. Katashima, U. Chung, T. Sakai, and M. Shibayama, “Correlation between Local and Global Inhomogeneities of Chemical Gels,” *Macromolecules*, vol. 46, no. 24, pp. 9772–9781, Dec. 2013, doi: 10.1021/ma400486h.
- [179] S. N. Soffer and A. Vázquez, “Network clustering coefficient without degree-correlation biases,” *Phys. Rev. E*, vol. 71, no. 5, p. 057101, May 2005, doi: 10.1103/PhysRevE.71.057101.
- [180] F. J. Vernerey, R. Long, and R. Brighenti, “A statistically-based continuum theory for polymers with transient networks,” *Journal of the Mechanics and Physics of Solids*, vol. 107, pp. 1–20, Oct. 2017, doi: 10.1016/j.jmps.2017.05.016.
- [181] R. W. Ogden and R. Hill, “Large deformation isotropic elasticity: on the correlation of theory and experiment for compressible rubberlike solids,” *Proceedings of the Royal Society of London. A. Mathematical and Physical Sciences*, vol. 328, no. 1575, pp. 567–583, Jun. 1972, doi: 10.1098/rspa.1972.0096.
- [182] K. M. Moerman, B. Fereidoonhezad, and J. P. McGarry, “Novel hyperelastic models for large volumetric deformations,” *International Journal of Solids and Structures*, vol. 193–194, pp. 474–491, Jun. 2020, doi: 10.1016/j.ijsolstr.2020.01.019.
- [183] T. Sakai, Y. Akagi, T. Matsunaga, M. Kurakazu, U. Chung, and M. Shibayama, “Highly Elastic and Deformable Hydrogel Formed from Tetra-arm Polymers,” *Macromolecular Rapid Communications*, vol. 31, no. 22, pp. 1954–1959, 2010, doi: 10.1002/marc.201000286.
- [184] A. Jangizehi, F. Schmid, P. Besenius, K. Kremer, and S. Seiffert, “Defects and defect engineering in Soft Matter,” *Soft Matter*, vol. 16, no. 48, pp. 10809–10859, Dec. 2020, doi: 10.1039/D0SM01371D.
- [185] G. Sanoja, X. P. Morelle, J. Comtet, C. J. Yeh, M. Ciccotti, and C. Creton, “Why is Mechanical Fatigue Different from Toughness in Elastomers? The Role of Damage by Polymer Chain Scission,” Feb. 2021, doi: 10.26434/chemrxiv.13712875.v2.
- [186] V. Ahlawat, S. S. Rajput, and S. Patil, “Elasticity of single flexible polymer chains in good and poor solvents,” *Polymer*, vol. 230, p. 124031, Sep. 2021, doi: 10.1016/j.polymer.2021.124031.

- [187] K. M. Schultz, A. D. Baldwin, K. L. Kiick, and E. M. Furst, “Gelation of Covalently Cross-Linked PEG–Heparin Hydrogels,” *Macromolecules*, vol. 42, no. 14, pp. 5310–5316, Jul. 2009, doi: 10.1021/ma900766u.
- [188] G. Sun, X.-Z. Zhang, and C.-C. Chu, “Effect of the molecular weight of polyethylene glycol (PEG) on the properties of chitosan-PEG-poly(N-isopropylacrylamide) hydrogels,” *J Mater Sci: Mater Med*, vol. 19, no. 8, pp. 2865–2872, Aug. 2008, doi: 10.1007/s10856-008-3410-9.
- [189] J. S. Temenoff, K. A. Athanasiou, R. G. Lebaron, and A. G. Mikos, “Effect of poly(ethylene glycol) molecular weight on tensile and swelling properties of oligo(poly(ethylene glycol) fumarate) hydrogels for cartilage tissue engineering,” *J. Biomed. Mater. Res.*, vol. 59, no. 3, pp. 429–437, Mar. 2002, doi: 10.1002/jbm.1259.
- [190] C. N. Likos, “Effective interactions in soft condensed matter physics,” *Physics Reports*, vol. 348, no. 4, pp. 267–439, Jul. 2001, doi: 10.1016/S0370-1573(00)00141-1.
- [191] M. Majka and P. F. Góra, “Analytical theory of effective interactions in binary colloidal systems of soft particles,” *Phys. Rev. E*, vol. 90, no. 3, p. 032303, Sep. 2014, doi: 10.1103/PhysRevE.90.032303.
- [192] G. M. Kavanagh and S. B. Ross-Murphy, “Rheological characterisation of polymer gels,” *Progress in Polymer Science*, vol. 23, no. 3, pp. 533–562, Jan. 1998, doi: 10.1016/S0079-6700(97)00047-6.
- [193] Y. Masubuchi, J.-I. Takimoto, K. Koyama, G. Ianniruberto, G. Marrucci, and F. Greco, “Brownian simulations of a network of reptating primitive chains,” *J. Chem. Phys.*, vol. 115, no. 9, pp. 4387–4394, Sep. 2001, doi: 10.1063/1.1389858.
- [194] K. Dikshit and C. J. Bruns, “Post-synthesis modification of slide-ring gels for thermal and mechanical reconfiguration,” *Soft Matter*, vol. 17, no. 20, pp. 5248–5257, May 2021, doi: 10.1039/D0SM02260H.
- [195] F. J. Vernerey and S. Lamont, “Transient mechanics of slide-ring networks: A continuum model,” *Journal of the Mechanics and Physics of Solids*, vol. 146, p. 104212, Jan. 2021, doi: 10.1016/j.jmps.2020.104212.
- [196] W. Hong, Z. Liu, and Z. Suo, “Inhomogeneous swelling of a gel in equilibrium with a solvent and mechanical load,” *International Journal of Solids and Structures*, vol. 46, no. 17, pp. 3282–3289, Aug. 2009, doi: 10.1016/j.ijsolstr.2009.04.022.
- [197] W. Hong, X. Zhao, J. Zhou, and Z. Suo, “A theory of coupled diffusion and large deformation in polymeric gels,” *Journal of the Mechanics and Physics of Solids*, vol. 56, no. 5, pp. 1779–1793, May 2008, doi: 10.1016/j.jmps.2007.11.010.
- [198] K. J. Mattern, C. Nakornchai, and W. M. Deen, “Darcy Permeability of Agarose-Glycosaminoglycan Gels Analyzed Using Fiber-Mixture and Donnan Models,” *Biophysical Journal*, vol. 95, no. 2, pp. 648–656, Jul. 2008, doi: 10.1529/biophysj.107.127316.
- [199] U. Akalp, S. J. Bryant, and F. J. Vernerey, “Tuning tissue growth with scaffold degradation in enzyme-sensitive hydrogels: a mathematical model,” *Soft Matter*, vol. 12, no. 36, pp. 7505–7520, 2016, doi: 10.1039/C6SM00583G.
- [200] F. J. Vernerey, “A mixture approach to investigate interstitial growth in engineering scaffolds,” *Biomech Model Mechanobiol*, vol. 15, no. 2, pp. 259–278, Apr. 2016, doi: 10.1007/s10237-015-0684-y.
- [201] V. Dhote and F. J. Vernerey, “Mathematical model of the role of degradation on matrix development in hydrogel scaffold,” *Biomech Model Mechanobiol*, vol. 13, no. 1, pp. 167–183, Jan. 2014, doi: 10.1007/s10237-013-0493-0.

- [202] S. L. Sridhar, M. C. Schneider, S. Chu, G. de Roucy, S. J. Bryant, and F. J. Vernerey, “Heterogeneity is key to hydrogel-based cartilage tissue regeneration,” *Soft Matter*, vol. 13, no. 28, pp. 4841–4855, 2017, doi: 10.1039/C7SM00423K.
- [203] T. Vicsek and A. Zafeiris, “Collective motion,” *Physics Reports*, vol. 517, no. 3, pp. 71–140, Aug. 2012, doi: 10.1016/j.physrep.2012.03.004.
- [204] D. M. Gordon, “The Ecology of Collective Behavior,” *PLOS Biology*, vol. 12, no. 3, p. e1001805, Mar. 2014, doi: 10.1371/journal.pbio.1001805.
- [205] E. Méhes and T. Vicsek, “Collective motion of cells: from experiments to models,” *Integrative Biology*, vol. 6, no. 9, pp. 831–854, 2014, doi: 10.1039/C4IB00115J.
- [206] A. P. Tabatabai, D. S. Seara, J. Tibbs, V. Yadav, I. Linsmeier, and M. P. Murrell, “Detailed Balance Broken by Catch Bond Kinetics Enables Mechanical-Adaptation in Active Materials,” *Advanced Functional Materials*, vol. 31, no. 10, p. 2006745, 2021, doi: <https://doi.org/10.1002/adfm.202006745>.
- [207] O. Peleg, J. M. Peters, M. K. Salcedo, and L. Mahadevan, “Collective mechanical adaptation of honeybee swarms,” *Nature Phys*, vol. 14, no. 12, pp. 1193–1198, Dec. 2018, doi: 10.1038/s41567-018-0262-1.
- [208] M. Tennenbaum, Z. Liu, D. Hu, and A. Fernandez-Nieves, “Mechanics of fire ant aggregations,” *Nature Materials*, vol. 15, no. 1, pp. 54–59, Jan. 2016, doi: 10.1038/nmat4450.
- [209] S. Phonekeo, T. Dave, M. Kern, S. V. Franklin, and D. L. Hu, “Ant aggregations self-heal to compensate for the Ringelmann effect,” *Soft Matter*, vol. 12, no. 18, pp. 4214–4220, 2016, doi: 10.1039/C6SM00063K.
- [210] N. J. Mlot, C. A. Tovey, and D. L. Hu, “Fire ants self-assemble into waterproof rafts to survive floods,” *PNAS*, vol. 108, no. 19, pp. 7669–7673, May 2011, doi: 10.1073/pnas.1016658108.
- [211] B. J. Adams, L. M. Hooper-Bùi, R. M. Strecker, and D. M. O’Brien, “Raft Formation by the Red Imported Fire Ant, *Solenopsis invicta*,” *J Insect Sci*, vol. 11, Dec. 2011, doi: 10.1673/031.011.17101.
- [212] F. J. Vernerey, T. Shen, S. L. Sridhar, and R. J. Wagner, “How do fire ants control the rheology of their aggregations? A statistical mechanics approach,” *Journal of The Royal Society Interface*, vol. 15, no. 147, p. 20180642, Oct. 2018, doi: 10.1098/rsif.2018.0642.
- [213] F. J. Vernerey, R. Long, and R. Brighenti, “A statistically-based continuum theory for polymers with transient networks,” *Journal of the Mechanics and Physics of Solids*, vol. 107, pp. 1–20, 2017, doi: 10.1016/j.jmps.2017.05.016.
- [214] M. Tennenbaum and A. Fernandez-Nieves, “Activity-driven changes in the mechanical properties of fire ant aggregations,” *Phys. Rev. E*, vol. 96, no. 5, p. 052601, Nov. 2017, doi: 10.1103/PhysRevE.96.052601.
- [215] M. Tennenbaum and A. Fernandez-Nieves, “Activity effects on the nonlinear mechanical properties of fire-ant aggregations,” *Phys. Rev. E*, vol. 102, no. 1, p. 012602, Jul. 2020, doi: 10.1103/PhysRevE.102.012602.
- [216] M. Murrell, P. W. Oakes, M. Lenz, and M. L. Gardel, “Forcing cells into shape: the mechanics of actomyosin contractility,” *Nature Reviews Molecular Cell Biology*, vol. 16, no. 8, Art. no. 8, Aug. 2015, doi: 10.1038/nrm4012.
- [217] R. Blackwell, O. Sweezy-Schindler, C. Baldwin, L. E. Hough, M. A. Glaser, and M. D. Betterton, “Microscopic origins of anisotropic active stress in motor-driven nematic liquid

- crystals,” *Soft Matter*, vol. 12, no. 10, pp. 2676–2687, Mar. 2016, doi: 10.1039/C5SM02506K.
- [218] N. J. Mlot, C. Tovey, and D. L. Hu, “Dynamics and shape of large fire ant rafts,” *Commun Integr Biol*, vol. 5, no. 6, pp. 590–597, Nov. 2012, doi: 10.4161/cib.21421.
- [219] S. Phonekeo, N. Mlot, D. Monaenkova, D. L. Hu, and C. Tovey, “Fire ants perpetually rebuild sinking towers,” *Royal Society Open Science*, vol. 4, no. 7, p. 170475, doi: 10.1098/rsos.170475.
- [220] J.-M. Neuhaus, M. Wanger, T. Keiser, and A. Wegner, “Treadmilling of actin,” *J Muscle Res Cell Motil*, vol. 4, no. 5, pp. 507–527, Oct. 1983, doi: 10.1007/BF00712112.
- [221] B. Bugyi and M.-F. Carlier, “Control of actin filament treadmilling in cell motility,” *Annu Rev Biophys*, vol. 39, pp. 449–470, 2010, doi: 10.1146/annurev-biophys-051309-103849.
- [222] M. D. Abramoff, P. J. Magalhães, and S. J. Ram, “Image processing with ImageJ,” *Biophotonics international*, 2004. <http://dspace.library.uu.nl/handle/1874/204900> (accessed Nov. 17, 2019).
- [223] C. A. Schneider, W. S. Rasband, and K. W. Eliceiri, “NIH Image to ImageJ: 25 years of image analysis,” *Nature Methods*, vol. 9, no. 7, Art. no. 7, Jul. 2012, doi: 10.1038/nmeth.2089.
- [224] C. T. Rueden *et al.*, “ImageJ2: ImageJ for the next generation of scientific image data,” *BMC Bioinformatics*, vol. 18, no. 1, p. 529, Nov. 2017, doi: 10.1186/s12859-017-1934-z.
- [225] *MATLAB R2019b*. The MathWorks Inc., 2019.
- [226] T. Vicsek and A. Zafeiris, “Collective motion,” *Physics Reports*, vol. 517, no. 3–4, pp. 71–140, Aug. 2012, doi: 10.1016/j.physrep.2012.03.004.
- [227] H.-P. Hsu, W. Paul, and K. Binder, “Standard Definitions of Persistence Length Do Not Describe the Local ‘Intrinsic’ Stiffness of Real Polymer Chains,” *Macromolecules*, vol. 43, no. 6, pp. 3094–3102, Mar. 2010, doi: 10.1021/ma902715e.
- [228] W. Thielicke and E. Stamhuis, “PIVlab – Towards User-friendly, Affordable and Accurate Digital Particle Image Velocimetry in MATLAB,” *Journal of Open Research Software*, vol. 2, no. 1, Art. no. 1, Oct. 2014, doi: 10.5334/jors.bl.
- [229] W. Thielicke and E. J. Stamhuis, “PIVlab - Time-Resolved Digital Particle Image Velocimetry Tool for MATLAB.” Sep. 06, 2019. doi: 10.6084/m9.figshare.1092508.
- [230] T. Speck, “Collective behavior of active Brownian particles: From microscopic clustering to macroscopic phase separation,” *Eur. Phys. J. Spec. Top.*, vol. 225, no. 11, pp. 2287–2299, Nov. 2016, doi: 10.1140/epjst/e2016-60022-8.
- [231] P. Siegle, I. Goychuk, and P. Hänggi, “Origin of Hyperdiffusion in Generalized Brownian Motion,” *Phys. Rev. Lett.*, vol. 105, no. 10, p. 100602, Sep. 2010, doi: 10.1103/PhysRevLett.105.100602.
- [232] M. R. Shaebani and H. Rieger, “Transient Anomalous Diffusion in Run-and-Tumble Dynamics,” *Front. Phys.*, vol. 7, 2019, doi: 10.3389/fphy.2019.00120.
- [233] A. W. Visser and U. H. Thygesen, “Random motility of plankton: diffusive and aggregative contributions,” *Journal of Plankton Research*, vol. 25, no. 9, pp. 1157–1168, Sep. 2003, doi: 10.1093/plankt/25.9.1157.
- [234] G. Ramos-Fernández, J. L. Mateos, O. Miramontes, G. Cocho, H. Larralde, and B. Ayala-Orozco, “Lévy walk patterns in the foraging movements of spider monkeys (*Ateles geoffroyi*),” *Behav Ecol Sociobiol*, vol. 55, no. 3, pp. 223–230, Jan. 2004, doi: 10.1007/s00265-003-0700-6.

- [235] L. Caprini, F. Cecconi, A. Puglisi, and A. Sarracino, “Diffusion properties of self-propelled particles in cellular flows,” *Soft Matter*, vol. 16, no. 23, pp. 5431–5438, Jun. 2020, doi: 10.1039/D0SM00450B.
- [236] Y.-F. Chen, H.-H. Wei, Y.-J. Sheng, and H.-K. Tsao, “Superdiffusion in dispersions of active colloids driven by an external field and their sedimentation equilibrium,” *Phys. Rev. E*, vol. 93, no. 4, p. 042611, Apr. 2016, doi: 10.1103/PhysRevE.93.042611.
- [237] X.-L. Wu and A. Libchaber, “Particle Diffusion in a Quasi-Two-Dimensional Bacterial Bath,” *Phys. Rev. Lett.*, vol. 84, no. 13, pp. 3017–3020, Mar. 2000, doi: 10.1103/PhysRevLett.84.3017.
- [238] M. A. Despósito, “Superdiffusion induced by a long-correlated external random force,” *Phys. Rev. E*, vol. 84, no. 6, p. 061114, Dec. 2011, doi: 10.1103/PhysRevE.84.061114.
- [239] J. Elgeti and G. Gompper, “Wall accumulation of self-propelled spheres,” *EPL*, vol. 101, no. 4, p. 48003, Feb. 2013, doi: 10.1209/0295-5075/101/48003.
- [240] Y. Fily, A. Baskaran, and M. F. Hagan, “Dynamics and density distribution of strongly confined noninteracting nonaligning self-propelled particles in a nonconvex boundary,” *Phys. Rev. E*, vol. 91, no. 1, p. 012125, Jan. 2015, doi: 10.1103/PhysRevE.91.012125.
- [241] Y. Fily, A. Baskaran, and M. F. Hagan, “Dynamics of self-propelled particles under strong confinement,” *Soft Matter*, vol. 10, no. 30, pp. 5609–5617, Jul. 2014, doi: 10.1039/C4SM00975D.
- [242] D. H. Sharp, “An overview of Rayleigh-Taylor instability,” *Physica D: Nonlinear Phenomena*, vol. 12, no. 1, pp. 3–18, Jul. 1984, doi: 10.1016/0167-2789(84)90510-4.
- [243] P. G. Saffman and G. I. Taylor, “The penetration of a fluid into a porous medium or Hele-Shaw cell containing a more viscous liquid,” *Proceedings of the Royal Society of London. Series A. Mathematical and Physical Sciences*, vol. 245, no. 1242, pp. 312–329, Jun. 1958, doi: 10.1098/rspa.1958.0085.
- [244] H. Wioland, E. Lushi, and R. E. Goldstein, “Directed collective motion of bacteria under channel confinement,” *New J. Phys.*, vol. 18, no. 7, p. 075002, Jul. 2016, doi: 10.1088/1367-2630/18/7/075002.
- [245] H. R. Vutukuri *et al.*, “Active particles induce large shape deformations in giant lipid vesicles,” *Nature*, vol. 586, no. 7827, Art. no. 7827, Oct. 2020, doi: 10.1038/s41586-020-2730-x.
- [246] T. Bochynek and S. K. A. Robson, “Physical and Biological Determinants of Collective Behavioural Dynamics in Complex Systems: Pulling Chain Formation in the Nest-Weaving Ant *Oecophylla smaragdina*,” *PLOS ONE*, vol. 9, no. 4, p. e95112, Apr. 2014, doi: 10.1371/journal.pone.0095112.
- [247] K. Devarajan, “The Antsy Social Network: Determinants of Nest Structure and Arrangement in Asian Weaver Ants,” *PLOS ONE*, vol. 11, no. 6, p. e0156681, Jun. 2016, doi: 10.1371/journal.pone.0156681.
- [248] A. Stabentheiner, H. Kovac, and R. Brodschneider, “Honeybee Colony Thermoregulation – Regulatory Mechanisms and Contribution of Individuals in Dependence on Age, Location and Thermal Stress,” *PLoS One*, vol. 5, no. 1, Jan. 2010, doi: 10.1371/journal.pone.0008967.
- [249] H. Jarimi, E. Tapia-Brito, and S. Riffat, “A Review on Thermoregulation Techniques in Honey Bees’ (*Apis Mellifera*) Beehive Microclimate and Its Similarities to the Heating and Cooling Management in Buildings,” *Future Cities and Environment*, vol. 6, no. 1, Art. no. 1, Aug. 2020, doi: 10.5334/fce.81.

- [250] W. Song, H.-Y. Kim, S.-I. Lee, and P. G. Jablonski, “Directional raids by army ants as an adaption to patchily distributed food: a simulation model,” *Anim Cells Syst (Seoul)*, vol. 22, no. 4, pp. 267–272, Jul. 2018, doi: 10.1080/19768354.2018.1497708.
- [251] T. Bochynek, B. Meyer, and M. Burd, “Energetics of trail clearing in the leaf-cutter ant *Atta*,” *Behav Ecol Sociobiol*, vol. 71, no. 1, p. 14, Dec. 2016, doi: 10.1007/s00265-016-2237-5.
- [252] G. L. Ryan, N. Watanabe, and D. Vavylonis, “A review of models of fluctuating protrusion and retraction patterns at the leading edge of motile cells,” *Cytoskeleton*, vol. 69, no. 4, pp. 195–206, 2012, doi: 10.1002/cm.21017.
- [253] C. Simon *et al.*, “Actin dynamics drive cell-like membrane deformation,” *Nat. Phys.*, vol. 15, no. 6, pp. 602–609, Jun. 2019, doi: 10.1038/s41567-019-0464-1.
- [254] S. P. Zimmerman, S. B. Asokan, B. Kuhlman, and J. E. Bear, “Cells lay their own tracks – optogenetic Cdc42 activation stimulates fibronectin deposition supporting directed migration,” *J Cell Sci*, vol. 130, no. 18, pp. 2971–2983, Sep. 2017, doi: 10.1242/jcs.205948.
- [255] G. Beaune *et al.*, “How cells flow in the spreading of cellular aggregates,” *Proc Natl Acad Sci U S A*, vol. 111, no. 22, pp. 8055–8060, Jun. 2014, doi: 10.1073/pnas.1323788111.
- [256] G. Alexandre, “Chemotaxis Control of Transient Cell Aggregation,” *J Bacteriol*, vol. 197, no. 20, pp. 3230–3237, Oct. 2015, doi: 10.1128/JB.00121-15.
- [257] B. J. DuChes, A. D. Doyle, E. K. Dimitriadis, and K. M. Yamada, “Durotaxis by Human Cancer Cells,” *Biophysical Journal*, vol. 116, no. 4, pp. 670–683, Feb. 2019, doi: 10.1016/j.bpj.2019.01.009.
- [258] J. H. Wen *et al.*, “Haptotaxis is cell type specific and limited by substrate adhesiveness,” *Cell Mol Bioeng*, vol. 8, no. 4, pp. 530–542, Dec. 2015, doi: 10.1007/s12195-015-0398-3.
- [259] A. Worley, A. B. Sendova-Franks, and N. R. Franks, “Social flocculation in plant–animal worms,” *Royal Society Open Science*, vol. 6, no. 3, p. 181626, 2019, doi: 10.1098/rsos.181626.
- [260] Y. Ozkan-Aydin, D. I. Goldman, and M. S. Bhamla, “Collective dynamics in entangled worm and robot blobs,” *PNAS*, vol. 118, no. 6, Feb. 2021, doi: 10.1073/pnas.2010542118.
- [261] T. Vicsek, A. Czirók, E. Ben-Jacob, I. Cohen, and O. Shochet, “Novel Type of Phase Transition in a System of Self-Driven Particles,” *Physical Review Letters*, vol. 75, no. 6, p. 1226, 1995.
- [262] P. Amorim, “Modeling ant foraging: A chemotaxis approach with pheromones and trail formation,” *Journal of Theoretical Biology*, vol. 385, pp. 160–173, Nov. 2015, doi: 10.1016/j.jtbi.2015.08.026.
- [263] P. Amorim, T. Goudon, and F. Peruani, “An ant navigation model based on Weber’s law,” *J. Math. Biol.*, vol. 78, no. 4, pp. 943–984, Mar. 2019, doi: 10.1007/s00285-018-1298-7.
- [264] E. Boissard, P. Degond, and S. Motsch, “Trail formation based on directed pheromone deposition,” *J. Math. Biol.*, vol. 66, no. 6, pp. 1267–1301, May 2013, doi: 10.1007/s00285-012-0529-6.
- [265] S. D. Ryan, “A model for collective dynamics in ant raids,” *J. Math. Biol.*, vol. 72, no. 6, pp. 1579–1606, May 2016, doi: 10.1007/s00285-015-0929-5.
- [266] N. R. Baumgartner and S. D. Ryan, “Interaction of red crabs with yellow crazy ants during migration on Christmas Island,” *Mathematical Biosciences*, vol. 330, p. 108486, Dec. 2020, doi: 10.1016/j.mbs.2020.108486.

- [267] I. D. Couzin and N. R. Franks, “Self-organized lane formation and optimized traffic flow in army ants,” *Proceedings of the Royal Society B: Biological Sciences*, vol. 270, no. 1511, pp. 139–146, 2003, doi: 10.1098/rspb.2002.2210.
- [268] R. C. Picu, “Mechanics of random fiber networks - A review,” *Soft Matter*, vol. 7, no. 15, pp. 6768–6785, 2011, doi: 10.1039/c1sm05022b.
- [269] M. R. Shaebani, A. Wysocki, R. G. Winkler, G. Gompper, and H. Rieger, “Computational models for active matter,” *Nature Reviews Physics*, vol. 2, no. 4, Art. no. 4, Apr. 2020, doi: 10.1038/s42254-020-0152-1.
- [270] A. Mogilner, L. Edelstein-Keshet, L. Bent, and A. Spiros, “Mutual interactions, potentials, and individual distance in a social aggregation,” *J Math Biol*, vol. 47, no. 4, pp. 353–389, Oct. 2003, doi: 10.1007/s00285-003-0209-7.
- [271] C. Dong, S. Aznavoorian, and L. A. Liotta, “Two phases of pseudopod protrusion in tumor cells revealed by a micropipette,” *Microvasc. Res.*, vol. 47, no. 1, pp. 55–67, Jan. 1994, doi: 10.1006/mvre.1994.1005.
- [272] E. Méhes and T. Vicsek, “Collective motion of cells: from experiments to models,” *Integr. Biol.*, vol. 6, no. 9, pp. 831–854, 2014, doi: 10.1039/C4IB00115J.
- [273] C. Reichhardt, J. Thibault, S. Papanikolaou, and C. J. O. Reichhardt, “Laning and clustering transitions in driven binary active matter systems,” *Phys. Rev. E*, vol. 98, no. 2, p. 022603, Aug. 2018, doi: 10.1103/PhysRevE.98.022603.
- [274] N. Nikola, A. P. Solon, Y. Kafri, M. Kardar, J. Tailleur, and R. Voituriez, “Active Particles with Soft and Curved Walls: Equation of State, Ratchets, and Instabilities,” *Phys. Rev. Lett.*, vol. 117, no. 9, p. 098001, Aug. 2016, doi: 10.1103/PhysRevLett.117.098001.
- [275] D. Loi, S. Mossa, and L. F. Cugliandolo, “Effective temperature of active matter,” *Phys. Rev. E*, vol. 77, no. 5, p. 051111, May 2008, doi: 10.1103/PhysRevE.77.051111.
- [276] R. Cini, G. Loglio, and A. Ficalbi, “Temperature dependence of the surface tension of water by the equilibrium ring method,” *Journal of Colloid and Interface Science*, vol. 41, no. 2, pp. 287–297, Nov. 1972, doi: 10.1016/0021-9797(72)90113-0.
- [277] W. R. Tschinkel, “The Morphometry of *Solenopsis* Fire Ants,” *PLOS ONE*, vol. 8, no. 11, p. e79559, Nov. 2013, doi: 10.1371/journal.pone.0079559.
- [278] W. R. Tschinkel, A. S. Mikheyev, and S. R. Storz, “Allometry of workers of the fire ant, *Solenopsis invicta*,” *Journal of Insect Science*, vol. 3, no. 1, Jan. 2003, doi: 10.1093/jis/3.1.2.
- [279] M. C. Marchetti *et al.*, “Hydrodynamics of soft active matter,” *Rev. Mod. Phys.*, vol. 85, no. 3, pp. 1143–1189, Jul. 2013, doi: 10.1103/RevModPhys.85.1143.
- [280] M. Saar, T. Gilad, T. Kilon-Kallner, A. Rosenfeld, A. Subach, and I. Scharf, “The interplay between maze complexity, colony size, learning and memory in ants while solving a maze: A test at the colony level,” *PLOS ONE*, vol. 12, no. 8, p. e0183753, Aug. 2017, doi: 10.1371/journal.pone.0183753.
- [281] T. Sakai *et al.*, “Design and Fabrication of a High-Strength Hydrogel with Ideally Homogeneous Network Structure from Tetrahedron-like Macromonomers,” *Macromolecules*, vol. 41, no. 14, pp. 5379–5384, Jul. 2008, doi: 10.1021/ma800476x.
- [282] T. Sakai, “Experimental verification of homogeneity in polymer gels,” *Polym J*, vol. 46, no. 9, pp. 517–523, Sep. 2014, doi: 10.1038/pj.2014.28.
- [283] S. Liese *et al.*, “Hydration Effects Turn a Highly Stretched Polymer from an Entropic into an Energetic Spring,” *ACS Nano*, vol. 11, no. 1, pp. 702–712, Jan. 2017, doi: 10.1021/acsnano.6b07071.



- [284] A. D. Drozdov and J. deC. Christiansen, “Tension–compression asymmetry in the mechanical response of hydrogels,” *Journal of the Mechanical Behavior of Biomedical Materials*, vol. 110, p. 103851, Oct. 2020, doi: 10.1016/j.jmbbm.2020.103851.
- [285] A. M. Sokac, “Seeing a Coastline Paradox in Membrane Reservoirs,” *Developmental Cell*, vol. 43, no. 5, pp. 541–542, Dec. 2017, doi: 10.1016/j.devcel.2017.11.013.
- [286] C. A. Schneider, W. S. Rasband, and K. W. Eliceiri, “NIH Image to ImageJ: 25 years of image analysis,” *Nature Methods*, vol. 9, no. 7, Art. no. 7, Jul. 2012, doi: 10.1038/nmeth.2089.
- [287] V. Pratt, “Direct least-squares fitting of algebraic surfaces,” *SIGGRAPH Comput. Graph.*, vol. 21, no. 4, pp. 145–152, Aug. 1987, doi: 10.1145/37402.37420.
- [288] Chernov, Nikolai, *Circle Fit (Pratt method)*. 2009. [Online]. Available: <https://www.mathworks.com/matlabcentral/fileexchange/22643-circle-fit-pratt-method>

## APPENDICES

### Appendix A. Supporting information for Chapter II

#### A.1 Boundary conditions

##### A.1.a A Lagrangian RVE Permits Controlled Deformation

To initially generate the extended periodic domain, the positions of the nodes,  $\mathbf{x}^\alpha$  ( $\alpha \in [1, \mathcal{N}]$ ) are replicated across every boundary according to:

$$\begin{aligned}
 \mathbf{x}^T &= \mathbf{x}^\alpha + \left[ +\frac{\partial x}{\partial y}, +h \right], \\
 \mathbf{x}^B &= \mathbf{x}^\alpha + \left[ -\frac{\partial x}{\partial y}, -h \right], \\
 \mathbf{x}^R &= \mathbf{x}^\alpha + \left[ +w, +\frac{\partial y}{\partial x} \right], \\
 \mathbf{x}^L &= \mathbf{x}^\alpha + \left[ -w, -\frac{\partial y}{\partial x} \right], \\
 \mathbf{x}^{TR} &= \mathbf{x}^\alpha + \left[ +w + \frac{\partial x}{\partial y}, +h + \frac{\partial y}{\partial x} \right], \\
 \mathbf{x}^{TL} &= \mathbf{x}^\alpha + \left[ -w + \frac{\partial x}{\partial y}, +h - \frac{\partial y}{\partial x} \right], \\
 \mathbf{x}^{BR} &= \mathbf{x}^\alpha + \left[ +w - \frac{\partial x}{\partial y}, -h + \frac{\partial y}{\partial x} \right], \\
 \mathbf{x}^{BL} &= \mathbf{x}^\alpha + \left[ -w - \frac{\partial x}{\partial y}, -h - \frac{\partial y}{\partial x} \right],
 \end{aligned} \tag{A.1}$$

where superscripts  $T$ ,  $B$ ,  $L$ , and  $R$  denote nodes replicated to the top, bottom, left, and right of the domain, respectively. By extension, double-lettered superscripts represent the corners (e.g.,  $TR$  denotes the top right corner).  $\partial x/\partial y$  and  $\partial y/\partial x$  represent the the relative change of  $x$  at the domain bounds as a function of  $y$ , and change of  $y$  as a function of  $x$ , respectively. Note that for computational efficiency, only the nearest nodes to each boundary, defined as those less than roughly the length of a single chain ( $Nb$ ) away, are replicated across their respective opposite bounds.

### A.1.b Eularian Conditions Prohibit Diffusion Beyond Domain Limits

To ensure that tracked nodes do not diffuse out of the simulation limits, a Eularian condition is enforced whereby any particle that exits the bounds of  $\Omega$  is re-positioned into the domain according to:

$$\begin{aligned} \mathbf{x}^\alpha \in \partial\Omega^T &= \mathbf{x}^\alpha - \left[ \frac{\partial x}{\partial y}, h \right], \\ \mathbf{x}^\alpha \in \partial\Omega^B &= \mathbf{x}^\alpha + \left[ \frac{\partial x}{\partial y}, h \right], \\ \mathbf{x}^\alpha \in \partial\Omega^R &= \mathbf{x}^\alpha - \left[ w, \frac{\partial y}{\partial x} \right], \\ \mathbf{x}^\alpha \in \partial\Omega^L &= \mathbf{x}^\alpha + \left[ w, \frac{\partial y}{\partial x} \right], \end{aligned} \tag{A.2}$$

where  $\mathbf{x}^\alpha \in \Omega$  denotes that node  $\alpha$  has moved into the  $T$ ,  $B$ ,  $L$ , and  $R$  periodic boundaries of the domain,  $\Omega$ , respectively. Once nodes are repositioned in  $\Omega$ , they are replicated at each time step according to the conditions of Appendix A.I.a.

### A.2 Domain size convergence

In order to select an appropriate initial square domain size (for which  $h = w$ ), the networks' global stress responses is examined. The smallest domain dimension (i.e.,  $w$  at full deformation) must be larger than the contour length of a single chain ( $Nb = 3.5 \zeta$ ). To enforce this, the minimum domain size considered in this work contains  $\mathcal{N} = 225$  nodes, which corresponded to initial domain dimensions of  $11.25 \times 11.25 \zeta$  and final dimensions of  $5.625 \times 22.5 \zeta$  (after 100% incompressible, uniaxial network stretch is applied), which satisfies the condition  $w > Nb$ . The ensemble averaged stress response of 10 trial networks, containing  $\mathcal{N} = 225$ ,  $\mathcal{N} = 400$ , and  $\mathcal{N} = 625$  nodes (which correspond to roughly 15, 20 and 25 nodes per edge, respectively) is displayed in **Fig. A.1**. Notably, there is no significant change in the measured stress response as the domain size is increased from 225 nodes to 625 nodes, and so the domain size was set to  $\mathcal{N} = 225$  for computational efficiency.

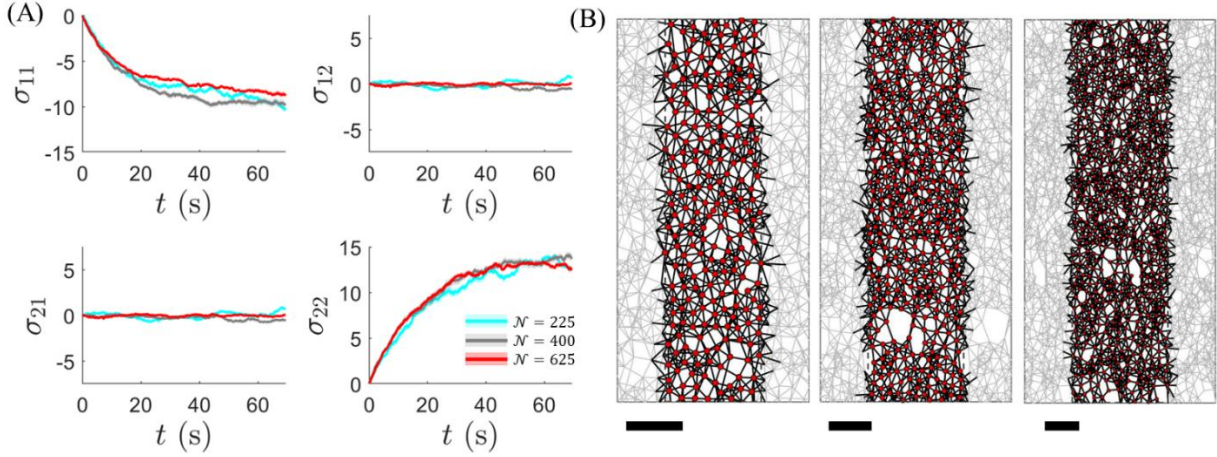


**Fig. A.1. Domain size convergence.** (A) The four components of virial stress, ensemble averaged over 10 distinct trials (each), are plotted for increasing domain sizes,  $N = 225$  nodes (blue),  $N = 400$  nodes (grey), and  $N = 625$  nodes (red). (B) Networks at  $\epsilon \approx 1$  are plotted from left to right for  $N = 225$  nodes,  $N = 400$  nodes, and  $N = 625$  nodes, respectively. Scale bars under each snapshot represent the contour length of a single chain,  $Nb$  (or  $3.5 \zeta$ ).

### A.3 Time step convergence

In order to select an appropriate time step size,  $\Delta t$ , the networks' stress responses, mean bond kinetic rates, and degree of homogenization were considered. The time step was initially set such that it was two orders of magnitude lower than the inverse of the stress-free bond detachment rate,  $k_d^{0-1} = 100$  s, or the highest strain rate investigated,  $\dot{\epsilon}^{-1} = 50$  s. As such, the largest time step considered was  $\Delta t = 0.5$  s. As depicted in **Fig. A.2**, decreasing  $\Delta t$  over  $\Delta t = [0.5, 0.1, 0.05, 0.01]$  s, did not influence the measured stress response of the networks (**Fig. A.2.A**). Nor did it impact the average measured bond kinetic rates and - by extension - the average coordination number of the network (**Fig. A.2.B**). In the scope of this work,  $\Delta t$  was conservatively set to 0.1% of the highest inverse strain rate or  $\Delta t = 0.05$  s, which is well below the convergence threshold while also allowing for relatively low computational time.

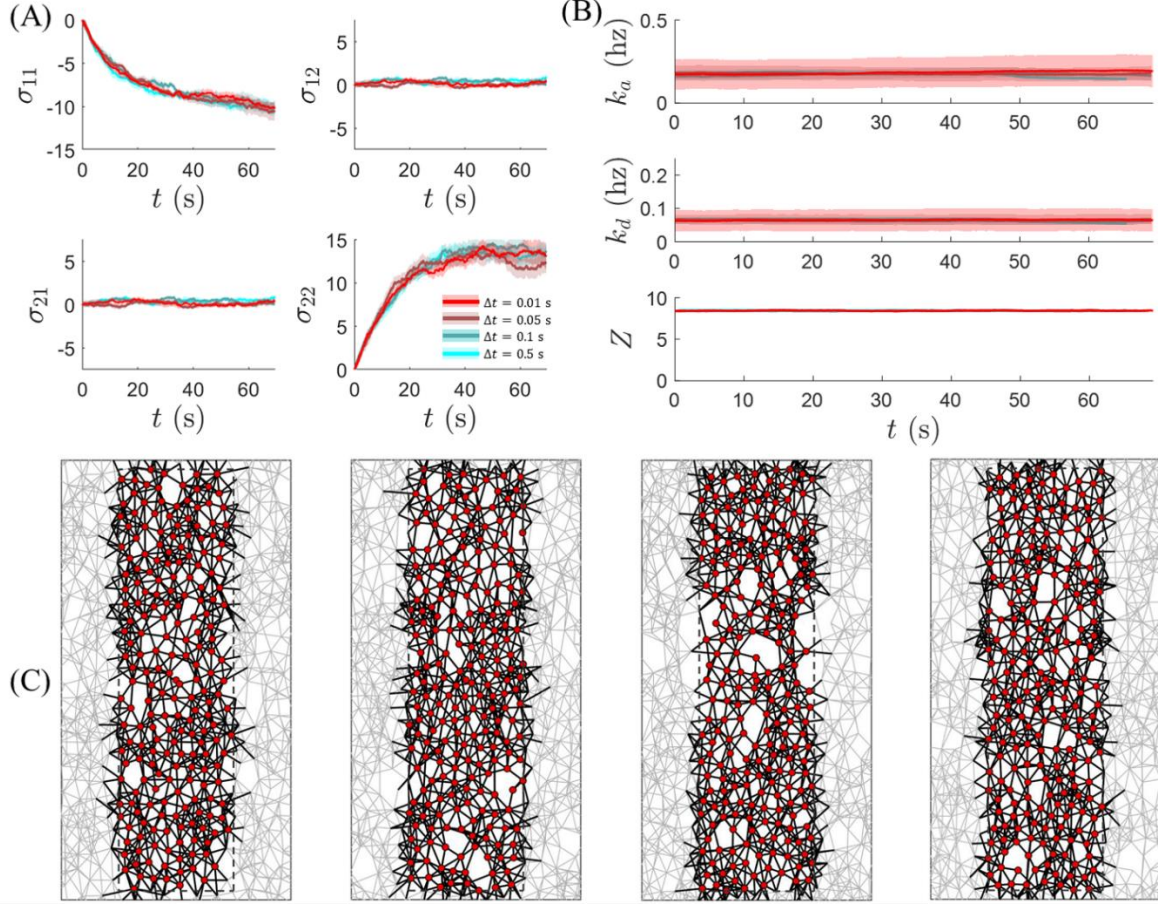


**Fig. A.2. Time step convergence.** (A) The four components of virial stress are plotted for decreasing timesteps,  $\Delta t = 0.5$  s (blue),  $\Delta t = 0.1$  s,  $\Delta t = 0.05$  s, and  $\Delta t = 0.01$  s (red). (B) The attachment (top) and detachment (center) rates are plotted with respect to time for the four respective time steps, along with the resulting average coordination number (bottom). (C) Networks at  $\epsilon \approx 0.9$  are plotted from left to right for  $\Delta t = 0.5$  s,  $\Delta t = 0.1$  s,  $\Delta t = 0.05$  s, and  $\Delta t = 0.01$  s, respectively.

#### A.4 Stress response of a network with Gaussian springs

As a benchmark comparison between the discrete framework and continuum approach, networks of Gaussian springs were modeled and deformed according to the load history of **Fig. 1.6.A** in the manuscript. Force-dependent detachment through Eyring's model was maintained in order to ensure that the networks achieved initial steady state and observed detailed balance. The normal stress response (ensemble averaged for fifty networks, each) during loading and relaxation is depicted in **Fig.**

**A.3.A** and **A.3.B**, respectively, for five different strain rates. As expected, the stress predicted by the discrete and continuum models are in good agreement during loading when Gaussian chains are used in both frameworks. However, since force-dependent bond dynamics were maintained, a non-exponential decay in stress is still observed during relaxation.

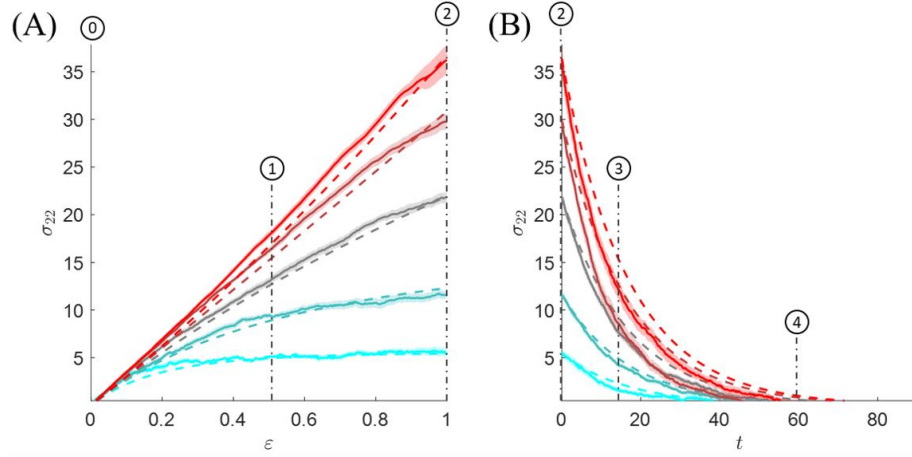


**Fig. A.3. Model validation against TNT.** (A) Normal stresses from creep experiments are plotted with respect to engineering strain,  $\epsilon = F_{22} - 1$ , for  $W \approx 1/8$  (cyan),  $W \approx 1/4$  (teal),  $W \approx 1/2$  (grey),  $W \approx 1$  (maroon), and  $W \approx 2$  (red). (B) Normal stresses from relaxation experiments are plotted with respect to time for three different initial values of stress. All results from the discrete model are plotted as continuous curves with standard error represented by the shaded region, and results from TNT are plotted as dotted curves.

## Appendix B. Supporting information for Chapter III

### B.1 The discrete network model

#### B.1.a Domain description, network initiation, and applied boundary conditions

The number of nodes,  $\mathcal{N} = 400$ , comprising each simulated network in this study was set based on the domain size convergence findings of Wagner, et al. (2021). First, a 2D volume element (VE) was defined with its center at Cartesian coordinates  $\mathbf{X} = [0,0]$  and square dimensions  $L = (\mathcal{N}/\rho)^{0.5}$ . Here,  $\rho$  is a tuning parameter with units of  $[\text{length}]^{-2}$  used to modulate the domain density until a roughly zero stress state occurred once steady state bond dynamics were reached. This occurred when tensile entropic chain forces were approximately equilibrated with repulsive volume exclusion forces, both of which depend on the nominal node spacing. Nodes were initially seeded into the VE using a Poisson point process. To impart the networks with both stable and dynamic bonds, each node was then designated as one of three types: (i) a universal crosslinker, (ii) a stable bond crosslinker, or (iii) a dynamic bond crosslinker. This was done to mimic the composition of networks such as the hydrogels investigated by Richardson, et al. (2018), thereby reproducing a physically possible means by which such networks may be synthesized. Universal crosslinkers were permitted to bond with either stable or dynamic crosslinkers. However, stable crosslinkers were not permitted bond to dynamic crosslinkers, and no intraspecies bonding was permitted amongst any of the three node types. The fraction of universal crosslinkers was maintained at 50%. However, the fraction of crosslinker types comprising the remaining 50% of nodes was swept over the range of 0 to 100% stable crosslinker.

Once the nodes were initially positioned and designated, they were permitted to bond with and detach from one another telechellically via the bond kinetics described

below. To reach steady state bond kinetics, bond reactions were allowed to occur for 100 timesteps (without applying any deformation to the VE bounds) until a steady state coordination number and end-to-end chain distribution were reached. To ensure ample temporal resolution, the discretized timestep,  $\Delta t$ , was set at least two orders of magnitude smaller than the bond dissociation timescale,  $k_d^{-1}$ . After every reconfiguration step, the networks were equilibrated per the description below. Note that the timescale of the network model is in arbitrary units of time such that  $k_d$  is simply normalized by the median value investigated throughout the manuscript.

### B.1.b Bond kinetics

Bond association is captured through the scaling law introduced in Wagner, et al. (2021)[3], giving the attachment rate as:

$$k_a = \tau_a^{-1} \left( \frac{b}{d} \right)^4, \quad (\text{B.1})$$

where  $b$  is the length of a single Kuhn segment,  $\tau_a$  is the time it takes a Kuhn segment to diffuse a distance of  $b$ , and  $d$  is the pairwise separation distance between neighboring nodes within cutoff distance  $d < l_c$ . Here,  $l_c = Nb$  where  $N$  is the number and of Kuhn segments in an attached chain so that  $l_c$  is its contour length. Both bond association and dissociation are treated as memoryless processes such that the probability of a reaction event occurring at time  $t$  follows[3]:

$$dP = k e^{-kt} dt, \quad (\text{B.2})$$

where  $k$  represents either the rate of bond association,  $k_a$ , or dissociation,  $k_d$ .

### B.1.c Pairwise forces

The ideal entropic force in a chain is given by[3]:

$$\mathbf{f}_t = 3k_b T \frac{\lambda}{\sqrt{Nb}} \frac{\mathbf{r}}{|\mathbf{r}|}, \quad (\text{B.3})$$



where  $k_b$  is the Boltzmann constant,  $T$  is the ambient temperature,  $\lambda = |\mathbf{r}|/\sqrt{N}b$  is the chain stretch, and  $\mathbf{r}$  is the end-to-end vector of a chain. Volume exclusion forces are captured via a phenomenological inverse potential for soft particles that yields a force-distance relation of [3]:

$$\mathbf{f}_r = \frac{\mathbf{d}}{|\mathbf{d}|} \begin{cases} -\gamma E \left( \frac{1}{R} - \frac{R^\gamma}{d^{\gamma+1}} \right), & d < R \\ 0, & d \geq R \end{cases}, \quad (\text{B.4})$$

where  $E$  defines the force scale,  $\gamma = 2$  is a scaling coefficient that modulates particle stiffness,  $\mathbf{d}$  is the end-to-end separation vector between nodes, and  $R = Nb$  is the cutoff distance.

#### B.1.d Force equilibration

Pairwise interactions are used to compute the unbalanced force on each node, denoted by  $\alpha$ , as  $\mathbf{f}^\alpha = \sum_\beta \mathbf{f}^{\alpha\beta}$ . Here,  $\mathbf{f}^{\alpha\beta}$  represents a single pairwise force, either  $\mathbf{f}_t$  or  $\mathbf{f}_r$ , between node  $\alpha$  and its  $\beta^{th}$  neighbor. Unbalanced forces are used to iteratively equilibrate each node's position after every VE deformation or network reconfiguration step (i.e., "timestep"). The position of node  $\alpha$  is updated from iteration  $k$  to  $k + 1$  according to:

$$\mathbf{x}_{k+1}^\alpha = \mathbf{x}_k^\alpha + \eta^{-1} \mathbf{f}^\alpha, \quad (\text{B.5})$$

where  $\eta$  is a numerical overdamping coefficient set to ensure stable convergence.

#### B.1.e Boundary conditions and loading history

The VEs were 2D periodic such that incremental changes to their four corners stretched or compressed the chains that transcended the four boundaries. Accordingly, incompressible deformations were applied to the four corners defining the VE via a symmetrical velocity gradient of the form,  $\mathbf{L} = [W, -W; -W, W]$ , where  $W = \dot{\epsilon}/k_d$  is a normalized strain rate known as the Weissenberg number and  $\dot{\epsilon}$  is the true strain rate. At high values of  $W$ , the deformation rate is far greater than the

intrinsic bond dissociation rate such that even dynamic networks behave elastically. To ensure that bond dynamics were negligible during loading and approximate a step function for stress relaxation, we here set  $W = 100$ . The networks were deformed until they reached a principal stretch of  $\lambda = 2$  (and normal stretch of  $1/2$ ), after which stress relaxation was allowed to occur for  $t^* \approx 4$  (where  $t^* = tk_d$ ). The loading history is depicted in **Fig. B.1** as the true strain with respect to normalized time.

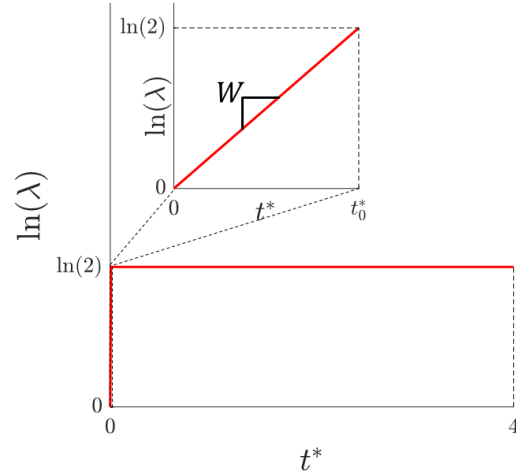


**Figure B.1. Applied loading history:** True strain,  $\ln \lambda$ , is plotted with respect to normalized time,  $t^* = tk_d$ . The inset displays  $\ln \lambda$  versus  $t^*$  (with a significantly dilated time axis) to illustrate the definition of  $W = \ln(\lambda)/t^*$ .

### B.1.f Parametric space

Detailed parametric values and sweeping ranges are provided in **Tables B.1** and **B.2**, respectively.

**Table B.1.** Detailed parametric definitions and values.

Parameter	Definition	Swept Values	Reason for Value
$\mathcal{N}$	Nodes per domain	400	Set to ensure convergence of stress response with respect to increasing domain size per Wagner, et al. (2021)
$\zeta$	Normalization length scale	$\sqrt{\mathcal{N}}$	Set such that each node occupies on order of 1-unit length <sup>2</sup>
$L^*$	Initial square domain dimensions	$\zeta \rho^{-0.5}$	Set such that each node occupies on order of 1-unit length <sup>2</sup>
$\rho^*$	Scaling coefficient to adjust domain density	1.78	Set to equilibrate entropic tensile forces with volume exclusion in initial networks.
$\tau_\alpha$	Kuhn segment diffusion timescale	$1 \times 10^{-9}$	Preserved from Wagner, et al. (2021)
$k_b T$	Normalized thermal energy scale	$5 \times 10^{-2}$	
$N$	Kuhn segments per chain	700	
$b^*$	Normalized Kuhn length	$5 \times 10^{-3}$	
$E$	Force scaling coefficient to adjust repulsion magnitude	1.25	
$\gamma$	Scaling coefficient to adjust repulsion stiffness	2	
$R^*$	Normalized volume exclusion cutoff distance	$N b^*$	
$\eta^*$	Normalized numerical damping viscosity	$1.5 \times 10^{-4}$	Set to ensure ample temporal resolution during reconfiguration
$\Delta t^*$	Discretized time	$\Delta t^* < 0.01 \cdot k_d^{-1}$	

**Table B.2.** Detailed sweeping ranges of free parameters.

Parameter	Definition	Swept Values
$f$	Fraction of stable bonds.	{0,10, ... 90,100}%
$k_d$	Normalized detachment rate	{0.01,0.1,1,10,100}
$z$	Functionality (i.e., no. of potential bonds per crosslink)	{4,8}

## B.2 Transient network theory derivations

### B.2.a Initial loading and stress normalization

Recall that the simple rule of mixture gives:

$$\boldsymbol{\sigma} = k_b T(c^s \mathbf{b} + c^d \boldsymbol{\mu}) + \pi \mathbf{I}, \quad (\text{B.6})$$

where, again,  $c^s = cP^s$  and  $c^d = cP^d$ . We aim to normalize this stress by the peak stress, which occurs at the time of loading cessation. Recalling that  $\boldsymbol{\mu}$  evolves according to (B.6):

$$\dot{\boldsymbol{\mu}} = \mathbf{L}\boldsymbol{\mu} + \boldsymbol{\mu}\mathbf{L}^T - k_d(\boldsymbol{\mu} - \mathbf{I}). \quad (\text{B.7})$$

and given  $W \gg 1$  (i.e., that  $\dot{\varepsilon} \gg k_d$ ), the rightmost term in (B.7) approach zero during loading, leaving:

$$\dot{\boldsymbol{\mu}} = \mathbf{L}\boldsymbol{\mu} + \boldsymbol{\mu}\mathbf{L}^T, \quad (\text{B.8})$$

where  $\mathbf{L} = \dot{\mathbf{F}}\mathbf{F}^{-1}$ ,  $\dot{\mathbf{F}} = \partial \mathbf{F} / \partial t$ , and  $\mathbf{F} = \text{diag}(\lambda^{-1}, \lambda)$ . For uniaxial extension occurring in the second principal direction, we are concerned with the evolution of  $\mu_{22}$ , which evolves according to:

$$\frac{\partial \mu_{22}}{\partial t} = 2\mu_{22}\lambda^{-1} \frac{\partial \lambda}{\partial t}. \quad (\text{B.9})$$

Integrating both sides with the condition  $\mu_{22}(\lambda = 1) = 1$  gives:

$$\mu_{22} = \lambda^2 = b_{22} \quad (\text{B.10})$$

for fast loading. Thus, substituting (B.10) into (B.6) for the stress component in the principal direction of stretch provides:

$$\sigma_{22}^{max} = ck_b T[p^s f + p^d(1 - f)]\lambda^2 + \pi. \quad (\text{B.11})$$

Similar analysis in the direction normal to stretch gives:

$$\sigma_{11}^{max} = ck_b T[p^s f + p^d(1 - f)]\lambda^{-2} + \pi, \quad (\text{B.12})$$

with the added traction-free boundary condition that  $\sigma_{11} = 0$ . Solving for  $\pi$  in (B.12) and substituting into (B.11) gives:

$$\sigma_{22}^{max} = ck_b T[p^s f + p^d(1 - f)]\left(\lambda^2 - \frac{1}{\lambda^2}\right). \quad (\text{B.13})$$

### B.2.b Stress relaxation

To begin stress relaxation, the strain rate is removed (i.e.,  $\mathbf{L} = \mathbf{0}$ ) such that (B.7) becomes:

$$\dot{\boldsymbol{\mu}} = -k_d(\boldsymbol{\mu} - \mathbf{I}). \quad (\text{B.15})$$

Taking the time at which stress relaxation begins as the reference time,  $t = 0$ , and solving (S15) for the principal components of  $\boldsymbol{\mu}$  gives:

$$\mu_{11} = (\mu_{11}^0 + 1)e^{-k_d t} - 1, \quad (\text{B.16})$$

and:

$$\mu_{22} = (\mu_{22}^0 + 1)e^{-k_d t} - 1, \quad (\text{B.17})$$

where, from (B.10),  $\mu_{11}^0 = \lambda^{-2}$  and  $\mu_{22}^0 = \lambda^2$  since  $W \gg 1$  during initial loading. Substituting (B.16) and (B.17) into (B.6) gives the principal components of each principal component of stress as:

$$\sigma_{11} = ck_b T \{p^s f \lambda^{-2} + p^d (1 - f)[(\lambda^{-2} + 1)e^{-k_d t} - 1]\} + \pi, \quad (\text{B.18})$$

and:

$$\sigma_{22} = ck_b T \{p^s f \lambda^2 + p^d (1 - f)[(\lambda^2 + 1)e^{-k_d t} - 1]\} + \pi. \quad (\text{B.19})$$

Applying the traction-free boundary condition (i.e.,  $\sigma_{11} = 0$ ), solving for  $\pi$ , and substituting  $\pi$  into (S19) gives the principal component of stress in the extensile direction as:

$$\sigma_{22} = ck_b T \left( \lambda^2 - \frac{1}{\lambda^2} \right) \{p^s f + p^d (1 - f)e^{-k_d t}\}. \quad (\text{B.20})$$

Finally, normalizing (B.20) by (B.13) provides the normalize tensile stress as:

$$\sigma^* = [p^s f + p^d (1 - f)e^{-k_d t}][p^s f + p^d (1 - f)]^{-1}. \quad (\text{B.21})$$

### B.2.c Incorporating the relaxation factor

Supposing that some fraction of stable bonds,  $1 - \xi$ , are sufficiently jammed by surrounding crosslinks or bonded into a stable bond scaffold such that they affinely follow the global deformation gradient,  $\mathbf{F}$ , without relaxation, while the remaining

fraction,  $\xi$ , can relax into lower energy conformations due to the reconfiguration of the surrounding network, then we may rewrite Eqn. (B.6) as:

$$\boldsymbol{\sigma} = ck_b T [p^s f(1 - \xi) \mathbf{b} + p^s f \xi \boldsymbol{\mu} + p^d(1 - f) \boldsymbol{\mu}] + \pi \mathbf{I}. \quad (\text{B.22})$$

As a simple first assumption, we have invoked that the rate of stable bond relaxation due to reconfiguration is synonymous with that of bond dissociation of neighboring dynamic bonds (i.e.,  $k_d$ ) through  $\boldsymbol{\mu}$ . Thus, during elastic loading,  $\boldsymbol{\mu} \rightarrow \mathbf{b}$  and (B.22) reverts to (B.13). As before, the condition that  $\sigma_{11} = 0$ , along with the definitions of  $\boldsymbol{\mu}$  from (B.16) and (B.17) are used to solve for  $\pi$ , which then allows that component of stress in the extensile direction be written:

$$\sigma_{22} = ck_b T \left( \lambda^2 - \frac{1}{\lambda^2} \right) [p^s f(1 - \xi) + p^s f \xi e^{-k_d t} + p^d(1 - f) e^{-k_d t}]. \quad (\text{B.23})$$

Once again normalizing (B.23) by (B.13) gives the normalized tensile stress as:

$$\sigma^* = [p^s f(1 - \xi) + p^s f \xi e^{-k_d t} + p^d(1 - f) e^{-k_d t}] [p^s f + p^d(1 - f)]^{-1}. \quad (\text{B.24})$$

#### B.2.D Hybrid networks with two dissociation timescales

Supposing that a hybrid network is comprised of two different types of dynamic bonds with two distinct dissociation timescales,  $k_s^{-1}$  and  $k_d^{-1}$ , such that that the former types of bonds detach significantly slower than the latter (i.e.,  $k_d^{-1} \ll k_s^{-1}$ ). Then Eqn. (2.22) may be rewritten as:

$$\boldsymbol{\sigma} = ck_b T [p^s f(1 - \xi) \boldsymbol{\mu}^s + p^s f \xi \boldsymbol{\mu}^d + p^d(1 - f) \boldsymbol{\mu}^d] + \pi \mathbf{I}. \quad (\text{B.25})$$

where  $\boldsymbol{\mu}^d$  and  $\boldsymbol{\mu}^s$  are the conformation tensors of the chains containing more and less dynamic bonds, respectively. These conformation tensors evolve according to  $\dot{\boldsymbol{\mu}}^s = -k_s(\boldsymbol{\mu}^s - \mathbf{I})$  and  $\dot{\boldsymbol{\mu}}^d = -k_d(\boldsymbol{\mu}^d - \mathbf{I})$ . In Eqn. (B.25), we have assumed that the coupled stress term relaxes at the faster dissociation rate of the more dynamic bonds (i.e., at a rate  $k_d$ ) since the dissociation of the relatively more stable bonds is considerably slower (i.e.,  $k_s \ll k_d$ ).

Here we apply simple shear conditions to approximate the parallel plate rheometry conducted by Richardson, et al. (2019) for which:

$$\mathbf{F} = \begin{bmatrix} 1 & \gamma & 0 \\ 0 & 1 & 0 \\ 0 & 0 & 1 \end{bmatrix}, \quad (\text{B.26})$$

and:

$$\mathbf{L} = \begin{bmatrix} 0 & \dot{\gamma} & 0 \\ 0 & 0 & 0 \\ 0 & 0 & 0 \end{bmatrix}, \quad (\text{B.27})$$

where  $\gamma$  is the peak shear strain and  $\dot{\gamma}$  is the shear rate. Again, during loading ( $\dot{\gamma} \gg k_d$  and  $\dot{\gamma} \gg k_s$ ),  $\boldsymbol{\mu}_s \rightarrow \mathbf{b}$  and  $\boldsymbol{\mu}_d \rightarrow \mathbf{b}$ , giving (B.25) as:

$$\boldsymbol{\sigma} = ck_b T [p^s f + p^d (1 - f)] \mathbf{b} + \pi \mathbf{I}. \quad (\text{B.28})$$

Solving for  $\mathbf{b} = \mathbf{F} \mathbf{F}^T$  and substituting into (B.28) gives the peak shear stress as:

$$\tau = ck_b T [p^s f + p^d (1 - f)] \gamma. \quad (\text{B.29})$$

During stress relaxation (i.e.,  $\mathbf{L} = \mathbf{0}$ ), given relatively small shear strain ( $\gamma \sim 0.1$ ) then the principal orientation of chain stretch remains relatively unaffected, and we may uphold the general relation (B.15) for both dynamic bond types (i.e., the shear components may be written  $\mu^s \approx \exp(-k_s t)$  and  $\mu^d \approx \exp(-k_d t)$ ). Therefore, the shear component of stress from (B.25) may be written as follows during stress relaxation:

$$\tau = ck_b T [p^s f (1 - \xi) e^{-k_s t} + p^s f \xi e^{-k_d t} + p^d (1 - f) e^{-k_d t}] \gamma. \quad (\text{B.30})$$

Normalizing (B.30) by the peak shear stress from (B.29) gives:

$$\tau^* = [p^s f (1 - \xi) e^{-k_s t} + p^s f \xi e^{-k_d t} + p^d (1 - f) e^{-k_d t}] [p^s f + p^d (1 - f)]^{-1}. \quad (\text{B.33})$$

### B.3 Extended network model results

#### B.3.a Bond dynamics, percolation, & the relaxation factor

**Fig. B.2** depicts the average measured bond dynamics over  $n = 10$  trials for networks with varied values of  $f$  and  $k_d$ . As expected, measured values of  $k_d$  closely match the input values and are independent of  $f$  (**Fig. B.2.A-B**). In contrast,  $k_a$  is directly correlated with  $k_d$  and inversely correlated with  $f$  (**Fig. B.2.C-D**). This is because dissociated bonds may only attach to neighboring bonds within a radial distance of

the maximum chain length. Therefore, any factor that influences the number of detached bonds within reach of each other influences  $k_a$ . Specifically, as  $k_d$  increases, so too does the number of attachment opportunities at a given time, and therefore  $k_a$  increases proportionately to  $k_d$ . These two effects are an artifact of a prescribed polymer diffusion timescale,  $\tau_0$ , (and therefore bond association timescale) that is significantly lower than the bond dissociation timescale (i.e.,  $k_d \ll k_a$ ). This is reflected in  $k_a/(k_a + k_d)$ , which indicates the steady state probability that a given dynamic bond is attached (**Fig. B.2.E-F**). While  $k_a/(k_a + k_d)$  remains close to unity and appears relatively independent of  $k_d$  when  $k_d \sim 0.01$  to 1, it eventually decreases when the dissociation rate is high (e.g.,  $k_d \sim 10$  to 100). This suggests that the intrinsic association rate,  $k_a$ , is somewhere on the order of 10 and that when  $k_d \gtrsim 10$ , attachment events are no longer dictated primarily by bonding opportunities but rather  $\tau_0$ .

Regarding the effects of stable bond fraction on bond dynamics, increasing  $f$  reduces the number of dynamic bonding opportunities and therefore decreases the effective  $k_a$  (**Fig. B.2.C-D**). Since  $k_a$  is lower for higher values of  $f$ ,  $k_a/(k_a + k_d)$  is as well (**Fig. B.2.E-F**), which influences the probability of dynamic bond percolation as discussed below. Interestingly, coordination has negligible influence on the measured bond dynamics. However, this independence is likely contingent on the allowance of redundant bonds between neighboring nodes, which ensures that  $k_a$  is more influenced by the number and distribution of nodes (as they govern bonding opportunities) than the total number of bonds. The relative independence of  $k_a$  and  $k_d$  is also reflected by the highly similar plots of attached bond probabilities,  $P^s = p^s f$ ,  $P^d = p^d(1 - f)$ , and  $P = P^s + P^d$  in **Fig. B.3**. However,  $P^d$  (and therefore  $P$ ) is slightly smaller (i.e., there are more dangling dynamic chains) at high  $k_d$  ( $k_d = 10$  or



100) and higher coordination ( $z = 8$ ), which suggests that attachment opportunities are saturated at the higher coordination number.

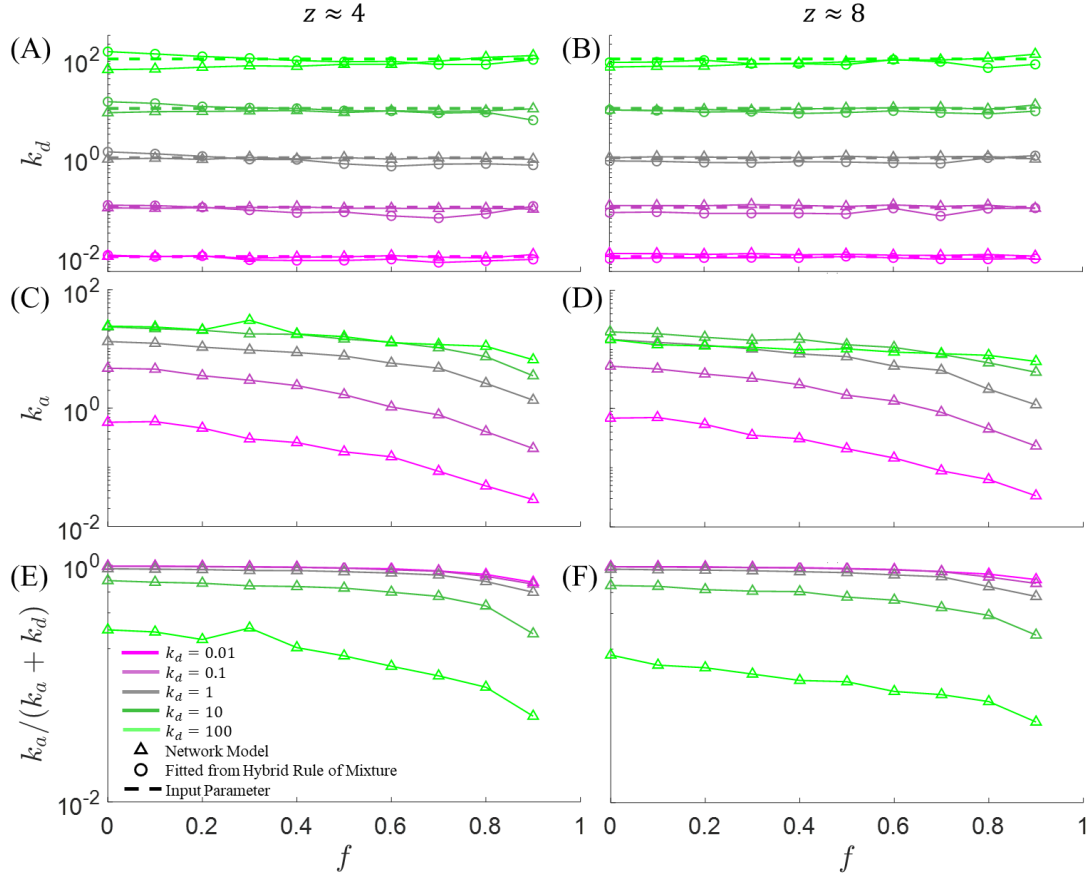


**Figure B.2. Bond dynamics as measured from discrete model.** (A-B) Average dynamic bond dissociation rate,  $k_d$ , is plotted with respect to the stable bond fraction,  $f$ , and input value of detachment rate,  $k_d$ , when coordination is (A)  $z = 4$  and (B)  $z = 8$ . (C-D) Average dynamic bond association rate,  $k_a$ , is plotted with respect to  $f$  and  $k_d$  for (C)  $z = 4$  and (D)  $z = 8$ . (E-F) Steady state attached dynamic bond fraction,  $k_a / (k_a + k_d)$ , is plotted with respect to  $f$  and  $k_d$  for (E)  $z = 4$  and (F)  $z = 8$ .

**Fig. B.4** depicts the average probabilities (over  $n = 10$  trials each) that the independent bond types form percolated networks when  $f$  and  $k_d$  are swept. **Fig. B.4.A-B** confirms that the probability of stable bond percolation is not dependent on  $k_d$ . Going from  $z = 4$  to  $z = 8$ , the stable bond percolation threshold (i.e., lowest fraction of bonds at which the networks may percolate) shifted to lower relative

fractions of stable bonds, from approximately  $f \sim 0.3$  to  $f \sim 0.2$ . Meanwhile, **Fig. B.4C-D** confirms that dynamic bond percolation is highly dependent on  $k_d$ , with higher values of  $k_d$  universally decreasing the probability that the dynamic bonds form a percolated network. Going from  $z = 4$  to  $z = 8$  the percolation threshold undergoes a shift from  $1 - f \sim 0.3$  to  $1 - f \sim 0.2$ . This directly mirrors the shift observed for the stable bond percolation threshold.

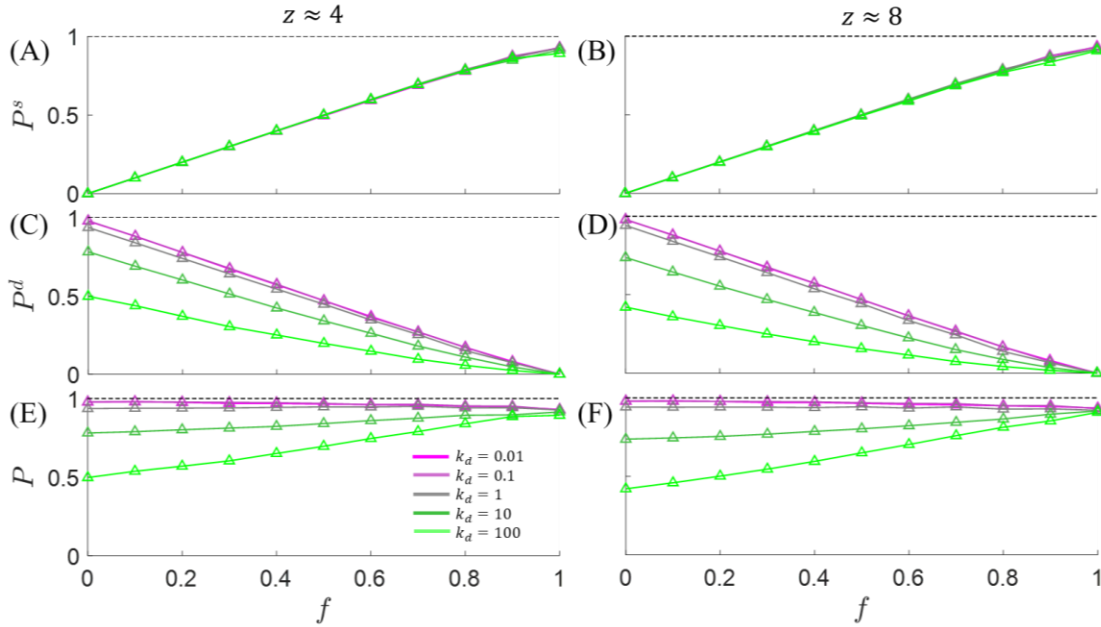


**Figure B.3. Bond attachment probabilities from discrete model.** (A-B) The average probability that a bond is stable and attached,  $P^s = fp^s$ , is plotted with respect to the stable bond fraction,  $f$ , and input value of detachment rate,  $k_d$ , when maximum coordination is (A)  $z = 4$  and (B)  $z = 8$ . (C-D) The average probability that a bond is dynamic,  $P^d = (1 - f)p^d$ , and attached is plotted with respect to  $f$  and  $k_d$  for (C)  $z = 4$  and (D)  $z = 8$ . (E-F) The probability that a given bond is attached,  $P = P^s + P^d$ , is plotted with respect to  $f$  and  $k_d$  for (E)  $z = 4$  and (F)  $z = 8$ .

**Fig. B.5** depicts the average ( $n = 10$ ) fitted values of  $1 - \xi$ , which represents the extent to which stable bonds are unable to relax, when  $f$  and  $k_d$  are swept. The scaling law given by:

$$\xi \sim 1 - \sqrt{\eta^2 + f^2(1 - \eta^2)}, \quad (\text{B.34})$$

is fitted to each discrete data set, where  $\eta$  represents the fraction of stable bonds that remain unable to relax in the limit  $f \rightarrow 0$ . Generally,  $\eta$  decreases as the dissociation rate increases, intuitively suggesting that higher bond dynamic beget lower fractions of jammed stable bonds when  $f \sim 0.1$ . Notably,  $\xi$  is not well predicted by (B.34) when  $z = 8$ , which is attributed to the fact that dynamic bonds in these networks saturate the bond attachment opportunities such that there exists a greater degree of detached stable bonds than in the networks with  $z = 4$ . Consequently, this reduces the effective fraction of attached stable bonds that are jammed at higher SB concentrations (**Fig. B.5.B**) below the asymptotic limit,  $1 - \xi = f$  ( $\eta \rightarrow 0$ ).

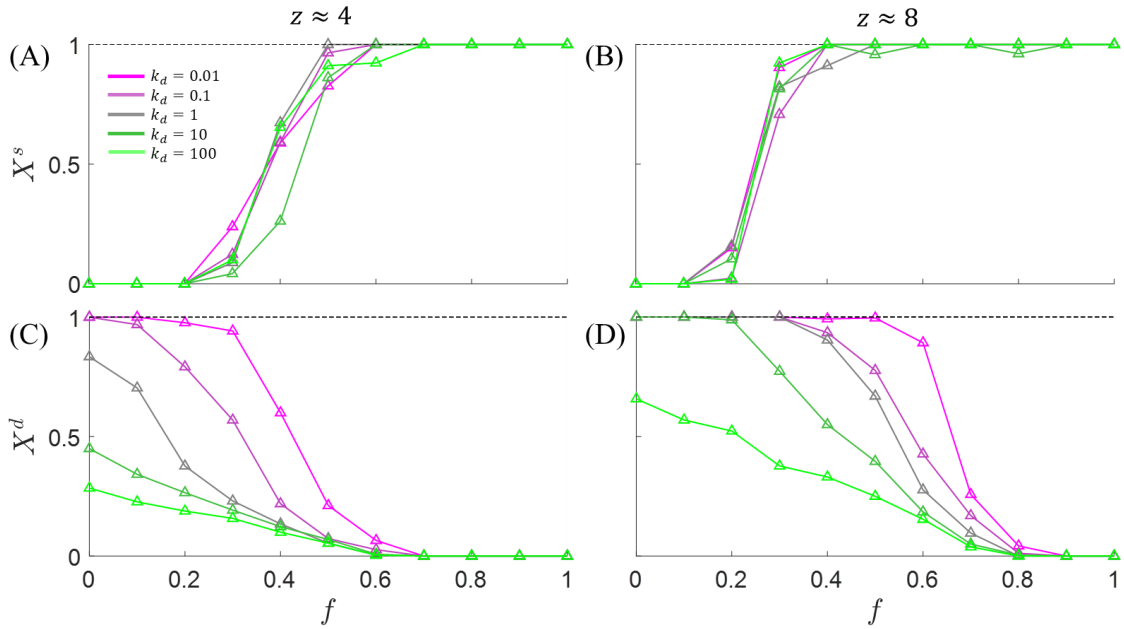


**Figure B.4. Decoupled network percolation probabilities.** (A-B) The average probability that the stable bonds independently form a percolated network,  $X^s$ , is plotted with respect to stable bond fraction,  $f$ , and input value of detachment rate,  $k_d$ , when maximum coordination is (A)  $z = 4$  and (B)  $z = 8$ . (C-D) The average probability that the dynamic bonds independently form a percolated network,  $X^d$ , is plotted with respect to  $f$  and  $k_d$  for (C)  $z = 4$  and (D)  $z = 8$ .

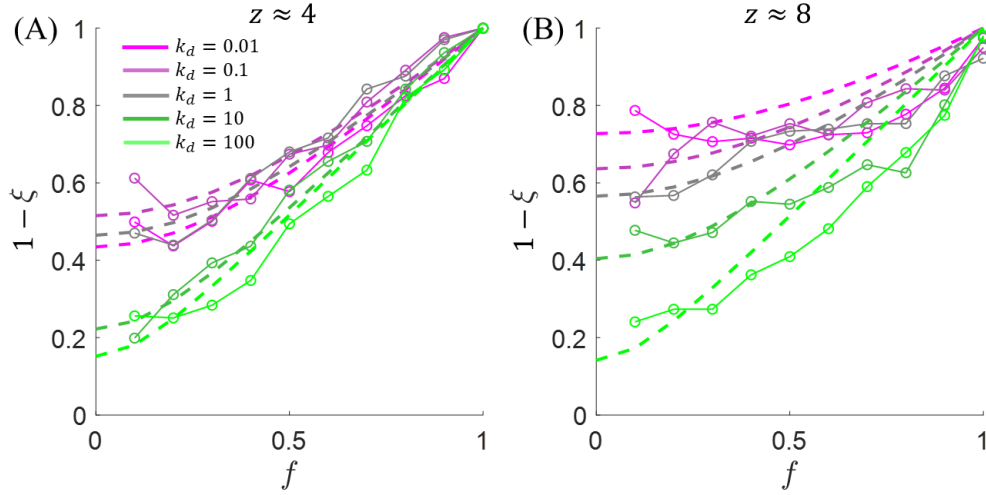


**Figure B.5. Effect of network coordination on stable bond relaxation.** (A-B) The stable bond immobilization fraction,  $1 - \xi$ , is plotted with respect to  $f$  for the ensemble average of  $n = 10$  networks with (A)  $z = 4$  and (B)  $z = 8$ .

### B.3.b Effects of chain length

A topologically influential parameter hypothesized to influence stable bond relaxation is the length of the chains. As such, chains with normalized lengths of  $L^* = 0.5$  and  $L^* = 2$  (where  $L^*$  is the contour length of a chain,  $Nb$ , normalized by the contour length of chains investigated earlier in this work) were used to generate and test the stress relaxation of *in silico* networks. Networks were generated and mechanically tested using the same procedure as earlier experiments (wherein  $L^* = 1$ ). The coupled ROM was subsequently fit to the data treating  $\xi$  as a fitting parameter. Stress relaxation results for shorter and longer chains are depicted in **Fig. B.6.A** and **B.6.B**, respectively. While the coupled ROM can predict the stress relaxation of the networks of longer chains without significant error, it is unable to do so for the networks of shorter chains at early stages of the relaxation process at which the discretely modeled networks relax significantly faster than the coupled ROM predicts through  $k_d$ .

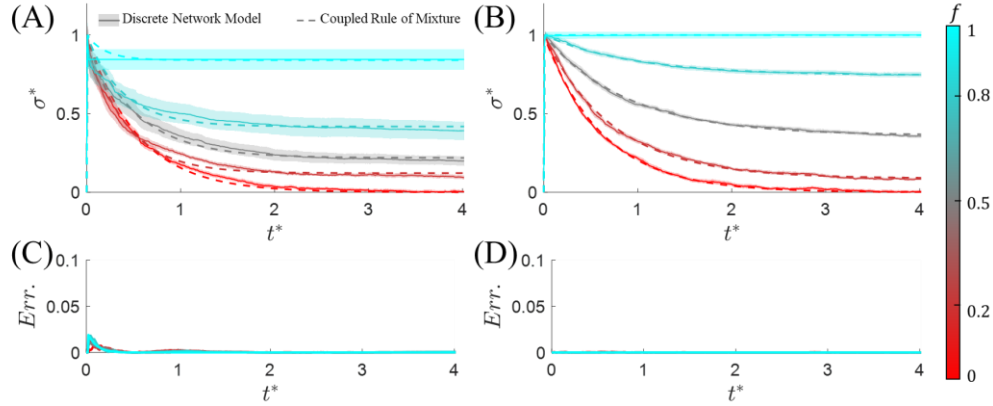


**Figure B.6. Fitting the coupled ROM to networks with variable chain length.** (A) Normalized stress,  $\sigma^*$ , is plotted with respect to normalized time,  $t^*$ , for the ensemble average of  $n = 10$  discrete simulations (solid curves with shaded S.E.) and as predicted by Eqn. (11) (dotted curves) when  $k_d = 1$  and chain length is doubled ( $L^* = 2$ ). (C-D) Absolute errors between the models'  $\sigma^*$  are plotted with respect to  $t^*$  for (C)  $L^* = 0.5$  and (D)  $L^* = 2$  (where  $L^*$  is the chain contour length normalized by the original chain length investigated).

The likely cause of this discrepancy is revealed by examining the degree of percolation in these short chain networks (**Fig. B.7.A**). **Fig B.7.A** indicates that even when  $f = 1$ , the stable bonds in the domain do not form percolated networks with 100% probability. As such, it is likely that stable bonds in short chain networks experience less entropic penalty (i.e., reduced conformational degrees of freedom) due to network structure, and are instead only constrained by steric interactions. The short timescale of relaxation that exists even for entirely stable bond networks likely results from floppy modes of cluster re-conformation and indicates that these networks are not sufficiently equilibrated during loading. Here, this is a numerical artifact and indicates that for short chain networks in which steric interactions dominate network topology, a lower residual force criterion is needed during equilibration. Alternatively, in systems with low connectivity loaded at rates exceeding the rate of floppy relaxation, another stress term governed by a shorter relaxation timescale may be necessary to include in the coupled ROM. Without this term, the coupled ROM should be applied only to percolated networks.

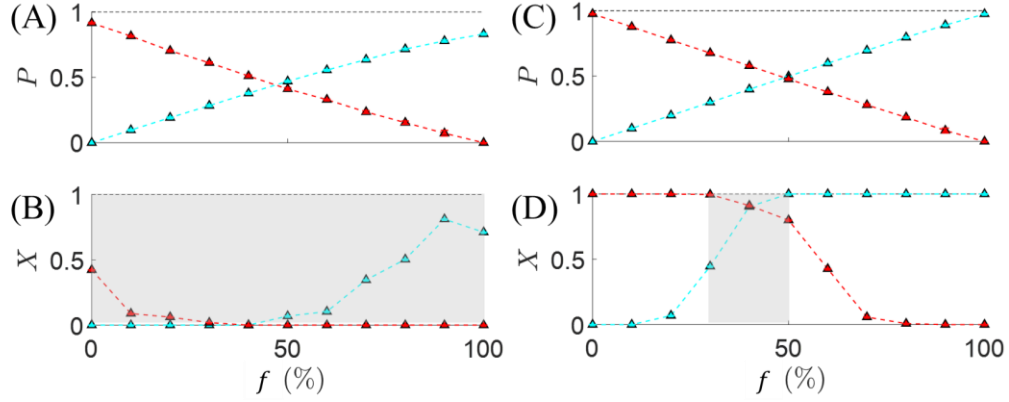


**Figure B.7. Effect of chain length on bond percolation.** (A-B) The probability that the stable (cyan) and dynamic (red) bonds independently form geometrically percolated networks ( $X^s$  and  $X^d$ ) are plotted with respect to  $f$  for (A)  $L^* = 0.5$  and (B)  $L^* = 2$  when  $z = 4$  and  $k_d = 1$ . (G-H) The regions shaded grey demark transition zones wherein simultaneous percolation of both bond types is possible ( $X > 0$ ).

## Appendix C. Supporting information for Chapter IV

### C.1 Domain size convergence study

To determine an appropriate RVE size, 10 kDa tetra-functional networks of  $\mathcal{N} \in \{100, 225, 400, 625, 900\}$  nodes were generated, swelled, and uniaxially extended in direction  $\mathbf{e}_2$  through the chronological processes described in **Section 4.3**. These networks correspond to approximately 10, 15, 20, 35, and 30 nodes per RVE edge, respectively. Strain was introduced at a constant strain rate (with traction free side boundaries) to a maximum stretch of  $\lambda = 4$ . Ten *in silico* experiments were conducted for each domain size and the ensemble averaged stress-stretch relations are depicted in **Fig. C.1**. It is clear from **Fig. C.1** that, while networks containing  $\mathcal{N} = 100$  or 225 nodes behaved more softly, no significant difference in mechanical response occurs between RVEs containing  $\mathcal{N} \in \{400, 625, 900\}$ . Therefore, all studies in this work are carried out with  $\mathcal{N} = 400$  nodes. In addition, we ensure that the domain size always exceeds  $L$  by a factor greater than two so that single chains cannot span opposing periodic boundaries of the RVE.

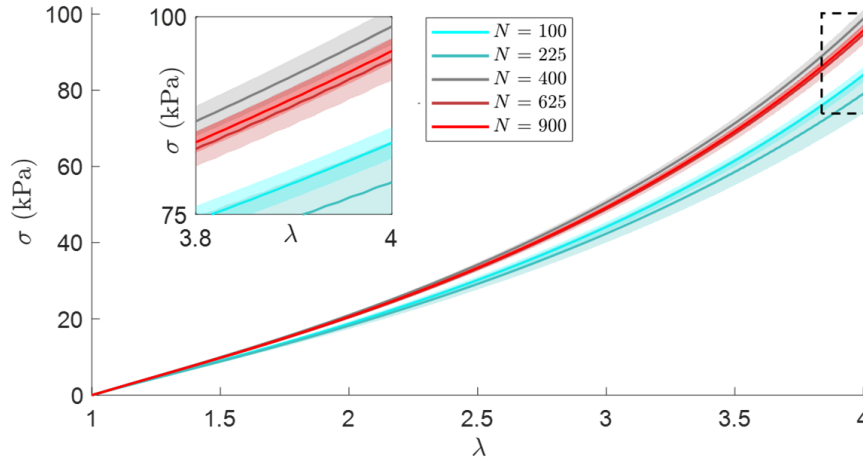


**Figure C.1. Domain size convergence of stress-stretch.** The stress responses of RVEs containing  $\mathcal{N} \in \{100, 225, 400, 625, 900\}$  nodes are displayed for networks stretched to  $\lambda = 4$ . The inset displays the stress-stretch response of the region outlined by the dashed box ( $\lambda \in [3.8, 4]$  and  $\sigma \in [75, 100]$  kPa) to emphasize overlap for the cases of  $\mathcal{N} \in \{400, 625, 900\}$ .

## C.2 Length scale and as-prepared concentration calibration

Given the nearly monodisperse nature of star-shaped PEG macromers [281], [282] one may compute the effective molar mass per arm as  $M_w/f$ . Given ethylene oxide's molar mass ( $M_{eg} = 44.05 \text{ kg mol}^{-1}$ ), then the number of mers in an arm is  $N_{arm} = M_{eg}f/M_w$ . We take the length of a single PEG mer as  $3.9 \text{ \AA}$  and treat each Kuhn segment as two mers [283] so that  $N = N_{arm}/2$  and  $b = 7.8 \text{ \AA}$ . In the numerical framework, we set the normalized length scale as  $L = Nb = 1$ . As such, conversion between SI units and the numerical frameworks length scale is given by the conversion:

$$1 = \frac{M_{eg}}{M_w}fb. \quad (\text{C.1})$$

The as-prepared polymer fraction is computed as the total polymer volume (or area in 2D),  $A_{star}$ , divided by the RVE size,  $A_{RVE}$ :

$$\phi = \frac{A_{star}}{A_{RVE}}. \quad (\text{C.2})$$

This as-prepared concentration is normalized by the overlap volume fraction, which is taken as:

$$\phi_{ol} = \frac{A_{star}}{\pi R_g^2}, \quad (\text{C.3})$$

where  $R_g$  is the radius of gyration for a single star-shaped macromer is estimated using [147]:

$$R_g^2 \sim Nf^{1/2}b^2, \quad (\text{C.4})$$

for low functionality star-polymers in theta solvent. Combining (C.2-C.4), one may write the normalized, as-prepared solute volume fraction as:

$$\phi^* = \frac{\pi Nf^{1/2}b^2}{A_{RVE}}. \quad (\text{C.5})$$

Ergo,  $\phi^*$  is controlled in the framework by tuning  $A_{RVE}$ .



### C.3 The extensile bulk modulus of a gel's polymer network

A critical consideration in fitting the analytical model to our numerical results is what form the bulk modulus of the polymer network,  $\kappa$ , takes and whether it evolves with the swelling ratio,  $J$ . Note that this is here defined as the extensile bulk modulus of solely the polymer network and does not constitute the overall bulk modulus of the gel, thus  $\kappa$  in this section is decoupled from the osmotic pressure of mixing. Furthermore, volume exclusion effects on  $\kappa$  are not considered, as these primarily matter for gels at high polymer concentrations or those undergoing compressive loading [284]. Fundamentally, the bulk modulus of a freely swelling gel's polymer network may be defined as its resistance to volumetric change through  $\kappa = \partial\sigma^h/\partial V$ . Since PEG-based gels (with  $M_w > 10 \text{ kDa}$ ) in theta solvent generally have polymer volume fractions on the order of  $\phi \sim 0.01 - 0.1$  [137], [142], [143], and entanglements have been shown to play little part in the swelling dynamics of these relatively homogenous gels [121], [143], we may neglect the effects of steric interactions between chains and crosslinks during swelling. Furthermore, assuming steady state swelling and that the gel is submersed in a sufficiently large solvent bath at thermodynamic equilibrium with its surroundings, then mixing (and therefore swelling) is not limited by solvent availability or transport and is therefore only resisted by the elastic tension of the polymer chains. As such,  $\kappa$  during swelling may be interpreted as entirely dependent on the elastic network properties.

The first component of the virial stress is synonymous with Cauchy stress for non-inertial networks and given by Eqn. (4.26). For linear springs,  $\mathbf{f} = K\mathbf{r}$ , and  $K$  is the stiffness of a single chain,  $K = 3k_bT/r_0^2$ ,  $V$  is the material volume ( $V = V_0J$ ), and  $V_0 = \mathcal{N}/c_0$  where  $\mathcal{N}$  is the number of chains that exists in the domain ( $\in \Omega$ ),  $c_0$  is the dry concentration of chains, and  $r_0 = \sqrt{N}b$  is initial mean end-to-end separation for ideal chains (i.e., in theta solvent). As such, Eqn. (4.26) may be rewritten as:

$$\sigma_v = \frac{c_0}{2NJ} \left( \frac{3k_bT}{Nb^2} \right) \sum_{\Omega} \mathbf{r} \otimes \mathbf{r}, \quad (\text{C.6})$$

Substituting the definition of  $\mathbf{r}$  as a function of chain stretch  $\lambda$  ( $\mathbf{r} = r_0 \lambda = \lambda \sqrt{N} b$ ) into (C.6) gives:

$$\sigma_v = \frac{3k_b T c_0}{2N J} \sum_{\Omega} \lambda \otimes \lambda. \quad (\text{C.7})$$

From (C.7), the hydrostatic component of stress may be written in 2D as:

$$\sigma^h = \frac{3k_b T c_0}{4N J} \text{tr}(\sum_{\Omega} \lambda \otimes \lambda), \quad (\text{C.8})$$

where for the case of isotropic swelling under the affine assumption:

$$\text{tr}(\sum_N \lambda \otimes \lambda) = N(\lambda_1 \lambda_1 + \lambda_2 \lambda_2) = 2N \lambda^2 = 2N J, \quad (\text{C.9})$$

Substituting this definition into (C.8), gives:

$$\sigma^h = \frac{3}{2} k_b T c_0. \quad (\text{C.10})$$

Thus,  $\kappa = \partial \sigma^h / \partial J = 0$ , at least at high volumetric strains for which the invoked assumptions apply (i.e., no polymer-polymer volume exclusion interactions).

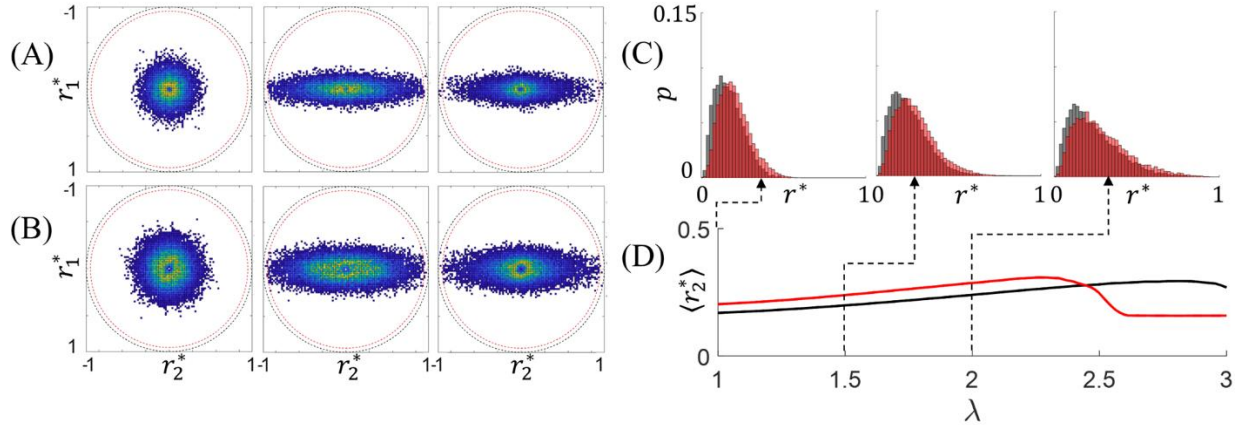


**Figure C.2. Chain distribution functions of gels with  $L = 177 \text{ nm}$  and different functionalities.** (A) The joint PDF of  $r^*$  is shown for the ensemble of ten 40k tetra-PEG gels at  $\lambda = 1$  (left), the measured yield stretch  $\lambda = 2.80$  (center), and the measured failure stretch  $\lambda = 3.25$  (right). (B) The joint PDF of  $r^*$  is shown for the ensemble of ten 80k octa-PEG gels at  $\lambda = 1$  (left), the measured yield stretch  $\lambda = 2.36$  (center), and the measured failure stretch  $\lambda = 2.52$  (right). (A-B) The extensile direction,  $e_2$ , is oriented horizontally. Dashed black circles indicate the chain contour length, while dashed red circles represent the deterministic scission length for chains. (C) The radial PDFs of  $r^*$  are shown for the 10k tetra- and 20k octa-PEG gels as black and red histograms, respectively. For direct comparison, these histograms are depicted at  $\lambda = 0$  (left),  $\lambda = 1.5$  (center), and  $\lambda = 2.0$ . Again, the chains in these two networks have the same contour length. (D) The average component of normalized chain end-to-end length in the principal direction of extension is plotted with respect to stretch. End-to-end lengths are normalized as  $r^* = r/L$  such that  $r^* \geq 0.95$  is not permitted.

## C.4 Extended 40k tetra- and 80k octa-PEG gel data

To demonstrate that the trends discussed in **Section 4.5.1** (with regards to short-armed tetra- and octa-functional networks) also apply the networks with longer chain lengths, we provide analogous figures to **Fig. 4.13**, **4.14** and **4.16**.

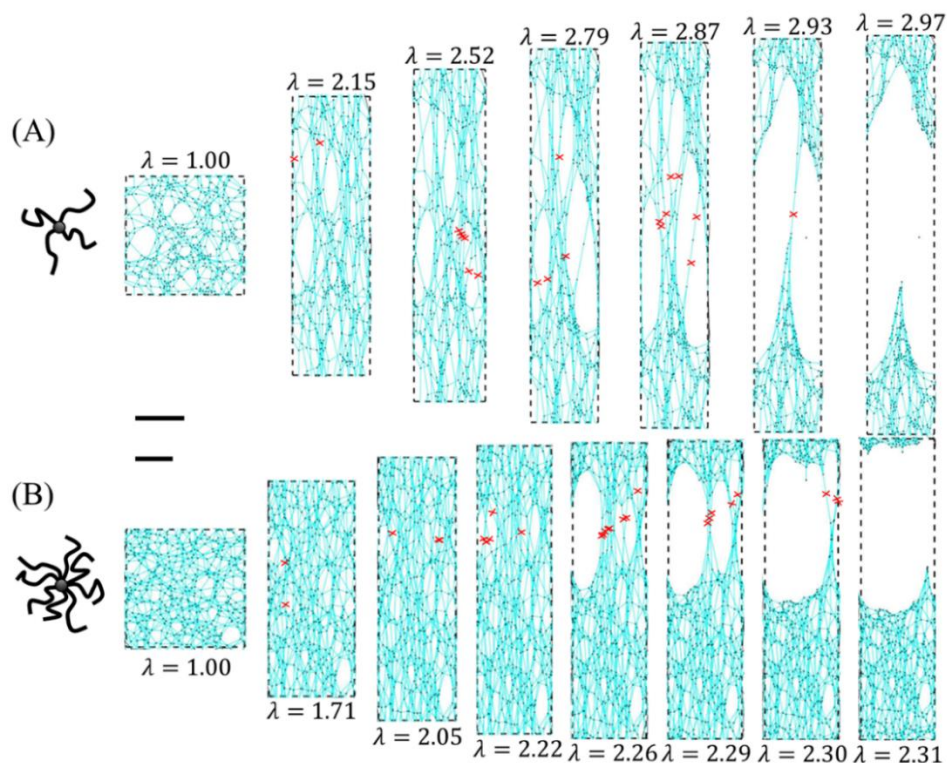


**Figure C.3. Fracture of gels with of gels with  $L = 177 \text{ nm}$  and different functionalities.** (A) A schematic of a tetra-functional macromer is depicted, alongside snapshots of a simulated 40k tetra-PEG gel as it undergoes uniaxial extension. (B) A schematic of an octa-functional macromer is depicted, alongside snapshots of a simulated 80k octa-PEG gel as it undergoes uniaxial extension. The sizes of the gel snapshots are indicated by their respective scale bars, each representing  $L$ . Red crosses in the gel snapshots demark which chains rupture before the next displayed snapshot.

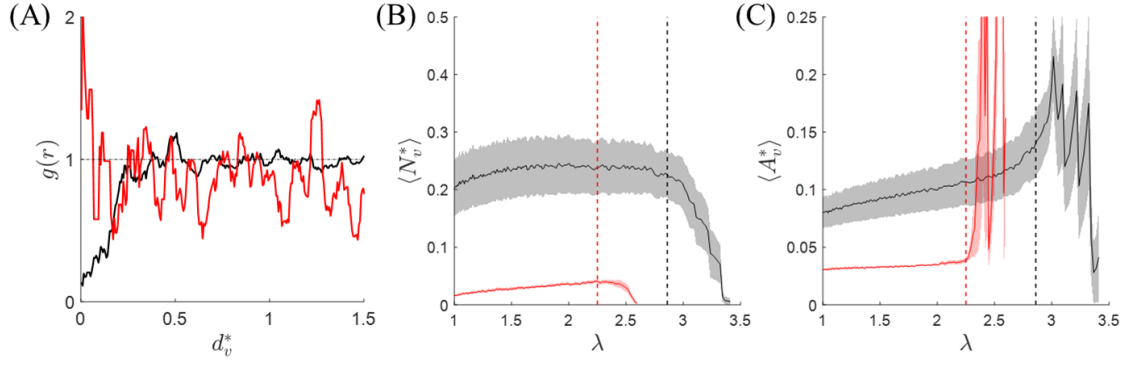


**Figure C.4. Void characteristics of gels with  $L = 177 \text{ nm}$  and different functionalities.** (A) The RDFs of ensembles of ten 40k tetra-PEG (black) and ten 80k octa-PEG (red) gels' void centroids are displayed at  $\lambda = 1$ . Unlike for the short-armed networks, there is no detectable correlation scale for voids the octa-functional networks. The distance between void centroids is normalized as  $d_v^* = d_v/L$ . (B) The average number of voids per macromer is plotted with respect to stretch. (C) The average void area (normalized as  $A_v^* = A_v/\pi L^2$ ) is plotted with respect to stretch. (B-C) Shaded regions represent S.E. of the mean. The vertical dotted lines denote the approximate stretches at which bond rupture events became significant ( $\lambda \approx 2.85$  – black,  $\lambda \approx 2.25$  – red).

## Appendix D. Supporting information for Chapter V

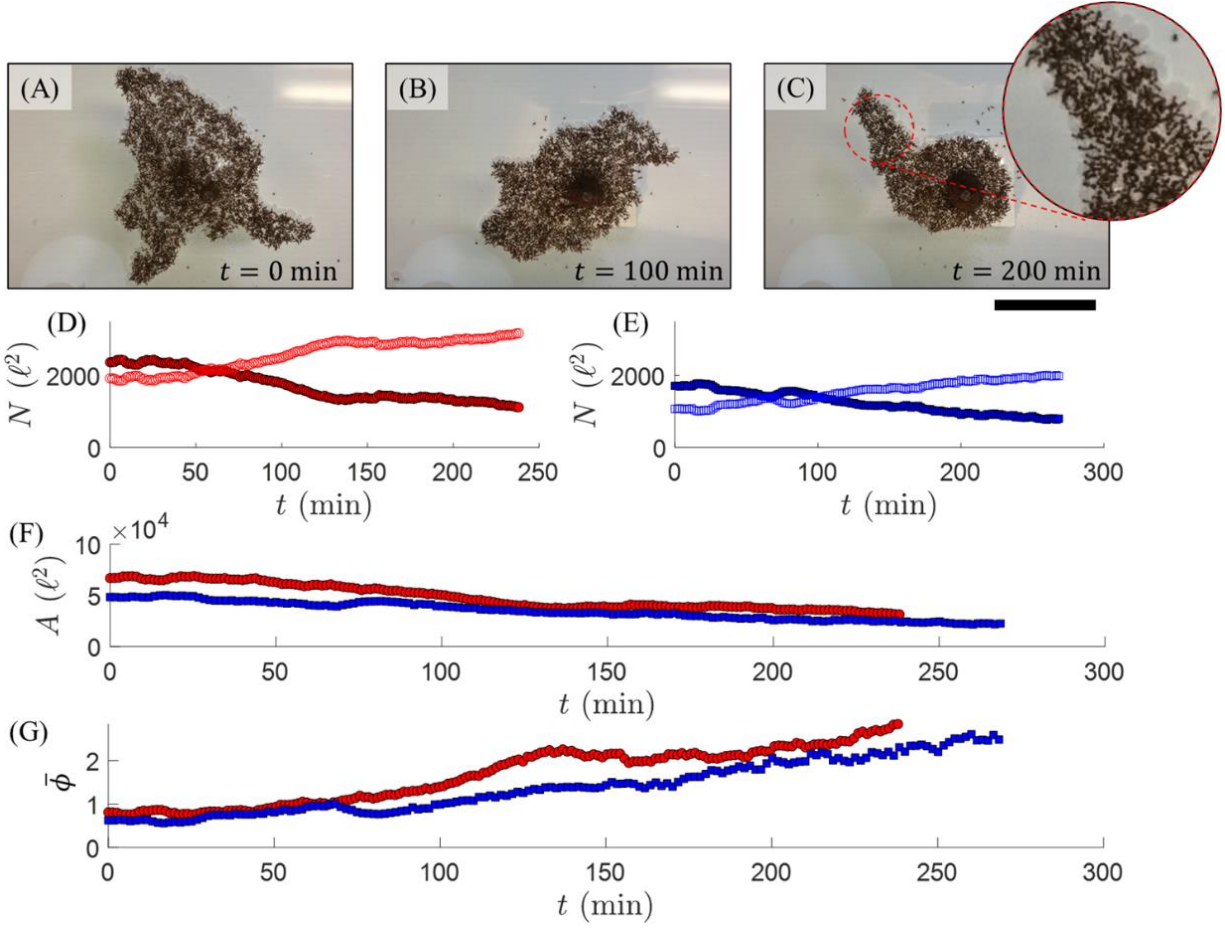


**Fig. D.1. Estimating surface packing fraction.** (A-C) Snapshots of an experimental raft are shown 100 *min* apart to illustrate the long-term decrease in raft area, as well as the packing of surface ants near the anchoring rod at long timescales. (A-C) correspond to the data shown as red in plots (D-G). The scale bar represents approximately  $20 \ell$  for each image. (D-E) The number of structural and free ants are displayed as filled and open discrete data, respectively. The data for each of the two experiments has been separated into plots (D) and (E) for visual clarity. Notably,  $\phi$  exceeds one for much of the experiments displayed, which – for a homogenous distribution of free ants – would lead to complete coverage of the structural layer by free ants everywhere; however, as illustrated by the inset in (C) in which the structural network and the water underneath remain clearly visible, the local free ant packing fraction far from the rod remained low and the free ants remained relatively dispersed. (F-G) The total raft area and corresponding mean surface packing fraction of ants,  $\bar{\phi}$ , are plotted, respectively, against time for two different experimental rafts (blue and red data, respectively). Notably, the surface packing fraction for both experiments increases in time as surface ants move towards the anchoring rod and become less active over the span of roughly 4 *hours*. In these regions, free ant packing fraction could locally reach and exceed  $\phi = 1$ , suggesting that more than two layers existed in these concentrated regions.



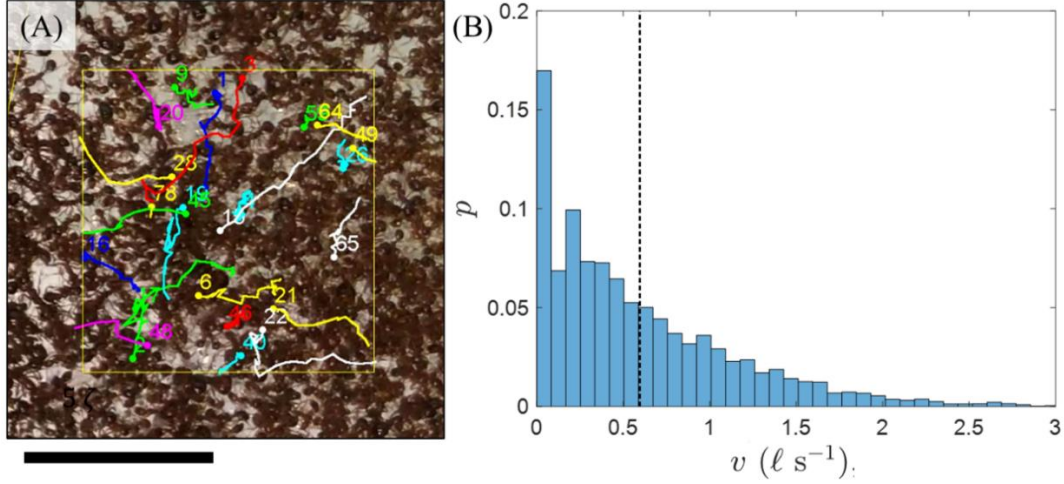


**Fig. D.2. Extended ant speed data:** (A) A sample snapshot of an ant raft overlaid with manually image tracked trajectories (scale bar represents  $5 \ell$ ). (B) The probability density function of surface ant speed is shown for a sample size of  $n = 19,970$  discrete frame-to-frame observations for 477 distinct ants. The mean ant speed over all observations,  $v_0 = 0.60 \pm 0.01 \ell s^{-1}$ , is indicated by a dotted line. The width of the bins depicted are greater than the estimated imaging error of approximately  $0.07 \ell s^{-1}$  as determined by the pixel width ( $\sim 0.008 \ell$ ) per frame duration ( $\Delta t = 0.25 s$ ), times the approximate number of pixels per an ant's petiole ( $\sim 2 \text{ pixels}$ ), the anatomical body part tracked in each ant.

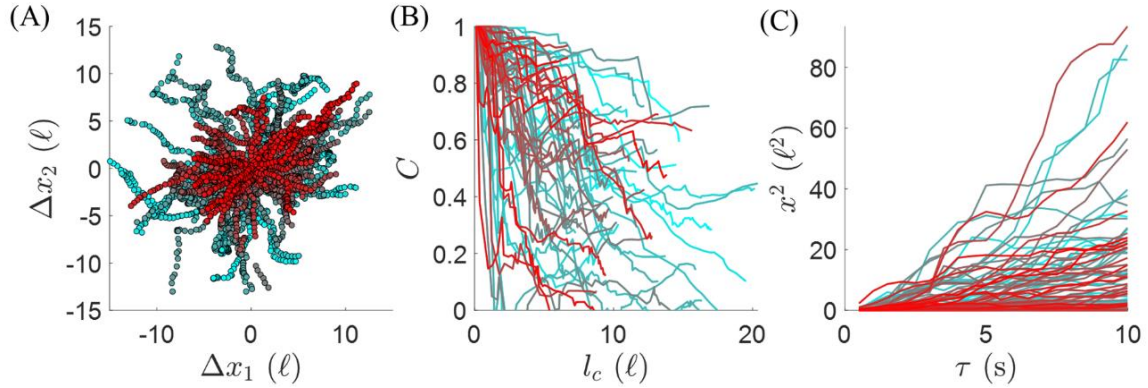


**Fig. D.3. Extended trajectory analysis data.** (A) The trajectory space of 433 ants image tracked in seven sample sets on the bulk (*i.e.*, without edge-encounters) of four separate ant rafts is displayed with each color shade representing a different ant. (B)  $C(l_c)$  is plotted for all ants tracked in (A). The decay in correlation for any given ant may be approximated according to  $C = e^{-l_c/l_p}$ , however this method assumes ideal trajectories of constant step size and turning angle, so is only used to approximate the order of ant persistence length and generally not a precise value. (C)  $x^2$  is plotted with respect to  $\tau$  for the full set of ants tracked in (A). Anomalous diffusion is apparent from the non-linearity of these data sets. Ants sometimes alternate between phases of super and sub-diffusive behavior as illustrated by the increase and plateauing of the tangent slopes within different regimes. The data in (B-C) are plotted continuously purely for illustrative purposes.

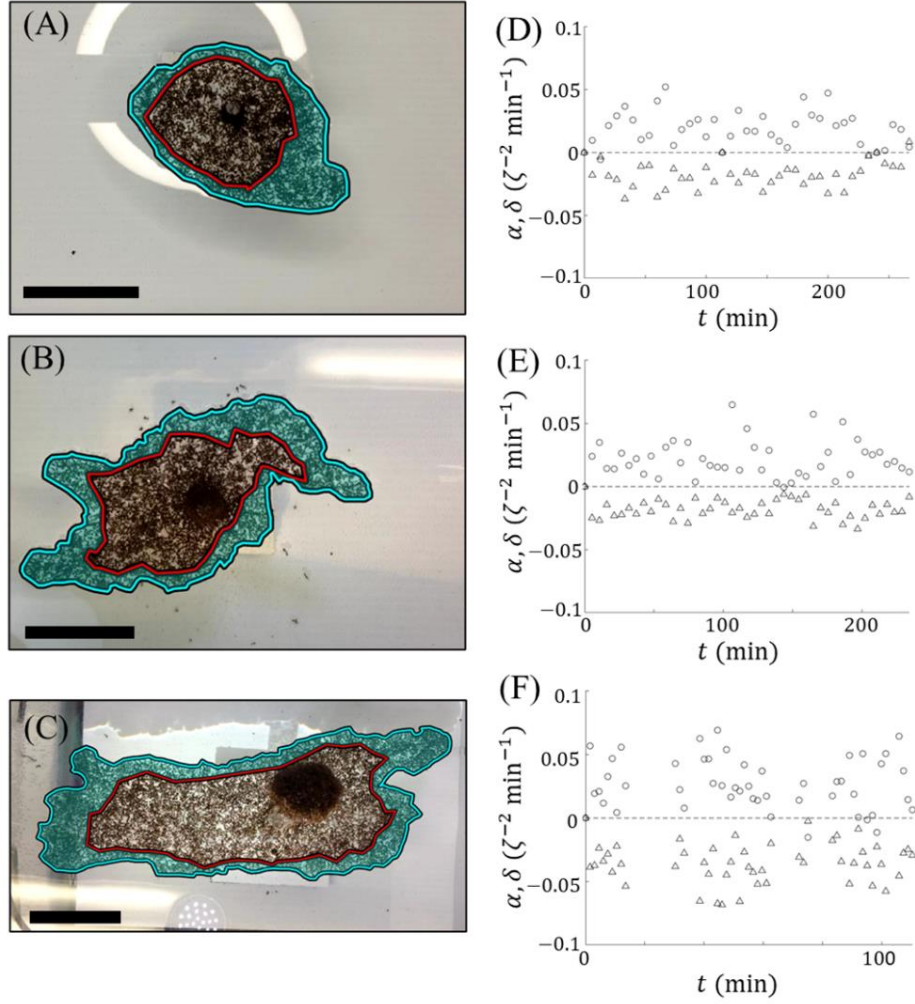


**Fig. D.4. Extended treadmilling dynamics data.** (A-C) Snapshots of 3 experiments of varying sizes from time-lapse footage are shown. The red contour represents structural ants who were originally at the raft perimeter at reference time,  $t_0$ , and flowed inwards in time. This contour circumscribes the area  $A_r$ . The region shaded in cyan represents the growth zone,  $A_g$  of newly deposited structural ants into the edge of the raft network since the initial time of tracking the structural ants. Note that both the red and cyan demarcations highlight structural ants. While free ants may walk within the region shaded in cyan, it is structural ants that provide raft scaffold and define the newly deposited growth zone,  $A_g$ . (D-F) The structural edge deposition ( $\alpha$  as circles) and structural exit ( $\delta$  as triangles) rates per unit raft area are plotted with respect to time in units of events per  $\zeta^2$  per *min* where  $\zeta = \rho_r^{-0.5}$  is the length scale that one square structural ant occupies. Presented in these units,  $\alpha$  and  $\delta$  may be thought of as the instantaneous areal expansion and reduction rates of the raft, respectively, and if the two values are approximately equal then raft area will be loosely conserved. Gaps in the data of (F) correspond to time spans during which portions of the raft exited the visible frame and from which data could not be accurately taken.

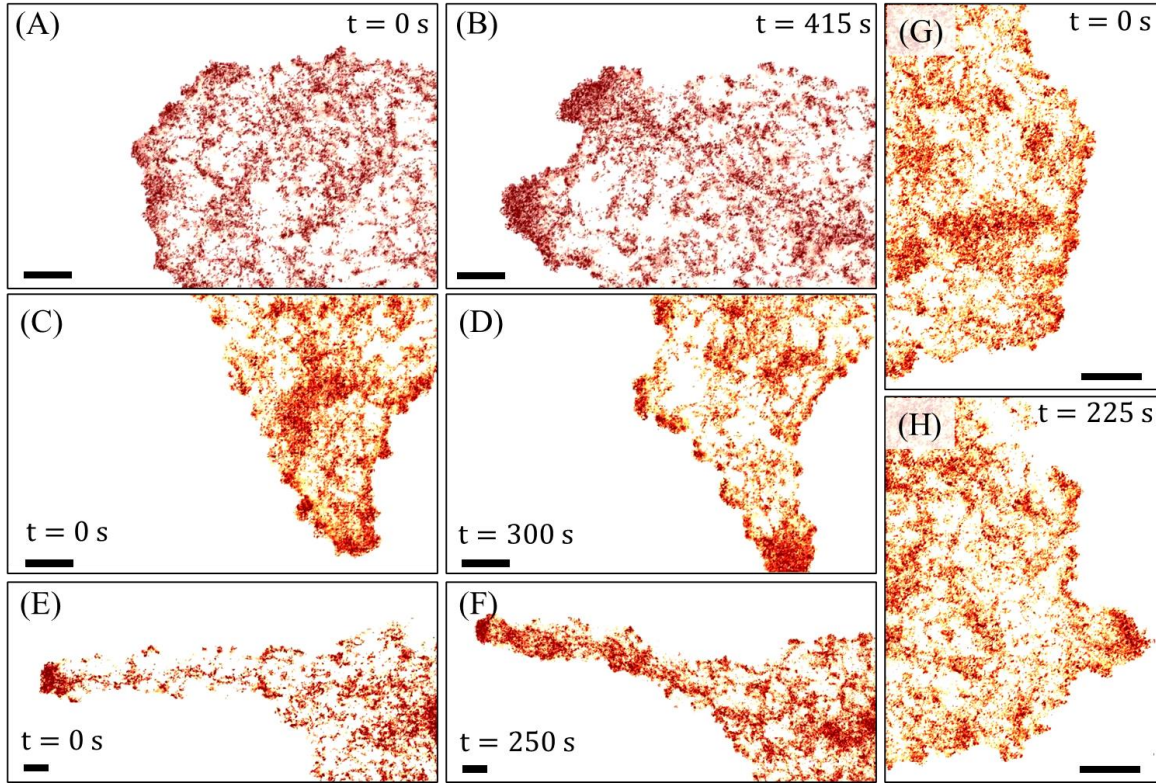


**Fig. D.5. Isolated free ant traffic.** These images denote the isolated positions of free ants in orange or red. (A-B) The initiation of two adjacent protrusions is displayed in a region of locally higher convex edge curvature. (C-D) The growth of a relatively young, and highly tapered protrusion is depicted. (E-F) Tip clustering and runaway growth of a more mature protrusions is displayed. (G-H) The initiation of a protrusion is depicted in a region of a raft with a relatively low initial edge curvature, indicating that while stronger confinement due to convex edge curvature may facilitate asymmetric growth, there are other factors that can lead to breaks in symmetry. All scale bars represent  $5 \ell$ .



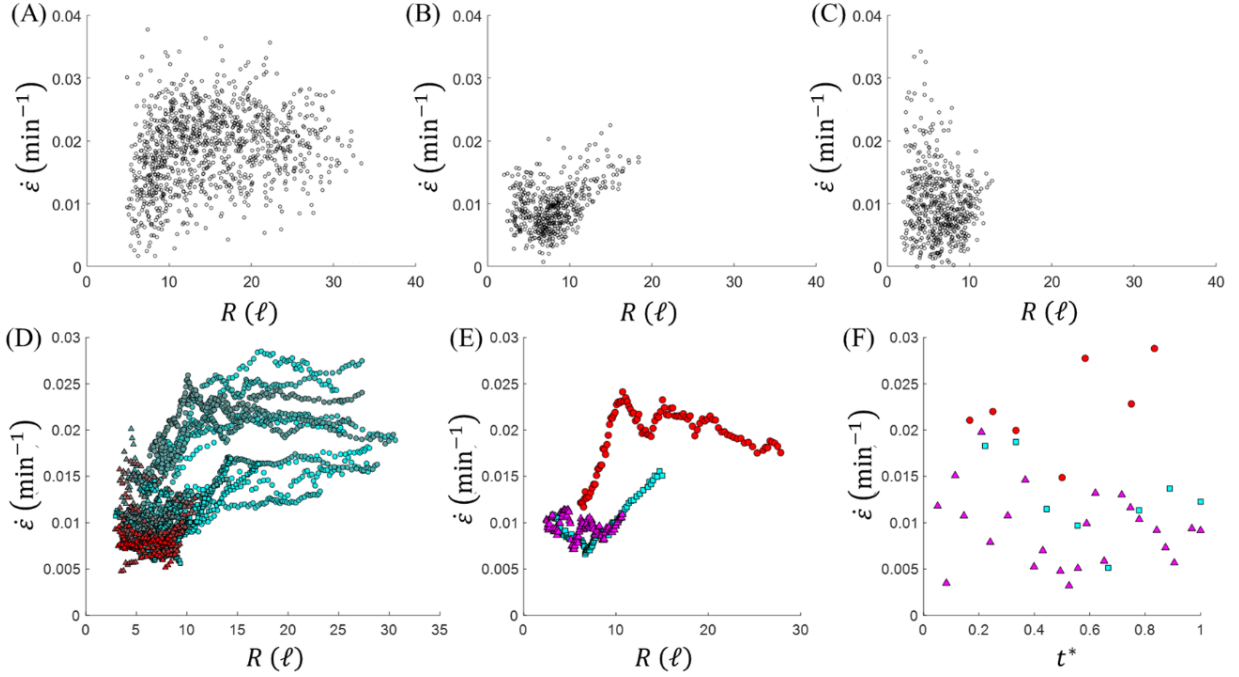


**Fig. D.6. Extended structural contraction data:** (A-C) The full set of observations of  $\dot{\epsilon}$  is plotted with respect to  $R$  for the largest to smallest raft experiments (A-C, respectively). There exists no significant correlation between  $\dot{\epsilon}$  and distance to the rod ( $R^2 = 0.08, 0.17$ , and  $0.00$  for A-C, respectively) indicating that the strain rate is spatially constant. (D) Given the high degree of noise in (E), moving averages of the ensemble data from all three experiments are plotted revealing that  $\dot{\epsilon}$  may decrease wherever  $R < 10 \ell$ . Circles, squares and triangles represent data sets from the largest to smallest experiments conducted, respectively. Different colors denote different sample sets of image-tracked structural ants across all experiments. (E) The moving averages of all  $\dot{\epsilon}$  data for each of three experiments is plotted with respect to  $R$ , revealing that the decrease in  $\dot{\epsilon}$  wherever  $R < 10 \ell$  is due subsists within a given experiment. This is likely due to clustering of free, but inactive ants near the rod (see **Fig. D.1.A-C**). This may inhibit the local structural exit rate that permits or drives contraction. Accordingly,  $\dot{\epsilon}$  was reported for distances  $> 10 \ell$  from the rod within the scope of this work. (F)  $\dot{\epsilon}$  is plotted with respect to normalized time,  $t^* = t/t_{max}$  for each of three experiments revealing no discernable trends in time. (D-E) Red circles, cyan squares and magenta triangles represent the largest, intermediate, and smallest experiments, respectively. In (E) and (F), red circles represent experiment 1 from (A), cyan squares represent experiment 2 from (B) and magenta triangles represent experiment 3 from (C).

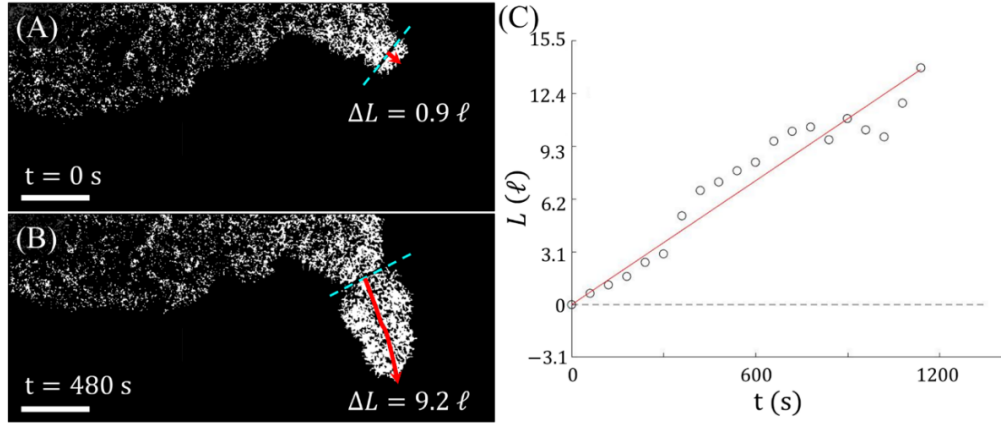


**Fig. D.7. Protrusion growth measurement sample:** (A-B) A binary image, in which white represents the raft and black represents water, is shown at the (A) start and (B) end of a 480 s duration to depict the growth of a protrusion. This may be loosely compared to the growth in the model depicted in Fig. 5.6.B-D. The protrusion's relative length  $L$  (red arrow) was measured from a set of reference ants image tracked in time (dotted cyan line) to the approximate tip of the growth. The frame-to-frame growth rate was taken as  $V = [L(t + \Delta t) - L(t)]/\Delta t$  where  $\Delta t$  is the time between frames. (C) The order of magnitude of  $V$  could also be approximated using the regression coefficient of the linear regression fit (red line) to the plot of  $L$  against time,  $t$  (black circles). Here,  $V \approx 1 \ell \min^{-1}$  ( $R^2 = 0.93$ ).

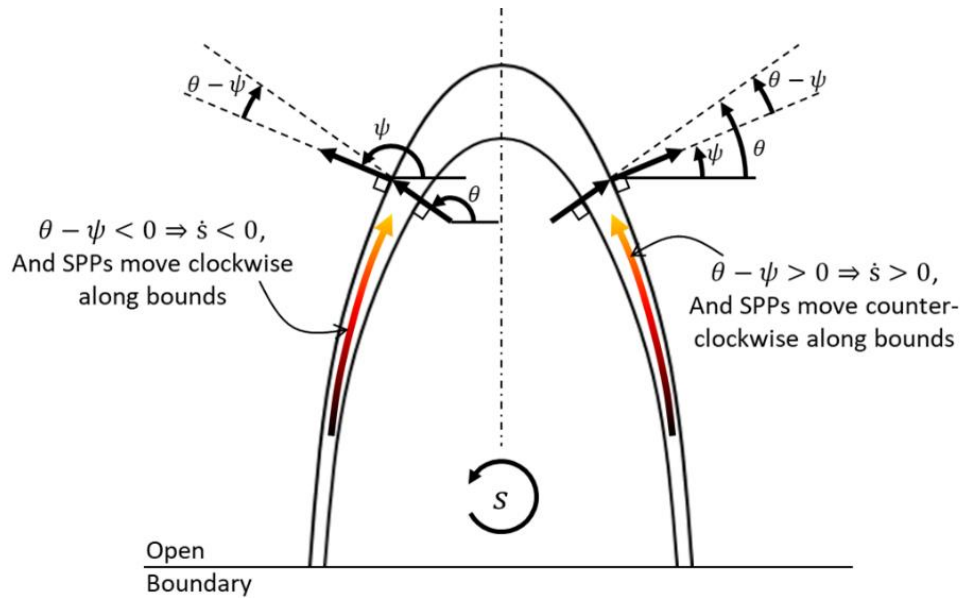


**Fig. D.8. Schematic of Local Growth-induced Gliding:** A schematic of a protrusion mesh that has undergone a step of growth illustrates how if the local orientation of SPPs ( $\theta$ ) does not change, the updated orientation of the local norms ( $\psi$ ) will induce a biased gliding of particles along the edges according to  $\dot{s} = v_0 \cos(\theta - \psi)$ . For the given boundary shape and evolution,  $\dot{s}$  will generally move from base-to-tip of the protrusion (from regions of lower to higher change in curvature due to  $\gamma$ ) and may explain one possible source of bias in the direction of edge deposition.  $\dot{s}$  is denoted by arrows with a color gradient whose hue of orange increases with the relative magnitude of  $\dot{s}$ , however this gradient is not to scale and is for illustrative purposes only.

**Table D.1.** Numerical Model Parameter Space.

Parameter	Description	Value	Units	Type
$\ell$	Average ant body length	2.93	mm	Measured Experimentally
$v_0$	Average ant speed	0.6	$\ell \text{ s}^{-1}$	Measured Experimentally
$\gamma_0$	Mean edge deposition rate	0.29	$\ell^{-1} \text{ min}^{-1}$	Estimated Experimentally
$\rho_0$	Edge deposition sensitivity parameter	0.9	$\ell^{-1}$	Set to Match Overall Growth Rate
$\beta$	Directional motion weighting coefficient	$\in [0,1,10]$	NA	Free Parameter

## Appendix E. Supporting information for Chapter VI

Here we provide further details on the numerical implementation of the model, including the algorithmic design and detailed derivations (as necessary), as well as a summary of the model's parameters, the method by which they were calibrated and extended parameter sweeps of  $\eta$ ,  $R$  and  $\mathcal{A}$ . Finally, methods for computing surface excess and edge curvature are described.

### E.1 General description

#### E.1.a Domain description

The numerical framework is carried out using MATLAB R2019b. It is a 2D planar, discrete model comprised of distinct nodes defined by some unique index number,  $i \in [1, \infty)$ , and unique Cartesian coordinates,  $\mathbf{X}_i = [x_i, y_i]$ . We locate the nodes inside of a square domain whose center is at position  $[0,0]$ . The nodes are initially positioned in a close-packed hexagonal lattice with unit length spacing between nearest neighbors. Each node position is then offset by some random amount in the range  $[-1/6, 1/6]$   $\zeta$  in both directions. At initial time,  $t = 0$ , each node is classified as either a structural agent (shown as cyan circles in **Fig. E.1**), or water node (shown as black dots in **Fig. E.1**). Structural agents represent structural ants, whereas water nodes represent vacant locations into which free agents may eventually park during edge deposition. To mimic initial experimental conditions, the initial shape of all simulated rafts is a circle with center  $[0,0]$  and some prescribed radius (**Fig. 6.5**). Every node within this circular boundary is initially defined as a structural agent. This ensures that any protrusions predicted by the model emerge due to spontaneous symmetry breaking as opposed to through user-enforced asymmetries. Freely active agents are

introduced to represent freely active ants (shown as red circles in **Fig. E.1**). The initial surface packing fraction is set to 1 free agent per structural agent, although the packing fraction naturally decreases in time as free agents bind into the structural network and a steady state flux of agents to and from each layer is reached. To simulate the movement of free ants on top of the raft, we require that free agents only occupy sites already designated as raft nodes. Additionally, to simplify the model, we enforce volume exclusion between freely active agents so that two free agents cannot occupy the same structural raft site simultaneously.

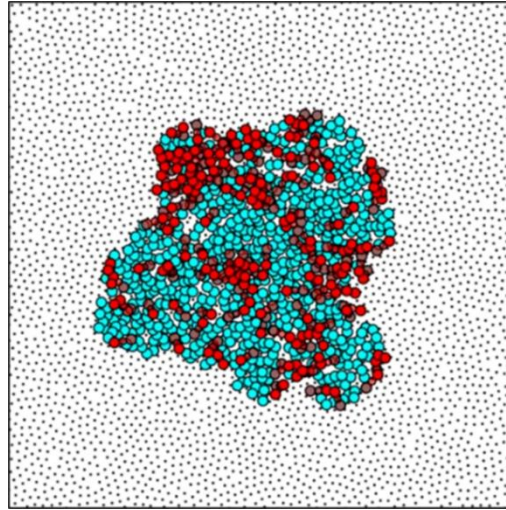


**Fig. E.1. Domain depiction.** A snapshot of the discrete numerical domain is shown with water nodes plotted as black dots, condensed structural agents plotted as cyan circles, and dispersed freely active agents plotted as red circles.

### E.1.b Length scales

Two length scales are referenced in this work. The first is that of the mean ant body length, taken as  $1 \ell = 2.93 \text{ mm}$ . Results are generally presented in this length scale for ease of comprehension and comparison to experimental results. However, the numerical model is normalized by a second length scale defined as  $1 \zeta = 1.81 \text{ mm}$ .  $1 \zeta^2$  is defined as the area a single ant in the structural raft network occupies (i.e.,  $1 \zeta =$

$\rho_r^{-0.5}$ , where  $\rho_r = 0.304 \text{ ants mm}^{-2}$  is the planar density of structural ants). This normalization enforces that the density of structural agents is maintained at 1 node per unit area ( $\zeta^2$ ), and the nominal separation between nodes is on the order of 1 unit length ( $\zeta$ ).

### E.1.c Time scale

We normalize the timescale by taking the average distance a freely active agent travels in one iteration,  $\langle d \rangle$ , divided by the average experimentally measured free ant speed,  $v_0$  (i.e.,  $\Delta t = \langle d \rangle / v_0$ ).

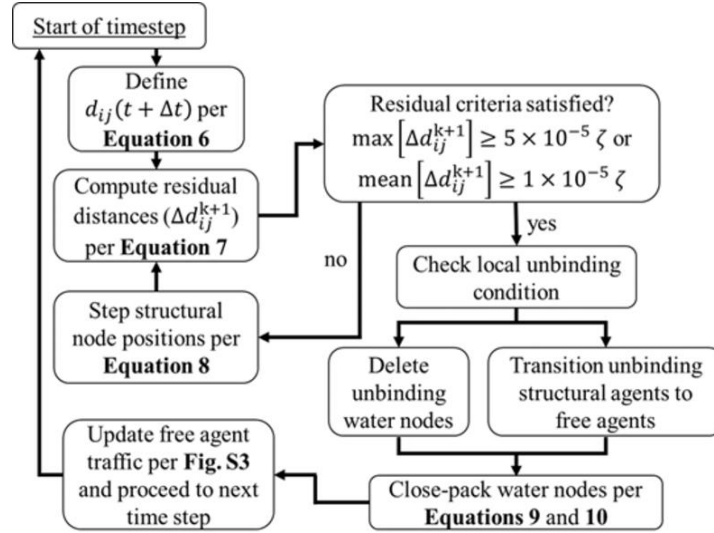


**Fig. E.2. Algorithmic chronology of structural agents and water nodes.** A flow chart details the algorithmic order in which positions of structural agents and water nodes are updated. The point at which unbinding events occur is also displayed.

## E.2 Simulating the structural network

The algorithmic chronology used to step the positions of structural agents, implement unbinding events, and update the close-packed positions of water nodes is

summarized in **Fig. E.2**. In the remainder of this section these processes are described in greater detail.

### E.2.a Structural network contraction

Given the experimentally measured contraction rate  $\dot{\varepsilon}$ , we apply a pairwise strain rate,  $\dot{d}$ , between connected neighbors within the raft. We do so by updating the pairwise separation vector,  $\mathbf{d}_{ij}$ , between all structural agents and their adjacent neighbors residing within some prescribed radius,  $R_r$ , about the node of interest. We conservatively set to  $R_r = 1.5 \ell$  to capture the bridging of raft voids that often occurs between structural ants.  $R_r = 1.5 \ell$  corresponds to roughly 4.5 mm or half the body length of some of the largest fire ants. To implement raft contraction, we update  $\mathbf{d}_{ij}$  at time  $t + \Delta t$  according to the forward Euler, exponential decay function:

$$\mathbf{d}_{ij}(t + \Delta t) = \mathbf{d}_{ij}(t) \exp[-\dot{d}\Delta t]. \quad (\text{E.1})$$

Taking  $\mathbf{d}_{ij}(t + \Delta t)$  as the targeted equilibrium separation at time,  $t + \Delta t$ , we then employ an overdamped approach to iteratively step the position of the nodes. The updated pairwise separation vector between neighbors  $i$  and  $j$  at iteration  $k$  is denoted by  $\mathbf{d}_{ij}^k = \mathbf{X}_i^k - \mathbf{X}_j^k$ , where  $\mathbf{d}_{ij}^1 = \mathbf{d}_{ij}(t)$  represents the initial separation at the start of the timestep. The iterative change in position is then given by:

$$\Delta \mathbf{d}_{ij}^{k+1} = \mathbf{d}_{ij}^k - \mathbf{d}_{ij}(t + \Delta t). \quad (\text{E.2})$$

The position of each structural agent is then updated according to:

$$\mathbf{X}_i^{k+1} = \mathbf{X}_i^k + \nu^{-1} \sum_j \Delta \mathbf{d}_{ij}^{k+1}, \quad (\text{E.3})$$

where  $\nu \in [1, \infty)$  is simply a pseudo-viscosity or over-damping scalar used for computational stability and  $\sum_j \Delta \mathbf{d}_{ij}^{k+1}$  is the net displacement due to all pairwise neighbors. The over-damping scalar was set such that residual displacements through  $\sum_j \Delta \mathbf{d}_{ij}^{k+1}$  converged towards zero. Given the updated coordinates  $\mathbf{X}_i^k$ , we then

re-calculate  $\mathbf{d}_{ij}^k$  for each neighbor, and iterate Eqns (E.2) and (E.3) until the residuals dip below some prescribed threshold. Here we define the residuals and their thresholds as  $\max[\Delta \mathbf{d}_{ij}^{k+1}] \leq 5 \times 10^{-5} \zeta$  and  $\text{mean}[\Delta \mathbf{d}_{ij}^{k+1}] \leq 1 \times 10^{-5} \zeta$ .

### E.2.b Close-packing water nodes

Since the rafts' structural networks contract in time, we need to ensure that water nodes remain closely packed to their perimeters so that binding events of freely active agents remain possible at the edge. To do this, we apply a radial linear velocity gradient to all water nodes that moves them towards the center of the domain,  $[0,0]$ , at the rate of  $\dot{d}$ , according to  $\Delta \mathbf{d}_i(t + \Delta t) = \mathbf{d}_i(t) \{1 - \exp[-\dot{d} \Delta t]\}$ , where  $\mathbf{d}_i$  is the separation vector of each water node with respect to  $[0,0]$ . To evenly space water nodes from each other, as well as the rafts' edges, we introduce Gaussian, pair-wise repulsive forces,  $\mathbf{F}_{ij}^r$ , between water nodes and their nearest structural agent or water node neighbors of the form:

$$\mathbf{F}_{ij}^r = \kappa \frac{\mathbf{d}_{ij}}{\sigma \sqrt{2\pi}} \exp \left[ -\frac{(d_{ij} - \mu)^2}{2\sigma^2} \right], \quad (\text{E.4})$$

where  $\sigma$  is the standard deviation of the curve,  $\mu = 0 \zeta$  is the mean, and  $\kappa$  is a scaling factor in units of pseudo-force. We use these values to step the positions of water nodes according to:

$$\mathbf{X}_i(t + \Delta t) = \mathbf{X}_i(t) + \frac{\Delta t}{\nu} \sum_j \mathbf{F}_{ij}^r, \quad (\text{E.5})$$

where  $\nu \in [1, \infty)$  is simply another pseudo-viscosity for computational stability, and  $\sum_j \mathbf{F}_{ij}^r$  is the net repulsive force due to all pairwise neighbors. Again, the pseudo-viscosity was set such that residual forces through  $\sum_j \mathbf{F}_{ij}^r$  converged towards zero. We found that  $\sigma = 0.5 \zeta$  and  $\kappa/\nu = 0.02$  provided a stable computational domain in which water nodes remained close-packed in an evenly distributed point field (as displayed in **Fig. E.1**), thus offering ample water DOF, for freely active agents on the edge of



the raft to deposit into. Note that the repulsive interactions between water nodes and their raft neighbors were one-way such that the structural agents could displace water nodes, but water nodes could not displace structural agents. This was done because the close packing of water nodes is a numerical method implemented to homogenize the domain (rather than any physical phenomena) and should not influence the position of structural agents in the model.

### **E.2.c Unbinding to maintain structural density**

Recall that we normalize the domain's unit length by  $\zeta$  such that the domain's nominal density,  $\rho_d$ , is approximately  $1 \text{ node } \zeta^{-2}$ . Since we observed that structural network density remains roughly constant, we enforce unbinding events in simulations when the domain density exceeds  $1 \text{ node } \zeta^{-2}$ . To ensure that nodes are removed from the densest locations with precision, we subdivide the domain into a square grid whose unit cell lengths,  $L_g$ , are  $\geq 1\zeta$ . The number of permissible nodes,  $N_p$ , within each grid cell becomes  $N_p = \rho_d L_g^2$ . For our purposes, we found that  $L_g = 2\zeta$  and  $N_p = 4$  nodes provided sufficient regional discretion to maintain a homogeneous domain (as seen in **Fig. E.1**).

After contraction but prior to the stepping of free agents, we conduct a count of the number of nodes occupying each grid site and if it exceeds  $N_p$ , we initiate a node deletion event. To introduce further specificity in which nodes to remove we calculate the pair-wise distance,  $d_{ij}$ , between each node in the pertinent grid space. If both nodes  $i$  and  $j$  belonging to the smallest value of  $d_{ij}$  occupy the grid space, one of the two is randomly selected for deletion. In the case that the removed node is a water node, we simply delete it. Stochastic deletion is counteracted by the enforced close-packing described in the previous section and together these practices ensure that

the density of water nodes is equivalent to that of the structural raft. New water nodes are seeded at the edge of the domain as needed to conserve their population. However, if the removed node is occupied by a structural agent, we convert it to a free agent positioned at the coordinates of the nearest empty structural node. This introduces unbinding of structural agents into the freely active layer wherever the local network density is high, consistent with what was observed experimentally [11]. By counting the number of unbinding events,  $N_u$ , at each time step and normalizing by the total number of structural ants,  $N_r$ , we can calculate the unbinding rate according to  $\delta = N_u/(N_r \Delta t)$ .

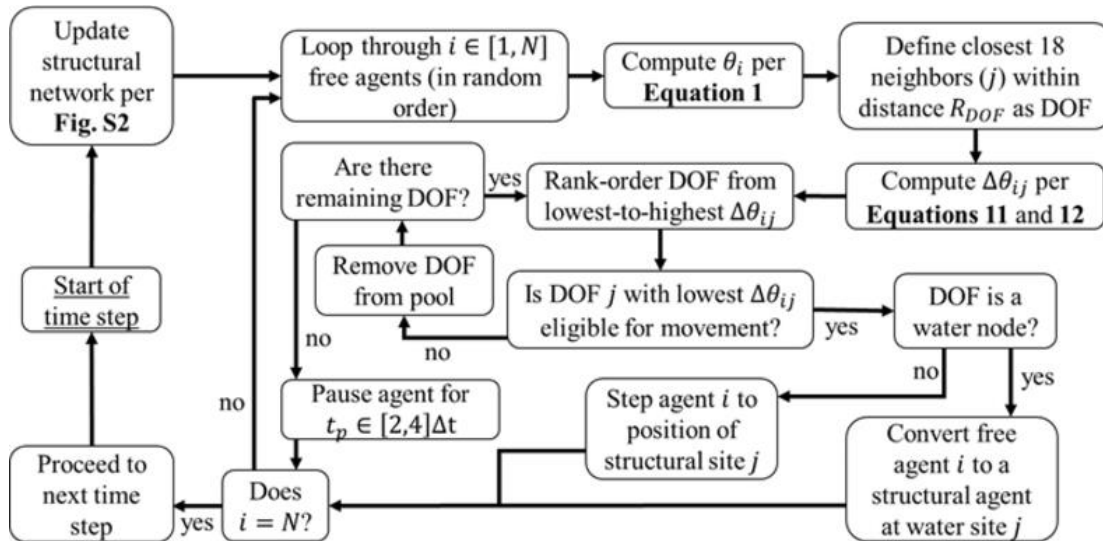


**Fig. E.3. Algorithmic chronology of freely active agents.** A flow chart details the algorithm by which movement is determined for each freely active agent, in each time step.

### E.3 Simulating the freely active ants

The algorithmic chronology used for determining movement of freely active agent  $i$  is summarized in **Fig. E.3**. As illustrated in **Fig. E.3**, the movement of free agents is updated after the contraction and unbinding outlined in **Fig. E.2**. In the remainder of this subsection, we detail the rules by which free agent motion is stepped, and then

derive Eqn. (E.1) for the effective pairwise edge repulsion felt by an agent due to a water node.

### **E.3.a Stepping free agent movement**

Mirroring the methods of Couzin and Franks (2003) [267] or Baumgartner and Ryan (2020) [266], we assign each free agent a preferred angle of movement,  $\theta_i$ , (as measured from the positive horizontal axis) prior to stepping its position. Here, this is achieved through the Vicsek model (Eqn. (6.1)) to capture experimentally observed local alignment effects [11]. Note that the directions of motion of free agents are dependent on those of the previous time step. Therefore, to initiate the movement of free agents at the start of the simulation (or whenever a structural agent transitions to a free agent) we assign each agent a random, instantaneous orientation,  $\theta_i \in [0, 2\pi]$  radians.

With the preferred angle of motion predicted, we assign every agent in the domain 18 DOF, which – in an equidistant hexagonal lattice– corresponds to two layers of nearest neighbors (here spanning  $2\zeta$ ). We opted to provide each node with 18 DOF based on three considerations: (1) the experimental observation that free ants frequently walk over one another, effectively passing  $2\zeta$  in one unit time; (2) the experimental observation that freely active ants may walk over voids in the raft of comparable dimensions to their own body length, effectively passing greater than  $1\zeta$  in one unit time; and (3) the realization that modeling free agents with 18 rotational DOF is roughly a threefold improvement in approximating the continuous space real ants occupy, over the 6 DOF offered by looking at only one layer of immediate node neighbors spanning  $1\zeta$ . The 18 DOF for each node are assigned in rank-order by

distance to neighboring nodes. To be a DOF, the neighboring node must reside within the distance,  $R_{DOF} \in (0, 2.5] \zeta$ , of the node of interest. To consistently achieve 18 DOF despite noise in the node distribution, the upper bound of this range was set  $1.25 \times$  greater than the distance needed to reach 18 nearest neighbors in a close-packed hexagonal lattice.

With the pool of DOF defined, we then calculate the relative angle,  $\vartheta_{ij}$ , of each  $j^{th}$  DOF with respect to the position of node  $i$  as measured with respect to the positive horizontal axis according to:

$$\vartheta_{ij} = \begin{cases} \text{atan2}(\mathbf{X}_j - \mathbf{X}_i), & y_j \geq y_i \\ 2\pi + \text{atan2}(\mathbf{X}_j - \mathbf{X}_i), & y_j < y_i \end{cases}, \quad (\text{E.6})$$

where  $\mathbf{X}_j$  is the position of each DOF,  $\mathbf{X}_i$  is position of the freely active agent, and  $y_i$  denotes the y-axis component of  $\mathbf{X}_i$ . We then calculate the absolute difference between  $\theta_i$  and  $\vartheta_j$ :

$$\Delta\theta_{ij} = \begin{cases} |\vartheta_{ij} - \theta_i|, & |\vartheta_{ij} - \theta_i| < \pi \\ 2\pi - |\vartheta_{ij} - \theta_i|, & |\vartheta_{ij} - \theta_i| \geq \pi \end{cases}, \quad (\text{E.7})$$

and take the minimum value to indicate which neighboring raft or water node the freely active agent would preferentially move to. The pool of DOF are then rank-ordered from smallest to largest  $\Delta\theta_{ij}$  and sequentially checked for eligibility of movement. All eligible DOF must reside within the turning limit  $\vartheta_j \in [-\pi/2, \pi/2]$  as discussed earlier. Structural DOF are only eligible if they are unoccupied by other free agents. Water DOF are eligible only if the edge deposition condition (Eqn. (6.5)) is satisfied. The free agent is stepped to the first DOF in the rank-ordered pool that proves eligible. In the case that no DOF are eligible, the agent pauses according to the following section. To eliminate bias and ensure randomization, the order in which the free agents' motions are updated is randomly determined at every timestep.

### E.3.b Pausing surface traffic

While updating the positions of a freely active agent, we run into cases where the pool of potential movement DOF is exhausted, and movement is interrupted. This occurs when all the DOF within the turning limit ( $\vartheta_{ij} \in [-\pi/2, \pi/2]$ ) are either occupied structural agents, or water nodes that do not satisfy the edge deposition condition (Eqn. (6.5)). We generally observe that real ants whose trajectories are interrupted tend to pause and stationarily explore the environment in front of them for approximately 1 to 10 s before turning around (i.e., turning greater than  $\pi/2$  radians) to explore elsewhere. Therefore, in cases where no DOF meet the set of eligibility criteria and the free agent's motion is interrupted, the agent is paused for some random time,  $t_p$ , in the range of  $[2, 4]\Delta t$ . After this time has elapsed, the free agent's orientation is randomly redefined according to the process used at particle initiation and the agent is permitted to resume motion in an uncorrelated direction. This mechanism generates traffic jams in confined regions, such as areas with higher local free agent densities and those confined by the rafts' edges (e.g., the tips of protrusions). Yet this also ensures that these traffic jams (or clusters) are not permanent features in the simulations. Instead, they dissipate at time scales correlating to both  $t_p$  and the cluster or traffic jam size, thus ensuring that clusters occur as they do in experiments.

### E.3.c Effective repulsion at the edge

A freely active agent is defined as encountering the edge of the raft when its preferred DOF is a water node. This is tantamount to it encountering the water head-on, and amounts to an initial perception cone [263], [267] of roughly  $\pm 15^\circ$  given the 18

movement DOF in this framework. However, once a water node is detected as the preferred movement DOF, the full  $360^\circ$  environment within detection radius  $R$  is considered. This treatment serves to capture two experimentally observed tendencies of free ants: (1) that free ants moving tangent to but directly near the raft's perimeter seem unperturbed by the water's presence to their left or right, and (2) free ants whose movement is halted by encountering water head-on tend to reach out and probe their environment each direction before making a movement decision. In any case, the local change in substrate at the edge of the raft results in some effective edge repulsion for those free agents which detect it. To model this edge force, we define some energetic potential at the site of every structural agent ( $U_\rho$ ), and another at the site of every water node ( $U_\omega$ ). These potentials will map the energy landscape whose local gradient ( $-\nabla_r U$ ) represents the edge repulsion force  $\mathbf{F}^r$ .

To gauge this landscape, we first consider the 1D pairwise energy gradient between a freely active agent at node  $i$  and its  $j^{th}$  detected neighbor (reference **Fig. E.4**). Applying the simplest assumption that the gradient between each pairwise set of nodes evolves linearly, then the magnitude of the local pairwise force occurring on a free agent at node  $i$  because of node  $j$  is given as  $f_{ij} = -\Delta U_{ij}/r_{ij}$  where  $\Delta U_{ij}$  is the step in energy from nodes  $i$  to  $j$  and  $r_{ij}$  is the distance between their centers. We make the distinction between structural and water neighbors by replacing the index  $j$  with  $\rho$  and  $\omega$  to represent structural and water nodes, respectively, such that two separate types of forces emerge: forces due to adjacent water nodes,  $f_{i\omega} = -\Delta U_{i\omega}/r_{i\omega}$ , and forces due to adjacent structural nodes,  $f_{i\rho} = -\Delta U_{i\rho}/r_{i\rho}$ . Note that a freely active agent always occupies a structural site, such that the local energy is  $U_\rho$ . Therefore,  $\Delta U_{i\omega} = U_\omega - U_\rho$ , which we denote as  $\Gamma$  throughout this work (**Fig. E.4.A**). This also means that  $\Delta U_{i\rho} = U_\rho - U_\rho = 0$  and no effective force emerges due to neighboring structural

sites (**Fig. E.4.B**). In 2D, we consider that a freely active agent detects all neighboring nodes within detection distance  $R$  so that the effective edge repulsion experienced is approximately equal to the sum of all pairwise contributions from nearby water nodes, or:

$$\mathbf{F}_i^\Gamma = -\nabla_r U \approx -\Gamma \sum_\omega r_{i\omega}^{-1} \hat{\mathbf{r}}_{i\omega}, \quad (\text{E.8})$$

where  $\hat{\mathbf{r}}_{i\omega}$  is the direction of the pairwise separation vector  $\mathbf{r}_{i\omega}$ . In the numerical framework, wherein  $R$  is on the order of the contact length scale (i.e.,  $R/\ell \sim 1$ , as determined experimentally [11]) we recognize that the separation distances, are all given by  $r_{i\omega} \approx R$ . Thus, we may take  $\Gamma/r_{i\omega}$  as a constant,  $f^\Gamma = \Gamma/R$  and rewrite Eqn E.8 as:

$$\mathbf{F}_i^\Gamma = -f^\Gamma \sum_\omega \hat{\mathbf{r}}_{i\omega}. \quad (\text{E.9})$$

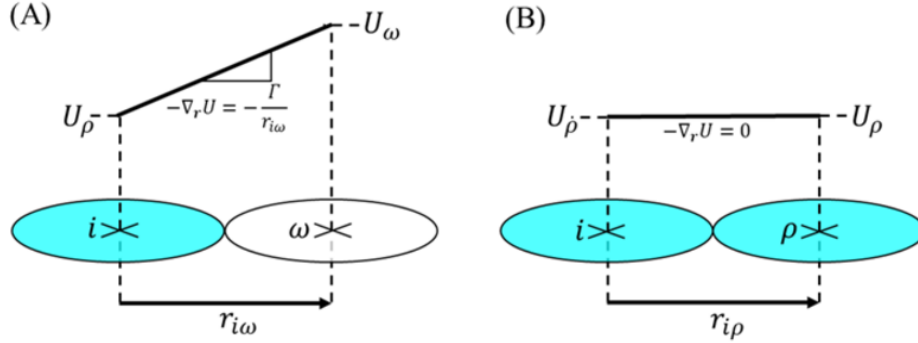


**Fig. E.4. Pairwise repulsive force.** (A) The origins of the pairwise repulsive force acting at the position of structural node  $i$  due to the proximity of water node  $\omega$  is illustrated in 1D. The force is taken as the gradient in energy landscape from  $\omega$  to  $i$ . (B) Similarly, the lack of any pairwise repulsive force acting at the positions between structural node  $i$  and structural node  $\rho$  is visually illustrated by the lack of a gradient in the local energy.

#### E.4 Model parameters

A summary of experimental and numerical values used throughout this work is provided in **Table E.1**. Experimental values of **Table E.1** were taken from Wagner, et al. (2021).

**Table E.1.** Commonly referenced values.

Symbol	Definition	Value	Units	Purpose
$\rho_r$	Planar density of structural ants.	0.30	ants mm <sup>-1</sup>	Used to define normalized length scale of model $\zeta$ .
$\zeta$	Occupancy length scale of one structural ant, $\zeta = \rho_r^{-0.5}$	1.8	mm	Defines model length scale.
$\ell$	Average body length of one ant.	2.9	mm	Used to normalize length scale of results.
$\dot{\epsilon}$	Contractile strain rate of the structural ant network.	1.6	% min <sup>-1</sup>	Used to calibrate the pairwise contraction rate $\dot{d}$ .
$\delta$	Exit rate of structural ants into the freely active layer.	$\sim 2 - 3$	% min <sup>-1</sup>	Matched between model and experiments to validate choice of $\dot{\epsilon}$ and exit threshold density $\rho_{thresh}$ .
$l_p$	Walking persistence length of free ants.	$\sim 20$	$\ell$	Used to calibrate noise parameter $\eta$ .
$v_0$	Mean free ant speed.	0.97	$\zeta$ s <sup>-1</sup>	Used to define timescale of model $\Delta t$ .
$\langle d \rangle$	Average distance traveled by free agent in one time step.	1.67	$\zeta$	Estimated as mean distance between adjacent movement DOF. Used to define $\Delta t$ .
$\Delta t$	Discrete timestep size, $\Delta t = \langle d \rangle / v_0$	0.6	s	Defines model time scale.
$\alpha$	Deposition rate of free ants into the structural layer at the edge.	$\sim 2 - 3$	% min <sup>-1</sup>	Used to identify when simulated rafts reached steady state treadmilling (when $\alpha \approx \delta$ ).

A summary of the model's free parameters is provided in **Table E.2**. The structural agent model contains just one free parameter, the contraction rate between nearest neighbors ( $\dot{d}$ ). However, this value was fixed to reproduce the global contraction rate,  $\dot{\epsilon}$ , of experimentally observed rafts [11]. The freely active agent model has three free parameters: (1) the radius of mutual influence between an agent and its nearest neighbors ( $R$ ); (2) activity ( $\mathcal{A}$ ); and (3) the noise parameter ( $\eta$ ). However,  $R$  and  $\eta$  were fixed to match the walking characteristics of experimental ants (See the Appendix E.5 section, below).



**Table E.2.** Free parameters of model.

Phase	Parameter	Type	Definition	Value	Units	Calibration
Structural State	$\dot{d}$	Fixed	Pairwise contraction rate between structural agents.	1.9	% min <sup>-1</sup>	Fixed to reproduce experimental global contraction rate.
Freely Active State	$R$	Fixed	Radius of mutual influence of surface agents.	$\leq 1$	$\ell$	Experimentally estimated as contact length scale between neighboring ants.
	$\eta$	Fixed	Noise parameter $\in [0,1]$	0.2	N/A	Fixed to reproduce experimental free ant trajectory persistence length.
	$L$ (or $\mathcal{A}$ )	Swept	Length scale defined by $L = \Gamma/f^a$ . Controls activity parameter through $\mathcal{A} = \ell/L$ .	$L \in [0.5,2]$ , $\mathcal{A} \in [3.2,0.8]$	$\ell$	Swept

## E.5 Model calibration

### E.5.a Pairwise strain

The numerical contractile strain rate was controlled using the parameter,  $\dot{d}$ , employed according to Eqn. (E.1). We calibrated  $\dot{d}$  by matching the global contractile strain and numerical exit rates ( $\dot{\epsilon}$  and  $\delta$ , respectively) to those of the experiments. Global decay was measured experimentally using particle image velocimetry on a rectilinear region of interest over a duration of 13 minutes and calculating the radial component of contractile speed,  $\dot{r}$ , towards the still reference frame (i.e., the stationary acrylic rod). A linear gradient in  $\dot{r}$  was found with respect to distance away from the stationary acrylic rod,  $r$ , suggesting a spatially constant  $\dot{\epsilon}$  [11] (**Fig. 6.3.A,C**). For a given experiment,  $\dot{\epsilon}$  was also found to be roughly constant in time, and isotropic [11]. The combination of spatially constant  $\dot{\epsilon}$  and isotropic contraction indicates that the mechanism of contraction occurs locally and homogenously throughout the bulk of the raft, rather than at a specific location such as the interface between the raft and the rod [11], hence the use of a locally applied pairwise contractile strain rate between neighboring structural agents. For the numerical results,  $\dot{\epsilon}$  was also

computed as the gradient in contractile speed towards the stationary raft point with respect to distance from said point (**Fig. E.3.B,C**). We found that  $\dot{\epsilon}$  matched between the model and experiments when  $\dot{d}$  was set to  $1.2 \times$  the desired global strain rate, likely due to affine effects within the network structure [268]. Note that the results presented in **Fig. E.3.C** of both experimental and simulated raft contraction represent the full data of 2D regions of interest but are projected onto one dimension (which is radial distance from the still reference point,  $r$ ).

### E.5.b Vicsek model parameters

The effects of altering  $R$  and  $\eta$  are illustrated through the phase table in **Fig. E.5**, wherein the surface traffic of freely active agents' in 2D domains with periodic boundary conditions is depicted at various values of these parameters. Note that to correctly mimic the conditions of the lattice model used in the raft framework, the agents are here also restricted to motion on a lattice, whose positions are set in a hexagonal close-packed configuration and then randomly offset by some amount  $\in [-1/6, 1/6] \zeta$  in each direction, as described above in Appendix E.1. Agent motion is also restricted to 18 DOF at every timestep and governed by the rules described in Appendix E.3. Moving from left to right, we see that the effect of decreasing  $\eta$  (or decreasing the rotational noise,  $\xi_i$  in Eqn. (6.1)) is to induce collective motion and directional flow. Likewise, moving from top to bottom, we see that increasing  $R$  (or increasing the range over which freely active agents are influenced by their neighbors) has a similar effect.

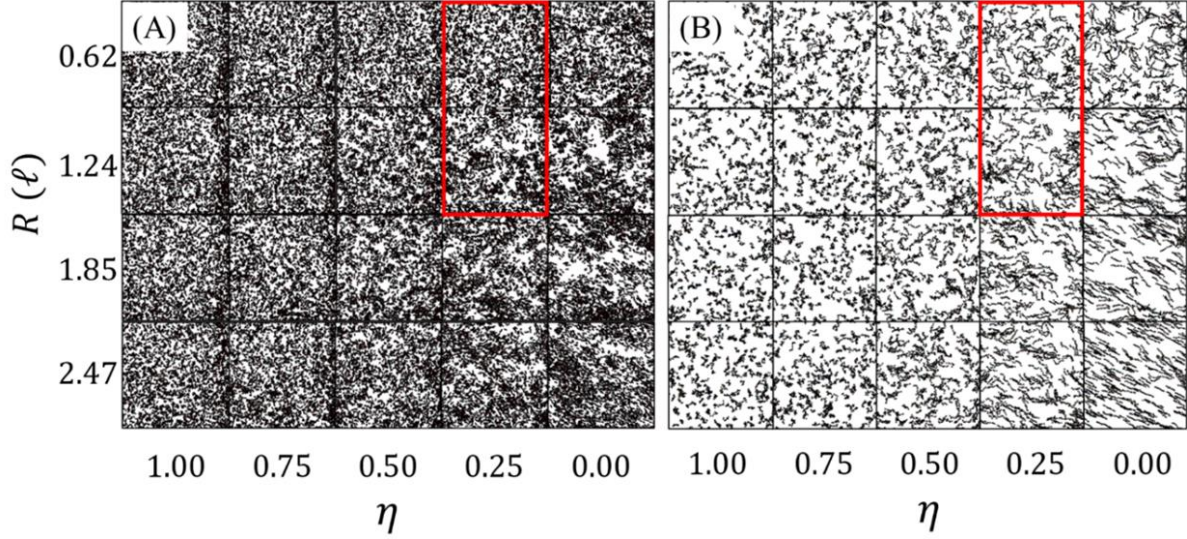


**Fig. E.5. Vicsek model phase diagrams.** Snapshots of the surface traffic of freely active agents in the numerical model are illustrated at a packing fraction of  $\phi = 0.24$ . The (A) full traffic, as well as (B) streamlines of just 10% of modeled agents composited from 10 time steps, are shown to illustrate the presence of clustering and directional motion, respectively. From top to bottom  $R$  is swept over the range  $R \in [0.62, 2.47] \ell$  and from left to right,  $\eta$  is swept over the range  $\eta = [1.00, 0]$  in increments of 0.25. The regional range that roughly matches experiments is outlined in red for each table. Although the agents' motions are confined to a lattice of nodes, the lattice is not depicted here for visual clarity.

From our previous work [11], we are aware that  $R$  is on the order of  $1 \ell$ , which gives us an estimation of the initial length-scale for the numerical value. Additionally, we found that the free ant trajectory persistence length,  $l_p$ , on the bulk of the raft is roughly  $15 - 20 \ell$ . Employing the method used in Wagner, et al. (2021), we also calculate  $l_p$  for simulated freely active agents in the parameter space given from **Fig. E.5**, yielding the heat map illustrated in **Fig. E.6**. Matching  $R$  and  $l_p$  to the approximate experimental values of  $0.9 \ell$  and  $15 \ell$ , respectively, we find that  $\eta \approx 0.2$ .

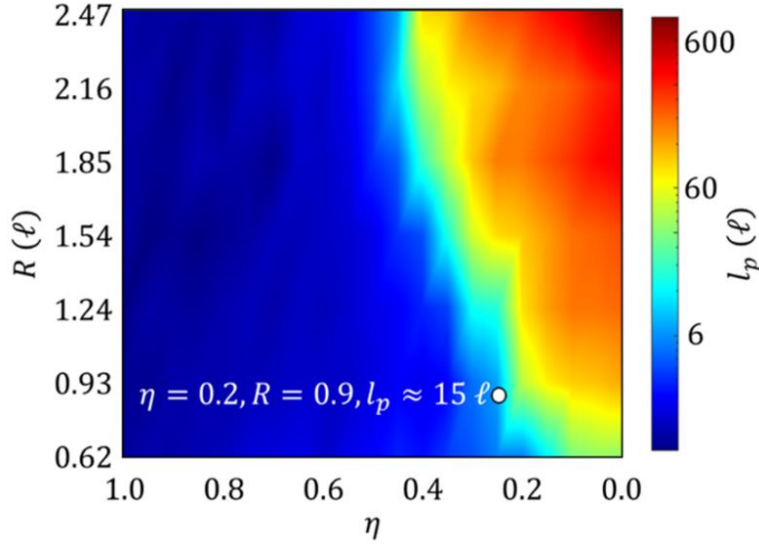


**Fig. E.6. Persistence length phase diagram.** An interpolated, 2D heat map illustrates how  $l_p$  evolves over the parameter space defined by  $R \in [0.62, 2.47] \ell$  and  $\eta \in [0, 1]$  in the numerical model. The point that matches the experimental data is plotted as a white dot.

### E.5.c Extended parameter sweep

With  $\eta$  set to 0.2,  $\mathcal{A}$  was swept over the range  $[0.81, 3.24]$ . The results presented in this manuscript were produced by fixing  $R$  at  $0.9 \ell$  to mimic experimental systems and examine the effects of local interactions only. However,  $R$  was supplementarily swept over the range of  $[0.62, 1.23] \ell$  to elucidate its effects on overall raft shape. Note that  $R \in [0.62, 1.23] \ell$  corresponds to  $R \in [0.5, 2] \zeta$  and  $\mathcal{A} \in [3.24, 0.81]$  corresponds to  $L \in [2, 0.5] \zeta$ , hence the respective choices for  $R$  and  $\mathcal{A}$  in this work. The extended phase table and heat maps of free agent packing fraction,  $\phi$ , and peak surface excess,  $S_{max}$ , are depicted in **Fig. E.7.A**, **E.7.C** and **E.7.D**, respectively. **Fig. E.7.B** depicts the combinations of  $R$  and  $\mathcal{A}$  that result in matching of  $S_{max}$  (red curve) and  $\phi$  (black curve) to those values from the experiments. While the two curves never intersect in the parameter space, this may be attributed to several factors including error in the

numerical measurement of surface excess and isotropic detection of neighboring agents within detection radius  $R$ .

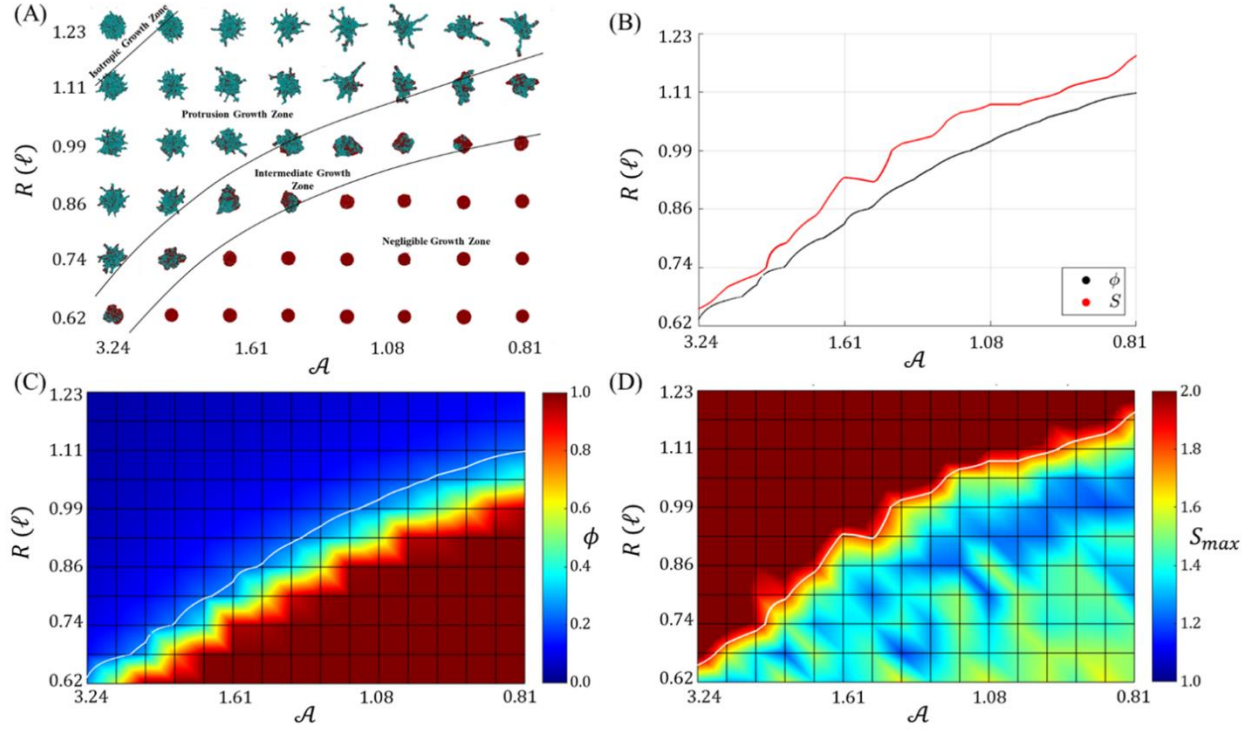


**Fig. E.7. Persistence length phase diagram.** (A) A phase table depicts the morphology of simulated rafts for different values of  $R$  and  $\mathcal{A}$  after approximately 1 hour of simulated time. (B) Interpolated curves with respect to  $R$  and  $\mathcal{A}$  depict the phase space in which the maximum surface excess  $S_{\max}$  (red) and packing fraction  $\phi$  (black) matched those of the experiments ( $\sim 1.8$  and  $\sim 0.24$ , respectively) to within 0.25%. (C) A heat map of  $\phi$  with respect to  $R$  and  $\mathcal{A}$  is shown with the white curve corresponding to the black curve from (B). (D) A heat map of  $S_{\max}$  is shown with respect to  $R$  and  $\mathcal{A}$  with the white curve corresponding to the red curve from (B).

## E.6 Measuring surface excess:

Recall that surface excess is calculated according to the relation  $S = C/(2\sqrt{\pi A})$ , where  $C$  is the raft's perimeter length and  $A$  is the raft's area. The way in which  $C$  is measured may significantly impact the estimated value of  $S$  due to the fractal nature of ant rafts' edges. Specifically, if the contour length is measured with resolution better than the length scale of the constituents' size, then  $C$  captures the surface roughness of the raft edge and is overestimated in accordance with the coastline paradox [285]. As such, a manual method of measuring  $C$  by tracing the perimeter of the raft in each frame using ImageJ [222], [224], [286] was preferred, as it allowed user discretion in capturing edge defects. This method was used for the experimental dotted line presented in **Fig. 6.6.C**, which coarsely estimates the maximum experimental surface excess on the order of 1.8.

Surface excess of numerical results was estimated by taking  $C$  as the number of structural agents on the perimeter and  $A$  as the total number of structural agents. This estimation of  $A$  is acceptable since the domain density is maintained at  $1 \text{ node } \zeta^{-2}$ , meaning each structural agent occupies a space of 1 square unit length. Similarly, this estimation of  $C$  relies on the fact that the nominal spacing between nodes is  $\sim 1 \zeta$ , such that adjacent structural agents in the perimeter may be assumed approximately 1 unit length apart. Perimeter structural agents were defined as agents with neighboring water nodes that reside within the threshold distance of nearest neighbors (i.e., are  $\leq 1 \ell$  or  $\leq 1.6 \zeta$  away). This method was used for expediency as it could be automated during simulation post-processing for the ensemble average presented in **Fig. 6.6.C**. However, the assumption of unit spacing ( $1 \zeta$ ) between adjacent edge agents may introduce error in the calculation of  $C$ .

To directly compare surface excess between experimental and model results, as done in **Fig. 6.6.K**, an alternative and controlled method was used. Both experimental and numerical videos of the raft evolution were imported into ImageJ and converted to binary images with the raft black and the background white. All black pixels that were not part of the raft were removed such that the raft was the only object in the image. Each image was then eroded twelve times to reduce surface roughness at the length scale of individual ants or agents, and then dilated twelve times to revert the rafts back to their original size. The image was then analyzed to measure  $A$  and  $C$  and calculate surface excess. Using this method for both the experimental and numerical results permits a more direct comparison between the two image sources.

It should be noted that regardless of the method employed, the fractal nature of ant rafts’ “coasts” ensures that surface excess is strongly impacted by the resolution with which  $C$  is measured [11]. While surface excess quantifies shape to some extent, it is here used to interpret qualitative and relative changes in global raft shape rather than draw absolute or quantitative conclusions.

## **E.7 Measuring tip radii**

To measure the radii of curvature of *in silico* rafts’ convex edges, the final frames of simulated rafts (for  $\mathcal{A} \in [0.81, 3.23]$ ) were uploaded into ImageJ [222], [224], [286]. Convex regions of edge curvature were visually identified, and the positions of each structural agent in the local vicinity were tracked using ImageJ’s “point tool”. Convex regions were mathematically delineated from their adjacent concave regions by inflection points in the local curvature with a moving average interval of  $(1\ell)$ . Data

outside the nearest inflection points was cropped. A circle was then fit to the remaining convex point data using the Pratt method [287], [288]. The radius of this circle was taken as the local radius of curvature,  $R_\kappa$ . If only one or two points remained within the dataset after cropping between inflection points (in which case the Pratt method would not work), then these regions were confirmed to contain just one or two agents and the corresponding radius was set to  $0.5 \ell$  or  $1 \ell$ , respectively. Once computed for every observation, the mean of all observations ( $\langle R_\kappa \rangle$ ) and standard error of the mean were calculated and reported in **Fig. 6.6.D**.